LMU LUDWIG-MAXIMILIANS-UNIVERSITÄT MÜNCHEN

Complex Transport Processes in Suspensions of Stiff Polymers

Tobias Munk

Dissertation

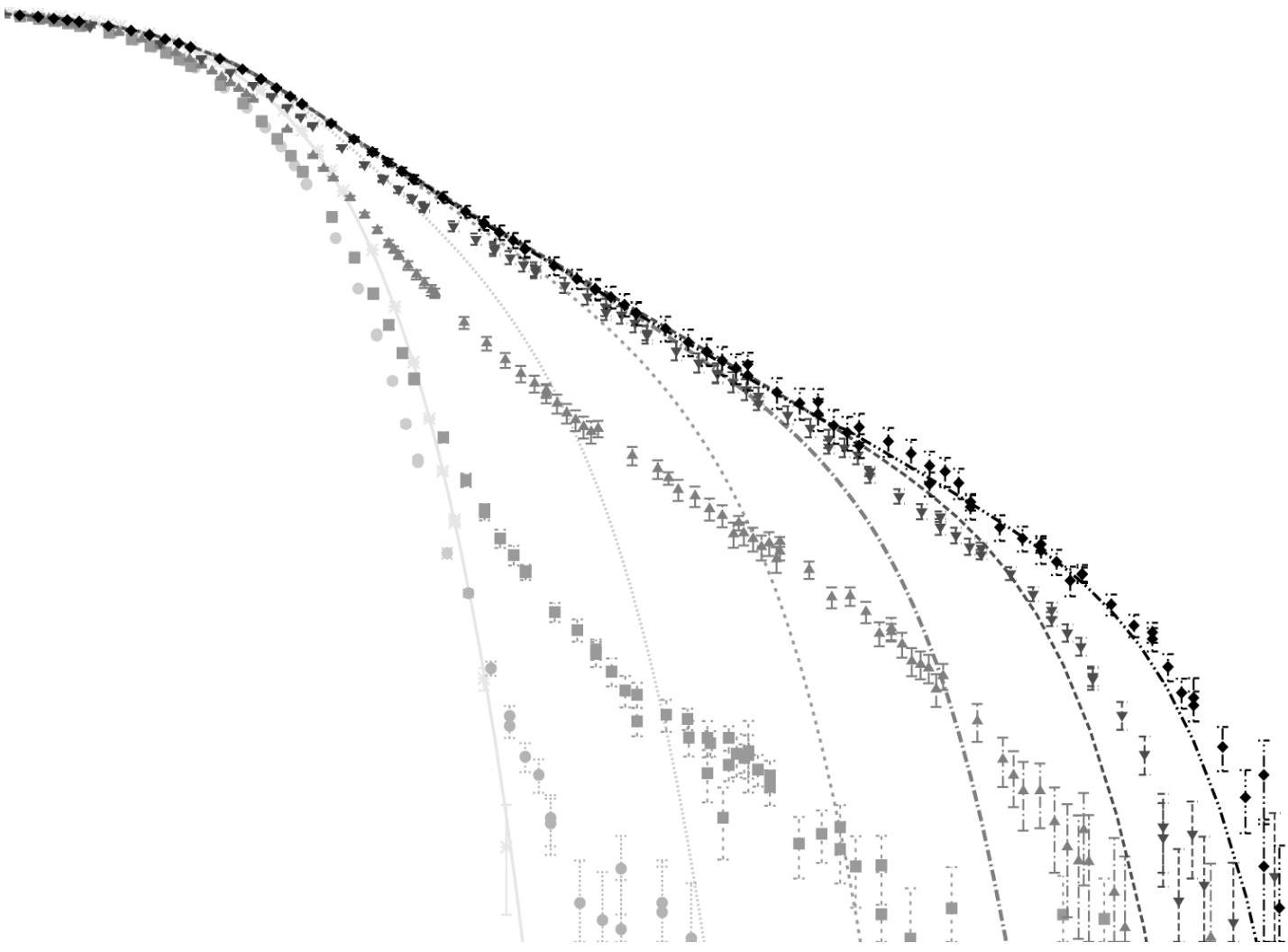

Complex Transport Processes in Suspensions of Stiff Polymers

Dissertation der Fakultät für Physik der Ludwig-Maximilians-Universität München

vorgelegt von

Tobias Munk

aus Osnabrück

am 10. Oktober 2008

Gutachter: Prof. Dr. Erwin Frey
Prof. Dr. Ulrich Gerland
Tag der mündlichen Prüfung: 18. November 2008

A veces tienes la suerte de encontrar una puerta abierta
raras veces encuentras detrás de esta puerta un mundo distinto, un horizonte nuevo
casi nunca consigues pasar por esa puerta.
Una vez tuve la suerte.

Zusammenfassung

Diffusive Transportprozesse auf der Nanometerskala spielen eine entscheidende Rolle für das Verständnis von kolloidalen Systemen jeglicher Art — in Anwendungen aus der Biologie sind sie gar von lebenswichtiger Bedeutung. In dieser Dissertation untersuche ich die Diffusion von Makromolekülen in verschiedenen Umgebungen anhand von drei typischen Modellszenarien.

Der zentrale Teil dieser Arbeit beschäftigt sich mit der Dynamik in Suspensionen dünner Stäbchen, wobei die Stabform eine Idealisierung anisotroper, länglicher Teilchen mikroskopischer Größe darstellt. Ein vereinfachtes Modell wird ausgearbeitet, welches das Problem auf die Bewegung eines einzelnen Stäbchens in einem zweidimensionalen Parcours von punktförmigen Hindernissen reduziert. Ich untersuche dieses Modell auf zweierlei Art: Zum einen habe ich Molekulardynamik-Simulationen entwickelt, die die Brownsche Bewegung des Stäbchens über neun Größenordnungen in der Zeit berechnen. Experimentell relevante Observablen werden dabei in statistisch exzellenter Qualität erfasst, u.a. die intermediäre Streufunktion mit einem Rauschpegel von 10^{-4}. Zum Zweiten formuliere ich eine analytische Beschreibung dieser Dynamik auf mesoskopischer Skala, basierend auf der Smoluchowski-Perrin-Gleichung der freien Diffusion. Erstmals präsentiere ich hierzu die geschlossene Lösung dieser Gleichung in zwei Dimensionen und zeige, dass man mithilfe der Messung zweier Diffusionskoeffizienten eine quantitative mesoskopische Theorie für Systeme mit Hindernissen gewinnt.

Der Vergleich der Simulationen mit der Theorie ermöglicht ein fundiertes quantitatives Verständnis der Dynamik in Suspensionen von Stäbchen, gekennzeichnet durch mehrere Zeit- und Längenskalen. Ich belege, dass die effektive Theorie bis hinab zu Längenskalen von der Größe des mittleren Teilchenabstands gültig ist und untermauere die bisher nicht verlässlich gestützten skalentheoretischen Vorhersagen von Doi und Edwards. Schließlich finde und erkläre ich ein intermediäres Potenzgesetz in den Streufunktionen. Dies interpretiere ich als ein neues generisches Charakteristikum der anisotopen Dynamik von Stäbchen in ungeordneten Suspensionen mit starker gegenseitiger räumliche Einschränkung.

In Ergänzung dieses Themenkomplexes beschäftigt sich der erste Teil der vorliegenden Arbeit mit dem diffusiven Transport in heterogenen Umgebungen fraktaler Geometrie — eine Fragestellung, die für die Dynamik beispielsweise in porösen Medien und in der sehr heterogen zusammengesetzten biologischen Zelle relevant ist. Im Rahmen des Lorentz-Modells bilde ich dieses Transportproblem ab auf die Diffusion eines einzelnen, isotropen Teilchens im Leerraum zwischen zufällig angeordneten harten Kugeln. Ich präsentiere umfangreiche Computersimulationen zusammen mit einer detaillierten Skalenanalyse der kritischen Dynamik in der Nähe des Perkolationsübergangs. In unmittelbarer Nähe des kritischen Punktes beobachte ich anomale Diffusion über vier Größenordnungen in der Zeit. Diese herausragende Genauigkeit ermöglicht die Darstellung der universellen dynamischen Skalenfunktion im sehr langsam konvergierenden Übergang zum anomalen Bewegungsgesetz, unter Einbeziehung universeller Korrekturen des Potenzverhaltens.

Der letzte Teil der Arbeit ist der Dynamik einzelner semiflexibler Filamente gewidmet, die z.B. im Zytoskelett der Zelle essentielle mechanische Aufgaben erfüllen. Die Bewegungsgleichung eines solchen Polymers in strömenden Flüssigkeiten drücke ich durch die Dynamik der Eigenmoden aus, unter Berücksichtigung der Zwangsbedingung longitudinaler Steifigkeit. Eine darauf aufbauende Analyse der Rotation eines Polymers in Scheerströmungen beleuchtet das charakteristische Verhalten der Modenspektren.

Zusammenfassend vertiefen meine Ergebnisse fundamental das Verständnis dynamischer Prozesse bei der Diffusion von Makromolekülen, mit konkreten Vorhersagen für auch experimentell messbare Größen. Besonders zu nennen ist hier die Streufunktion einer Suspension von Stäbchen, deren intermediäres Potenzverhalten ich als ein universelles Merkmal der Reptationsbewegung von Stäbchen ansehe.

Contents

Zusammenfassung v

1 Introduction **1**
1.1 Diffusion in heterogeneous environments 4
1.2 Anisotropic diffusion of strongly hindered rods 5
1.3 Mode dynamics of a semiflexible polymer 6

2 Critical dynamics of Brownian particles in a heterogeneous environment **7**
2.1 The Lorentz model 8
2.2 Transport on percolation networks 10
2.3 Simulation details 11
2.3.1 Ballistic particles 11
2.3.2 Brownian particles 12
2.4 Simulation results 13
2.4.1 Ballistic particles 15
2.4.2 Brownian particles 17
2.4.3 Dynamic scaling 18
2.5 Conclusion 20

3 The Smoluchowski-Perrin equation for the diffusion of rods **21**
3.1 Unhindered anisotropic motion 22
3.1.1 The scattering function 23
3.1.2 Orientational relaxation 24
3.2 Perturbation theory for the characteristic function 24
3.2.1 The integral equation with a force acting longitudinally 25
3.2.2 Perturbative solution 25
3.2.3 Unconstrained initial angle 28
3.3 Full solution for the intermediate scattering function 28
3.3.1 Scattering from the center of mass 30
3.3.2 Scattering from the whole rod 30
3.4 Brownian dynamics simulations of a freely diffusing rod 32
3.4.1 Comparison of simulations and Smoluchowski-Perrin theory 33
3.4.2 Intermediate scattering functions 35

4 Anisotropic diffusion in semi-dilute suspensions of rods **39**
4.1 A model for sterically interacting rods 39
4.2 Simulations of Langevin dynamics with point-like obstacles 41
4.2.1 Velocity-autocorrelation function 42

4.2.2 Convergence of the diffusion coefficients . . . 43
4.2.3 The emergence of anisotropic diffusion . . . 44
4.3 Entangled dynamics and the tube concept . . . 45
4.3.1 Conclusion . . . 48
4.4 Effective Perrin theory . . . 50
4.4.1 Anisotropic diffusion . . . 51
4.4.2 Driving by a longitudinal force . . . 54
4.4.3 Correlation functions of fourth order: non-Gaussian parameter . . . 55
4.5 Self-intermediate scattering function . . . 56
4.5.1 Origin of the power law . . . 59
4.5.2 Angle-resolved scattering . . . 61
4.5.3 Scattering from the whole rod . . . 61
4.6 Conclusion . . . 64

5 Dynamics of dilute semiflexible polymers in a flow field 67
5.1 A spectral method for single filaments . . . 68
5.1.1 Normal mode analysis . . . 71
5.1.2 Perturbation expansion . . . 72
5.2 Results from Brownian dynamics simulations . . . 74
5.2.1 Verification without flow field . . . 74
5.2.2 Motion in shear flow . . . 75
5.2.3 Statistics of tumbling in shear . . . 80
5.3 Effective bundle dynamics . . . 81
5.4 Conclusion . . . 83

6 Summary and outlook 85

Acknowledgment 87

A Short-time velocity correlations 89

B Supplementary material for the dynamics of a rod 93
B.1 Perturbation theory for the characteristic function: longitudinal force . . . 93
B.2 Equivalence of Smoluchowski and Langevin formulation . . . 94
B.3 Varying the microscopic ratio of the diffusion coefficients . . . 95

C Supplementary material for the dynamics of a semiflexible polymer 97
C.1 The Stochastic integration . . . 97
C.2 Eigenfunctions . . . 97

D List of publications 99

Bibliography 101

List of Figures

1.1 Images of tobacco mosaic viruses and Nanorods . . . 2
1.2 Polymer network of filamentous actin . . . 3
1.3 Electron tomogram of a yeast cell . . . 4

2.1 2D trajectory of a Brownian particle in the Lorentz model . . . 12
2.2 Convergence of the macroscopic diffusion coefficient in the Lorentz Model . . . 13
2.3 Velocity-autocorrelation function for Brownian dynamics at fixed density . . . 14
2.4 Mean-square displacement of the Lorentz model . . . 14
2.5 Critical power law close to the localization transition . . . 15
2.6 Critical behavior of the Mean-square displacement . . . 16
2.7 Non-Gaussian parameter for Brownian particles in the Lorentz model . . . 17
2.8 Scaling plots of the mean-square displacements . . . 19

3.1 Diffusion coefficients of a freely diffusing rod . . . 34
3.2 Mixed correlation functions of a freely diffusing rod . . . 34
3.3 Non-Gaussian parameters of a freely diffusing rod . . . 35
3.4 Intermediate scattering function (ISF) of the center of mass, for free diffusion . . . 36
3.5 ISF with rotational degrees of freedom, for free diffusion . . . 37
3.6 Scattering from the whole rod, for free diffusion . . . 37

4.1 Illustration of an entangled needle in a plane . . . 40
4.2 Velocity-autocorrelation function of a rod in a semi-dilute system . . . 42
4.3 Convergence of the rotational diffusion coefficient in the semi-dilute regime . . . 43
4.4 Typical trajectories of a needle in semi-dilute systems . . . 44
4.5 Rotational diffusion coefficient, proof of Doi-Edwards scaling . . . 46
4.6 Movie snapshots of the reptation dynamics . . . 47
4.7 Body-frame mean-square displacement in the entangled regime . . . 47
4.8 Density dependence of various diffusion coefficients . . . 48
4.9 Scaling of the tube diameter of the entangled needle . . . 49
4.10 Time domains in the mean-square displacement of a rod in semi-dilute systems . . . 50
4.11 Time-dependent diffusion coefficients in space-fixed frame, effective Perrin theory . . . 51
4.12 Second order crosscorrelation function . . . 53
4.13 Comparison of trajectory at high density and zero density . . . 53
4.14 Mean-square displacement of a rod with longitudinal force . . . 54
4.15 Diffusion coefficients of a rod with with longitudinal force . . . 54
4.16 Non-Gaussian parameter of rotation and center of mass translation . . . 55
4.17 Non-Gaussian parameter in the space-fixed frame . . . 55

4.18 Intermediate scattering function (ISF) of the center of mass of a rod 56
4.19 ISF for fixed wavenumber and varying density 57
4.20 ISF for four fixed wavevectors, validity of effective Perrin theory 58
4.21 ISF as a function of the wavenumber, for two semi-dilute densities 59
4.22 ISF as a function of the rescaled wavenumber 60
4.23 ISF with rotational degrees of freedom, at a large density 61
4.24 ISF for scattering from the whole rod, medium density 62
4.25 ISF for scattering from the whole rod, large density 63
4.26 ISF for the whole rod, fixed wavenumbers 64

5.1 Sketch of a semiflexible polymer 69
5.2 Mean squared amplitudes of the normal modes of a semiflexible polymer 74
5.3 Relative errors of the mean squared mode amplitudes 75
5.4 Time dependence of the mean-square displacement of the end-to-end distance . . . 76
5.5 Sketch of a semiflexible filament in shear flow 76
5.6 Sample trajectories for a filament in shear flow 77
5.7 Power spectral densities of the end-to-end distance 78
5.8 Power spectral density of the tension modes and the angular modes 79
5.9 Relative power spectral densities of a system with with shear flow 80
5.10 Tumbling frequency of semiflexible polymers in shear flow 81
5.11 Mode dependent stiffness of a semiflexible bundle, as a function of λ 82
5.12 Bending energy transferred to modes of a semiflexible bundle in elongational flow . . 83

A.1 Model for the collision of an isotropic Brownian particle with a wall 89
A.2 Velocity-autocorrelation function of a point-like particle moving between two walls . 91

B.1 Rotational diffusion coefficient of a rod for different microscopic diffusivities 95

Chapter 1

Introduction

For classical transport processes on the microscopic scale, one of the central paradigms of physics is in most cases irrelevant: energy conservation. All dynamics taking place in such systems is diffusive, i.e., the moving objects incessantly exchange energy with a heat bath. The resulting stochastic fluctuations always contribute dominantly to the dynamics, at least as long as lifelike systems are considered that are not principally driven by some energy input. This thesis is devoted to the theoretical understanding of such diffusive processes on the micro- and nanoscale, with the focus on models for the motion of macromolecules in heterogeneous environments.

Several properties of the molecules and their environment render the dynamics nontrivial and enrich substantially the picture formed by Robert Brown, Albert Einstein and other in the last centuries. From the point of view of a tagged diffusing macromolecule, the space it explores in real systems is usually filled with other objects, reducing the accessible volume considerably. Several materials found in nature even have fractal structure, such that the transport, taking place within, traverses routes of self-similar geometry. This alters fundamentally the laws of motion and induces phase transitions in the dynamic processes, in addition to the geometric percolation problem in the underlying static structure; both are controlled by the fraction of available volume. Turning the attention from the environment to the moving molecules themselves, their shape changes not only the individually preferred direction of motion due to friction—even more important, dense collections of markedly anisotropic objects evoke entanglement effects caused by the steric interactions among each other. In highly packed situations, the combined influences of shape and excluded volume also yield a variety of structural and dynamical phase transitions resulting in different nuances of reduced motility. Besides shape of the molecules and structure of the environment, the last feature we mention here having major influence on the dynamics are internal degrees of freedom of the diffusing objects. An example relevant for the motion of macromolecules are elastic deformations, like bend and twist, which may also have effects back on the aforementioned topics.

Given such an abundance of highly complex dynamic problems, the present work aims to deepen the understanding of one sample scenery that aggregates several of the mentioned aspects. Stiff polymers combine the interesting effects of an extreme shape anisotropy with internal elastic degrees of freedom—when suspended in solutions they constitute a strongly interacting system subject to complex dynamic and structural processes. Such highly anisotropic, rod-shaped objects of micrometer or nanometer size are numerous in nature and technology. Some examples are the tobacco mosaic virus, a nanometer sized virus of rodlike appearance, carbon nanotubes, a material remarkably versatile in physical properties, and asbestos fibers, fibrous crystals which

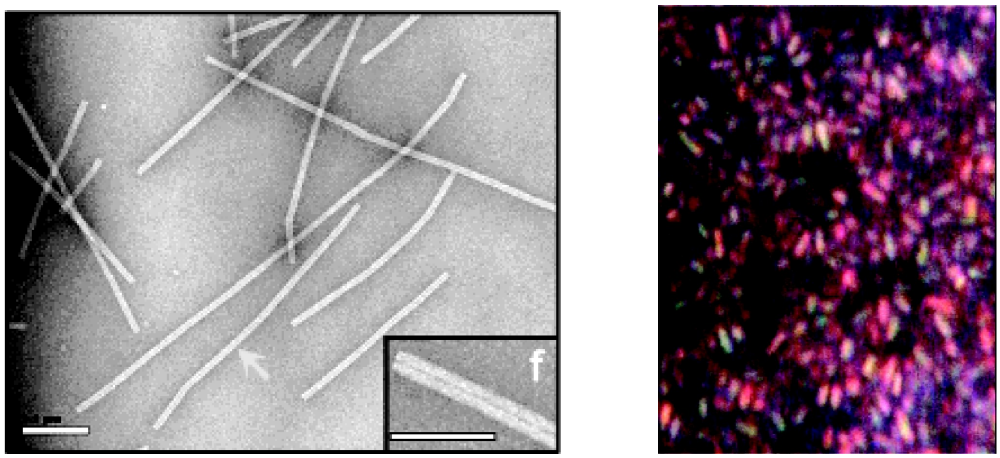

Figure 1.1: Left: TEM of labeled tobacco mosaic viruses. The scale bar represents 200nm in the big photo, 100nm in the small one. The aspect ratio varies from 15 to more than 50 [110]. Right: Optical microscope image of monodisperse Selenium rod-like colloidal particles of length 820nm and aspect ratio 3.6, at a particle volume fraction of 0.042 [105].

gained notoriety for serious health problems they cause when inhaled. An electron micrograph of tobacco mosaic viruses is shown in Fig. 1.1, revealing their strongly prolonged profile. In the same figure, a snapshot of an optical microscope shows ellipsoidal colloids as used for experiments disclosing some features of colloidal dynamics. In biology, various types of stiff filaments play a vital role for the mechanical stability and transport logistics of a cell. F-actin filaments for instance form the cytoskeleton, a randomly structured scaffold stabilizing the cell; furthermore, they are responsible for cell locomotion and build the mechanical frame for muscular activity. Microtubuli are another biological type of stiff rod-like macromolecules; they span across the whole cell, push it apart during cell division, and constitute a runway for motor proteins that are responsible for active transport within the cell. Fig. 1.2 exemplifies the emerging filamentous network structures by an image of a crosslinked F-actin network.

Here we want to concentrate on dynamic aspects of disordered suspensions of stiff polymers. Relating to the above-mentioned examples, this corresponds to the idealized situation of an isotropic disordered assembly of rodlike objects in solution, free to diffuse around apart from the steric interactions of the colloidal particles itself. The complexity of the task still is overwhelming, and this work, too, is not able to present a complete solution that embraces all different facets of the problem. Instead we deal with three model systems that isolate different fundamental components of the overall problem, this way elucidating basic building blocks that are essential for understanding the full system.

As the pivotal part we present an analysis of the anisotropic diffusion in dense suspensions of rods. We aim to expound and understand the implications of the dynamic interactions between the suspended particles; they yield mutual constraints on all partaking rods, restricting severely the dynamically accessible volume transverse to the orientation of the rods, whereas the longitudinal motility is affected much less. This is termed a spatial *entanglement*, in the non quantum mechanical meaning of the word, to be distinguished from structural phase transitions, that arise in suspensions of densely packed rods when the particle volume fraction becomes appreciable. These transitions to ordered phases often mask the dynamic entanglement, when not care is taken of a large enough aspect ratio—as a consequence few is known about these interesting dynamic

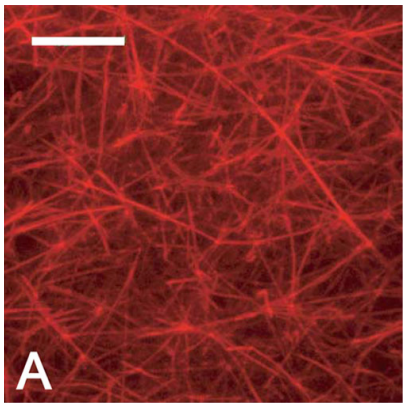

Figure 1.2: Confocal image (projection of 5μm height) of a F-actin network with fascin cross-links; the scale bar denotes a length of 10μm [134].

effects in isotropic suspensions. Since this is however an indispensable element of understanding suspensions of stiff filaments, we develop and evaluate a model system that pinpoints these properties. The model neglects elasticity and excluded volume, approximates the interactions by a single particle dynamics, and moreover reduces the dimension of the embedding space. These simplifications are a prerequisite to make possible an investigation on all relevant timescales—thereby we are able to formulate an effective theory that excellently describes the collective dynamics, far in excess of the approximations of the model.

In extension of this central part, two related problems with different focus pave the way for a more complex description of suspensions of stiff polymers. First, a model is evaluated that neglects the shape asymmetry of the diffusing particles, in favor of an elaborate examination of excluded volume effects. The model describes the motion of noninteracting isotropic particles in an environment with excluded volume of fractal structure. This environment represents the large class of heterogeneous materials, defined by internal length scales covering wide ranges in magnitude. The dynamics observed in such systems can be either diffusive, corresponding to a more or less unhindered motion, or localized, i.e., spatially constrained, or even anomalous, when the large range of length scales is reflected in a likewise width of time scales. An example where this becomes important also for the dynamics of stiff polymers is the internal structure found in biological cells, as visualized in Fig. 1.3: Apart from filamentous objects, the cell is filled with a large amount of proteins, membranes, vesicles, etc., such that diffusion within this molecular crowd can be modeled as an obstacle course of self-similar conformation. Usually, the characteristic timescales for the motion of the obstacles and that of the tracer particle are very different, hence the obstacle positions can be approximated as fixed on the scale of the moving particle. This leads to percolation problems for the trajectories in the accessible space, dealt with in the context of the Lorentz model. We exploit this model by computer simulations and a dynamic scaling theory close to the localization transition, substantiating also the relevance for real systems.

Finally, we examine another fundamental aspect of the dynamics of stiff polymers: the lateral elasticity of their backbone. Here, we consider dilute suspensions of semiflexible polymers, such that any interaction between different polymers can be neglected and only single filament dynamics is relevant. The standard model covering elasticity aspects of polymer dynamics is the wormlike chain model, where the integral of the squared local curvature is drawn on as a measure of the bending energy. We address a generic problem of computer simulations of this model: Simulations of stiff polymers in discretized real space encounter difficulties to follow the short time stochastic dynamics on the smallest contributing spatial scale, when simultaneously properties are to be measured that are relevant on timescales of several orders of magnitude larger. As an

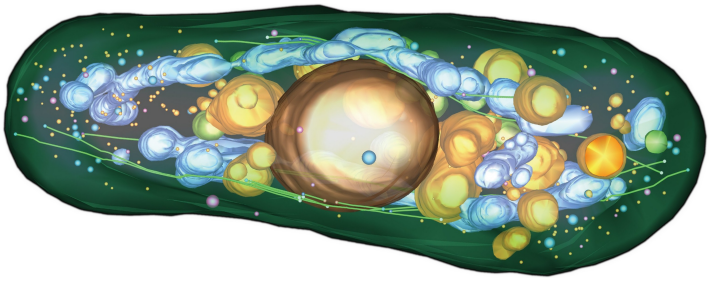

Figure 1.3: Three-dimensional visualization of an electron tomogram of a yeast cell, showing plasma membrane, microtubules and light vacuoles (green), nucleus, dark vacuoles and dark vesicles (gold), mitochondria and large dark vesicles (blue) and light vesicles (pink) [75].

alternative, we work out a formulation in mode space that naturally deals with the dynamics in the stiff rod limit. In this spatially continuous representation, the deviations of the conformation of a semiflexible polymer from the limit of a straight rod are calculated by accounting for the dynamics of the eigenmodes of successively smaller wavelength. This formulation might serve as an option to introduce flexibility effects in the theory of rod suspensions. As an additional benefit, it opens up the possibility for the simulation of the dynamics of bundles of stiff filaments, by means of the effective stiffness that can be attributed to a bundle of filaments. This way, the multi-particle dynamics of bundles is reduced to an effective single particle system.

The models under consideration in this theoretical work have in common the reduction of multi-particle dynamics to effective systems with only one particle moving. In the main part, this allows for the formulation of an effective theory for the dynamics of stiff rods, which we manifest to grasp all dynamic aspects above certain length and timescales. We argue in detail for the validity of these effective approaches, supported by preliminary simulations that inspect dynamic properties of the environment. Hydrodynamic interactions, and more specific, hydrodynamic backflow effects, are not discussed in any of the systems under consideration. Although of long-range, we expect them not to be of major influence on the problems in question [126]. Summarizing all the above, the findings of this thesis are gathered to contribute to the theoretical understanding of properties connected to, but not only relevant to the dynamics within suspensions of stiff polymers.

In the remaining part of this introduction we briefly summarize the contents of each of the three major parts of this thesis. The publications compiled so far from it are listed in Appendix D.

1.1 Diffusion in heterogeneous environments

In Chapter 2, we investigate the dynamic properties of a classical tracer particle in a random, disordered medium. In particular, we focus on the critical dynamics close to the localization transition, i.e., when the excluded volume in the disordered medium becomes so large that the particle gets trapped. To this end, we study a versatile model for transport in disordered environments that goes back to Lorentz: A pointlike particle moves in a three-dimensional environment randomly filled with hard spheres that can overlap each other.

For Lorentz models obeying Newtonian and diffusive motion at the microscale, we have performed large-scale computer simulations, covering up to 10 decades in simulated time. We demonstrate that universality holds at long times in the immediate vicinity of the transition, and deduce the critical power law of the diffusion coefficient. A thorough analysis of the dynamic scaling function of the mean-square displacement is worked out, describing the crossover from anomalous transport to diffusive motion. The dynamic scaling function is found to vary extremely slowly, and spans at least 5 decades in time. For its extraction, one has to allow for the leading universal correc-

tions to scaling, due to the slow convergence to the asymptotic regime. When comparing diffusive motion with Newtonian dynamics, the former is characterized by considerably longer transient regimes in the approach to the critical power laws, and requires also a substantially larger correction amplitude for the dynamic scaling.

Our findings suggest that apparent power laws with varying exponents generically occur and dominate experimentally accessible time windows as soon as the heterogeneities cover a decade in length scale—only the large range of time covered by our simulations allows for the reliable identification of the correct critical exponents. We extract the divergent length scales, characteristic for the continuous phase transition, and quantify the spatial heterogeneities in terms of the non-Gaussian parameter.

1.2 Anisotropic diffusion of strongly hindered rods

Slender rods in concentrated suspensions constitute strongly interacting systems with rich dynamics: Transport slows down drastically, caused by the topological constraints that neighboring filaments impose upon each other, and as a consequence, the anisotropy of the motion can become arbitrarily large. We set up a model system for the entanglement dynamics of stiff polymers, in which an infinitely thin needle explores a planar course of point obstacles. The model includes the essential interaction mechanism between rods, but still is simple enough to allow for the in-depth analysis by as well computer simulations as analytical methods.

A comprehensive theory for the dynamics of suspensions of rods is an open problem, and even the free diffusion of a single rod in a plane has not been solved until now. In Chapter 3, we present the solution of the Smoluchowski-Perrin equation for the diffusion of a rod in a two dimensions, anticipating its later evaluation as an effective theory. Complementary to the solution for the intermediate scattering function obtained this way, we work out a perturbative approach, yielding simple expressions for the moments. The chapter is completed by computer simulations of the free diffusion of a rod, validated in comparison with the analytical results.

The constrained dynamics of the entanglement model is scrutinized in Chapter 4. Large-scale simulations provide a quantitative foundation of the tube concept for stiff polymers, by proving the conjectured scaling relations from the fast transverse equilibration to the slowest process of orientational relaxation. We determine the rotational diffusion coefficient of the tracer, its angular confinement, and the tube diameter.

Based on the exact solution of the Smoluchowski-Perrin equation, we develop a mesoscopic description of the dynamics down to the length scale of the interparticle distance. It is in quantitative agreement with the Brownian dynamics simulations in the dense regime. In examining the mean-square displacement we exhibit the dynamic transitions between constrained motion inside the tube, anisotropic diffusion with strong coupling of rotation and translation, and ultimately, isotropic diffusion with density-dependent diffusion coefficients. The anisotropic motion entails notably non-Gaussian statistics, as revealed by a comparison of the non-Gaussian parameter with the predictions from the theory. In exploring the mesoscopic description we discuss in detail several experimentally relevant scattering functions. In particular, we show that the tube confinement is characterized by a power law decay of the intermediate scattering function with exponent 1/2.

1.3 Mode dynamics of a semiflexible polymer

Chapter 5 presents a novel method to investigate the dynamics of a single semiflexible polymer, subject to anisotropic friction in a viscous fluid. In contrast to previous approaches, we do not rely on a discrete bead-rod model, but introduce a suitable normal mode decomposition of a continuous space curve. Elastic energy of lateral bending is assigned to the filament according to the wormlike chain model, and boundary conditions are chosen to allow for free fluctuations in the solvent.

By means of a perturbation expansion for stiff filaments we derive a closed set of coupled Langevin equations in mode space for the dynamics in two dimensions. The formulation takes into account exactly the local constraint of inextensibility, and is evaluated to linear order in the mode amplitudes, but quadratically in the expansion parameter. The stochastic differential equations obtained this way are solved numerically, with parameters adjusted to describe the motion of actin filaments. We analyze the mode spectrum as well as the mean square displacement, the latter displaying the power law expected for semiflexible filaments. For the tumbling motion in shear flow, we find transient algebraic decays in the power spectral densities, and identify a crossover regime in the scaling of the tumbling frequency.

Chapter 2

Critical dynamics of Brownian particles in a heterogeneous environment

Heterogeneous materials abound in synthetic products and in nature; they are composed of domains of different materials or phases, with characteristic dimensions covering a wide range of length scales. A physical understanding of their macroscopic properties, such as mechanical elasticity, electrical conductivity, particle transport, or fluid permeability has far reaching consequences for applications in material science, nano-chemistry, oil recovery, and even biology. Examples include anomalous transport of tracers in porous soil columns [24], slow diffusion of sodium ions in sodium silicates [109, 158], and transport in colloidal gels close to gelation [1, 28, 125, 130, 167] In biology, the dense packing of differently sized proteins, lipids, and sugars in the cell cytoplasm is summarized as macromolecular crowding [36, 37, 60]. It leads to a suppression of diffusion with increasing molecular weight [6] and to anomalous diffusion [132], observed in eukaryotes [21, 59, 102, 148, 161] and bacteria [53].

Transport of tagged ions, macromolecules, or nanoparticles in such heterogeneous environments is strongly hindered, since the presence of a variety of components reduces the accessible volume to a small fraction of three-dimensional space. In computer simulations, one observes a drastic suppression of the diffusion coefficient by up to several orders of magnitude upon decreasing the porosity, i.e., the fraction of the non-excluded volume. There, the medium is often modeled by randomly placed obstacles [82, 143, 149, 157], but recent studies investigate also realistically reconstructed media, e.g., Vycor glass [77] and North Sea chalk [78].

In the above examples, three major transport phenomena are observed: normal diffusion, immobilization or localization, and anomalous transport. We will demonstrate in the following that all three aspects may be unified into the concept of transport in a disordered, heterogeneous medium with a percolation transition; such a transition entails a critical point with a divergent correlation length. The asymptotic behavior of this length scale in the critical region, together with the intrinsic properties at criticality, is encoded in the renormalization group flow; therefrom, all macroscopic observables (such as the diffusion coefficient) can be inferred in principle. This leads to the postulate of universality: systems sharing the same critical point exhibit the same universal scaling laws in the critical regime. Consequently, one expects a generic mechanism for slow, anomalous transport in a heterogeneous environment.

In a recent study on the Lorentz model, i.e., for a ballistic tracer in a porous medium, we have shown that a continuum percolation transition of the accessible volume is responsible for the suppression of the diffusion coefficient [72]. We have successfully applied the theory of critical dy-

namic scaling to explain the dynamics over many decades of time and length scales, covering a large range of porosities. This analysis will be extended and further substantiated here. In addition, we present simulation results for Brownian particles in a porous medium, modeling macroscopic particles, e.g., proteins, that experience thermal fluctuations from a solvent. Universality implies that the long-time behavior of dynamic observables close to the transition is independent of the microscopic details. It predicts that the critical exponents of the anomalous diffusion and the scaling of the diffusion coefficient are the same and moreover that the scaling functions coincide. The equivalence of ballistic and Brownian particles is well known for molecular and colloidal glasses [52], and it is expected to hold generally for slow dynamics. By a direct comparison of ballistic and Brownian particles, we test this hypothesis and give an estimate of the asymptotic scaling regime. The latter is essential for the interpretation of experiments, since it allows to assess the applicability of the asymptotic laws to a specific measurement window.

Let us summarize the different transport phenomena briefly. Diffusion is well known and understood since more than a century now [46, 65]. It is connected with Brownian motion, observed for a large particle kicked around by the surrounding gas or solvent molecules. The corresponding mean-square displacement grows linearly in time,

$$\delta r^2(t) := \left\langle \Delta \boldsymbol{R}(t)^2 \right\rangle = 2d\,D\,t, \tag{2.1}$$

where $\Delta \boldsymbol{R}(t)$ denotes the displacement of the particle after a sufficiently long time lag t, d is the space dimension, and $\langle \ldots \rangle$ an appropriate average. The phenomenon of localization is reflected in a plateau in the mean-square displacement, defining the localization length ℓ,

$$\delta r^2(t) = \text{const} = \ell^2. \tag{2.2}$$

Particles may be immobilized due to chemical binding, or they get trapped in cages formed by the surroundings.

Anomalous transport is certainly the most fascinating phenomenon among the three. Contrary to normal diffusion, it is not simply a consequence of the central limit theorem; in particular, it requires the non-trivial presence of either a broad distribution of time scales or long-ranged correlations [17]. The mean-square displacement exhibits a power law growth with a fractal exponent,

$$\delta r^2(t) \sim t^{2/d_\mathrm{w}}; \tag{2.3}$$

here we shall discuss subdiffusion, $d_\mathrm{w} > 2$. In most cases, it originates in one of two mechanisms: binding to finite traps with a broad distribution of binding rates, or confined motion in a spatially non-uniform, heterogeneous medium. Both scenarios may be easily distinguished experimentally, since binding rates obey an Arrhenius law in general, and thus, the dynamic coefficients are very sensitive to temperature changes. Steric interaction in contrast is insensitive to temperature and often conveniently modeled by hard potentials.

In the following two sections we first introduce the Lorentz model and collect some results from its connection to the theory of continuum percolation, essential for the subsequent analysis.

2.1 The Lorentz model

The Lorentz model is a generic model covering all of the above aspects of transport in a heterogeneous environment. It has attracted the attention of researchers in statistical physics over more than a century by now and was applied to various contexts. Lorentz introduced the model in 1905

as a microscopic justification of the Drude conductivity of a metal [98]: a non-interacting electron gas is scattered off randomly distributed ions. Equivalently, one may think of a single ballistic and point-like tracer particle with velocity $v = |\boldsymbol{v}|$, exploring the void space between randomly, uniformly, and independently placed scatterers of number density n. A hard-core interaction with the scatterers is usually employed, yielding impenetrable obstacles of radius σ. This interaction potential is equivalent to a tracer particle and obstacles sharing the same radius $\sigma/2$. The kinetic energy of the particle is conserved, and the unit time and length scales are set by σ and $t_0 := v^{-1}\sigma$, respectively. The only control parameter of the model is the dimensionless obstacle density $n^* := n\sigma^d$; it is directly linked with the porosity of the medium,

$$\phi = \exp(-4\pi n^*/3). \tag{2.4}$$

Statistical averages include different initial positions (restricted to the void space) and velocities (with fixed magnitude) and different realizations of the disorder; in particular, the tracer particle is not restricted to the percolating cluster.

Although the model is a deterministic system, the initial velocity of the particle is quickly randomized by subsequent collisions with the obstacles, yielding diffusive motion on large time scales. Such a stochastic trajectory may be thought of as a hopping process with a general distribution of waiting times $p_\tau(\tau)$ and displacements $p_{\boldsymbol{a}}(\boldsymbol{a})$, cf. Ref. 17. Provided that the first and second moments exist, uncorrelated steps generate diffusive motion on large time scales with diffusion coefficient

$$D = \frac{\langle \boldsymbol{a}^2 \rangle}{2d\langle \tau \rangle} = \frac{v^2 \langle \tau^2 \rangle}{2d\langle \tau \rangle}; \tag{2.5}$$

the second form refers to a ballistic particle with fixed kinetic energy. In the Lorentz model, the collisions constitute a Poisson process with average rate τ_c^{-1}, thus the waiting time distribution has first and second moments $\langle \tau \rangle = \tau_c$ and $\langle \tau^2 \rangle = 2\tau_c^2$, respectively. The mean collision rate follows from the condition to encounter no obstacles in a corridor of volume $\pi\sigma^2(v\tau_c) = 1/n$ in $d = 3$ dimensions, and thus $\tau_c^{-1} = \pi n^* v/\sigma$. Since the differential scattering cross-section for a sphere is isotropic, it corresponds to the transport cross-section describing the transfer of momentum; subsequent collisions are uncorrelated in the dilute limit, $n^* \to 0$. Under these conditions, Eq. (2.5) yields the correct diffusion coefficient [98],

$$D_0 = \frac{v\sigma}{3\pi n^*} \quad \text{for} \quad n^* \to 0, \tag{2.6}$$

recovering the leading order in an asymptotic low-density expansion [155, 160].

At finite densities, spatial correlations between obstacles induce persistent anti-correlations of the velocity, which are reflected in a negative tail of the velocity-autocorrelation function [39, 150], $\psi(t) = \langle \boldsymbol{v}(t) \cdot \boldsymbol{v}(0) \rangle / v^2 \sim -t^{-d/2-1}$ for $t \to \infty$. Since the integral over $\psi(t)$ is related to the diffusion coefficient, such a tail reduces D. The long-time tail can be thought of as a consequence of backscattering events preferring the return of the particle to its origin, emphasizing the importance of the topology of the obstacle matrix. The exponent of the tail is universal, i.e., it does not depend on the density of the scatterers. But as the density is increased, a pre-asymptotic, negative tail emerges, which suppresses the diffusion coefficient additionally [55, 56, 70, 100]. At a critical obstacle density n_c^*, the pre-asymptotic tail persists for all times, yielding exactly zero diffusivity.

At higher densities, diffusion is absent too: the tagged particle is trapped, and the mean-square displacement saturates. The transition from diffusion to localization has the signatures of a continuous phase transition; it exhibits power-law divergences of physical quantities with universal critical exponents. In particular, the diffusion coefficient vanishes with a power law upon approaching

the critical density,

$$D \sim |n^* - n_c^*|^\mu. \tag{2.7}$$

The localization transition was predicted by a mode-coupling approach [55, 56, 108] and by a mapping to continuum percolation [81, 104]. The direct link between the Lorentz model and continuum percolation, however, was established only recently [72]; it is substantiated further by the data presented in Section 2.4. Since the interpretation of the data depends on some results of continuum percolation theory, the next section summarizes briefly its central results; more details are found in Ref. 72 and Publication D.2.

2.2 Transport on percolation networks

In the Lorentz model, the transport of a particle in the percolating void space may be understood as a random hopping process between the nodes of the network with lattice constant ξ. Hence, the motion of such a particle is diffusive at scales much larger than the correlation length ξ. Note that ξ also characterizes the linear dimension of the largest finite clusters. Along the fractal chains of the network, however, the dynamics is slow and exhibits anomalous transport characterized by the walk dimension $d_w > 2$,

$$\left\langle \Delta \boldsymbol{R}(t)^2 \right\rangle_{\text{chain}} \sim t^{2/d_w}. \tag{2.8}$$

The time scale associated with ξ obeys $t_x \sim \xi^{d_w}$, and diffusion is observed for long times, $t \gg t_x$, with a coefficient according to Eq. (2.5). If the particle starts at *any* cluster, the diffusion coefficient is given by

$$D = P_\infty \xi^2 / t_x \sim |\epsilon|^\beta \xi^{2-d_w}, \tag{2.9}$$

where the factor P_∞ allows for the zero diffusion coefficient of particles on finite clusters, and the separation parameter ϵ is defined for the Lorentz model by $\epsilon := (n^* - n_c^*)/n_c^*$. Recalling $D \sim |\epsilon|^\mu$ from Eq. (2.7), and with the critical exponent ν of the correlation length, $\xi \sim |\epsilon|^{-\nu}$, the conductivity exponent is related to the walk dimension by

$$\mu = (d_w - 2)\nu + \beta. \tag{2.10}$$

In the above calculation, the diffusion coefficients of particles from different clusters were averaged. Instead of taking the cluster average in the end, one may average already the mean-square displacement. Then, the relevant dynamic length scale is the root-mean-square cluster radius [69, 72],

$$\ell \sim |\epsilon|^{-\nu+\beta/2}, \tag{2.11}$$

and anomalous transport is characterized by the dynamic exponent z different from d_w (Ref. 10),

$$\delta r^2(t) \sim t^{2/z} \quad \text{for} \quad t \ll t_x. \tag{2.12}$$

The crossover time scale t_x, being the same for all clusters, is not affected by the cluster average. It holds $\ell^z \sim \xi^{d_w} \sim t_x$, and therewith $D \sim \ell^2/t_x \sim \ell^{2-z}$, which yields a scaling relation connecting μ and z,

$$z = \frac{2\nu - \beta + \mu}{\nu - \beta/2}. \tag{2.13}$$

z is expected to deviate from its universal value on lattices for $d \geq 3$; moreover, z can be calculated from the geometric exponents ν and β which are believed to equal their universal lattice values [35]; in three dimensions, we use $\nu = 0.88$ and $\beta = 0.41$ throughout this work [140], evaluating Eq. (2.13) to $z = 6.25$.

2.3 Simulation details

Molecular Dynamics simulations allow for a direct numerical analysis of the dynamic properties of the Lorentz model without resorting to random resistor networks. Thus, a quantitative description over the full density range becomes accessible. Ballistic trajectories are produced by means of a standard simulation algorithm already employed by Bruin [19]. It is combined with a method for calculating correlation functions online, optimized for exponentially large time scales. For Brownian particles, we have extended this simulation algorithm to include stochastic forces similar to recently discussed ideas [133].

2.3.1 Ballistic particles

We use an event-oriented simulation algorithm, since the tracer particle and the obstacles interact via a hard-core potential. The algorithm propagates the particle freely from collision to collision, in each case calculating the precise point in time of the next interaction with an obstacle. If the particle is located at $\boldsymbol{r}$ with velocity $\boldsymbol{v}$, it possibly hits a single obstacle in the coordinate origin after the time interval [1]

$$t_{\mathrm{coll}} = -\frac{b}{v^2} - \frac{1}{v^2}\sqrt{b^2 - v^2(r^2-\sigma^2)}, \tag{2.14}$$

where $b = \boldsymbol{v}\cdot\boldsymbol{r}$. If $b > 0$, the particle departs from the obstacle and no collision will take place. If the radicand becomes negative, the particle misses the obstacle. The particle is scattered specularly, its post-collisional velocity is

$$\boldsymbol{v}' = \boldsymbol{v} - 2(\boldsymbol{v}\cdot\hat{\boldsymbol{\sigma}})\,\hat{\boldsymbol{\sigma}}, \tag{2.15}$$

where $\hat{\boldsymbol{\sigma}} = (\boldsymbol{v}\,t_{\mathrm{coll}} + \boldsymbol{r})/\sigma$ specifies the surface normal at the collision point.

Therewith, the implemented algorithm is straightforward: In a preparation step, the obstacle positions and the initial phase space coordinates of the particle are chosen randomly from a uniform distribution, under the constraint that the particle starts in the void space and $|\boldsymbol{v}| = v$. To reduce the number of collision tests, the simulation box is divided into small cubic cells, on average containing one or two obstacles; only obstacles from the cell where the particle is located and from neighboring cells are considered. Then, repeated collision tests and propagation of the particle to the next collision point yield the trajectory.

Since a single trajectory can consist of several billion collisions, one easily runs out of computer memory if one would store the complete trajectory. An efficient blocking scheme ("order-n algorithm", see Ref. 45) takes care of this issue by arranging the trajectory on a logarithmic time grid and simultaneously calculating various correlation functions $C(t;t_0)$. The algorithm already averages over different time origins t_0 ("moving time average"), which are, however, not necessarily uncorrelated, especially for short time intervals $t - t_0$. Hence, we will not infer any estimate of the statistical error from this averaging procedure. Rather, a set of N_t trajectories with different initial positions for each of N_r different realizations of the obstacle disorder is simulated, and the statistical error is estimated from $N_t \times N_r$ independent measurements. At each density, we have simulated at least $N_r = 20$ realizations of the disorder. At intermediate densities, the total number of trajectories has been chosen $N_t \times N_r > 100$. This value has been increased up to 600 at very high densities, where the phase space is highly decomposed into small, disconnected parts.

[1] The numerical error can be reduced using $t_{\mathrm{coll}} = \min[q/v^2, (r^2-\sigma^2)/q]$, where $q = -b + \sqrt{b^2 - v^2(r^2-\sigma^2)}$ and $b < 0$. This formula avoids the calculation of the difference between two almost equal numbers which would occur for $b^2 \gg v^2(r^2-\sigma^2)$.

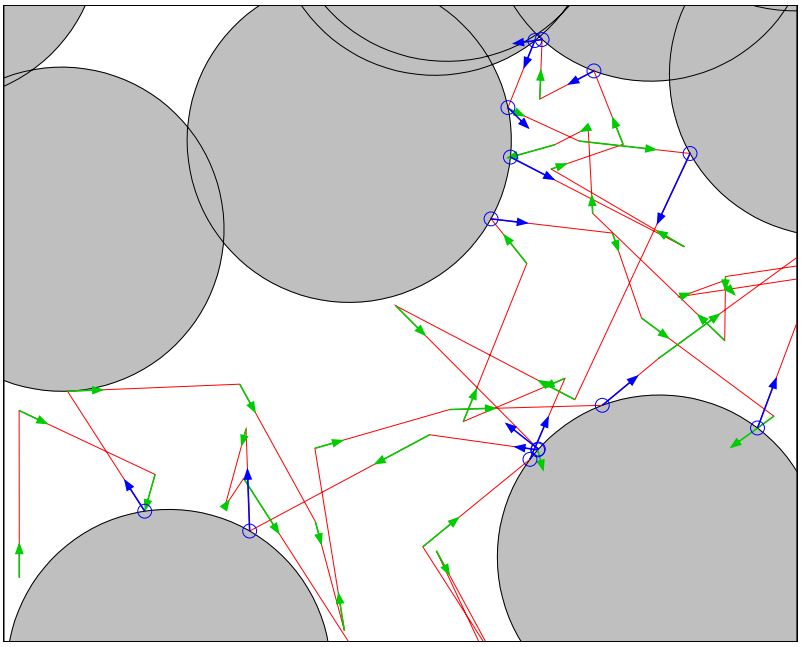

Figure 2.1: Typical particle trajectory in two dimensions, demonstrating the Brownian dynamics algorithm. Collisions with an obstacle are indicated by blue circles. Arrows indicate the direction and magnitude of the velocity after a collision (blue/dark) and after drawing a new velocity from the Boltzmann distribution (green/gray).

The longest trajectories span about 10^{10} collisions, the demand on CPU time for such a trajectory was about 15 hours on a single AMD Opteron 248 processor core.

All numerical results presented in this work refer to fixed dimensionality, $d = 3$. The simulation box has periodic boundaries, and its linear size was chosen as $L = 200\sigma$. A detailed finite-size analysis can be found in Publication D.2.

2.3.2 Brownian particles

When the pores between the obstacles are filled with some solvent, the tracer particle performs Brownian motion on microscopic time and length scales. By another Einstein relation, the solvent's friction coefficient and temperature yield the coefficient D_0^{B} of free diffusion. It may be combined with an intrinsic length scale in the system, e.g., the obstacle radius σ, yielding a microscopic time scale $t_0 := \sigma^2/D_0^{\mathrm{B}}$. All averages for Brownian particles will refer to the canonical ensemble throughout the article.

The overdamped dynamics of the tracer may be described by an effective stochastic force, caused by incessant collisions with solvent molecules. We have extended the above simulation algorithm by taking advantage of a coarse-grained scheme, where the ballistic trajectory is frequently interrupted by an equilibration with the solvent. After each fixed time interval τ_{B} a new velocity is assigned to the tracer particle, randomly drawn from the normalized Boltzmann distribution,

$$p_{\boldsymbol{v}}(\boldsymbol{v}) \propto \exp\left(-\frac{mv^2}{2k_{\mathrm{B}}T}\right). \tag{2.16}$$

Any hydrodynamic interactions are neglected. Such a simulation scheme for Brownian particles with hard-core interactions was carefully tested recently [133]; a similar approach was already studied by Alley [4], where the equilibration was restricted to the instants of particle collisions. Fig. 2.1 exemplifies the motion in two dimensions, demonstrating the velocity changes along the trajectory caused by events of collision and equilibration.

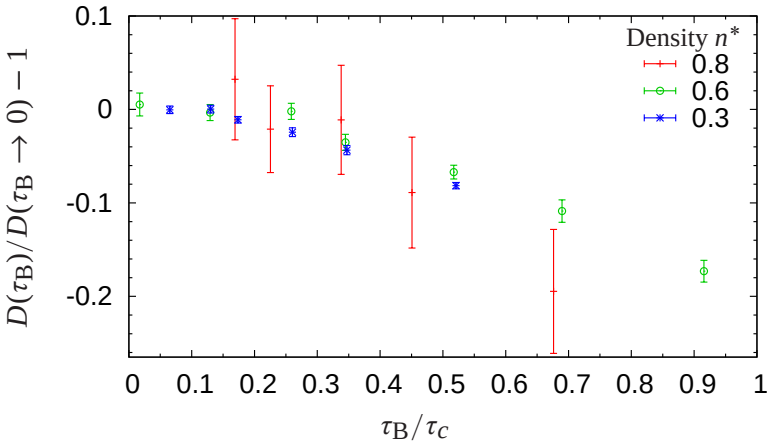

Figure 2.2: Convergence of the macroscopic diffusion coefficient of the Brownian particle for decreasing time interval τ_B at different densities. The limits $D(\tau_B \to 0)$ are estimated by averaging over results for $\tau_B \le 0.15\, v^{-1}\sigma$.

Without obstacles, the algorithm yields a τ_B-dependent diffusion coefficient, cf. Eq. (2.5),

$$D_0^B = \frac{\langle v^2 \rangle \tau_B}{2d} = \frac{k_B T}{2m}\tau_B. \tag{2.17}$$

The obtained motion is obviously only diffusive for times larger than τ_B. To model Brownian motion at all physically relevant time scales, one has to choose τ_B smaller than the shortest time scale of the system; in the present problem, this is the average time interval τ_c between collisions with obstacles. The dependence of the diffusion coefficient on τ_B is shown in Fig. 2.2. We consider the value of τ_B sufficiently small when the macroscopic diffusion coefficient does not depend on τ_B anymore, resulting in $\tau_B \approx 0.3\tau_c$ at criticality, $n^* = 0.839$.

Considering the velocity-autocorrelation function $\psi(t) = \langle \boldsymbol{v}(0) \cdot \boldsymbol{v}(t) \rangle / v^2$ for the combined algorithm of Brownian dynamics and ballistic collisions, one would naively expect that all correlations in the velocity vanish immediately for times $t > \tau_B$. This seems reasonable, since a new velocity drawn at random should be uncorrelated to the previous value. The presence of excluded volume, however, induces correlations for particles sufficiently close to an obstacle if the Brownian update interval and the mean interval between collisions are comparable, $\tau_B \approx \tau_c$. As a consequence, $\psi(t)$ shows periodic anticorrelations for times $t > \tau_B$, with the periodicity interval τ_B and an exponentially decaying amplitude. This effect is demonstrated in Fig. 2.3 for several different values of τ_B. Since the focus of this work is on the long-time properties, we defer a more detailed explanation to Appendix A.

2.4 Simulation results

We have simulated trajectories of ballistic and Brownian tracer particles over a wide range of obstacle densities, above and below the localization transition (Fig. 2.4). The mean-square displacement exhibits three distinct regimes: at short times, $t \ll t_0$, transport is not hindered by the obstacles, and the intrinsic dynamics of the particle is observed, either ballistic or Brownian. In both cases, this regime is followed by a regime of anomalous transport to be discussed in detail later. At large time scales, $t \gg t_x$, and below the localization transition, generic diffusive behavior is recovered. Above the critical density, the particles are trapped and $\delta r^2(t)$ is bounded by ℓ^2, the mean-square cluster size. At the critical density, the dynamics becomes neither diffusive nor trapped, and transport remains anomalous for all times.

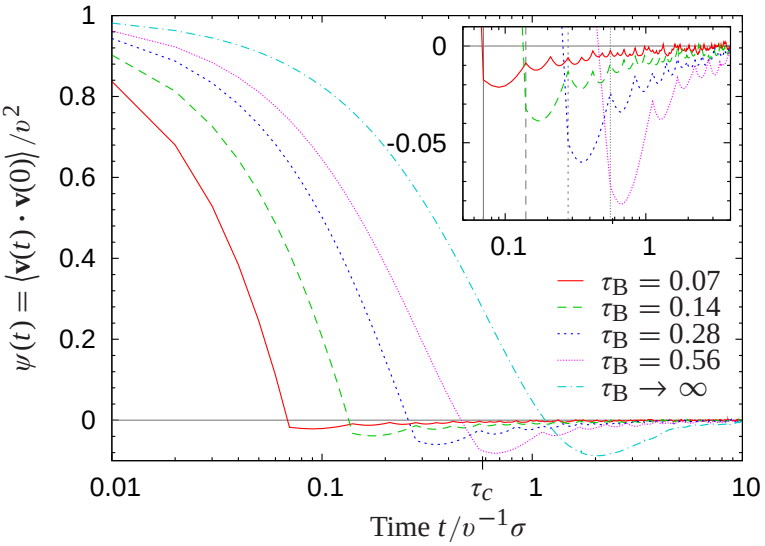

Figure 2.3: Velocity-autocorrelation function $\psi(t)$ obtained from the Brownian dynamics algorithm, at density $n^* = 0.6$. Simulation results are shown for four different time intervals τ_B and for the limiting case $\tau_B \to \infty$, equivalent to a ballistic particle. $\psi(t)$ does not vanish immediately for $t > \tau_B$, but oscillates with frequency $1/\tau_B$. On the x-axis, the mean collision rate τ_c^{-1} is also indicated, varying inappreciably with τ_B. Inset: magnification of the velocity anti-correlations; vertical gray lines indicate τ_B of the data with the corresponding dashing pattern. Note that the chosen τ_B are multiples of the smallest one.

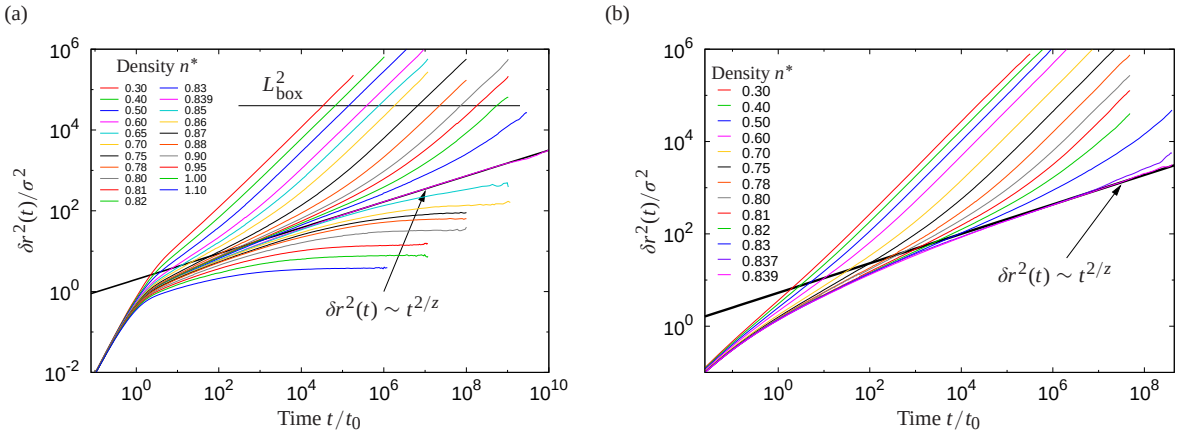

Figure 2.4: Mean-square displacement $\delta r^2(t)$ of the Lorentz model with (a) ballistic and (b) Brownian particles. The obstacle density n^* increases from top to bottom; thick black lines indicate the long-time asymptote for anomalous transport at criticality, $\delta r^2(t) \sim t^{2/z}$ with $z = 6.25$.

2.4.1 Ballistic particles

Let us discuss ballistic particles first. Diffusion coefficients were extracted from the mean-square displacements, $D = \partial_t \delta r^2 (t \to \infty)/6$. They vanish as a critical density n_c^* is approached from below according to a power law, $D \sim |n^* - n_c^*|^\mu$. The exponent μ could be fitted to these data; such a fit, however, depends on a simultaneous determination of the critical density n_c^*. We will rather use a theoretical prediction for μ that relies on the mapping to random resistor networks [D.2]; therewith, a first test of its validity is obtained. The central hyperscaling relation attained by the mapping has equivalently been proven by means of an expansion of the renormalization group equations to arbitrary order in $\epsilon = 6 - d$ [141], resulting in the relation

$$\mu = \max\left[(d-2)\nu + (1-\alpha)^{-1}, \mu^{\mathrm{lat}}\right], \tag{2.18}$$

where μ^{lat} is the universal exponent for lattice percolation. Eq. (2.18) together with the result $\alpha = 1/2$ from Machta and Moore [104] provides $\mu = \nu + 2 \approx 2.88$. This prediction is clearly corroborated by our results: in Fig. 2.5, the diffusion coefficient obeys the power law over five orders of magnitude, with a deviation of less than 15%.

The knowledge of μ allows to fit the critical density quite precisely by means of a rectification plot, showing $D^{1/\mu}$ against n^* on a linear scale; see Fig. 2.5c. We obtain $n_c^* = 0.839(4)$, which coincides with the percolation threshold of the void space [35, 80, 129, 152], $n_{\mathrm{perc}}^* = 0.8363(24)$. The interpretation is that the particle will eventually squeeze through any gap, no matter how narrow. There are no regions on a cluster which are too improbable to be visited by the particle after an infinitely long time. This means furthermore that the particle will diffuse as long as its surrounding phase space is connected with infinity.

In the localized regime, $n^* > n_c^*$, the long-time limit of the mean-square displacement directly yields the mean cluster radius, $\delta r^2(t) \simeq \ell^2$ for $t \gg t_\times$. Then, the correlation length ξ is easily accessible upon observing that the mean quartic displacement $\delta r^4(t) := \langle \Delta \boldsymbol{R}(t)^4 \rangle$ scales for long times

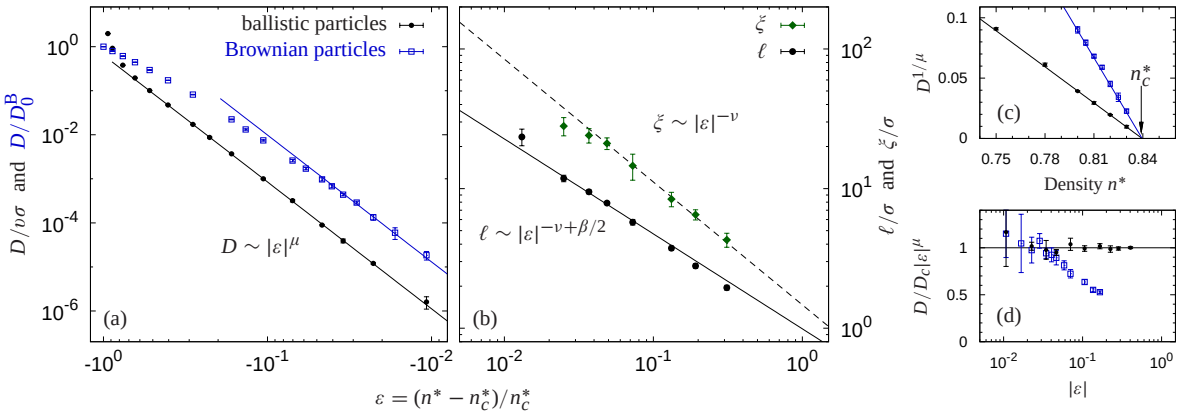

Figure 2.5: Critical power law behavior close to the localization transition; black closed symbols refer to ballistic particles, blue open squares to Brownian ones. (a) As the localization transition is approached, the diffusion coefficient D vanishes with exponent $\mu = 2.88$. Units are $v\sigma$ for ballistic and D_0^{B} for Brownian particles. (b) The localization length ℓ diverges with exponent $\nu - \beta/2$ and can clearly be distinguished from the correlation length, $\xi \sim |\epsilon|^{-\nu}$. (c) Rectification of the diffusion coefficient close to the critical density. Fitting a straight line to the closest five data points yields the critical density n_c^*. (d) Comparing D with its asymptotic behavior $D_c|\epsilon|^\mu$ on a semi-logarithmic scale reveals that the deviation from the power law is less than 10% for ballistic particles, except for the smallest data point.

as [72]

$$\delta r^4(t) \simeq \xi^2 \ell^2 \quad \text{for} \quad t \gg t_\times; \tag{2.19}$$

this relation is taken as definition for ξ. The extracted length scales ℓ and ξ diverge at the localization transition with exponents $\nu - \beta/2 = 0.68$ and $\nu = 0.88$, respectively, according to Eqs. (2.11) and (2.9); see Fig. 2.5b. The values for the exponents are taken from lattice percolation [140], and thus our data corroborate that the geometric exponents from lattices apply equally to continuum percolation [35]. Further, the localization length ℓ is identified with the mean-cluster size, as already anticipated by our notation, and clearly contrasted with the correlation length ξ. Both length scales are relevant for the dynamics as proposed in Ref. 72. In particular, our results corroborate the interpretation of the dynamic properties of the Lorentz model in terms of random walks on percolation clusters.

There is a competing prediction [63] $\mu = \nu + 3/2$, which is also found in text books [10]. A third, maybe naive guess suggests $\mu^{\text{lat}} \approx 2.0$, the universal value for lattice percolation in $d = 3$ dimensions [140]. We will allow for these alternative predictions by a sensitive and unbiased test based on Eq. (2.13), which relates the different values of μ to different exponents z for the anomalous transport. The latter can be inferred directly at the critical density $n^* = 0.839$ from the subdiffusive behavior of the mean-square displacement, growing as $\delta r^2(t) \sim t^{2/z}$ for long times, see Fig. 2.6. In the double-logarithmic plot, our data exhibit a slope manifestly smaller than expected from the alternative values for z. The data, however, collapse very well with a slope $2/z = 2/6.25$ corresponding to $\mu = 2.88$. For $t > 10^5 \sigma/v$, we find a deviation of the mean-square displacement from this asymptotic behavior by less than 7% over time scales spanning 4 decades, see inset. In conclusion, only the value $\mu = 2.88$ is consistent with our data, the other two candidates can clearly be ruled out. Hence, the hyperscaling relation, Eq. (2.18), with the value $\alpha = 1/2$ holds for the Lorentz model.

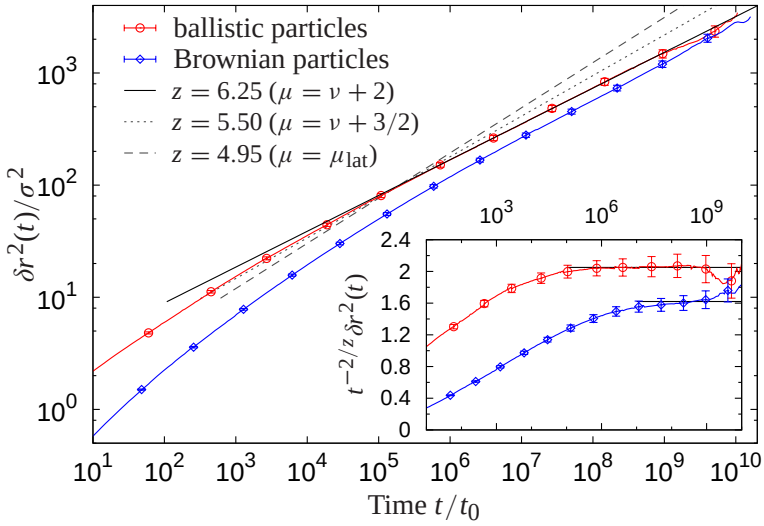

Figure 2.6: Critical behavior of the mean-square displacement at $n^* = 0.839 \approx n_c$ for ballistic and Brownian particles. Straight lines represent power laws $t^{2/z}$, where z is related to μ by Eq. (2.13). Three predicted values of μ are compared: the scaling relations $\mu = \nu + 2$ (Ref. 104) and $\mu = \nu + 3/2$ (Ref. 63) from Eq. (2.18) as well as the value on lattices, $\mu^{\text{lat}} = 2.0$. Our data are compatible only with the prediction by Machta and Moore [104]. Inset: as a most sensitive test, the same data are rectified employing $\mu = \nu + 2$; straight lines indicate the estimated long-time limits. The convergence for long times provides compelling support for this value of μ.

2.4.2 Brownian particles

For Brownian particles, the different microscopic dynamics becomes immediately apparent in the short time regime of the mean-square displacement, see Fig. 2.4b. While ballistic particles show a pronounced bending to diffusive or subdiffusive motion at the time scale of the collisions τ_c, Brownian particles are hardly effected by the obstacles at low densities. At higher densities, the excluded volume induces a transient subdiffusive regime again; the crossover from microscopic diffusion to the subdiffusive regime, however, is considerably more spread out.

From universality arguments one expects that the diffusion coefficient vanishes again at some critical density with a power law that has the same exponent μ as in the case of ballistic particles. Plotting $D^{1/\mu}$ against density n^* indeed yields a straight line, see Fig. 2.5c. In addition, one infers that the critical density for Brownian and ballistic particles is the same, emphasizing that the transition is due to geometric rather than dynamic effects. Yet the asymptotic power law is markedly slower approached as in the ballistic case.

The slow convergence for overdamped microdynamics is mostly pronounced in the mean-square displacement at criticality, see Fig. 2.6. For $t \approx 10^6 t_0$, it is still more than 10% off—about a factor 100 slower than for ballistic particles. Nevertheless, anomalous diffusion with the same dynamic exponent z is ultimately observed.

The spatially heterogeneous character of the medium renders the motion non-Gaussian, i.e., the distribution of particle displacements after a given time lag deviates from a Gaussian distribution. In supercooled liquids, dynamic heterogeneities have been quantified in terms of the non-Gaussian parameter [85], defined as [16]

$$\alpha_2(t) := \frac{3}{5}\frac{\delta r^4(t)}{\left[\delta r^2(t)\right]^2} - 1. \tag{2.20}$$

At moderate densities, the presence of the obstacles lets $\alpha_2(t)$ rise to values around 1 at intermediate times, until it decays to a finite value close to zero, see Fig. 2.7. This finite long-time limit is due to particles trapped in finite clusters; it diverges as criticality is approached. At criticality, the non-Gaussian parameter is predicted to grow with a power law [72], $\alpha_2(t) \sim t^{\beta/(2\nu-\beta+\mu)}$, as a consequence of the competition between the localization length ℓ and the correlation length ξ.

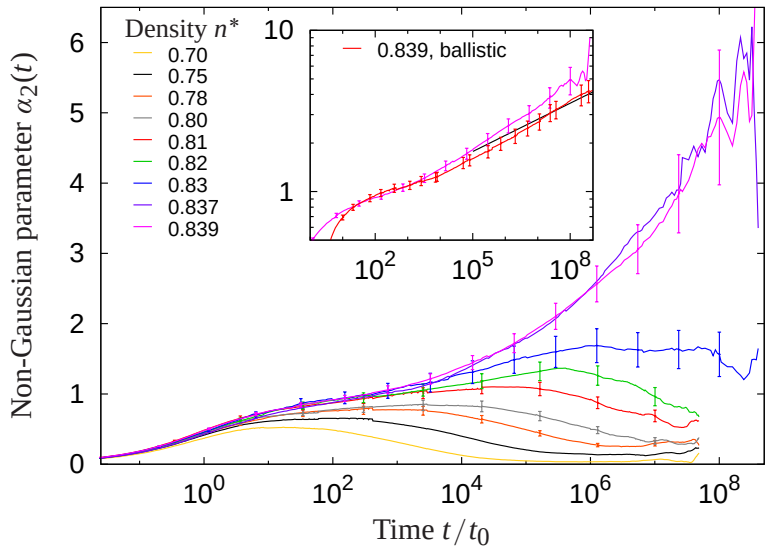

Figure 2.7: The non-Gaussian parameter for Brownian particles yields finite values in the long-time limit, and it increases substantially as the localization transition is approached. Inset: at criticality, $\alpha_2(t)$ grows with a power law in time; the predicted exponent 0.097 is indicated by a straight line.

Our data provide evidence for a strong increase of $\alpha_2(t)$ close to n_c^*, and a double-logarithmic plot yields straight lines. The predicted exponent is very small, $\beta/(2\nu-\beta+\mu) = 0.097$, and difficult to observe, but compatible with our data.

2.4.3 Dynamic scaling

A more stringent test of the universality of ballistic and Brownian particles compares dynamic scaling functions. The dynamic scaling ansatz for the mean-square displacement reads

$$\delta r^2(t;\epsilon) \simeq t^{2/z}\widehat{\delta r}^2_{\pm}(t/t_\times) \tag{2.21}$$

for $\epsilon \to 0$, $t \gg \tau_0$, and with the crossover time scaling as $t_\times \sim \ell^z$. Note that the relevant length scale for the mean-square displacement is the mean cluster size ℓ rather than the correlation length ξ, due to the infinite life time of the percolation clusters. The subscript $\pm$ at the scaling functions refers to the sign of ϵ, discriminating the different behaviors in the long-time limit. In the following, we will restrict the discussion to the diffusive regime, $\epsilon < 0$. The scaling function $\widehat{\delta r}^2_-(\hat{t})$ with $\hat{t} := t/t_\times$ interpolates between anomalous diffusion at criticality and normal diffusion for long times; thus

$$\widehat{\delta r}^2_-(\hat{t}) \simeq \begin{cases} A & \text{for} \quad \hat{t} \to 0, \\ A'\,\hat{t}^{1-2/z} & \text{for} \quad \hat{t} \to \infty. \end{cases} \tag{2.22}$$

The crossover time may be defined quantitatively by matching both regimes, $At_\times^{2/z} = 6Dt_\times$, implying that $t_\times \sim D^{z/(2-z)}$ for $\epsilon \to 0$. For ballistic particles, the diffusion coefficient observes nicely the asymptotic law $D \sim |\epsilon|^\mu$, see Fig. 2.5d, and plotting $\delta r^2(t)/At^{2/z}$ vs. $t|\epsilon|^{2\nu-\beta+\mu}$ yields a satisfactory data collapse, see Fig. 2b in Ref. 72. For Brownian particles however, our data for the diffusion coefficients are not yet in the asymptotic regime and show significant deviations from this behavior. Rescaling the mean-square displacements with $t_\times$ in terms of ϵ is not expected to lead to data collapse. Instead, let us rescale time with the measured diffusion coefficients, $t_\times \propto D^{-(2\nu-\beta+\mu)/\mu}$, allowing for the deviations of D from its asymptotic behavior, see Fig. 2.8a; the exponent evaluates to $(2\nu-\beta+\mu)/\mu \approx 1.47$. All curves collapse in the diffusive regime ($\hat{t} \gg 1$) by construction; but in the critical regime ($\hat{t} \ll 1$), the data fan out, and asymptotic convergence to a constant may only be anticipated.

Such a behavior hints at corrections to the leading scaling behavior, which carry some fading reminiscence of the microscopic structure. One has to distinguish between analytic corrections, which depend, e.g., on the choice of the separation parameter, and universal corrections with non-integer powers (or logarithmic terms). In the case of ballistic particles [72], we have identified the leading correction as a universal power law, and excellent data collapse has been achieved in the critical regime too by allowing for these terms. We have argued that the scaling ansatz for the mean-square displacement including the leading correction reads

$$\delta r^2(t;\epsilon) \simeq t^{2/z}\widehat{\delta r}^2_{\pm}(\hat{t})\left[1 + t^{-y}\Delta_\pm(\hat{t})\right]. \tag{2.23}$$

The exponent y is universal and will be discussed below. The correction function $\Delta_\pm(\hat{t})$ is universal too, but unknown. At criticality, it reduces to a constant, $\Delta_\pm(0) =: C$, and the mean-square displacement obeys

$$\delta r^2(t;\epsilon=0) \simeq At^{2/z}\left(1 + Ct^{-y}\right). \tag{2.24}$$

The dynamic correction exponent y can be related to the static correction exponent Ω via the exponent relation

$$yd_\mathrm{w} = \Omega d_\mathrm{f}; \tag{2.25}$$

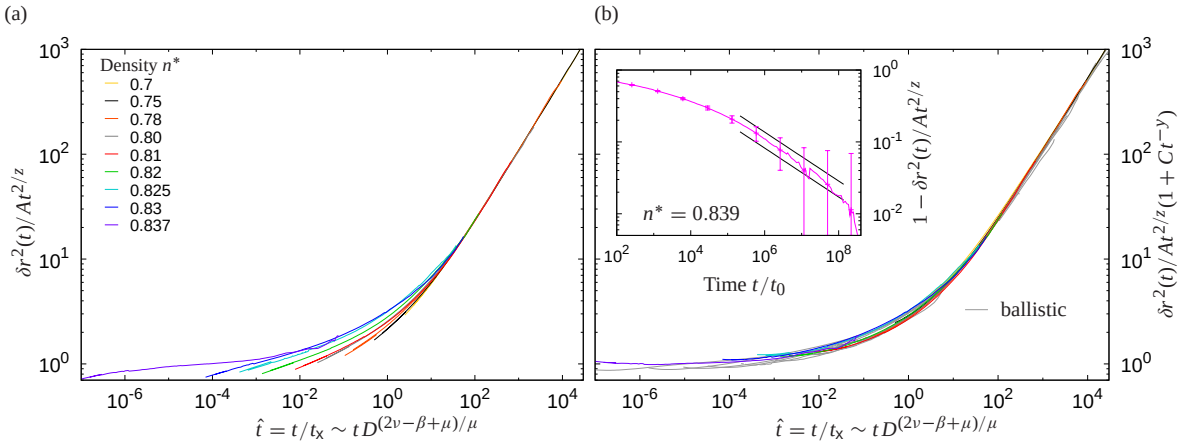

Figure 2.8: Scaling plots of the mean-square displacements for Brownian particles. Anomalous transport in the critical regime corresponds to a constant for $\hat{t} \to 0$. Time is rescaled with the measured diffusion coefficients. (a) Scaling at leading order: as $n^* \to n_c^*$, data converge to 1 for small $\hat{t}$, and an asymptotic data collapse may be anticipated. The amplitude A was determined from the inset of Fig. 2.6. (b) Inclusion of corrections to scaling at leading-order, Eq. (2.23) with $\Delta_-(\hat{t}) = C = -9.5t_0^y$, yields excellent data collapse onto the scaling function $\widehat{\delta r^2_-}(\hat{t})$. Rescaled and corrected mean-square displacements for ballistic particles ($C = -0.8t_0^y$) are added in gray from Fig. 2b of Ref. 72. The perfect match of Brownian and ballistic scaling functions substantiates universality of both systems. Inset: the corrections at criticality, $n^* = 0.839$, decay with a power law for long times, see Eq. (2.24). The exponent $y = 0.34$ is nicely corroborated over two decades in time, and the amplitude can be limited to the range $-9 \le Ct_0^{-y} \le -15$ (straight lines).

d_w denotes the walk dimension introduced in Eq. (2.3) and $d_f = d - \beta/\nu$ is the fractal space dimension. This relation has been derived by Höfling [69] within a cluster-resolved scaling theory for percolation. The main idea of the derivation is to consider a propagator for tracer particles restricted to clusters of size s. Including an irrelevant parameter of the propagator, similar as in Ref. 72, generates the leading dynamic correction, Eq. (2.23), as well as the leading correction to the cluster size distribution n_s,

$$n_s \sim s^{-\tau}\left[1 + O\left(s^{-\Omega}\right)\right] \quad \text{for} \quad s \to \infty, \tag{2.26}$$

with the Fisher exponent $\tau = 1 + d/d_f$. For lattice percolation in $d = 3$, the cluster size distribution has been analyzed with extensive Monte Carlo simulations [99], and the static correction exponent has been determined to $\Omega = 0.64 \pm 0.02$. Assuming that lattice and continuum percolation share the same geometric exponents, one calculates for the three-dimensional Lorentz model $y = 0.34$.

For ballistic particles, the corrections are dominant in the critical regime, and they are well described by approximating $\Delta_\pm(\hat{t}) \approx C$. The corrections to the diffusion coefficient are encoded in $\Delta_-(\hat{t})$ for large $\hat{t}$. They are not small for Brownian particles, and such a simple approximation will fail. But if these deviations are taken into account by hand as above, it seems reasonable to use $\Delta_\pm(\hat{t}) \approx C$ again. The value of C may be fitted at the critical density by means of Eq. (2.24), see inset of Fig. 2.8b. Our data corroborate the correction exponent over two decades in time, but the determination of C is hindered due to statistical noise; the data permit a range $9 \le C \le 15$ (in units $t_0 = 1$). Note that the correction amplitude is substantially larger than for ballistic particles, explaining the poor convergence to the long-time asymptote. Away from the critical density, we have rescaled the mean-square displacements again, taking into account the discussed corrections. Plotting $\delta r^2(t)/At^{2/z}(1 + Ct^{-y})$ vs. time rescaled with the measured diffusion coefficients in

Fig. 2.8b, the data collapse perfectly onto the the scaling function $\widehat{\delta r^2_-}(\hat{t})$.

The universality hypothesis predicts further that different systems are described by the same scaling functions, provided the latter encode the renormalization flow between the same two fixed points; in the present example, the fixed points are given by the critical point and the diffusive long-time limit. In Fig. 2.8b, we have also included the collapsed mean-square displacements for ballistic particles from Ref. 72. An excellent match with the data for Brownian particles is observed, including the crossover regime over more than 5 non-trivial decades in time. Whence the amplitude A and the diffusion coefficients are determined (cf. Figs. 2.5 and 2.6), no adjustable parameter enters the plot. One concludes that a single universal scaling function $\widehat{\delta r^2_-}(\hat{t})$ describes the crossover from anomalous to normal diffusion for both ballistic and Brownian particles.

2.5 Conclusion

The dynamics of ballistic and Brownian particles was investigated in a heterogeneous environment close to the localization transition. It has been demonstrated that both systems share the same phenomenology on scales where the microscopic details are not resolved anymore. We have further corroborated our previous findings that the localization transition is induced solely by a change in the topology of the medium: the percolation transition of the void space. Most importantly, our data substantiate that both Brownian and ballistic particles in a percolating medium belong to the same dynamic universality class. Taking into account the leading corrections to scaling, we have extracted the universal scaling function for the crossover from anomalous, subdiffusive transport to normal diffusion. The crossover is found to vary remarkably slowly, spanning at least 5 decades in time. In addition, it is an interesting observation that the asymptotic regime is much slower approached by Brownian particles; this statement refers equally well to the asymptotic behavior of the mean-square displacement and to the suppression of the diffusion coefficient upon approaching the localization transition. As a consequence, to observe the genuine asymptotic power law of the anomalous transport is an experimental challenge; very large time windows are required to distinguish universal behavior from transient crossover phenomena.

Although the divergent length scales ℓ and ξ cover only a decade in the investigated parameter regimes, we find anomalous transport already over many decades in time. These findings suggest that in experimentally accessible time windows, it is likely to observe apparent power laws with varying exponents, even if the spatial heterogeneities extend just over a decade in length scale. In particular, the Lorentz model provides a generic mechanism for anomalous transport in spatially heterogeneous media.

As mentioned in the introduction, protein transport in cells is anomalous due to the macromolecular crowding. For possible applications to such highly complex systems, the robustness of the presented scenario has to be discussed. Since the constituents of a cell interact certainly not via a hard potential, it is tempting to replace the obstacles by soft spheres. As long as the kinetic energy of the (ballistic) particle is fixed, the dynamics of a single hard particle, however, can be mapped one-to-one to a soft potential. A canonical ensemble seems more natural for a soft potential, but subsequent averaging with the Boltzmann weight smears out the transition and the critical properties since some fast particles can always overcome the obstacles. We have checked for the two-dimensional Lorentz model that this approach indeed reproduces simulation data for the diffusion coefficient [112].

Chapter 3

The Smoluchowski-Perrin equation for the diffusion of rods

Brownian motion of highly anisotropic particles is considerably more complex than the diffusion of spherical objects, which is essentially understood since the seminal works by Einstein and von Smoluchowski. A shape anisotropy results in diffusion coefficients that depend on the direction of motion in the body frame, thus inducing a coupling of translation to the orientation. This anisotropic dynamics has been investigated in recent experiments measuring diffusion coefficients of micrometer sized ellipsoids and rods by single particle tracking [12, 64, 116]; in particular, non-Gaussian statistics has been observed [64]. Likewise in dynamic light scattering, the rotational and translational diffusion coefficients were determined simultaneously [26]. For these dilute systems, the ratio of diffusion parallel and perpendicular to the long symmetry axis was limited to values up to $D_\parallel / D_\perp \approx 4$ in quasi two-dimensional confinement.

Considerably higher values of this ratio have been observed in simulations of semi-dilute suspensions of slender rods, yielding $D_\parallel / D_\perp$ up to values of 50 [14, 23]. This increase in anisotropy is caused by the steric constraints imposed by surrounding rods; thereby the transverse and rotational motion is suppressed, whereas the longitudinal transport is barely influenced [144]. An intermediate regime of anisotropic diffusion has been derived for ballistic needles within kinetic theory [119] and was observed in simulations [73].

For a finite width b, the rods undergo a phase transition to the nematic phase at densities of the order of $1/bL^2$ as predicted by Onsager [118]. The dynamics in this ordered phase becomes trivially anisotropic and splits into a fast diffusion along the nematic director axis and slower diffusion perpendicular to it. Such a pronounced anisotropic diffusion has been observed in simulations of nematic elongated ellipsoids [3] and spherocylinders [83, 101]. Experiments have also clearly demonstrated orientation-dependent diffusion in colloidal nanorods in the isotropic and nematic phase [151] and in various liquid crystalline phases of *fd* viruses [96, 97]. The phenomena connected with the nematic phase transition are essentially understood and will not be discussed here.

In the isotropic phase, experiments and computer simulations have been restricted to determine the diffusion coefficients from the mean-square displacements. The complex interplay of translational and rotational motion as exemplified for a single free ellipsoid [64] has not been studied for the strongly hindered motion in solution yet. In principle, one should characterize the dynamics in terms of an intermediate scattering function or a van Hove correlation function, as has been done recently for the smectic phase [96].

A general theory for the anisotropic motion of rods in entangled suspensions is a long-standing problem, due to the intricacy of the many-body interaction. In particular, such a theory should include memory effects from the translation-rotation coupling and explain the emergence of new macroscopic time and length scales. To account for phenomena which depend on the simultaneous interaction with many particles, a non-perturbative approach is required. Substantial progress would be achieved in terms of an effective one-particle theory that allows for quantitative predictions.

For this purpose, we work out in detail in the present chapter the single particle theory for a rod diffusing freely in a two-dimensional embedding space (Secs. 3.1-3.3), and the corresponding simulations of an unhindered motion (Sec. 3.4). In the subsequent Chapter 4 we then argue and substantiate quantitatively that this free theory can in fact serve as an excellent effective description for the dynamics in suspensions.

3.1 Unhindered anisotropic motion

Already at the level of a *single, free* rod the problem is involved; the theoretical description of the diffusion of rods goes back to the thirties of the previous century, when Perrin developed a theory for the motion of ellipsoids [123, 124], based on the work of Einstein [34] and Smoluchowski [139]. The full statistical information on the dynamics of a diffusing rod is encoded in the probability distribution

$$\Psi(\boldsymbol{R},\boldsymbol{u},t;\boldsymbol{R}_0,\boldsymbol{u}_0)=\left\langle\delta\big(\boldsymbol{R}-\boldsymbol{r}(t)\big)\delta\big(\boldsymbol{R}_0-\boldsymbol{r}(0)\big)\delta\big(\boldsymbol{u}-\boldsymbol{e}_u(t)\big)\delta\big(\boldsymbol{u}_0-\boldsymbol{e}_u(0)\big)\right\rangle, \tag{3.1}$$

with the the center of mass position $\boldsymbol{R}$, the orientational unit vector $\boldsymbol{u}$, and the initial coordinates $\boldsymbol{R}_0$ and $\boldsymbol{u}_0$ at time $t=0$, respectively. The corresponding time dependent variables for specific realizations of the ensemble are denoted by $\boldsymbol{r}(t)$ and $\boldsymbol{e}_{\boldsymbol{u}}(t)$. The central equation governing the time evolution of $\Psi(\boldsymbol{R},\boldsymbol{u},t;\boldsymbol{R}_0,\boldsymbol{u}_0)$ is the Smoluchowski equation, combining rotational diffusion and anisotropic translational diffusion [11, 31],

$$\partial_t\Psi=-D_{\rm rot}\hat{L}^2\Psi+\partial_{\boldsymbol{R}}\cdot\left[(D_\parallel-D_\perp)\boldsymbol{u}\,\boldsymbol{u}+D_\perp\mathbb{1}\right]\cdot\partial_{\boldsymbol{R}}\Psi, \tag{3.2}$$

where $\hat{L}^2$ denotes the angular part of the Laplacian. All microscopic parameters, i.e., temperature, length and diameter of the rod, and viscosity of the medium, are condensed in three transport coefficients: the diffusion coefficients for motion parallel and perpendicular to the instantaneous orientation $\boldsymbol{e}_{\boldsymbol{u}}$, $D_\parallel$ and $D_\perp$, and the corresponding one for rotation, $D_{\rm rot}$. The single time probability of a freely diffusing rod is a constant, since the problem is time-translation invariant as well as isotropic and homogeneous in a statistical sense, $\Psi_0:=\Psi(\boldsymbol{R},\boldsymbol{u})=\left\langle\delta\big(\boldsymbol{R}-\boldsymbol{r}(t)\big)\delta\big(\boldsymbol{u}-\boldsymbol{e}_u(t)\big)\right\rangle=1/(\text{volume of phase space})$. We focus in the following on the dynamics of the two-point conditional probability density $\Psi(\boldsymbol{R},\boldsymbol{u},t|\boldsymbol{u}_0)=\left\langle\delta\big(\boldsymbol{R}-\boldsymbol{r}(t)\big)\delta\big(\boldsymbol{u}-\boldsymbol{e}_u(t)\big)\right\rangle_{\rm f}=\Psi(\boldsymbol{R},\boldsymbol{u},t;\boldsymbol{R}_0,\boldsymbol{u}_0)/\Psi_0$, where the restricted average $\langle\cdot\rangle_{\rm f}$ includes only trajectories starting at the origin, $\boldsymbol{R}_0=0$, at time $t=0$ with an orientational vector $\boldsymbol{u}_0$; correspondingly, the initial condition reads $\Psi(\boldsymbol{R},\boldsymbol{u},t=0|\boldsymbol{u}_0)=\delta(\boldsymbol{R})\delta(\boldsymbol{u}-\boldsymbol{u}_0)$.

The full formal solution for the Fourier transform of Ψ in three dimensions was given in Ref. 5; its quantitative evaluation is still missing, although certain aspects are well understood [11, 31]. Equation (3.2) is trivially solved for isotropic diffusion, $D_\perp=D_\parallel$, and at macroscopic time scales, $t\gg 1/D_{\rm rot}$, where the translation-rotation coupling is relaxed. Then, the second term may be averaged over $\boldsymbol{u}$, yielding the average diffusion coefficient. To the best of our knowledge, the solution $\Psi(\boldsymbol{R},\boldsymbol{u},t)$ of the Smoluchowski-Perrin equation has not been discussed for two-dimensional

systems—this gap is filled in the present chapter. The angular configuration in two dimensions is represented by a single angle ϑ, with the orientational vector $\boldsymbol{u} = (\cos\vartheta, \sin\vartheta)$ and the differential operator $\hat{L}^2 = -\partial_\vartheta^2$. Note furthermore that the initial condition for the probability density, $\Psi(\boldsymbol{R}, \vartheta, t = 0|\vartheta_0) = \delta(\boldsymbol{R})\delta(\vartheta, \vartheta_0)$, contains a δ-function that is 2π-periodic in its argument.

3.1.1 The scattering function

The central quantity to be measured in simulations and scattering experiments is the constrained self-intermediate scattering function $F_{\mu\nu}(\boldsymbol{k}, t|\vartheta_0)$, representing the angle-resolved scattering response of the center of mass of the rod [11]; at the same time it serves as generating function for the moments of Ψ. The intermediate scattering function is the two-point correlation function of the Fourier transform of the particle density $\varrho(\boldsymbol{R}, \vartheta) = \delta(\boldsymbol{R} - \boldsymbol{r}(t))\delta(\vartheta - \theta(t))$,

$$F_{\mu\nu}(\boldsymbol{k}, \boldsymbol{q}, t) = \left\langle \varrho_\mu(\boldsymbol{k}, t)\varrho_\nu(\boldsymbol{q}, 0)^* \right\rangle = \left\langle \mathrm{e}^{-\mathrm{i}\boldsymbol{k}\cdot\boldsymbol{r}(t)}\mathrm{e}^{\mathrm{i}\boldsymbol{q}\cdot\boldsymbol{r}(0)}\mathrm{e}^{-\mathrm{i}\mu\theta(t)}\mathrm{e}^{\mathrm{i}\nu\theta(0)} \right\rangle. \tag{3.3}$$

Several symmetry properties simplify the analysis of the intermediate scattering function. Translational invariance requires that the function does not change when the spatial coordinates are shifted by a constant vector $\boldsymbol{a}$,

$$\begin{aligned} F_{\mu\nu}(\boldsymbol{k}, \boldsymbol{q}, t) &= \left\langle \mathrm{e}^{-\mathrm{i}\boldsymbol{k}\cdot[\boldsymbol{r}(t)+\boldsymbol{a}]}\mathrm{e}^{\mathrm{i}\boldsymbol{q}\cdot[\boldsymbol{r}(0)+\boldsymbol{a}]}\mathrm{e}^{-\mathrm{i}\mu\theta(t)}\mathrm{e}^{\mathrm{i}\nu\theta(0)} \right\rangle \\ &= \mathrm{e}^{-\mathrm{i}(\boldsymbol{k}-\boldsymbol{q})\cdot\boldsymbol{a}} \left\langle \mathrm{e}^{-\mathrm{i}\boldsymbol{k}\cdot\boldsymbol{r}(t)}\mathrm{e}^{\mathrm{i}\boldsymbol{q}\cdot\boldsymbol{r}(0)}\mathrm{e}^{-\mathrm{i}\mu\theta(t)}\mathrm{e}^{\mathrm{i}\nu\theta(0)} \right\rangle. \end{aligned} \tag{3.4}$$

Hence we conclude that the two scattering wavevectors measured from the initial and the final position have to coincide, $\boldsymbol{k} = \boldsymbol{q}$, and $F_{\mu\nu}(\boldsymbol{k}, t)$ is translational invariant in the center of mass. In the following, we usually set the initial position to the origin, $\boldsymbol{r}(0) = 0$, so the scattering function with unconstrained initial angle relates to the constrained one by

$$F_{\mu\nu}(\boldsymbol{k}, t) = \frac{1}{2\pi}\int_0^{2\pi} \mathrm{d}\vartheta_0\, F_{\mu\nu}(\boldsymbol{k}, t|\vartheta_0) = \left\langle \mathrm{e}^{-\mathrm{i}\boldsymbol{k}\cdot\boldsymbol{r}(t)}\mathrm{e}^{-\mathrm{i}\mu\theta(t)}\mathrm{e}^{\mathrm{i}\nu\vartheta_0} \right\rangle, \tag{3.5}$$

with the constraint one defined by $F_{\mu\nu}(\boldsymbol{k}, t|\vartheta_0) = \left\langle \mathrm{e}^{-\mathrm{i}\boldsymbol{k}\cdot\boldsymbol{r}(t)}\mathrm{e}^{-\mathrm{i}\mu\theta(t)}\mathrm{e}^{\mathrm{i}\nu\vartheta_0} \right\rangle_{\mathrm{f}}$. A similar symmetry argument concerning rotational invariance is less powerful, since a rotation R_ξ of the probe about an angle ξ couples changes in the center of mass vector and the angles,

$$F_{\mu\nu}(\boldsymbol{k}, t) = \left\langle \mathrm{e}^{-\mathrm{i}\boldsymbol{k}\cdot(R_\xi\cdot\boldsymbol{r}(t))}\mathrm{e}^{-\mathrm{i}\mu(\theta(t)+\chi)}\mathrm{e}^{\mathrm{i}\nu(\theta(0)+\chi)} \right\rangle = \mathrm{e}^{\mathrm{i}(\nu-\mu)\chi} \left\langle \mathrm{e}^{-\mathrm{i}\left(R_\xi^{-1}\cdot\boldsymbol{k}\right)\cdot\boldsymbol{r}(t)}\mathrm{e}^{-\mathrm{i}\mu\theta(t)}\mathrm{e}^{\mathrm{i}\nu\theta(0)} \right\rangle. \tag{3.6}$$

One concludes that $F_{\mu\nu}(\boldsymbol{k}, t)$ is diagonal in the helicities μ, ν only if $\boldsymbol{k} = 0$, and that the nondiagonal expressions are not translational invariant in the angle. We can, however, halve the number of matrix elements by considering the invariance of the two-dimensional dynamics of a symmetric rod with respect to a rotation about π:

$$F_{\mu\nu}(\boldsymbol{k}, t) = \left\langle \mathrm{e}^{-\mathrm{i}\boldsymbol{k}\cdot\boldsymbol{r}(t)}\mathrm{e}^{-\mathrm{i}\mu(\theta(t)+\pi)}\mathrm{e}^{\mathrm{i}\nu(\theta(0)+\pi)} \right\rangle = \mathrm{e}^{\mathrm{i}(\nu-\mu)\pi} \left\langle \mathrm{e}^{-\mathrm{i}\boldsymbol{k}\cdot\boldsymbol{r}(t)}\mathrm{e}^{-\mathrm{i}\mu\theta(t)}\mathrm{e}^{\mathrm{i}\nu\theta(0)} \right\rangle. \tag{3.7}$$

Thus $\nu - \mu = 2n, n \in \mathbb{Z}$, so $F_{\mu\nu}(\boldsymbol{k}, t)$ has only components with either μ and ν both even, or both odd.

Some more important symmetry relations for the scattering function in two dimensions can be found,

$$F_{\mu\nu}(-\boldsymbol{k}, t) = F_{\mu\nu}(\boldsymbol{k}, t), \tag{3.8a}$$

$$F_{-\mu,-\nu}(\boldsymbol{k}, t) = F_{\mu\nu}\big((k_x, -k_y), t\big), \tag{3.8b}$$

$$F_{\mu\nu}(\boldsymbol{k}, t) = F_{\nu\mu}\big((-k_x, k_y), t\big). \tag{3.8c}$$

The first one follows from the fact that a change of the sign of $\boldsymbol{k}$ is equivalent to a rotation about π, and the dynamics is invariant under such a rotation, as already utilized above. The second relation, Eq. (3.8b), is derived by a change of sign in the angles, which equals a reflection about the x-axis. Eq. (3.8c) finally exploits a change of sign in the angles and a reversal of time. The latter imposes a sign change in $\Delta\boldsymbol{r}(t)$, or, equivalently, in $\boldsymbol{k}$.

The dynamics of $F_{\mu\nu}(\boldsymbol{k},t)$ is analytically accessible via the characteristic function $G_{\boldsymbol{k}}(\vartheta,t|\vartheta_0)$, the spatial Fourier transform of the probability density,

$$G_{\boldsymbol{k}}(\vartheta,t|\vartheta_0)=\int \mathrm{e}^{-\mathrm{i}\boldsymbol{k}\cdot\boldsymbol{R}}\,\Psi(\boldsymbol{R},\vartheta,t|\vartheta_0)\mathrm{d}^2R=\left\langle \mathrm{e}^{-\mathrm{i}\boldsymbol{k}\cdot\boldsymbol{r}(t)}\delta\big(\vartheta,\theta(t)\big)\right\rangle_{\mathrm{f}}. \tag{3.9}$$

The scattering function relates to the characteristic function by essentially a Fourier transformation in the orientation,

$$F_{\mu\nu}(\boldsymbol{k},t|\vartheta_0)=\int_0^{2\pi}\mathrm{e}^{-\mathrm{i}\mu\vartheta}\mathrm{e}^{\mathrm{i}\nu\vartheta_0}G_{\boldsymbol{k}}(\vartheta,t|\vartheta_0)\mathrm{d}\vartheta. \tag{3.10}$$

Whenever the angular information is not in our focus, we will refer to the case $\mu=\nu=0$ by $F(\boldsymbol{k},t|\vartheta_0):=F_{00}(\boldsymbol{k},t|\vartheta_0)$. Similarly, for diagonal helicities one index is skipped, $F_\mu(\boldsymbol{k},t|\vartheta_0):=F_{\mu=\nu}(\boldsymbol{k},t|\vartheta_0)$.

The equation of motion of $G_{\boldsymbol{k}}$ is obtained from the Smoluchowski-Perrin equation (3.2),

$$\boxed{\partial_t G_{\boldsymbol{k}}=D_{\mathrm{rot}}\partial_\vartheta^2 G_{\boldsymbol{k}}-\left[D_\perp k^2+(D_\parallel-D_\perp)(\boldsymbol{k}\cdot\boldsymbol{u})^2\right]G_{\boldsymbol{k}}.} \tag{3.11}$$

This is the basic equation for all subsequent analysis.

3.1.2 Orientational relaxation

The pure rotational diffusion described by the Smoluchowski-Perrin equation (3.11) is solved straightforwardly, since it does not couple to the spatial degrees of freedom—a statement only valid in this direction. The decay of the correlation with respect to the initial orientation is obtained from the characteristic function for $\boldsymbol{k}=0$, resulting in a diffusion equation, $\partial_t G_0=D_{\mathrm{rot}}\partial_\vartheta^2 G_0$, with the initial condition $G_0(\vartheta,t=0|\vartheta_0)=\delta(\vartheta,\vartheta_0)$. The solution is found by a separation of variables

$$G_0(\vartheta,t|\vartheta_0)=\frac{1}{2\pi}\sum_{m=-\infty}^{\infty}\mathrm{e}^{-m^2D_{\mathrm{rot}}t}\mathrm{e}^{\mathrm{i}m(\vartheta-\vartheta_0)}, \tag{3.12}$$

where the summation over integer values of m reflects the periodicity in ϑ. Useful observables are those which share this property, hence all expectation averages are obtained as functions of

$$\left\langle \mathrm{e}^{-\mathrm{i}n\theta(t)}\right\rangle_{\mathrm{f}}=\int_0^{2\pi}\mathrm{e}^{-\mathrm{i}n\vartheta}G_0(\vartheta,t|\vartheta_0)\mathrm{d}\vartheta=\mathrm{e}^{-n^2D_{\mathrm{rot}}t}\mathrm{e}^{-\mathrm{i}n\vartheta_0}. \tag{3.13}$$

For measurable observables, only the real part of this expression is of concern. As an example, the orientational correlation function is obtained from $n=1$, $\langle\boldsymbol{e}_{\boldsymbol{u}}(t)\cdot\boldsymbol{e}_{\boldsymbol{u}}(0)\rangle_{\mathrm{f}}=\mathrm{e}^{-D_{\mathrm{rot}}t}$, provided $\vartheta_0=0$.

3.2 Perturbation theory for the characteristic function

Important information can already be obtained from Eq. (3.11) in the limit of $kL\ll 1$. This leads, e.g., to exact expressions for the moments $\langle[\Delta\boldsymbol{r}(t)]^n\rangle$. A perturbation theory in kL will serve this purpose.

3.2.1 The integral equation with a force acting longitudinally

Before proceeding to formulate Eq. (3.11) in a way suitable for a perturbative approach we briefly introduce an additional feature. The Smoluchowski-Perrin equation (3.2) can be extended to contain Hamiltonian or non-Hamiltonian external forces acting on the rod. Since experiments have been performed in which the rod is driven by a constant force F acting parallel to its axis [29], we include such a force in the analysis of this section; other forces can be treated similarly. To account for the parallel force $f := F/k_BT$, the term $-fD_\parallel \boldsymbol{u}\cdot\partial_{\boldsymbol{R}}\Psi$ has to be added on the right-hand side of Eq. (3.2). Correspondingly, the time evolution of the characteristic function becomes

$$\partial_t G_{\boldsymbol{k}} = D_{\mathrm{rot}}\partial_\vartheta^2 G_{\boldsymbol{k}} - \left[D_\perp k^2 + (D_\parallel - D_\perp)(\boldsymbol{k}\cdot\boldsymbol{u})^2\right] G_{\boldsymbol{k}} - \mathrm{i}fD_\parallel \boldsymbol{k}\cdot\boldsymbol{u}\, G_{\boldsymbol{k}}. \tag{3.14}$$

In defining the operators $\hat{\mathscr{H}}_0 := -D_{\mathrm{rot}}\partial_\vartheta^2$ and $\hat{V} = \hat{V}(\vartheta(t)) := D_\perp k^2 + (D_\parallel - D_\perp)(\boldsymbol{k}\cdot\boldsymbol{u})^2 + \mathrm{i}fD_\parallel \boldsymbol{k}\cdot\boldsymbol{u}$, the characteristic function obeys a Schrödinger equation in imaginary time,

$$\partial_t G_{\boldsymbol{k}} = -\hat{\mathscr{H}}_0 G_{\boldsymbol{k}} - \hat{V} G_{\boldsymbol{k}}. \tag{3.15}$$

We formalize the theory by introducing a Dirac notation, in which the characteristic function is the angular representation of a time-dependent operator, $G_{\boldsymbol{k}}(\vartheta,t|\vartheta_0) = \langle\vartheta|\hat{G}_{\boldsymbol{k}}(t)|\vartheta_0\rangle$. The bras and kets are orthonormal and complete, $\langle\vartheta|\vartheta'\rangle = \delta(\vartheta,\vartheta')$ and $\int_0^{2\pi}\mathrm{d}\vartheta\,|\vartheta\rangle\langle\vartheta| = \mathbb{1}$. It is favorable to change to a countable basis $|m\rangle$, by

$$\langle\vartheta|m\rangle = \frac{1}{\sqrt{2\pi}}\mathrm{e}^{\mathrm{i}m\vartheta}. \tag{3.16}$$

One checks that with these definitions $\langle m|n\rangle = \delta_{mn}$, and $\sum_{m=-\infty}^{\infty}|m\rangle\langle m| = \mathbb{1}$. This basis is chosen to represent an eigenbasis of the unperturbed operator in Eq. (3.15),

$$\hat{\mathscr{H}}_0|n\rangle = n^2 D_{\mathrm{rot}}|n\rangle. \tag{3.17}$$

In terms of the matrix elements of the operator $\hat{G}_{\boldsymbol{k}}$, the intermediate scattering function is expressed as

$$F_{\mu\nu}(\boldsymbol{k},t|\vartheta_0) = \sum_{n=-\infty}^{\infty}\langle\mu|\hat{G}_{\boldsymbol{k}}(t)|n\rangle\mathrm{e}^{-\mathrm{i}\vartheta_0(n-\nu)}. \tag{3.18}$$

The Schrödinger equation (3.15) may conveniently be transformed into an integral equation, including the initial condition $\hat{G}_{\boldsymbol{k}}(t=0) = \mathbb{1}$,

$$\hat{G}_{\boldsymbol{k}}(t) = \mathrm{e}^{-\hat{\mathscr{H}}_0 t} - \int_0^t \mathrm{e}^{-\hat{\mathscr{H}}_0(t-s)}\hat{V}\hat{G}_{\boldsymbol{k}}(s)\mathrm{d}s. \tag{3.19}$$

This will serve as the starting point of a time-dependent perturbation theory in $\hat{V}$.

3.2.2 Perturbative solution

The integral equation (3.19) may be iterated similar to the Born series in quantum mechanics,

$$\hat{G}_{\boldsymbol{k}}(t) = \mathrm{e}^{-\hat{\mathscr{H}}_0 t} - \int_0^t \mathrm{d}s\,\mathrm{e}^{-\hat{\mathscr{H}}_0(t-s)}\hat{V}\mathrm{e}^{-\hat{\mathscr{H}}_0 s} + \int_0^t \mathrm{d}s\int_0^s \mathrm{d}s'\mathrm{e}^{-\hat{\mathscr{H}}_0(t-s)}\hat{V}\mathrm{e}^{-\hat{\mathscr{H}}_0(s-s')}\hat{V}\mathrm{e}^{-\hat{\mathscr{H}}_0 s'} + \mathscr{O}(\hat{V}^3).$$

Then the matrix elements of interest are obtained to second order in $\hat{V}$ as[1]

$$\langle\nu|\hat{G}_{\boldsymbol{k}}(t)|n\rangle = \mathrm{e}^{-\nu^2 D_{\mathrm{rot}}t}\left\{\delta_{\nu n} - \langle\nu|\hat{V}|n\rangle\tau_{n^2-\nu^2}(t) + \sum_{m=-\infty}^{\infty}\langle\nu|\hat{V}|m\rangle\langle m|\hat{V}|n\rangle D_{\mathrm{rot}}^{-2}T^{m^2-\nu^2}_{n^2-m^2}(t)\right\}, \tag{3.20}$$

[1] Within the perturbation calculation, the helicities in Eq. (3.18) have a different sign, and similarity all other indices of the countable basis Eq. (3.16). This effects the Equations (3.20), (3.23), (3.25), (3.26), (3.32), and (3.38), as well as Eqs. (B.1) and (B.2).

with the integrals

$$\tau_j(t) := \int_0^t \mathrm{e}^{-jD_{\mathrm{rot}}s}\mathrm{d}s = \begin{cases} t, & j=0, \\ \frac{1}{jD_{\mathrm{rot}}}\left(1-\mathrm{e}^{-jD_{\mathrm{rot}}t}\right), & j\neq 0, \end{cases} \tag{3.21}$$

$$T_l^j(t) := D_{\mathrm{rot}}^2\int_0^t\int_0^s \mathrm{e}^{-jD_{\mathrm{rot}}s}\mathrm{e}^{-lD_{\mathrm{rot}}s'}\mathrm{d}s'\mathrm{d}s = \begin{cases} \frac{1}{2}D_{\mathrm{rot}}^2t^2, & l=0\wedge j=0, \\ \frac{D_{\mathrm{rot}}}{j}\left(\tau_j(t)-t\mathrm{e}^{-jD_{\mathrm{rot}}t}\right), & l=0\wedge j\neq 0, \\ D_{\mathrm{rot}}\frac{\tau_j(t)-\tau_{j+l}(t)}{l}, & l\neq 0. \end{cases} \tag{3.22}$$

For the explicit formulation of the solution Eq. (3.20) we still need the matrix elements of the perturbation operator:

$$\langle m|\hat{V}|n\rangle = \bar{D}k^2\delta_{mn} + \frac{D_a}{2}\left(k_-^2\delta_{m+2,n}-k_+^2\delta_{m-2,n}\right) + \mathrm{i}f\frac{D_\parallel}{2}\left(k_-\delta_{m+1,n}+k_+\delta_{m-1,n}\right), \tag{3.23}$$

where we have introduced the complex wavevector components $k_\pm := k_x \pm \mathrm{i}k_y$, and the isotropic and anisotropic diffusion coefficients

$$\bar{D} := \frac{D_\parallel + D_\perp}{2}, \quad D_a := \frac{D_\parallel - D_\perp}{2}. \tag{3.24}$$

In case of a vanishing force we obtain five matrix elements,

$$\begin{aligned}\langle \nu|\hat{G}_{\boldsymbol{k}}(t)|n\rangle|_{f=0} = \mathrm{e}^{-\nu^2D_{\mathrm{rot}}t}\Bigg\{&\left[1-\bar{D}k^2t+\bar{D}^2k^4\frac{t^2}{2}+\frac{D_a^2k^4}{4D_{\mathrm{rot}}^2}\left(T^{4(1+\nu)}_{n^2-(\nu+2)^2}(t)+T^{4(1-\nu)}_{n^2-(\nu-2)^2}(t)\right)\right]\delta_{\nu,n} \\ &+\frac{D_a}{2}\left[-\tau_{4(1+\nu)}(t)+\frac{\bar{D}k^2}{D_{\mathrm{rot}}^2}\left(T_0^{4(1+\nu)}(t)+T^0_{n^2-\nu^2}(t)\right)\right]k_-^2\delta_{\nu+2,n} \\ &+\frac{D_a}{2}\left[-\tau_{4(1-\nu)}(t)+\frac{\bar{D}k^2}{D_{\mathrm{rot}}^2}\left(T_0^{4(1-\nu)}(t)+T^0_{n^2-\nu^2}(t)\right)\right]k_+^2\delta_{\nu-2,n} \\ &+\frac{D_a^2}{4D_{\mathrm{rot}}^2}\left(T^{4(1+\nu)}_{n^2-(\nu+2)^2}(t)k_-^4\delta_{\nu+4,n}+T^{4(1-\nu)}_{n^2-(\nu-2)^2}(t)k_+^4\delta_{\nu-4,n}\right)\Bigg\}+\mathscr{O}\left(k^6\right),\end{aligned} \tag{3.25}$$

leading to the second order correlation function with diagonal helicities

$$\begin{aligned}F_\nu(\boldsymbol{k},t|\vartheta_0)|_{f=0} = \mathrm{e}^{-\nu^2D_{\mathrm{rot}}t}\Bigg\{&\left[1-\bar{D}k^2t+\bar{D}^2k^4\frac{t^2}{2}+\frac{D_a^2k^4}{4D_{\mathrm{rot}}^2}\left(T^{4(1+\nu)}_{-4(1+\nu)}(t)+T^{4(1-\nu)}_{-4(1-\nu)}(t)\right)\right] \\ &+\frac{D_a}{2}\left[-\tau_{4(1+\nu)}(t)+\frac{\bar{D}k^2}{D_{\mathrm{rot}}^2}\left(T_0^{4(1+\nu)}(t)+T^0_{4(1+\nu)}(t)\right)\right]k_-^2\mathrm{e}^{\mathrm{i}2\vartheta_0} \\ &+\frac{D_a}{2}\left[-\tau_{4(1-\nu)}(t)+\frac{\bar{D}k^2}{D_{\mathrm{rot}}^2}\left(T_0^{4(1-\nu)}(t)+T^0_{4(1-\nu)}(t)\right)\right]k_+^2\mathrm{e}^{-\mathrm{i}2\vartheta_0} \\ &+\frac{D_a^2}{4D_{\mathrm{rot}}^2}\left(T^{4(1+\nu)}_{4(3+\nu)}(t)k_-^4\mathrm{e}^{\mathrm{i}4\vartheta_0}+T^{4(1-\nu)}_{4(3-\nu)}(t)k_+^4\mathrm{e}^{-\mathrm{i}4\vartheta_0}\right)\Bigg\}+\mathscr{O}\left(k^6\right).\end{aligned} \tag{3.26}$$

The additional terms for nonzero force are given in Appendix B.1, together with an explicit expression for $\nu = 0$. Note that the dependence of Eq. (3.26) on ϑ_0 is always given by powers of $k_\pm\mathrm{e}^{\mp\mathrm{i}\vartheta_0}$—this property originates from rotational symmetry and holds to all orders in k.

From $F(\boldsymbol{k},t|\vartheta_0)$ all moments are obtained by derivatives, e. g., $\langle\Delta x(t)^2\rangle_\mathrm{f} = -\partial_{k_x}^2 F(\boldsymbol{k},t|\vartheta_0)|_{\boldsymbol{k}=0}$; when $v \neq 0$ this yields observables measuring the coupling of translation and rotation. Some of the moments for zero force have been calculated by Han et al. [64] from the Langevin equations equivalent to Eq. (3.2). The mean displacements vanish unless a nonzero force is present,

$$\langle\Delta x(t)\rangle_\mathrm{f} = fD_\parallel\tau_1(t)\cos(2\vartheta_0), \qquad \langle\Delta y(t)\rangle_\mathrm{f} = fD_\parallel\tau_1(t)\sin(2\vartheta_0). \tag{3.27}$$

For the higher moments we simplify the notation by $\delta x^n(t) := \langle\Delta x(t)^n\rangle_\mathrm{f}$, and correspondingly for y. So the second moments in the space-fixed frame read

$$\delta x^2(t) = 2\bar{D}t + 2D_a\tau_4(t)\cos(2\vartheta_0) + \frac{f^2D_\parallel^2}{D_\mathrm{rot}}\left[t - \tau_1(t) + \frac{\tau_1(t)-\tau_4(t)}{3}\cos(2\vartheta_0)\right], \tag{3.28}$$

$$\delta y^2(t) = 2\bar{D}t - 2D_a\tau_4(t)\cos(2\vartheta_0) + \frac{f^2D_\parallel^2}{D_\mathrm{rot}}\left[t - \tau_1(t) - \frac{\tau_1(t)-\tau_4(t)}{3}\cos(2\vartheta_0)\right], \tag{3.29}$$

$$\langle\Delta x(t)\Delta y(t)\rangle_\mathrm{f} = \left[2D_a\tau_4(t) + \frac{f^2D_\parallel^2}{3D_\mathrm{rot}}\big(\tau_1(t)-\tau_4(t)\big)\right]\sin(2\vartheta_0), \tag{3.30}$$

$$\delta\boldsymbol{r}^2(t) = 4\bar{D}t + 2\frac{f^2D_\parallel^2}{D_\mathrm{rot}}\big(t-\tau_1(t)\big). \tag{3.31}$$

As an example for a correlation function that includes orientational degrees of freedom,

$$\Big\langle\Delta x(t)^2\mathrm{e}^{-iv[\theta(t)-\vartheta_0]}\Big\rangle_\mathrm{f} = \mathrm{e}^{-v^2D_\mathrm{rot}t}\left\{2\bar{D}t + D_a\left[\tau_{4(1+v)}(t)\mathrm{e}^{\mathrm{i}2\vartheta_0} + \tau_{4(1-v)}(t)\mathrm{e}^{-\mathrm{i}2\vartheta_0}\right]\right\}. \tag{3.32}$$

This and the remaining results of this section are given for vanishing force. The expression for y corresponding to Eq. (3.32) differs only by the sign in front of D_a. The moments of fourth order are obtained by

$$\frac{\delta x^4(t)}{4!} = \bar{D}^2\frac{t^2}{2} + \bar{D}D_at\tau_4(t)\cos(2\vartheta_0) + \frac{D_a^2}{8D_\mathrm{rot}}\left\{t - \tau_4(t) + \frac{\tau_4(t)-\tau_{16}(t)}{3}\cos(4\vartheta_0)\right\}, \tag{3.33}$$

$$\frac{\delta y^4(t)}{4!} = \bar{D}^2\frac{t^2}{2} - \bar{D}D_at\tau_4(t)\cos(2\vartheta_0) + \frac{D_a^2}{8D_\mathrm{rot}}\left\{t - \tau_4(t) + \frac{\tau_4(t)-\tau_{16}(t)}{3}\cos(4\vartheta_0)\right\}, \tag{3.34}$$

$$\big\langle\Delta x(t)^2\Delta y(t)^2\big\rangle_\mathrm{f} = 4\bar{D}^2t^2 + \frac{D_a^2}{D_\mathrm{rot}}\left[\big(t-\tau_4(t)\big) - \big(\tau_4(t)-\tau_{16}(t)\big)\cos(4\vartheta_0)\right]. \tag{3.35}$$

Additional insight in the statistics is gained by combining the preceding results to non-Gaussian parameters,

$$\frac{\delta x^4(t)}{3} - \big(\delta x^2(t)\big)^2 = \frac{D_a^2}{D_\mathrm{rot}}\left[t - \tau_4(t) - 2D_\mathrm{rot}\tau_4(t)^2\right] + \frac{D_a^2}{D_\mathrm{rot}}\left[\frac{\tau_4(t)-\tau_{16}(t)}{3} - 2D_\mathrm{rot}\tau_4(t)^2\right]\cos(4\vartheta_0)$$

$$= \frac{\delta y^4(t)}{3} - \big(\delta y^2(t)\big)^2, \tag{3.36}$$

$$\frac{\delta\boldsymbol{r}^4(t)}{2} - \big(\delta\boldsymbol{r}^2(t)\big)^2 = 4\frac{D_a^2}{D_\mathrm{rot}}\big(t-\tau_4(t)\big). \tag{3.37}$$

Several of these results are displayed and discussed in more detail in Sec. 3.4, in combination with data from computer simulations of the stochastic process that corresponds to the Smoluchowski-Perrin equation.

3.2.3 Unconstrained initial angle

When the constraint of a fixed initial orientation is released, the problem is isotropic with respect to $\boldsymbol{k}$. Then the scattering function is considerably simpler, since an integration over ϑ_0 removes all angular dependencies,

$$F_\nu(\boldsymbol{k},t) = \mathrm{e}^{-\nu^2 D_{\mathrm{rot}} t}\left\{1-\bar{D}k^2 t + \frac{D_a^2 k^4}{4D_{\mathrm{rot}}^2}\left(T^{4(1+\nu)}_{-4(1+\nu)}(t)+T^{4(1-\nu)}_{-4(1-\nu)}(t)\right) - f^2\frac{D_\parallel^2 k^2}{4D_{\mathrm{rot}}^2}\left(T^{1+2\nu}_{-2\nu-1}(t)+T^{1-2\nu}_{2\nu-1}(t)\right)\right\} + \mathcal{O}\left(k^6, fk^5, f^2k^4, f^3k^3\right) \quad (3.38)$$

All moments of a specific are identical apart from numerical factors, e.g., $\delta x^2(t) = \delta y^2(t) = 2\bar{D}t + f^2 D_\parallel^2\big(t-\tau_1(t)\big)/D_{\mathrm{rot}}$, and, for $f=0$,

$$\frac{\langle \Delta x(t)^4\rangle}{4!} = \frac{\langle \Delta y(t)^4\rangle}{4!} = \frac{\langle \Delta x(t)^2\Delta y(t)^2\rangle}{8} = \bar{D}^2\frac{t^2}{2} + \frac{D_a^2}{8D_{\mathrm{rot}}}\big(t-\tau_4(t)\big). \quad (3.39)$$

The square of the displacement, $\Delta\boldsymbol{r}(t)^2$, is spatially isotropic by definition, thus all observables derived from it are in any case independent of the initial direction, e.g., Eqs. (3.31) and (3.37) .

3.3 Full solution for the intermediate scattering function

In the previous section we obtained a perturbative solution of the Smoluchowski-Perrin equation. It becomes already quite messy in the second order, and will necessarily fail for $|\boldsymbol{k}L| \gtrsim 1$. A full analytic solution of Eq. (3.11) is possible in terms of a series expansion of Mathieu functions. From this, the only remaining step towards the solution for the probability density $\Psi(\boldsymbol{R},\vartheta,t|\vartheta_0)$ is a Fourier back transform.

The spatial Fourier transform of the Smoluchowski-Perrin equation, Eq. (3.11), may be rewritten

$$\partial_t G_{\boldsymbol{k}} = D_{\mathrm{rot}}\partial_\vartheta^2 G_{\boldsymbol{k}} - k^2\left[\bar{D} + D_a\cos 2(\vartheta-\varphi)\right]G_{\boldsymbol{k}},$$

by introducing polar coordinates for the wave vector, with $\tan\varphi := k_y/k_x$. Since $\boldsymbol{k}$ is a fixed parameter in this equation and the whole system π-periodic in the angle ϑ, we may shift ϑ such that $\vartheta' := \vartheta - \varphi \in [0,2\pi]$, and obtain

$$\partial_t G_{\boldsymbol{k}} = D_{\mathrm{rot}}\partial_{\vartheta'}^2 G_{\boldsymbol{k}} - k^2\left[\bar{D} + D_a\cos 2\vartheta'\right]G_{\boldsymbol{k}}. \quad (3.40)$$

For convenience, we rename the new angle $\vartheta' \to \vartheta$. We could equally choose the coordinate systems such that $\boldsymbol{k} = k\hat{\boldsymbol{e}}_x$ and thus directly arrive at Eq. (3.40). A separation of the time dependence by the ansatz

$$G_{\boldsymbol{k}}(\vartheta t|\vartheta_0) = g_{\boldsymbol{k}}(\vartheta|\vartheta_0)\mathrm{e}^{-\lambda t}$$

results in the Mathieu equation [2, 7]

$$0 = \partial_\vartheta^2 g_{\boldsymbol{k}}(\vartheta|\vartheta_0) + \left[a - 2q\cos 2\vartheta\right]g_{\boldsymbol{k}}(\vartheta|\vartheta_0), \quad (3.41)$$

with the parameter

$$q = \frac{D_a k^2}{2D_{\mathrm{rot}}}, \quad (3.42)$$

and the eigenvalue

$$a = \frac{\lambda - \bar{D}k^2}{D_{\mathrm{rot}}}.$$

The eigenfunctions of the Mathieu equation fall into four classes: the even functions, $\mathrm{ce}_j(\vartheta, q)$, and the odd functions, $\mathrm{se}_j(\vartheta, q)$, with period π for j even, and period 2π for j odd, respectively.[2] The general solution of Eq. (3.41) is thus a linear combination of the even and odd eigenfunctions

$$g_{\boldsymbol{k}}(\vartheta|\vartheta_0) = \sum_{j=0}^{\infty} \left[A_j(\vartheta_0)\mathrm{ce}_j(\vartheta, q) + B_j(\vartheta_0)\mathrm{se}_j(\vartheta, q) \right]. \tag{3.43}$$

For beginning both parts of the sum at $j = 0$, we define here and in the following $\mathrm{se}_0 \equiv 0$. Due to orthogonality, the coefficients can be determined by

$$A_j(\vartheta_0) = \int_0^{2\pi} \mathrm{ce}_j(\vartheta, q) g_{\boldsymbol{k}}(\vartheta|\vartheta_0)\mathrm{d}\vartheta, \quad B_j(\vartheta_0) = \int_0^{2\pi} \mathrm{se}_j(\vartheta, q) g_{\boldsymbol{k}}(\vartheta|\vartheta_0)\mathrm{d}\vartheta. \tag{3.44}$$

We obtain a representation of the δ-function,

$$\delta(\vartheta, \vartheta') = \sum_{j=0}^{\infty} \left[\mathrm{ce}_j(\vartheta, q)\mathrm{ce}_j(\vartheta', q) + \mathrm{se}_j(\vartheta, q)\mathrm{se}_j(\vartheta', q) \right]. \tag{3.45}$$

The coefficients $A_j(\vartheta_0)$ and $B_j(\vartheta_0)$ are fixed by the initial condition for the generating function,

$$G_{\boldsymbol{k}}(\vartheta, t = 0|\vartheta_0) \equiv g_{\boldsymbol{k}}(\vartheta|\vartheta_0) \stackrel{!}{=} \delta(\vartheta, \vartheta_0). \tag{3.46}$$

From comparing Eq. (3.45) and Eq. (3.43) we get $A_j(\vartheta_0) = \mathrm{ce}_j(\vartheta_0, q)$, $B_j(\vartheta_0) = \mathrm{se}_j(\vartheta_0, q)$, hence the full solution of the time dependent generating function reads

$$G_{\boldsymbol{k}}(\vartheta, t|\vartheta_0) = \sum_{j=0}^{\infty} \left[\mathrm{e}^{-\lambda(a_j,k)t}\mathrm{ce}_j(\vartheta_0, q)\mathrm{ce}_j(\vartheta, q) + \mathrm{e}^{-\lambda(b_j,k)t}\mathrm{se}_j(\vartheta_0, q)\mathrm{se}_j(\vartheta, q) \right]. \tag{3.47}$$

The decay rate $\lambda = \lambda(a, k) = aD_{\mathrm{rot}} + \bar{D}k^2$ depends on the corresponding even and odd eigenvalues, $a \to a_j(q)$ and $a \to b_j(q)$, respectively. The constrained intermediate scattering function $F_{\mu\nu}(\boldsymbol{k}, t|\vartheta_0)$ is now calculated by an integration over ϑ, and the unconstrained function by an additional average over ϑ_0:

$$\boxed{F_{\mu\nu}(\boldsymbol{k}, t) = \mathrm{e}^{-k^2\bar{D}t} \sum_{j=0}^{\infty} \left\{ \mathrm{e}^{-a_{n_j}(q)D_{\mathrm{rot}}t} A_\mu^{(n_j)}(q) A_\nu^{(n_j)}(q) + \mathrm{e}^{-b_{n_j}(q)D_{\mathrm{rot}}t} B_\mu^{(n_j)}(q) B_\nu^{(n_j)}(q) \right\},} \tag{3.48}$$

with the coefficients

$$A_\nu^{(j)}(q) := \frac{1}{\sqrt{2\pi}} \int_0^{2\pi} \cos(\nu\vartheta)\mathrm{ce}_j(\vartheta, q)\mathrm{d}\vartheta, \tag{3.49a}$$

$$B_\nu^{(j)}(q) := \frac{1}{\sqrt{2\pi}} \int_0^{2\pi} \sin(\nu\vartheta)\mathrm{se}_j(\vartheta, q)\mathrm{d}\vartheta. \tag{3.49b}$$

[2] We use the normalization $\int_0^{2\pi} \mathrm{ce}_j^2(\vartheta, q)\mathrm{d}\vartheta = 1$ and $\int_0^{2\pi} \mathrm{se}_j^2(\vartheta, q)\mathrm{d}\vartheta = 1$. The eigenfunctions are complete and orthonormal in the interval $0 \le \vartheta \le 2\pi$ [2].

The relevant indices n_j depend on the values of the helicities. From symmetry we know that μ and ν are either both even or both odd, see Eq. (3.7). For μ,ν even, only even j contribute, and when μ,ν are odd, j must be odd, too. So

$$n_j = \begin{cases} 2j, & \mu,\nu \text{ even}, \\ 2j+1, & \mu,\nu \text{ odd}, \end{cases} \tag{3.50}$$

including $b_0 \equiv 0$ and $B_\nu^{(0)} \equiv 0$ for simplicity in the summation. Note that although $\mathrm{se}_{2j+1}(\cdot)$ is 2π-periodic, the integrand of $B_\nu^{(2j+1)}(\cdot)$, ν odd, has a period of π, and thus correctly reflects the symmetry of the problem.

3.3.1 Scattering from the center of mass

When the center of mass only is observed, i.e., the helicities are set to zero, the unconstrained scattering function reduces to

$$F(\boldsymbol{k},t) = \mathrm{e}^{-k^2\tilde{D}t} \sum_{j=0}^{\infty} \mathrm{e}^{-a_{2j}(q)D_{\mathrm{rot}}t} \left[A_0^{(2j)}(q)\right]^2. \tag{3.51}$$

The convergence of the sum in Eq. (3.51) is determined by the magnitude of q. The eigenvalues $a_j(q)$ and $b_j(q)$ are ordered ascendingly in j; furthermore, the coefficients fulfill $A_0^{(2j)}(q) = \mathcal{O}(q^j)$. Hence for $q \ll 1$, the low-j terms yield the major contributions to the sum, $F(\boldsymbol{k},t) = \mathrm{e}^{-k^2\tilde{D}t}\left[\mathrm{e}^{q^2 D_{\mathrm{rot}}t/2}\left(1-q^2/8\right) + \mathrm{e}^{-4D_{\mathrm{rot}}t}q^2/8 + \mathcal{O}\left(q^4\right)\right]$ representing the first correction to isotropic diffusion. Thus $q^2 \lesssim 1$ defines the macroscopic regime, corresponding to $(kL_{\mathrm{rot}})^4 \lesssim 4$, and $L_{\mathrm{rot}} := \sqrt{D_a\tau_{\mathrm{rot}}}$ is derived as the relevant macroscopic scale.

The opposite limit, $q \gg 1$, is relevant when D_{rot} becomes very small; this will be important for the analysis in Sec. 4.5. The asymptotic expansion $a_j(q) \simeq -2q + (4j+2)\sqrt{q} + \mathcal{O}(1)$ reveals a reduction of the exponential prefactor in Eq. (3.51) to $\mathrm{e}^{-k^2 D_\perp t}$, and a large number of terms contribute. Then, the terminal relaxation is ruled by an exponential with decay rate

$$\tau_{\mathrm{term}}^{-1} := k\sqrt{2D_a D_{\mathrm{rot}}} + k^2 D_\perp. \tag{3.52}$$

3.3.2 Scattering from the whole rod

In the theory for the intermediate scattering function we have so far considered the scattering response from the center of mass $\boldsymbol{r}(t)$ of a rod. To account for a response from an arbitrary position along the rod, one needs to find the correlations of the Fourier transformed density for a certain position $s \in [-L/2, L/2]$ along the contour, $\varrho^{\mathrm{rod}}(\boldsymbol{k},t,s) := \mathrm{e}^{-\mathrm{i}\boldsymbol{k}\cdot[\boldsymbol{r}(t)+s\boldsymbol{u}(t)]}$. The corresponding scattering function reads

$$F^{\mathrm{rod}}(\boldsymbol{k},t,s,s') := \left\langle \varrho^{\mathrm{rod}}(\boldsymbol{k},t,s)\varrho^{\mathrm{rod}}(\boldsymbol{k},0,s')^* \right\rangle = \left\langle \mathrm{e}^{-\mathrm{i}\boldsymbol{k}\cdot[\boldsymbol{r}(t)+s\boldsymbol{u}(t)]}\mathrm{e}^{\mathrm{i}\boldsymbol{k}\cdot[\boldsymbol{r}(0)+s'\boldsymbol{u}(0)]} \right\rangle. \tag{3.53}$$

When the full rod induces a response in the measurements, as is the case, e.g., in neutron scattering, the contour parameter is integrated out [31],

$$\varrho^{\mathrm{rod}}(\boldsymbol{k},t) := \frac{1}{L}\int_{-L/2}^{L/2} \mathrm{e}^{-\mathrm{i}\boldsymbol{k}\cdot[\boldsymbol{r}(t)+s\boldsymbol{u}(t)]}\mathrm{d}s = \mathrm{e}^{-\mathrm{i}\boldsymbol{k}\cdot\boldsymbol{r}(t)}\,\mathrm{sinc}\left(\boldsymbol{k}\cdot\boldsymbol{u}(t)\frac{L}{2}\right). \tag{3.54}$$

The sinc-function employed here is defined by $\mathrm{sinc}(x) := \sin(x)/x$. This leads to the normalized intermediate scattering function

$$F^{\mathrm{rod}}(k,t) := \frac{\left\langle \varrho^{\mathrm{rod}}(\boldsymbol{k},t)\varrho^{\mathrm{rod}}(\boldsymbol{k},0)^*\right\rangle}{\left\langle \left|\varrho^{\mathrm{rod}}(\boldsymbol{k},0)\right|^2\right\rangle} \tag{3.55}$$

$$= \frac{\left\langle \mathrm{e}^{-\mathrm{i}\boldsymbol{k}\cdot\Delta\boldsymbol{r}(t)}\,\mathrm{sinc}\left(\boldsymbol{k}\cdot\boldsymbol{u}(t)\tfrac{L}{2}\right)\mathrm{sinc}\left(\boldsymbol{k}\cdot\boldsymbol{u}(0)\tfrac{L}{2}\right)\right\rangle}{\mathscr{N}\left(\frac{kL}{2}\right)}, \tag{3.56}$$

with the norm given by a hypergeometric function ${}_pF_q(\cdot)$,

$$\mathscr{N}\left(\frac{kL}{2}\right) := {}_1F_2\left(\frac{1}{2};\frac{3}{2},2;-\left(\frac{kL}{2}\right)^2\right). \tag{3.57}$$

The expression (3.56) can conveniently be measured in simulations.[3]

For the analytical description it is useful to find a formulation in terms of the Mathieu eigenfunctions and the results of the previous section. We rotate the coordinate system such that $\boldsymbol{k}$ is directed along the x-axis, $\boldsymbol{k} = k\hat{\boldsymbol{e}}_x$, and translate to $\boldsymbol{r}(0) = 0$. Then Eq. (3.53) is simplified to

$$F^{\mathrm{rod}}(k,t,s,s') = \left\langle \mathrm{e}^{-\mathrm{i}kx(t)}\mathrm{e}^{-\mathrm{i}k[s\cos\theta(t)-s'\cos\theta(0)]}\right\rangle. \tag{3.58}$$

The exponentials containing the contour parameters are Fourier transformed, reflecting their 2π-periodicity,

$$\mathrm{e}^{-\mathrm{i}ks\cos\theta(t)} = \sum_{\nu=-\infty}^{\infty}(-\mathrm{i})^\nu J_\nu(ks)\mathrm{e}^{-\mathrm{i}\nu\theta(t)}, \tag{3.59}$$

with the Bessel functions[4] $(-\mathrm{i})^\nu J_\nu(z) = I_\nu(-\mathrm{i}z) = \int_0^{2\pi}\mathrm{e}^{\mathrm{i}\nu\theta}\mathrm{e}^{-\mathrm{i}z\cos\theta}\mathrm{d}\theta/2\pi$. When inserted into Eq. (3.58), we get

$$F^{\mathrm{rod}}(k,t,s,s') = \sum_{\mu,\nu=-\infty}^{\infty}(-1)^{(\mu+3\nu)/2}J_\mu(ks)J_\nu(ks')F_{\mu\nu}(k\boldsymbol{e}_x,t), \tag{3.60}$$

by taking advantage of the unconstrained intermediate scattering function $F_{\mu\nu}(k\hat{\boldsymbol{e}}_x,t)$ as given in Eq. (3.5). Note that symmetry requires that the indices μ and ν are either both even or both odd, as proven in Eq. (3.7), thus $\mu+3\nu$ is always even. We conclude that the knowledge of the center of mass scattering functions $F_{\mu\nu}(\boldsymbol{k},t)$ is sufficient to determine the scattering response from arbitrary positions s, s' along the rod.

To obtain a result for scattering from the rod as a whole, we have to integrate the arclength parameters in Eq. (3.60) over the length of the rod. Only the summands with both indices even contribute,

$$F^{\mathrm{rod}}(k,t) = \frac{1}{\mathscr{N}(kL/2)L^2}\int_{-L/2}^{L/2}\mathrm{d}s\int_{-L/2}^{L/2}\mathrm{d}s'F^{\mathrm{rod}}(k,t,s,s')$$

$$= \mathscr{N}\left(\frac{kL}{2}\right)^{-1}\sum_{\mu,\nu=-\infty}^{\infty}\mathscr{I}_\mu\left(\frac{kL}{2}\right)\mathscr{I}_\nu\left(\frac{kL}{2}\right)F_{2\mu,2\nu}(k\hat{\boldsymbol{e}}_x,t). \tag{3.61}$$

[3] A numerical analysis of the norm $\mathscr{N}(x)$ in the interval $x\in[10,200]$ reveals as the major contribution a hyperbola, $\mathscr{N}(x)\approx 1/x$. It is modified by a rapidly oscillating term of small amplitude, which furthermore decays with increasing x.

[4] Useful symmetries of the Bessel functions $J_\nu(z)$ and modified Bessel functions $I_\nu(z)$:

$$J_\nu(-z) = (-1)^\nu J_\nu(z), \qquad I_\nu(-z) = (-1)^\nu I_\nu(z),$$
$$J_{-n}(z) = (-1)^n J_n(z), \qquad I_{-n}(z) = I_n(z), \qquad n\in\mathbb{Z}.$$

The integrated Bessel functions $\mathscr{I}_n(x) := \int_{-x}^{x} I_{2n}(\mathrm{i}u)\mathrm{d}u/2x$ can be expressed in terms of the generalized hypergeometric function ${}_pF_q(\cdot)$,

$$\mathscr{I}_n(x) = \frac{(-1)^n}{2n+1}\frac{1}{(2n)!}\left(\frac{x}{2}\right)^{2n} {}_1F_2\left(n+\frac{1}{2}; n+\frac{3}{2}, 2n+1; -\left(\frac{x}{2}\right)^2\right). \tag{3.62}$$

The evaluation of the expression (3.61) is simplified by inserting Eq. (3.48) and interchanging the summations. From the definitions of the Mathieu coefficients, Eqs. (3.49), we infer the symmetries $A_{-\mu}^{(j)} = A_{\mu}^{(j)}$ and $B_{-\mu}^{(j)} = -B_{\mu}^{(j)}$, and conclude that the sums containing the odd eigenfunctions $B_{2\mu}^{(2j)}$ vanish. The sums over the even eigenfunctions are rearranged, and with the abbreviation $\tilde{k} := kL/2$ we obtain the result

$$F^{\mathrm{rod}}(k,t) = \frac{\mathrm{e}^{-k^2\bar{D}t}}{\mathscr{N}(\tilde{k})}\sum_{j=0}^{\infty}\mathrm{e}^{-a_{2j}(q)D_{\mathrm{rot}}t}\left\{\mathscr{I}_0(\tilde{k})^2\left(A_0^{(2j)}\right)^2 + 4\mathscr{I}_0(\tilde{k})A_0^{(2j)}\sum_{\mu=1}^{\infty}\mathscr{I}_\mu(\tilde{k})A_{2\mu}^{(2j)}\right.$$
$$\left. + 4\sum_{\mu=1}^{\infty}\mathscr{I}_\mu(\tilde{k})^2\left(A_{2\mu}^{(2j)}\right)^2 + 8\sum_{\mu=2}^{\infty}\sum_{\nu=1}^{\mu-1}\mathscr{I}_\mu(\tilde{k})\mathscr{I}_\nu(\tilde{k})A_{2\mu}^{(2j)}A_{2\nu}^{(2j)}\right\}. \tag{3.63}$$

Although more complex than Eq. (3.48), this expression poses no new fundamental difficulties, since all terms in curly brackets are time independent.

3.4 Brownian dynamics simulations of a freely diffusing rod

To sample trajectories from the probability distribution $\Psi(\boldsymbol{R},\vartheta,t;\vartheta_0)$, the Smoluchowski-Perrin equation (3.2) is transformed into the equivalent Langevin equations for the center of mass $\boldsymbol{r}(t)$ and the angle of orientation $\theta(t)$ [153]. The center of mass motion is conveniently written in the body-fixed frame, in terms of the longitudinal displacement $r_\parallel(t) := \int_0^t \dot{\boldsymbol{r}}(t')\cdot\boldsymbol{u}(t')\mathrm{d}t'$, and the transverse one $r_\perp(t) := \int_0^t \dot{\boldsymbol{r}}(t')\cdot\boldsymbol{u}_\perp(t')\mathrm{d}t'$, with $\boldsymbol{u}_\perp = (-\sin\theta,\cos\theta)$ in two dimensions. In this representation, the dynamics decouples,

$$\partial_t r_\parallel(t) = \sqrt{2D_\parallel^0}\,\xi_\parallel(t), \tag{3.64a}$$

$$\partial_t r_\perp(t) = \sqrt{2D_\perp^0}\,\xi_\perp(t), \tag{3.64b}$$

with zero mean Gaussian noise $\langle\xi_\parallel(t)\xi_\parallel(t')\rangle = \delta(t-t')$, and $\langle\xi_\perp(t)\xi_\perp(t')\rangle = \delta(t-t')$, as well as a vanishing crosscorrelation $\langle\xi_\parallel(t)\xi_\perp(t')\rangle = 0$. An Einstein relation fixes the amplitude of the noise, $D_\parallel^0 = k_BT/\gamma_\parallel$, with the friction constant $\gamma_\parallel$ for longitudinal motion, and correspondingly for the transverse diffusion, $D_\perp^0 = k_BT/\gamma_\perp$.[5] Equivalently, an integration of Eqs. (3.64) relates the diffusion coefficient to the mean-square displacement,

$$\left\langle\Delta r_\parallel^2(t)\right\rangle = 2D_\parallel^0\Delta t, \quad \left\langle\Delta r_\perp^2(t)\right\rangle = 2D_\perp^0\Delta t. \tag{3.65}$$

[5] One possibility to derive this Einstein relation is to consider Brownian motion in a potential U; the Langevin equation corresponding to Eqs. (3.64) is

$$\partial_t x(t) = -\frac{1}{\gamma}\partial_x U(x) + \sqrt{2D}\xi(t).$$

From the equivalent Smoluchowski equation,

$$\partial_t\Psi(x,t) = \frac{1}{\gamma}\partial_x\big(\partial_x U(x)\big)\Psi(x,t) + D\partial_x^2\Psi(x,t),$$

one obtains an equilibrium solution which has to equal the Boltzmann distribution, $\Psi_{\mathrm{eq}}(x) \propto \mathrm{e}^{-U(x)/k_BT}$, thus $D = k_BT/\gamma$, as given in the main text.

The rotational motion is formulated along the same lines,[6]

$$\partial_t \theta(t) = \sqrt{2D^0_{\rm rot}}\,\xi_r(t), \quad \langle \xi_r(t)\xi_r(t')\rangle = \delta(t-t'). \tag{3.67}$$

For the friction constants we use the result of first order hydrodynamics of a slender rod [31]; they yield for the diffusion coefficients the relations

$$D^0_\perp = D^0_\parallel/2, \quad D^0_{\rm rot} = 6D^0_\parallel/L^2. \tag{3.68}$$

Eqs. (3.64) and (3.67) are integrated numerically to obtain representative trajectories [64, 145, 146]. The simplest iteration scheme is sufficient, i.e., the Euler forward iteration, since the dynamics is exclusively determined by additive noise [84]. The timestep $i+1$ of size τ_B then reads, in a dimensionless notation,

$$\frac{\Delta r^\parallel_{i+1}}{L/2} = \sqrt{2\frac{D^0_\parallel}{(L/2)^2}\tau_B}\,\xi^\parallel_i, \quad \frac{\Delta r^\perp_{i+1}}{L/2} = \sqrt{\frac{D^0_\parallel}{(L/2)^2}\tau_B}\,\xi^\perp_i, \quad \Delta\theta_{i+1} = \sqrt{3\frac{D^0_\parallel}{(L/2)^2}\tau_B}\,\xi^r_i, \tag{3.69}$$

with three uncorrelated Gaussian noise contributions of unit variance, $\langle \xi_i\xi_j\rangle = \delta_{i,j}$. The size of the time step, τ_B, sets a lower bond for the validity of the results with reference to the theory of diffusion. τ_B has to be chosen sufficiently small such that the processes in observation do not depend on it any more. This will be discussed in more detail in Sec. 4.2, when other timescales enter the problem. The transformation of the position increment to the lab frame is a rotation about the angle θ_i,

$$\Delta \boldsymbol{r}_i \equiv \begin{pmatrix}\Delta x_i\\ \Delta y_i\end{pmatrix} = \boldsymbol{S}\cdot\begin{pmatrix}\Delta r^\parallel_i\\ \Delta r^\perp_i\end{pmatrix}, \quad \text{with the rotation matrix } \boldsymbol{S} := \begin{pmatrix}\cos\theta_i & -\sin\theta_i\\ \sin\theta_i & \cos\theta_i\end{pmatrix}. \tag{3.70}$$

In Sec. 3.2.1 the free diffusion has been amended by a force acting on the rod longitudinal to its orientational unit vector $\boldsymbol{u}$. This is easily introduced also into the Langevin equations in the body frame, by addition of the force $F/\gamma_\parallel = fD^0_\parallel$ on the right-hand side of Eq. (3.64a),

$$\partial_t r_\parallel(t) = fD^0_\parallel + \sqrt{2D^0_\parallel}\xi_\parallel(t). \tag{3.71}$$

From this and Eqs. (3.64b), (3.67) one obtains the Smoluchowski-Perrin equation (3.14). In Appendix B.2, some more details are given concerning the transformation between the Smoluchowski and the Langevin equations referred to above.

3.4.1 Comparison of simulations and Smoluchowski-Perrin theory

As a crosscheck, we evaluate by Brownian dynamics simulations several of the observables derived theoretically in Secs. 3.2 and 3.3. First, we consider the time dependence of the diffusion coefficients, as derived from the mean-square displacement. The observation of the diffusion of a rod

[6] The Einstein relation for $D_{\rm rot}$ can also be obtained by regarding Brownian motion of $\theta(t)$ to be derived by coarse graining the stochastic process in the angular velocities $\omega = \partial_t\theta$. In three dimensions, the time evolution of the angular momentum $\boldsymbol{L} = I\boldsymbol{\omega}$ is

$$\partial_t \boldsymbol{L} = -\gamma_r\boldsymbol{\omega} + \gamma_r\sqrt{2D_{\rm rot}}\,\boldsymbol{\xi}_r, \quad \left\langle \boldsymbol{\xi}_r(t)\boldsymbol{\xi}_r^{\mathsf T}(t')\right\rangle = \mathbb{1}\delta(t-t'), \tag{3.66}$$

with the moment of inertia $I = mL^2/12$. From the solution of this Ornstein-Uhlenbeck process one obtains $\lim_{t\to\infty}\langle \boldsymbol{\Omega}(t)\boldsymbol{\Omega}(t)\rangle = \mathbb{1}\gamma_r D_{\rm rot}/I$, consistent with equipartition for each component, $I\langle\Omega_j^2\rangle/2 \stackrel{!}{=} k_BT/2$, if $D_{\rm rot} \equiv k_BT/\gamma_r$. In an overdamped environment, the inertia term of Eq. (3.66) can then be neglected.

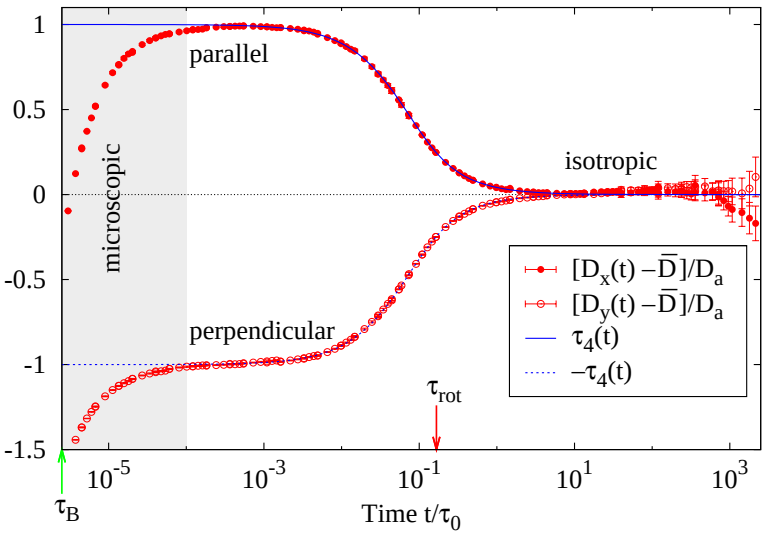

Figure 3.1: Deviation of diffusion coefficients in the space-fixed frame from the isotropic values. The rod is initially oriented along the x-axis. For very small times, $t \approx \tau_B$, reminders of the microscopics of the algorithm are still visible in the approach of the parallel and perpendicular plateaus (shaded). Blue lines display the analytic expressions, Eqs. (3.28) and (3.29).

in the body-fixed frame intrinsically shows different diffusion coefficients in the longitudinal and transverse directions, by construction of Eqs. (3.68). In contrast, the dynamics in the space-fixed frame with fixed initial orientation only shows a transient anisotropy, since the memory of the initial orientation is lost when the rod starts to rotate. In the mean-square displacements given in Eqs. (3.28) and (3.29) this is reflected in the exponential decays at the timescale $\tau_{rot} := D_{rot}^{-1}$, hidden in $\tau_4(t)$. Fig. 3.1 displays this transition from anisotropic to isotropic diffusion in the time-dependent diffusion coefficients $D_x(t) := \delta x^2(t)/2t$, and correspondingly for $D_y(t)$. They are normalized such that the anisotropic motion is represented by the values ± 1, and the isotropic part converges to 0 for $t \gg \tau_{rot}$.

Correlations between the mean-square displacement of the center of mass and angular displacements can be measured by taking the real part of Eq. (3.32), e.g., $\langle \Delta x(t)^2 \cos[\nu \Delta\theta(t)] \rangle$. This is displayed in Fig. 3.2 for $\nu = \{1,2,3\}$. The results show maxima at $t = \tau_0/\nu^2 D_{rot}$, i.e., in the transitional region where the rotational dynamics sets in and drives the loss of the memory of the initial

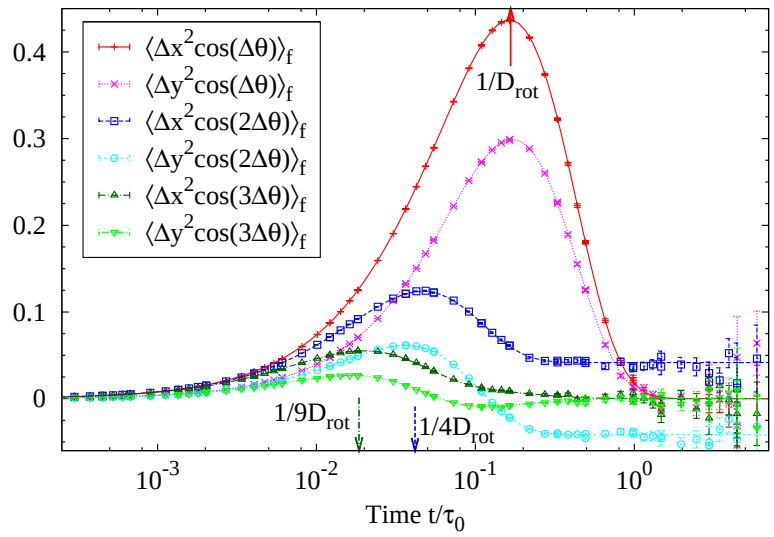

Figure 3.2: Mixed correlation functions of center of mass and angular displacement in the space-fixed frame, for three values of the helicity ν, in units $(L/2)^2$. The analytic curves (lines) are derived from Eq. (3.32). Arrows point to the ν-dependent position of the maxima, $1/\nu^2 D_{rot}$. In case of $\nu = 2$, the plateau value $\pm D_a \cos(2\vartheta_0)/4D_{rot}$ is approached at large times, i.e., $D_{rot} t \gg 1$.

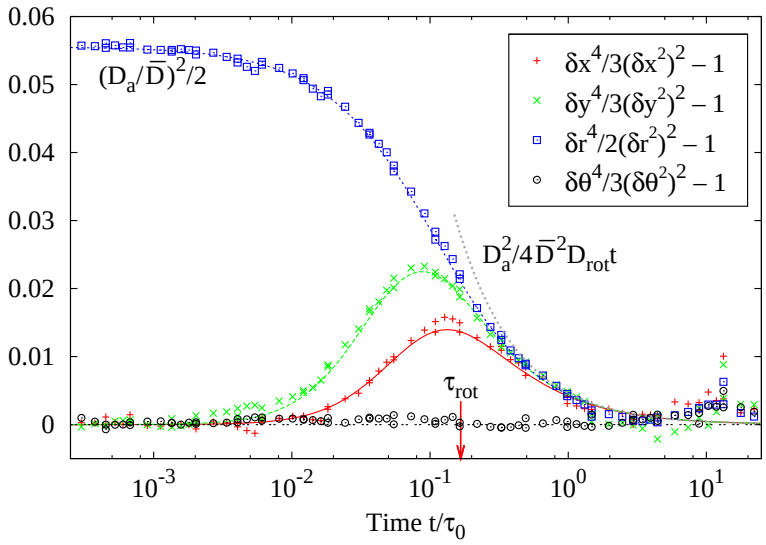

Figure 3.3: Several non-Gaussian parameters in comparison between simulations (symbols) and analytic curves (lines). The analytic expressions can essentially be found in Eqs. (3.36) and (3.37).

orientation. Fig. 3.3 shows various non-Gaussian parameters. The center of mass non-Gaussian parameter has the plateau value $(D_a/\bar{D})^2/2$ for time $t \ll \tau_{\mathrm{rot}}$, and decays algebraically, $\sim t^{-1}$, in the opposite regime. At the same timescale τ_{rot}, the lab frame non-Gaussian parameters show a peak, indicating a non-Gaussian time window in the transition between short time Gaussian dynamics close to the initial position, and long term isotropic statistics, when the rod rotated away from its initial orientation. The rotational dynamics finally is a purely Gaussian process, hence it's non-Gaussian parameter equals zero for all times.

3.4.2 Intermediate scattering functions

Finally, we validate the results for the intermediate scattering function $F(\boldsymbol{k}, t) \equiv F_0(\boldsymbol{k}, t)$.[7] Scattering measurements introduce as an additional length scale the wavevector $\boldsymbol{k}$, defining the inverse of the spatial scale that is probed. A variation of $\boldsymbol{k}$ then allows for a full spatial and temporal characterization of the system. The macroscopic results, $q^2 \lesssim 1$, are governed by a simple exponential, as argued for in Sec. 3.3.1. Since both D_{rot} and D_a are of order one for free diffusion, $k \equiv |\boldsymbol{k}|$ essentially dictates the magnitude of $q = D_a k^2/2D_{\mathrm{rot}}$, resulting in $(kL)^2 \ll 48$ for the macroscopic regime. The scattering function is plotted for various k in Fig. 3.4, displaying also the single exponential for $kL \leq 2$. For larger k, this simple expression is not sufficient, but the Smoluchowski-Perrin theory correctly coincides with the simulation results. With the rescaling used in Fig. 3.4, the curves coincide again for $kL \gg 1$, since the the quadratic term in the asymptotic expression Eq. (3.52) dominates; the difference between both limiting cases however is small, since all diffusion coefficients of the same order one.

Nonvanishing helicities in $F_{\mu\nu}(\boldsymbol{k}, t)$ open up an interplay between spatial and orientational degrees of freedom, as can already be inferred from the macroscopic limit of the Smoluchowski-Perrin equation. In this limit, the asymmetry of the center of mass diffusion can be neglected, $D_a = 0$, and the equation of motion (3.40) is much simpler,

$$\partial_t G_{\boldsymbol{k}} = D_{\mathrm{rot}} \partial_\vartheta^2 G_{\boldsymbol{k}} - k^2 \bar{D} G_{\boldsymbol{k}}. \tag{3.72}$$

[7] We calculate the series expansion in terms of Mathieu functions with Wolfram Mathematica® within arbitrary precision arithmetics. The evaluation of the series is truncated when the relative contribution of the last n terms is smaller than a threshold ϵ. We usually choose $n \in [10, 40]$ and $\epsilon = 0.1\%$.

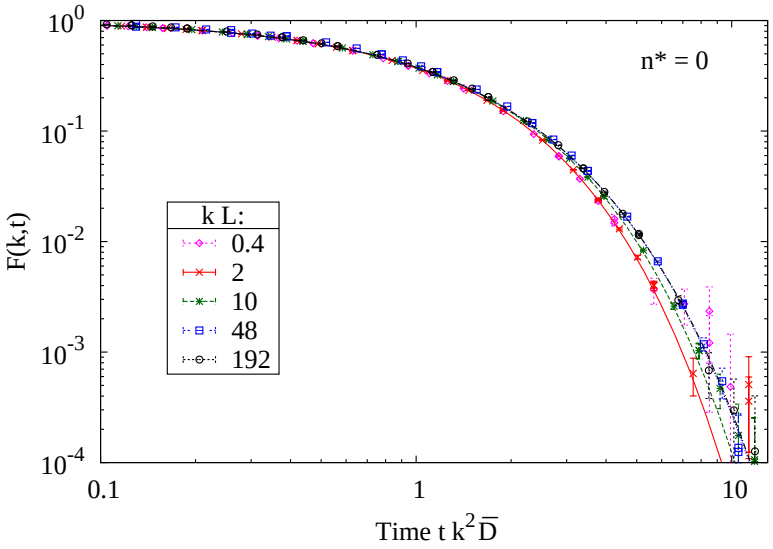

Figure 3.4: Intermediate scattering function of the center of mass of a freely diffusing rod, with symbols displaying simulations results, and color-coded lines Smoluchowski-Perrin theory, Eq. (3.51). Time is rescaled by $k^2\bar{D}$, such that the initial decay coincides for all curves. The red curve is undistinguishable from the simple exponential $e^{-k^2\bar{D}t}$; all scattering functions with $k/L \leq 2$ fall onto this curve.

With the initial condition $G_{\boldsymbol{k}}(\vartheta, t=0|\vartheta_0) = \delta(\vartheta,\vartheta_0)$ this yields as solution for the characteristic function,

$$G_{\boldsymbol{k}}(\vartheta, t|\vartheta_0) = \frac{1}{2\pi}\sum_{m=-\infty}^{\infty} e^{-(m^2 D_{\mathrm{rot}}+k^2\bar{D})t} e^{\mathrm{i}m(\vartheta-\vartheta_0)}, \tag{3.73}$$

where the periodicity in the angle requires $m \in \mathbb{Z}$. Eq. (3.73) is a slight extension of the solution for free rotation, Eq. (3.12), with the isotropic diffusion of the center of mass amended by an exponential. By integration we obtain the scattering function,

$$F_{\mu\nu}(k,t) = e^{-(\nu^2 D_{\mathrm{rot}}+k^2\bar{D})t}\delta_{\mu\nu}, \tag{3.74}$$

diagonal in the helicities. In this macroscopic description, the center of mass and angular degrees of freedom can only be differentiated when $\nu^2 D_{\mathrm{rot}} \approx k^2\bar{D}$. As soon as one of the two terms is considerably larger than the other, it dominates the exponential decay, and the other contribution will not be visible in the scattering function.

In a parameter range where both factors are relevant, Fig. 3.5 shows the diagonal part of the scattering function for free diffusion. As expected, deviations from the macroscopic formulation are visible when k is sufficiently large for resolving the slight microscopic anisotropy in the free diffusion, $kL/2\pi \gtrsim 1$; in addition, the scattering from the orientational degrees of freedom must not dominate to be able to distinguish this microscopic property.

An interpretation similar to that given in the context of Fig. 3.4 can be repeated for the scattering from the whole rod, shown in Fig. 3.6. For the unhindered motion displayed here, the single exponential $e^{-k^2\bar{D}t}$ governs the time evolution of Eq. (3.63) as long as $kL \lesssim 1$, although the coefficients are more complex. In the figure this is visible for $kL \leq 4$. Even for wavenumbers of bigger magnitude the deviations from the single exponential are small; the curves are however not a simple exponential. Results for large k again fall onto the same curve, since the diffusion coefficients are all of order one; this is still worth a note since it will change drastically in the next chapter. Interestingly, the curve for a wavevector in the transitional region, $kL = 10$, interpolates in time between the two limit cases: For $k^2\bar{D}t \lesssim 1$ it coincides with the functions of larger k-values, and for $k^2\bar{D}t \gtrsim 4$ it follows those for smaller k. As expected, the Smoluchowski-Perrin theory matches excellently also in Fig. 3.6.

From the present and the preceding section we deduce that the Brownian dynamics algorithm based on Eqs. (3.69) perfectly generates trajectories according to the Smoluchowski-Perrin theory presented in Secs. 3.2 and 3.3, and that the evaluation of the scattering functions in terms of Mathieu eigenfunctions reliably gives the correct results.

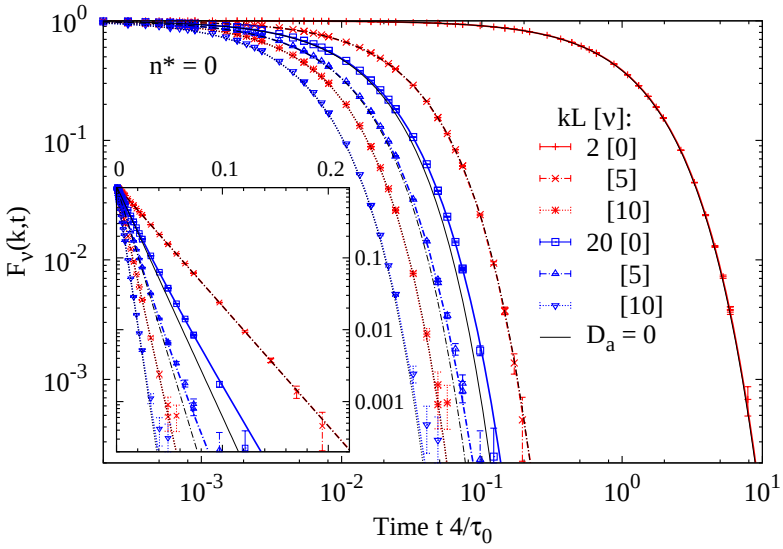

Figure 3.5: $F_\nu(k,t)$ for different wavenumbers k and helicities $\mu = \nu$, at $n^* = 0$. Symbols: simulation, lines: Perrin theory. The black lines display the macroscopic approximation Eq. (3.74), respectively. A linear axis for $F_\nu(k,t)$ in the inset emphasizes the single exponentials.

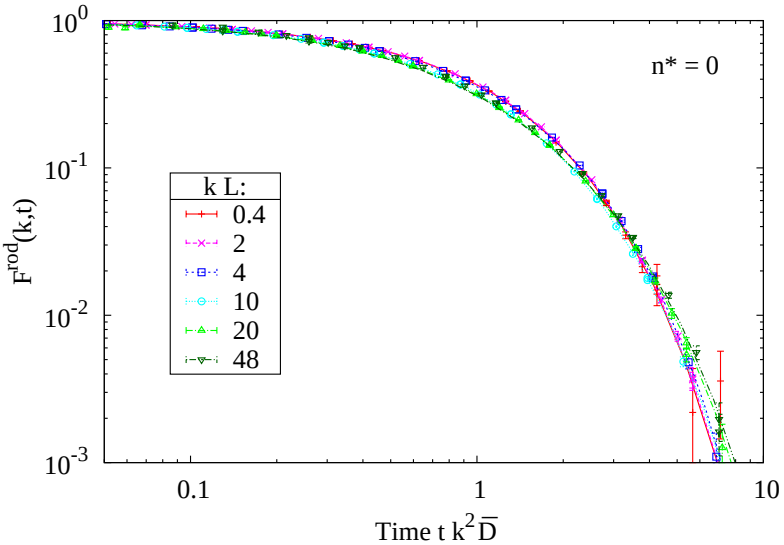

Figure 3.6: Scattering response from the whole rod, for unhindered diffusion. Data points show simulation results, color-coded lines the corresponding Perrin theory. The red and magenta curves are undistinguishable from the simple exponential $e^{-k^2 \bar{D} t}$.

Chapter 4

Anisotropic diffusion in semi-dilute suspensions of rods

The dynamics of semi-dilute suspensions of rods is a highly complex many-body problem due to the interactions of the suspended particles. Even the most basic step, the probability density for the propagation of *two* interacting particles, has only been solved for isotropic objects [156]. In the preceding chapter we have however solved analytically the *single* particle diffusion for a rod, up to a Fourier transformation. According to this Smoluchowski-Perrin theory, the dynamics of the rod is completely determined by the three diffusion coefficients $D_\parallel$, $D_\perp$, and D_{rot}. In the present chapter we will demonstrate that the complex many body problem can be described by an effective single particle system, by using the measured diffusion coefficients of semi-dilute systems as input parameters. This is a remarkable step yielding a new level of understanding of complex anisotropic diffusion processes, and we work out in detail the spatial and temporal constraints for the validity of this approach.

We study a model for the sterically constrained dynamics of rods that naturally induces anisotropic diffusion of arbitrarily large ratios $D_\parallel / D_\perp$. The model is set up in a two-dimensional environment, as explained in Sec. 4.1; the dynamic properties we focus on are however equally present in a three-dimensional embedding space. The model and therefore this whole chapter addresses *isotropic* suspensions of rods far from phase transitions that are caused by a significant ratio of excluded volume. This is implied by the term "semi-dilute" in the spirit of Doi and Edwards [31]; we however will synonymously use "dense" in the following, since the context has already been expounded in Chapter 1 and the introduction of Chapter 3. Extensive computer simulations of the two-dimensional model (Sec. 4.2) make possible an analysis of the dynamics over nine decades in time. They allow for the first time for a quantitative discussion of the tube model of Doi and Edwards [30], proposed 30 years ago; this is presented in Sec. 4.3. In the subsequent Secs. 4.4 and 4.5 the simulations set the reference for the validation of the effective theory. In particular, we compare mean-square displacements and the intermediate scattering function with their exact results from Chapter 3. Furthermore, we have discovered an intermediate algebraic decay in the scattering function, characteristic for the anisotropic sliding motion.

4.1 A model for sterically interacting rods

The dynamic processes of entangled solutions of, e.g., biopolymers cover many decades in time, posing a tremendous challenge both to experiments and simulations. For flexible polymers, the

reptation concept is well established; in the case of biopolymers, only the confining tube has been observed experimentally [79]. Computer simulations of entangled polymer solutions encounter major difficulties to follow the reptation motion; yet they give insight into the relaxation within the tube [128]. Progress beyond simple scaling arguments depends crucially on the design of generic models, which are as simple as possible to follow the dynamics for sufficiently long times, yet complex enough to display key aspects of the underlying microscopic processes.

We propose the following class of models to explore single-filament transport in polymer networks: consider the motion of a tagged polymer in a plane, entangled in a course of immobilized obstacles; the latter represent the topological constraints due to the neighboring filaments. The reduction of dimensionality still captures the physics of entanglement since the reptation motion is essentially one-dimensional [27, 33]. Stiff polymers are rather straight and therefore can be embedded in a plane, neglecting the torsion of their space curve. The orientation of the confining tube is persistent on the longest time scale of interest; thus in video microscopy experiments, the non-trivial reptation motion of a labeled polymer found initially in the focal plane takes place in this plane. As a benefit of the simplification, the computational complexity is lowered substantially, permitting a thorough investigation of slow dynamic processes.

It is essential to characterize and understand several limiting cases. Specifically, we aim to a description of the effects of dynamic entanglement that arise in suspensions of highly anisotropic object, like rods. The physics of entanglement is singled out in the limit of hard-core interaction, vanishing width of the polymers, and zero extension of the obstacles. Then, all ramifications of excluded volume are eliminated, all configurations are permitted and equally likely, and all non-trivial dynamic correlations are due to entanglement. In particular, the limit circumvents the nematic phase transition.

In summary, the model considers the overdamped motion of a single rod with zero width, exploring a plane with point-like, and hard obstacles; see Fig. 4.1. The latter are distributed randomly, independently, and uniformly in the plane with an average number density n. Then, the topology of the network of obstacles is characterized by the mesh size $\xi := n^{-1/2}$, i.e., the typical distance between obstacles. The degrees of freedom of the needle encompass the center-of-mass position $\boldsymbol{R}$ and the unit vector of orientation $\boldsymbol{u} = (\cos\theta(t), \sin\theta(t))$, parametrized by a single angle θ. The physical properties of this system are controlled by a single dimensionless parameter, the reduced density $n^* := nL^2$, where L denotes the length of the rod. Equivalently, the *entanglement index* $\mathrm{pE} := -\log_{10}(\xi/L)$ quantifies the relative importance of entanglement. The model is closely related

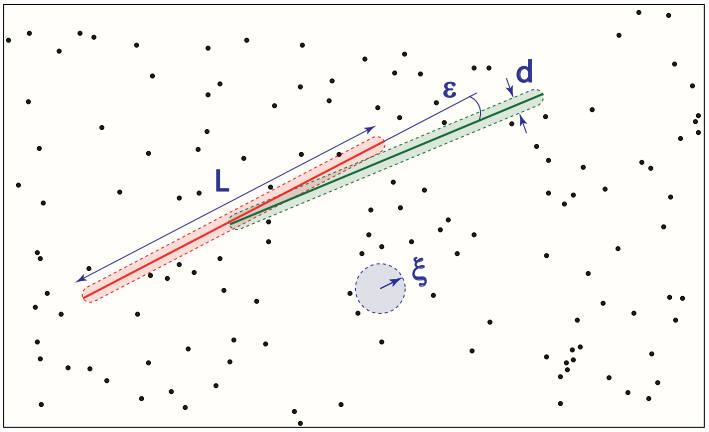

Figure 4.1: Illustration of an entangled needle in a plane. The relevant length scales are the length of the needle L and the mesh size of the network ξ. The surrounding point obstacles confine the needle to a tube (shaded areas) of width d, a renewed tube (green) is tilted against the old one (red) by an angle $\epsilon = d/L$. (Illustration by Felix Höfling)

to three-dimensional suspensions of rods when considering a planar section. A tagged rod found initially in this plane is approximately confined to it by the neighboring rods for times shorter than the orientational relaxation time, $t \ll \tau_{\mathrm{rot}} := D_{\mathrm{rot}}^{-1}$, the largest time scale present in the system. The constrained motion of the rod then corresponds to diffusion in a planar course of localized intersection points.

4.2 Simulations of Langevin dynamics with point-like obstacles

For the simulation of models of rod suspensions, the Brownian dynamics algorithm presented in Sec. 3.4 has to be expanded to include an interaction mechanism. One possibility is to introduce short-range potentials that approximately avoid overlaps and the crossing of trajectories [14, 23, 126, 145]. In a different approach, Ramanathan and Morse [128] combined Brownian dynamics of wormlike threads with Monte Carlo methods to reject dynamic moves that are sterically not possible. The major problem occurring with these techniques is that it is difficult to obtain data for dense systems and sufficiently long times, i.e., until the rotational dynamics is relaxed. Towards these aims, event driven dynamics is better suited; it is adapted to Brownian dynamics by introducing pseudo velocities for the propagation between two timesteps of the Brownian dynamics algorithm. In this spirit, Tao et al. [146] have worked out a close approximation to an event driven algorithm for three-dimensional rodlike colloids.

For the model we present here, the random displacements drawn according to Eqs. (3.69) are divided by the time interval τ_B and this way interpreted as pseudo velocities. These random velocity changes in time intervals τ_B represent the coarse-grained interaction with the solvent—in between these intervals, the simulated motion of the rod is ballistic, and collisions with the hard obstacles in the neighborhood are calculated from momentum and energy conservation. The pseudo velocities are only a technical tool and have no physical meaning. By construction, the diffusion coefficients in the simulations are independent of the size of the Brownian time grid τ_B, e.g.,

$$\frac{\delta r_{\parallel}^2(t)}{2t} = \frac{N\left\langle \left(\Delta r_i^{\parallel}\right)^2 \right\rangle}{2N\tau_B} = D_{\parallel}^0.$$

As a consequence, the mean pseudo velocities are inversely proportional to τ_B,

$$\left\langle v_{\parallel}^2 \right\rangle := \left\langle \left(\frac{\Delta r_i^{\parallel}}{\tau_B} \right)^2 \right\rangle = \frac{2D_{\parallel}^0}{\tau_B}, \tag{4.1}$$

which is an unphysical side effect.

The crucial step of the collision part of the algorithm is the exact calculation of the next collision times. This amounts to the solution of a highly nonlinear equation, which is in this case analytically not possible. The numeric solution, however, can be obtained reliably and to any numerically representable precision by taking advantage of interval arithmetics. For this purpose we have implemented an interval Newton algorithm [66], as explained in detail in the PhD thesis of Höfling [69].[1]

The calculation of the collision times is also the most time-consuming part of the algorithm. Apart from the obstacle density $n^* = nL^2$, the timestep τ_B has major influence on the duration of

[1] The algorithm uses the interval arithmetic library of the boost C++ library project, in combination with the correctly rounded mathematical library CRlibm. This guarantees the accurate computation of the collision times. To increase efficiency, a dynamic cell list reduces considerably the amount of necessary calculations.

this calculations. This is founded by the frequent velocity changes, making necessary new calculations for the next collisions each time. Thus it is indispensable to find a reliable criterion such that τ_B can be chosen as large as possible, while still guaranteeing physically correct results. The Langevin algorithm is designed to correctly generate diffusive dynamics for $t \gg \tau_B$. The presence of obstacles introduces new length scales, which are translated to timescales by dividing by a velocity. Hence the timestep τ_B has to be chosen in relation to the relevant timescale induced by the obstacles, in a way that the simulations correctly produce diffusive trajectories in confined systems. This can be validated on the microscale by observing features of the velocity-autocorrelation function, and on the macroscopic scale by the measurement of diffusion coefficients. The next two paragraphs are devoted to these subjects.

4.2.1 Velocity-autocorrelation function

The dynamics of the rod in the two-dimensional model system is very different for the two components in the body frame, the longitudinal and the transverse motion. The longitudinal diffusion is completely independent of the obstacle density, since the excluded volume of the obstacles vanishes as well as the diameter of the rod. Thus the autocorrelation function of the parallel velocity is not affected by a nonzero n^*, and may serve as a generic example for the velocity-autocorrelation function of Brownian dynamics simulations. Physically, this observable always vanishes, since there are no correlations in the velocity of freely diffusing objects. Computationally, this is true for $t > \tau_B$, as shown in Fig. 4.2. For $0 \le t \le \tau_B$, the velocity-autocorrelation decays linearly from $\langle v_\parallel^2 \rangle$ to zero—a consequence of the moving time window of the average calculation in the simulations.

In contrast, the transverse motion of the rod is strongly affected by the presence of obstacles. The microscopic timescale introduced by the obstacles is the mean time between subse-

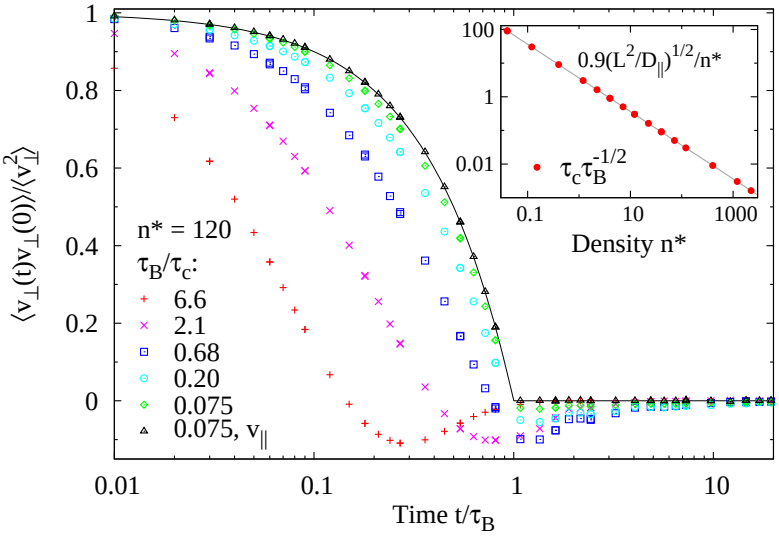

Figure 4.2: Autocorrelation function of the perpendicular velocity in the body frame, $v_\perp(t) := \boldsymbol{v}(t) \cdot \boldsymbol{u}_\perp(t)$, at $n^* = 120$ and for different values of the simulation timestep τ_B. The negative tails are a consequence of the collision dynamics and vanish if $\tau_B/\tau_{\text{coll}} \ll 1$. The black triangles and the black line display the autocorrelation of the parallel velocity, $v_\parallel(t) := \boldsymbol{v}(t) \cdot \boldsymbol{u}(t)$. *Inset:* Mean time between obstacle encounters, τ_c, rescaled with $\sqrt{\tau_B}$. Red bullets show simulation data; for the functional from represented by the gray line the prefactor has been fitted.

quent encounters of obstacles by the rod, τ_c. Only when $\tau_B \ll \tau_c$, the perpendicular velocity-autocorrelation function approaches the generic case of no correlations for $t > \tau_B$ and a linear decay before. For larger timesteps, $\tau_B \approx \tau_c$, the microscopic collision dynamics of the algorithm becomes visible by negative tails indicating the reflections of $v_\perp$. Note that even for $t > \tau_B$ the perpendicular velocity-autocorrelation does not vanish, but weakly oscillates at negative values with period τ_B. This is a consequence of the inaccessible volume in phase space, in the same manner as already mentioned in Sec. 2.3.2. A detailed explanation is given in Appendix A.

We conclude that a choice $\tau_B \lesssim \tau_c$ should be sufficient for the simulations to generate valid physics on timescales much larger than τ_B. One has to bear in mind, however, that the rate of encounters itself depends on the magnitude of τ_B via the pseudo velocities, cf. Eq. (4.1). For a derivation of the functional form of τ_c it is useful to refer to the tube model by Doi and Edwards [31]: The constraints of the obstacles surrounding the rod are interpreted as an effective "tube" in which the rod moves by sliding longitudinally, and only very small steps in the rotation are possible. The diameter d of the tube is estimated by allowing only one obstacle inside of it, $nLd \approx 1$. With this,

$$\tau_{\mathrm{coll}} \approx \frac{d}{\langle v_\perp \rangle} = \sqrt{\frac{\tau_B L^2}{D_\parallel^0}} \frac{1}{n^*}. \tag{4.2}$$

The inset of Fig. 4.2 displays the density dependence of this result, and the values obtained from the simulations for different τ_B.

4.2.2 Convergence of the diffusion coefficients

The size of the timestep not only has consequences for the microscopic dynamics, but also influences macroscopic observables. From the simulations one can obtain density-dependent diffusion coefficients by measuring the long time asymptotic form of the mean-square displacements. The results thereof may spuriously depend on the size of τ_B, if it is not chosen small enough, as explained in the previous section. As an example, the rotational diffusion constant is defined from

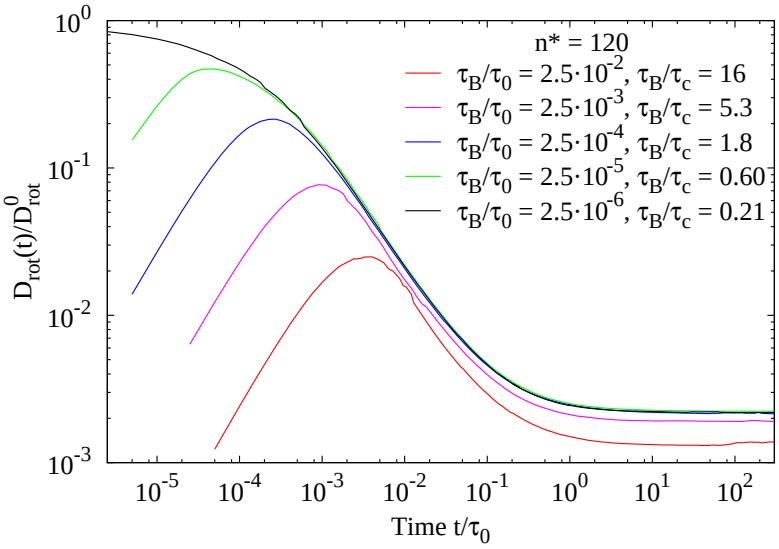

Figure 4.3: Convergence of the long-time limit of the rotational diffusion coefficient with decreasing microscopic Brownian timestep τ_B. For this data, $D_{\mathrm{rot}}^0 = 24 D_\parallel / L^2$.

the mean-square angular displacement $\delta\theta^2(t) := \langle \Delta\theta(t)^2 \rangle$ by

$$D_{\mathrm{rot}}(n^*) := \lim_{t\to\infty} \frac{\delta\theta^2(t)}{2t}. \tag{4.3}$$

Other diffusion coefficients are defined accordingly. Only for the body frame longitudinal motion the relation is trivial; this direction of motion is not affected by obstacles as long as the excluded volume vanishes, hence $D_\parallel \equiv D_\parallel^0$. The full time dependence of D_{rot} is displayed in Fig. 4.3, i.e., Eq. (4.3) without evaluating the limit. The asymptotic value for large times becomes independent of τ_B for $\tau_B/\tau_c < 1$; otherwise, the simulations give incorrect results. The maximum visible in the data for $\tau_B/\tau_c \geq 0.60$ indicates the transition in the simulations algorithm from free ballistic flights to overdamped Brownian motion. The value of the maximum grows in approaching $D_{\mathrm{rot}}(t\to 0)/D_{\mathrm{rot}}^0 \to 1$ due to the increasing pseudo velocity, as given in Eq. (4.1).

The computational costs per simulated time unit scale approximately $\sim n^{*2}$ for $n^* \gg 1$, comprising the appropriate adjustment of the timestep.

4.2.3 The emergence of anisotropic diffusion

Whereas the preceding two sections dealt with the correct handling of the algorithm at a fixed density, physically most interesting effects are observed in varying n^*—more precisely, in the regime towards large n^*. Already a visual inspection of the center of mass trajectories of a rod points to a central peculiarity. Three sample trajectories for different number densities $n^* = nL^2$ in are shown in Fig. 4.4. In case of $n^* = 4$, the motion still is quite isotropic on the scale of this figure. When the density becomes higher, the rod is more and more restricted to the direction parallel to its local orientation. The isotropy of the trajectory is lost, and at $n^* = 400$, the rod can only proceed by large zigzag moves enforced by the constraining obstacles close to the rod. Note that this anisotropy does not in any way go back to the slight anisotropic friction of the rod in a solvent, as introduced by slender rod hydrodynamics, Eq. (3.68). The observed phenomenon is an obstacle-induced dynamic entanglement effect and can be explained in terms of the tube concept, subject of the next section.

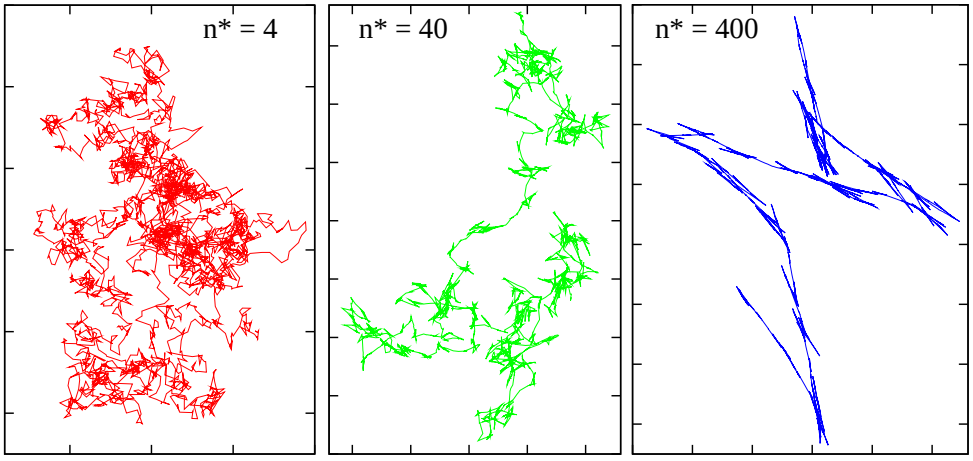

Figure 4.4: Typical trajectories of the center of the needle for overdamped dynamics; the obstacles are omitted for clarity. With increasing entanglement, the needle is confined to a narrowing "tube", and reptation dynamics emerges. In terms of the entanglement index $\mathrm{pE} := -\log_{10}(\xi/L)$, introduced in Sec. 4.3: $n^* = 4$ is equivalent to $\mathrm{pE} = 0.3$, $n^* = 40$ to $\mathrm{pE} = 0.8$, and $n^* = 400$ to $\mathrm{pE} = 1.3$.

4.3 Entangled dynamics and the tube concept

For a three-dimensional suspension of needles of number density n, Doi and Edwards [30] conjectured an asymptotic suppression of the rotational diffusion coefficient, $D_{\rm rot} \sim n^{-2}$ as $n \to \infty$. The slow dynamics at long times is expected to be universal irrespective of the microscopic motion; so far, research focused on ballistic needles, i.e., without solvent. Early molecular dynamics simulations of such needle liquids [43, 44, 106] show substantial deviations from Enskog theory. It was pointed out that the Doi-Edwards scaling of $D_{\rm rot}$ is approached only very slowly and difficult to observe. Semiquantitative agreement was found using a pseudo-dynamics [32]; yet, the Doi-Edwards scaling has not been validated by a simulation of the dynamics. Within an elaborate Boltzmann-Enskog theory [119], the onset of anisotropic diffusion from the dilute regime has been explained recently.

Large scale simulations of the model set forth in Sec. 4.1 make possible for the first time to analyze quantitatively the constraint dynamics and the predicted scaling behavior. We compare ballistic [69] and overdamped micro-dynamics of the needle. In the ballistic case, the total kinetic energy is conserved, and its value sets the overall time scale $\tau_0 := L/v$ of the problem; v denotes the root mean-square velocity. For overdamped dynamics, the time scale τ_0 is defined via the coefficient of unhindered diffusion along the axis of the needle, $\tau_0 = L^2/D_\parallel^0$. Diffusion coefficients of the rotational motion have been extracted from the long-time behavior of the mean-square angular displacement $\delta\theta^2(t) := \langle \Delta\theta(t)^2 \rangle \simeq 2D_{\rm rot}t$ and are shown on a double-logarithmic plot in Fig. 4.5a. In the investigated density range, the diffusion coefficient $D_{\rm rot}$ varies over seven nontrivial decades. For dilute systems, $n^* \ll 1$, it depends on the micro-dynamics: In the ballistic case, the diffusion coefficient is suppressed in quantitative agreement with a Boltzmann theory [69], $D_{\rm rot} = 10.5/n^*\tau_0$. For overdamped motion, the needle is unaffected by the obstacles, and the diffusion coefficient is just given by $D_{\rm rot}^0$. Once the mesh size becomes comparable to the length of the needle, $\xi \approx L$, the isotropy of rotational dynamics breaks down and a different transport mechanism develops [113]. With growing entanglement, the needle is increasingly caged by the obstacle array, and eventually, its rotational motion is strongly hindered. Fig. 4.4 illustrates the emergence of reptation-like dynamics, accompanied by a drastic suppression of the diffusion coefficient $D_{\rm rot}$. For $nL^2 \geq 10^2$, the data follow an asymptotic power law, $D_{\rm rot} \sim (n^*)^{-2}$, over more than four decades in the diffusion coefficient. As a most sensitive test, Fig. 4.5b compares $D_{\rm rot}$ to its asymptotic behavior for increasing entanglement. Our results show that the mechanism of reptation is universal for ballistic and overdamped motion of the needle, which will be substantiated further in the subsequent analysis.

The asymptotic suppression of $D_{\rm rot}$ is rationalized by employing the concept of a confining tube [30]. In this picture, the surrounding obstacles reduce the accessible volume of the needle to a tube of diameter d and length L. The diameter is estimated from the requirement to encounter no obstacles in the tube, $d \approx 1/nL = \xi^2/L$. The constrained motion is illustrated in Fig. 4.4 and 4.6: the transverse and rotational degrees of freedom are essentially frozen, permitting only displacements along the axis of the tube. After traveling half its length, the needle is confined to a new tube tilted against the previous one on average by an angle $\epsilon \approx d/L$. The time $\tau_{\rm d}$ to disengage from a current tube is estimated from the free longitudinal motion inside the tube, $\tau_{\rm d} \approx \tau_0$, independent of the density. Eventually, the orientation performs a random walk with step size ϵ and constant rate $1/\tau_{\rm d}$; hence, the diffusion coefficient scales as

$$D_{\rm rot} \simeq D_{\rm rot}^\infty := \frac{\epsilon^2}{2\tau_{\rm d}} \sim \frac{1}{n^2L^4\tau_0} \qquad \text{for} \quad n^* \to \infty. \tag{4.4}$$

The given arguments apply likewise to ballistic and overdamped dynamics of the needle. In both cases, our data in Fig. 4.5 provide ample evidence for such a behavior, unprecedented in the literature.

The quality of our data allows us to verify and quantify the assumptions of the tube model in detail on the basis of the mean-square displacements. Fig. 4.7 visualizes mean-square displacements in the semi-dilute regime, $n^* \gg 1$. We define the displacement in the *body-fixed* frame along the axis as $\Delta R_\parallel(t) := \int_0^t \dot{\boldsymbol{R}}(t') \cdot \boldsymbol{u}(t') \mathrm{d}t'$, and similarly the transverse part $\Delta R_\perp(t)$. The parallel mean-square displacement, $\delta r_\parallel^2(t) := \langle \Delta R_\parallel(t)^2 \rangle$, is not affected by the obstacles at all, due to zero excluded volume. Consequently, the parallel diffusion coefficient is independent of the density, $D_\parallel \equiv D_\parallel^0$. In contrast, the perpendicular mean-square displacement $\delta r_\perp^2(t)$ and the mean-square angular displacement $\delta\vartheta^2(t)$ enter a plateau beyond a density-dependent time scale τ_{conf}. The plateau reflects the local confinement to an effective cage built up by the surrounding obstacles, i.e., the tube. Its diameter $d \approx 1/nL$ leads to a relation for the time when the confinement becomes effective, $\tau_{\mathrm{conf}} := d^2/D_\perp^0 \approx 1/n^2L^2D_\perp^0$. At the time scale $\tau_0 = L^2/D_\parallel$, the rod moves a distance comparable to its length L, hence it leaves the tube and the mean-square displacements become diffusive again. From the long-time asymptotes, the diffusion coefficients are read off,

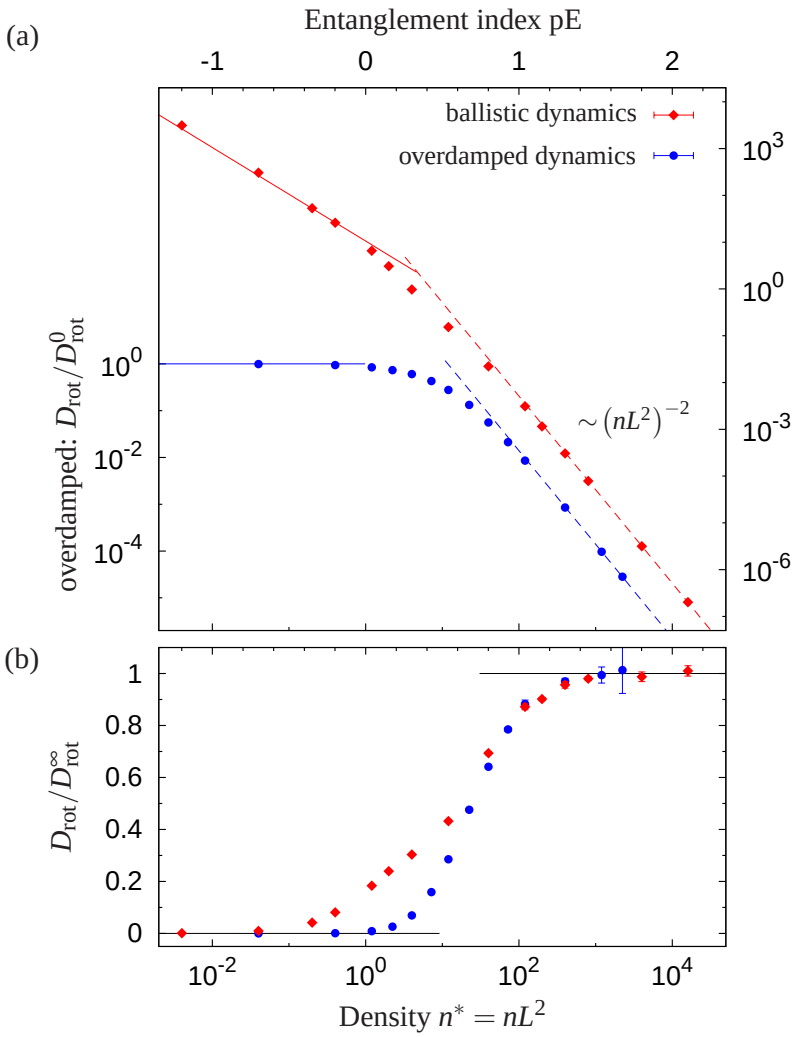

Figure 4.5: Simulation results for the rotational diffusion coefficient. (a) Dashed lines are asymptotic fits to the predicted Doi-Edwards scaling, $D_{\mathrm{rot}}^\infty = A(n^*)^{-2}$; the red solid line shows the result from a Boltzmann theory, $D_{\mathrm{rot}} = 10.5/n^*\tau_0$ [69]. (b) Deviation from the asymptotic behavior; note the different prefactors A in D_{rot}^∞ for ballistic and overdamped dynamics.

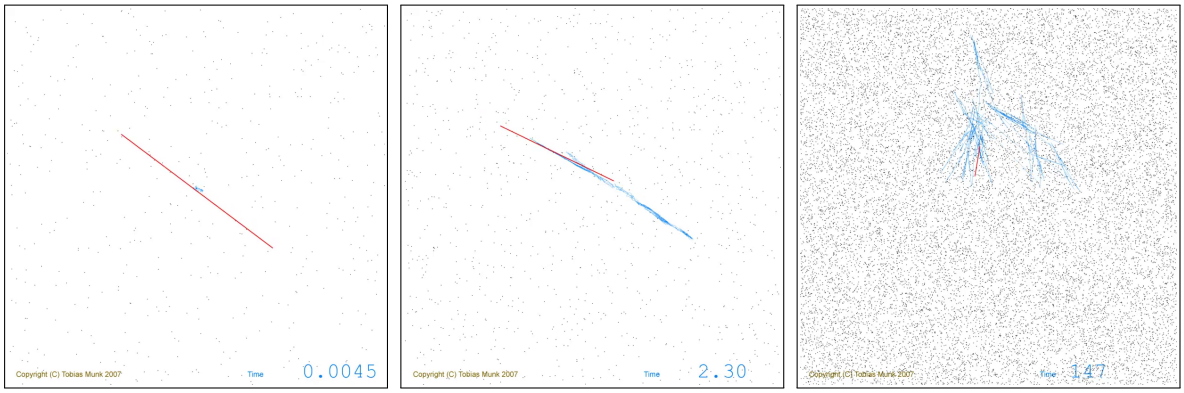

Figure 4.6: Reptation dynamics of an entangled needle; three snapshots from the supplementary movie of Publication D.3. The movie illustrates the typical motion on three different time and length scales for density $n^* = 120$ (pE = 1.04). In the first part, the stochastic fluctuations of the overdamped micro-dynamics as well as the individual collisions with the obstacles are resolved. One observes the confinement of the needle to a tube by the obstacles. The translational motion on this time scale is much smaller than the extension of the needle. The second part is sped up by a factor of 256 and shows the back and forth sliding of the needle and the remodeling of the tube. The orientational relaxation becomes apparent in the third part of the movie in which time elapses yet 64-times faster. Several hundred tube renewals occur before the needle rotates significantly. The blue line maps out the trajectory of the center of the needle as time progresses; positions of successive frames are joined by straight lines ignoring the intermediate displacements. At the bottom, the time lapse is displayed in units of $\tau_0 = L^2/D_\parallel^0$.

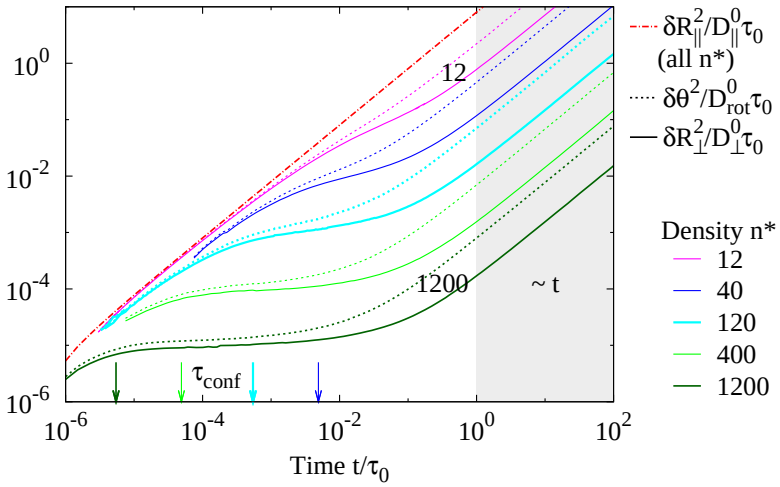

Figure 4.7: Simulated body-frame mean-square displacement in the entangled regime. For each density, three observables are shown: The mean-square displacement parallel to the rod's axis (topmost, dash-dotted), perpendicular (solid), and the mean-square angular displacement (broken). Arrows at the bottom indicate τ_{conf} for the corresponding density; the diffusive regime is shaded.

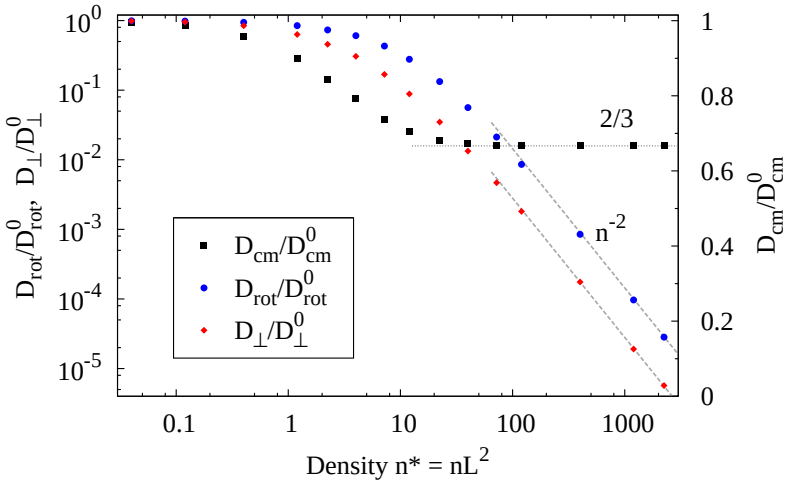

Figure 4.8: Density dependence of the diffusion coefficient of the center of mass (right axis), of rotational motion, and of perpendicular diffusion in the body frame (both at the left axis). Data for $D_{\rm rot}$ are identical with the overdamped dynamics data from Fig. 4.5. The constant value approached asymptotically by $D_{\rm cm}(t)/D^0_{\rm cm}$ is derived in Eq. (4.5).

e.g., $D_\perp(n^*) = \lim_{t\to\infty}\partial_t \delta r^2_\perp(t)/2$, as done in the context of Fig. 4.5 for the rotational diffusion. Fig. 4.8 demonstrates the huge suppression of the perpendicular and rotational diffusion coefficients: both scale with obstacle density as n^{-2}, as has been argued by Szamel [144]. The amplitude of the perpendicular diffusion is smaller than that of $D_{\rm rot}$, by a ratio $D_\perp/D_{\rm rot} \approx 0.05L^2$. A consequence of the vanishing perpendicular component is the saturation of the center of mass diffusion,

$$\frac{D_{\rm cm}(t)}{D^0_{\rm cm}} = \frac{D_\parallel + D_\perp(t)}{D_\parallel + D^0_\perp} \overset{n^*\gg 1}{\longrightarrow} \frac{2}{3}; \tag{4.5}$$

the numerical value relates to the slender rod approximation, as given in Eq. (3.68). For the largest simulated density, $n^* = 2240$, the anisotropy ratio approaches a value of $D_\parallel/D_\perp \approx 10^5$. Note again that these large ratios in dense systems do not require an anisotropy on the microscale; rather the anisotropic motion is generated dynamically from the strong interaction with many obstacles.

The square root of the plateau values in the mean-square angular displacement and the transverse mean-square displacement can be used as definitions of the tilt angle ϵ and the plateau diameter d. Both follow the expected scaling laws over two decades in Fig. 4.9, with the measured prefactors $d = 1.3/nL$, and $\epsilon = 1.3/n(L/2)^2 = 4.0d/L$.

4.3.1 Conclusion

Our results unambiguously prove the conjectured scaling relations for $D_{\rm rot}$, ϵ, and d. Thus, the model reflects the generic Doi-Edwards scenario, demonstrating that the essential physics due to entanglement is captured. The predicted scaling behavior is, however, only observed in highly entangled systems with large entanglement index, pE $\gtrsim 1$. In this regime, the trajectories indeed exhibit pronounced reptation with the typical sliding motion, see Fig. 4.4. The scaling is also robust with respect to a variation of the ratio $L^2 D^0_{\rm rot}/D^0_{\rm cm}$, as demonstrated in Appendix B.3.

For weaker entanglement, $0 <$ pE $\lesssim 1$, the rotational dynamics is still suppressed due to topological constraints, but the Doi-Edwards scaling is obscured by crossover phenomena. The deviations from the predicted behavior are highlighted in Fig. 4.5b by extracting the apparent amplitude of the power law. At pE = 1, where the filament length already exceeds the mesh size by a factor 10, the amplitude is still 15% below its true asymptotic value. One concludes that in order to observe the scaling with an accuracy of 1%, even stronger entanglement is required, pE $\gtrsim 1.6$.

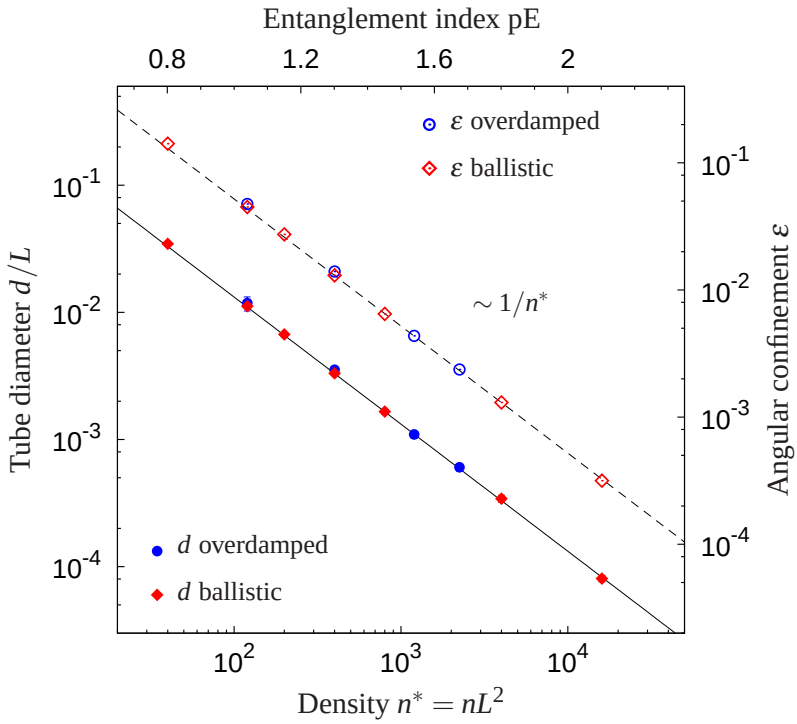

Figure 4.9: Dependence of the tube diameter on the entanglement index. The tube diameter d was measured as the plateau value of the transverse mean-square displacement. For both overdamped and ballistic dynamics, it is proportional to the angular confinement ϵ. Both quantities follow the predicted scaling; straight lines are fits to this power law determining the prefactors, $d = 1.3\xi^2/L$ and $\epsilon = 1.3/n(L/2)^2$.

In real polymer solutions, the entanglement constraints are dynamically released and generated on a time scale comparable to τ_d. Within an extended model accounting for this renewal process of the obstacles, we have checked that the observed Doi-Edwards scaling is robust [71].

For highly entangled networks, the finite filament width in experimental situations may become relevant. Eventually, a phase transition to a nematic order occurs for long rods at $n_{3d}bL^2 \simeq 1$ as has been estimated by Onsager, where n_{3d} denotes the three-dimensional number density of rods of diameter b. The density of obstacles of our two-dimensional representation is then calculated to $n \approx n_{3d}L$, hence the nematic regime is expected for $n^* b/L = nbL \gtrsim 1$. For reconstituted F-actin solutions with filaments of $L \approx 50\,\mu$m [79] and $b = 7$ nm, we estimate that nematic effects are relevant only for $n^* \gtrsim 7000$ or pE $\gtrsim 1.9$, provided one can neglect the small bending flexibility.

A finite stiffness for the polymer introduces another length scale, the persistence length, quantifying the distance over which the polymer appears as a straight rod. Due to thermal noise, there are transverse undulations which effectively blow up the width of the polymer. It is an open question if the finite flexibility assists for the tube remodeling resulting in an enhanced rotational diffusion, or if the additional effective volume leads to further slowing down.

4.4 Effective Perrin theory

The tube concept yields a very successful theoretical description in two respects: First, it offers an explanation for the effects of entangled dynamics in suspensions of rods on a coarse grained microscopic scale, proven by the correct scaling of the parameters of the local constraints, ϵ and d. Second, based on this coarse grained microscopics it explains the asymptotic long time behavior in terms of diffusion coefficients. By construction, however, it is not a dynamic theory. We will prove in the remaining parts of this chapter that the Smoluchowski-Perrin theory serves this purpose, although originally set up for unhindered diffusion. This way, the large gap in time scales is filled, too, which is present in between the dynamics at the coarse grained microscopic scale, and the macroscopic regime of the diffusion constants, see Fig. 4.10.

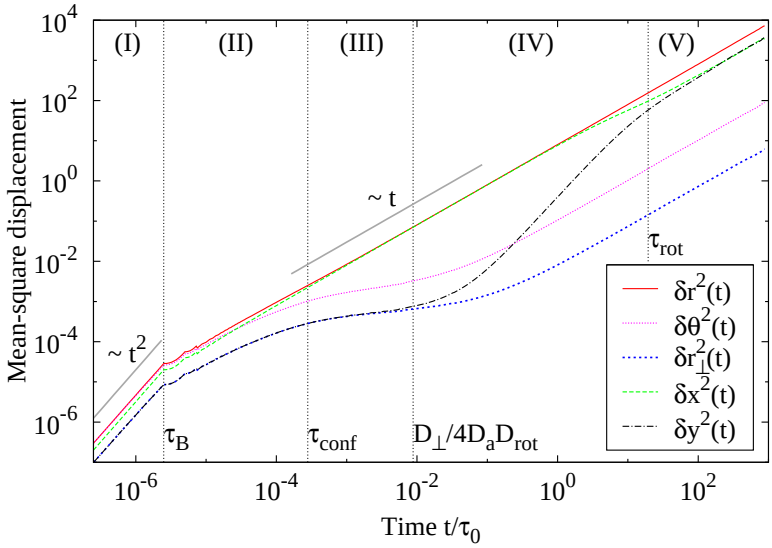

Figure 4.10: Time domains found in mean-square displacements from simulations; complement to Fig. 4.7 for fixed $n^* = 120$. Spatial displacements are shown in units of $(L/2)^2$.

(I): $t < \tau_B$. Ballistic regime of technical origin; the algorithm calculates the trajectories ballistically until the diffusive dynamics becomes effective at $t = \tau_B$. Cf. Sec. 4.2.

(II): $\tau_B \leq t \lesssim \tau_{\text{conf}}$. Microscopic diffusive regime, governed by the Langevin equations given in Sec. 3.4.

(III): $\tau_{\text{conf}} < t \lesssim D_\perp/4D_aD_{\text{rot}}$. Dynamics inside the tube. Its diameter d defines the transition between the regimes (II) and (III), by setting a spatial constriction to the perpendicular motion, $\tau_{\text{conf}} := d^2/D_\perp^0$. The transverse and rotational motion are suppressed, therefore at a plateau. Cf. Sec. 4.3.

(IV): $D_\perp/4D_aD_{\text{rot}} < t < \tau_{\text{rot}}$. Transitional region between confined motion inside the tube and fully relaxed long time limit. $\delta r_\perp^2(t)$ and $\delta\theta^2(t)$ cross over to diffusion, indicating that the rod now has gained the possibility to rotate and move sideways, by means of a zigzag motion that couples rotation and translation. A rotation or transverse motion with unchanged center of mass is not possible, but longitudinal displacements of length L within a time $\tau_0 := L^2/D_\parallel$ enable the rod to rotate step-by-step. $\delta y^2(t)$ increases $\sim t^2$ in the transition from plateau to isotropic diffusion. The timescale for the onset of this region is derived in Sec. 4.4.

(V): $t \gtrsim \tau_{\text{rot}}$. Diffusive long time dynamics—all relaxation processes had time to evolve. The slowest relaxation is given by the rotational dynamics, hence $\tau_{\text{rot}} := D_{\text{rot}}^{-1}$ defines the onset of regime (V). Diffusion coefficients can be measured in this domain, as done in Sec. 4.3.

The idea is to use the solutions of the Smoluchowski-Perrin equation with the measured diffusion coefficients $D_\parallel, D_\perp(n^*), D_{\rm rot}(n^*)$ also in the presence of obstacles to obtain a prediction for time-dependent mean-square displacements, and later also the intermediate scattering function. Such an effective Perrin theory is obviously valid on macroscopic time and length scales, i.e., for $t \gg \tau_{\rm rot}$ and $k^{-1} \gg L_{\rm rot} := \sqrt{D_a \tau_{\rm rot}}$. We will show that in fact it constitutes a quantitative *mesoscopic* theory in the dense regime, $n^* \gg 1$. That such an approach should work in principle has been anticipated earlier for dense needle liquids [119].

4.4.1 Anisotropic diffusion

As a first exemplification, the effective theory elucidates the remarkable time evolution associated with the huge anisotropy, as generated by the model for entangled rods in Sec. 4.3. A characteristic crossover between anisotropic and isotropic dynamics is seen clearly when plotting the time-dependent diffusion coefficients in a *space-fixed* frame, $D_x(t) := \partial_t \langle \Delta x(t)^2 \rangle_{\rm f}/2$ and $D_y(t) := \partial_t \langle \Delta y(t)^2 \rangle_{\rm f}/2$, where the subscript 'f' indicates that the initial orientation is fixed to the x-axis. The memory of the orientation is lost only at times larger than $\tau_{\rm rot} \sim n^2$, resulting in a time window of anisotropic diffusion that is significantly prolonged with increasing density, see Fig. 4.11. The analytic expressions for the comparison with simulated mean-square displacements have been derived in Eqs. (3.28) and (3.29). For the model in discussion here, the effective Perrin approach requires the measurement of only two parameters in the simulations, $D_\perp(n^*)$ and $D_{\rm rot}(n^*)$; the third diffusion coefficient $D_\parallel \equiv D_\parallel^0$ is a constant, due to the lack of excluded volume. Fig. 4.11 reveals excellent agreement between effective Perrin theory and simulations, down to the time scale τ_0.

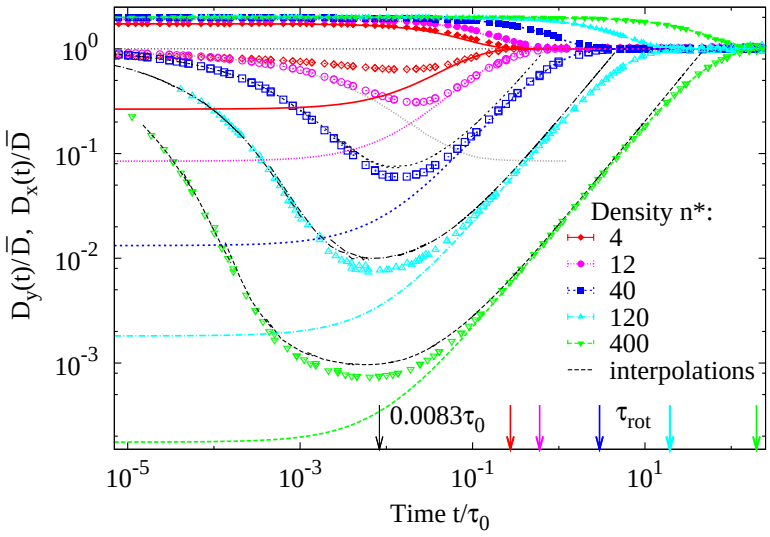

Figure 4.11: Diffusion coefficients of the center of mass in the space-fixed frame, relative to the isotropic values $\bar{D}(n^*)$. Filled symbols display the simulation results for the coefficient of diffusion parallel to the fixed initial orientation, $D_x(t)/\bar{D} \geq 1$, open symbols the corresponding perpendicular diffusion, $D_y(t)/\bar{D} \leq 1$. Color-coded lines show the Smoluchowski-Perrin theory, and the dashed black lines the interpolation between the space-fixed frame and the body frame, Eq. (4.8). Color-coded arrows at the bottom axis indicate $\tau_{\rm rot}$ for the different densities. The broken gray line represents the measured $D_\perp(t)/\bar{D}$ at $n^* = 12$ for comparison.

For short times, $t \ll \tau_0$, the space- and body-fixed frames coincide, implying $D_x(t) \simeq D_\parallel(t)$ and $D_y(t) \simeq D_\perp(t)$. In this regime, only the density independent motion longitudinal to the initial orientation matches to the effective theory; the double logarithmic plot exposes large discrepancies for the transverse motion. This is to be expected due to the large suppression of the coefficient of perpendicular diffusion, compare Fig. 4.8. Microscopically starting with a dynamics according to the free diffusion constants, Eqs. (3.68), the simulation data can converge to the predictions of the effective picture only after a sufficiently large number of encounters of obstacles in the environment. This happens in the region beyond, but still close to the minimum in the measured $D_y(t)$. The position of this minimum can approximately be determined by expanding the result from the Perrin theory, $D_y(t) = D_\perp + 4D_a D_{\mathrm{rot}} t + \mathcal{O}\left(t^2\right)$. The minimum in the simulations results is located in the proximity of the transition from the constant to a linear increase in the expression from Smoluchowski-Perrin theory, thus at $t \approx D_\perp / 4D_a D_{\mathrm{rot}}$; this timescale defines the beginning of region (IV) in Fig. 4.10. Since $D_\perp(n^*)$ and $D_{\mathrm{rot}}(n^*)$ scale identically for large densities with a ratio $D_\perp / D_{\mathrm{rot}} \approx 0.2 D_\perp^0 / D_{\mathrm{rot}}^0$, we can approximate the position of the minimum further, $t \approx (D_\perp / D_{\mathrm{rot}})/2D_\parallel \approx 0.0083\,\tau_0$. This position is indicated at the bottom axis of Fig. 4.11, and a visual inspection of simulation data and effective Perrin theory suggests that the latter constitutes the correct quantitative description beyond a time in the region $0.0083 < t/\tau_0 < 1$.

To understand the transition that appears in the dynamics with the onset of rotation close to the minimum in the measured $D_y(t)$, it is useful to work out an approximation for the mean-square displacement in the space-fixed frame that implements both the constrained dynamics at short times and the loss of the initial orientation at larger times. The velocities in the space-fixed frame are obtained from the body frame Langevin equations by the rotation given already in Eq. (3.70), $\dot{\boldsymbol{r}}(t) = \boldsymbol{S} \cdot \left(\dot{r}_\parallel(t), \dot{r}_\perp(t)\right)^{\mathsf{T}}$. In the body frame, the stochastic dynamics is decoupled, hence the averages factorize when writing the squared displacement in the space-fixed frame in terms of the body frame variables,

$$\left\langle \Delta y(t)^2 \right\rangle_{\mathrm{f}} = \int_0^t \mathrm{d}s \int_0^t \mathrm{d}s' \left[\left\langle \dot{r}_\parallel(s) \dot{r}_\parallel(s') \right\rangle \left\langle \sin\theta(s) \sin\theta(s') \right\rangle_{\mathrm{f}} + \left\langle \dot{r}_\perp(s) \dot{r}_\perp(s') \right\rangle \left\langle \cos\theta(s) \cos\theta(s') \right\rangle_{\mathrm{f}} \right]. \quad (4.6)$$

The processes we want to elucidate here are the dynamics inside the tube and the tube renewal, i.e., a regime with still small angular displacements. Thus we expand the trigonometrics, and exploit the invariance of the parallel dynamics by using the delta correlated parallel velocities, Eq. (3.64a),

$$\delta y(t)^2 = \delta r_\perp^2(t) + 2D_\parallel \int_0^t \mathrm{d}s \left\langle \theta(s)^2 \right\rangle_{\mathrm{f}} + \mathcal{O}\left(\theta^3, \dot{r}_\perp^2 \theta^2\right). \quad (4.7)$$

This expression relates the transverse mean-square displacement in the space-fixed frame to the corresponding one in the body frame and the mean-square angular displacement. A derivative with respect to time yields an approximation for the diffusion coefficient,

$$D_y(t) \approx \frac{1}{2} \partial_t \delta r_\perp^2(t) + D_\parallel \left\langle \theta(t)^2 \right\rangle_{\mathrm{f}}, \quad (4.8)$$

correctly interpolating the mesoscopic regime in Fig. 4.11.

A crosscorrelation of spatial and angular displacements is shown in Fig. 4.12. As long as there is essentially no rotation, i.e., for $t \ll \tau_0$, the features of the center of mass displacements are preserved: in the microscopic regime $\left\langle \Delta y^2(t) \cos\Delta\theta(t) \right\rangle_{\mathrm{f}}$ starts diffusive, proportional to $2D_\parallel^0 t$, and enters a plateau, indicating the confinement at large identities. Around $t = D_\perp / D_{\mathrm{rot}} D_\parallel \approx 0.017\,\tau_0$, a time window of strong rotation-translation coupling sets in, commencing in a slope

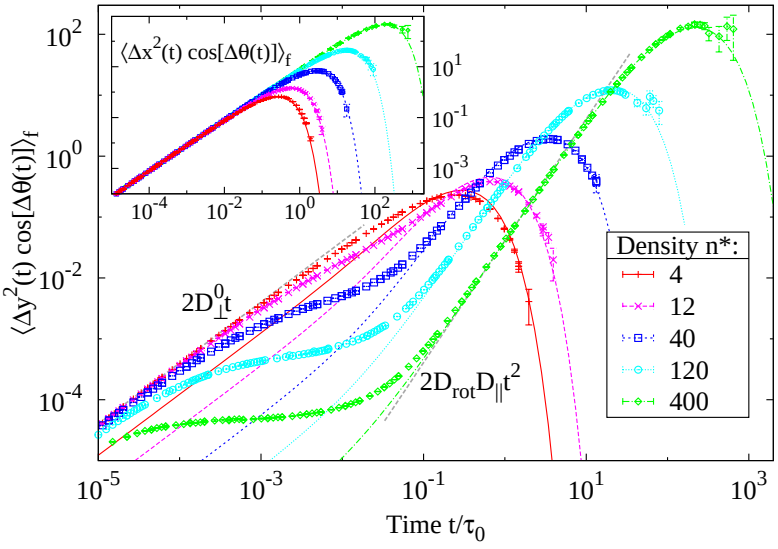

Figure 4.12: Crosscorrelation of the angular displacement with the center of mass displacement perpendicular to the initial orientation, in units $(L/2)^2$. The corresponding plot for free diffusion is given in Fig. 3.2. The inset shows the same observable for displacement longitudinal to the initial orientation; in this case, the results from the Smoluchowski-Perrin equation (lines) match the simulation data (symbols) at all times.

$2D_{\rm rot}(D_\parallel - 2D_\perp)t^2$ that is obtained from a quadratic expansion of Eq. (3.32). With the onset of the rotational relaxation at $t = \tau_{\rm rot}$ the maximum is approached, and by then, the freely diffusing orientation suppresses further correlations exponentially.

From the preceding analysis we conclude that the effective Perrin theory quantitatively represents the dynamics of rod suspensions for times $t \gg (D_\perp/D_{\rm rot})/2D_\parallel \approx 0.0083\,\tau_0$ in the observables analyzed so far. Conversely this also means that the density dependent diffusion coefficients utilized within the effective theory may be used for Brownian dynamics simulations of *free* systems, displaying identical dynamics as suspensions, if considered on sufficiently large timescales. For a qualitative visual analysis this is indicated in Fig. 4.13 by displaying parts of two trajectories: one obtained in a system with density $n^* = 400$ and microscopic diffusion constants according to Eqs. (3.68), and the other without obstacles, but with diffusion coefficients measured from the $n^* = 400$-system. There is no salient visible difference in the qualitative features, which again supports the effective approach.

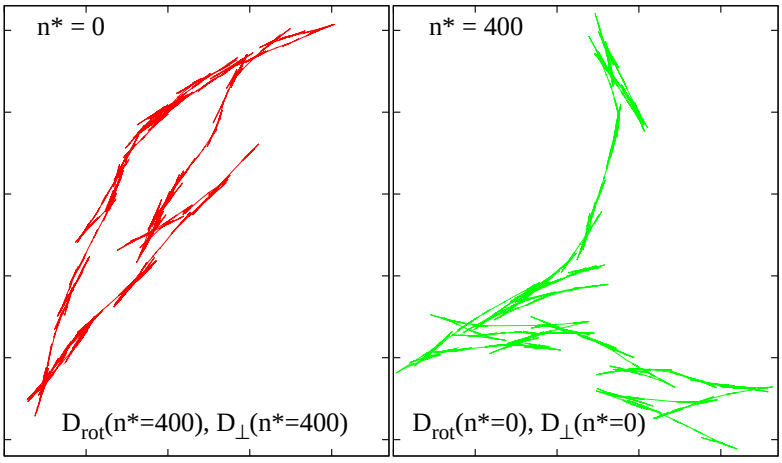

Figure 4.13: Left: center of mass trajectory at zero density, with diffusion constants $D_{\rm rot}(n^* = 400)$ and $D_\perp(n^* = 400)$. Right: trajectory at density $n^* = 400$, with $D^0_{\rm rot}$, $D^0_\perp$. Spatial resolution and time window are identical; the shortest resolved timestep here is $0.05\tau_0$.

4.4.2 Driving by a longitudinal force

Introducing a longitudinal force in the Langevin equations of a rod yields a ballistic component in the longitudinal displacement, compare Eq. (3.71). In $\delta r_\parallel^2(t)$, it will always be the dominant contribution for large times, $t \gg \tau_0$; other observables are influenced depending on the relative magnitude of the force. Fig. 4.14 exemplary displays the center of mass displacement. Three time regimes are visible: diffusive motion for short times, $t \ll 4\bar{D}/f^2 D_\parallel^2$, and long times, $t \gg 4\bar{D}/f^2 D_\parallel^2 + 2/D_{\mathrm{rot}}$, and in between an intermediate force-driven ballistic regime, enlarging with the magnitude of the force. Theory matches excellently, hence the superdiffusive motion observed in experiments [29] can probably be accounted to the simple propulsion mechanism included in our model.

Fig. 4.15 shows the variation of the diffusion coefficients with the longitudinal driving, for a fixed medium density. There is no obvious simple scaling visible in the displayed parameter region, so this behavior might deserve a more detailed analysis in a future work.

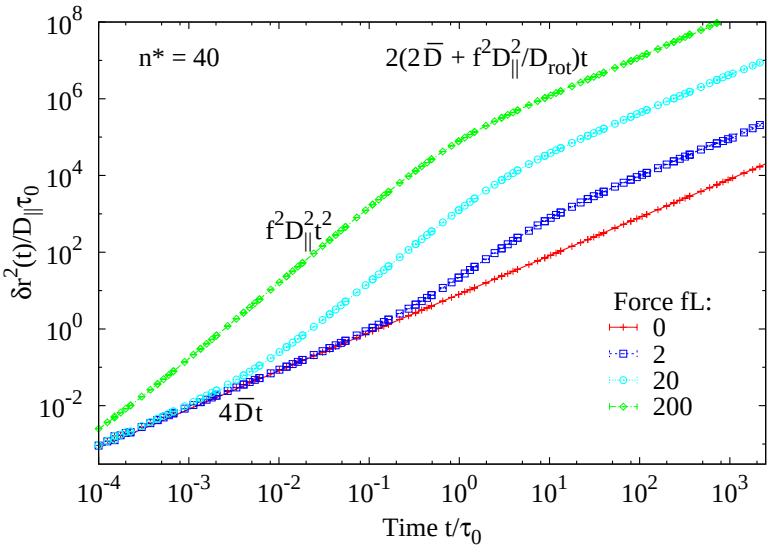

Figure 4.14: Mean-square displacement of the center of mass of a rod, with varying force directed longitudinal to its orientation, at a density $n^* = 40$. Symbols show simulation results, color-coded lines the effective Perrin theory, Eq. (3.31).

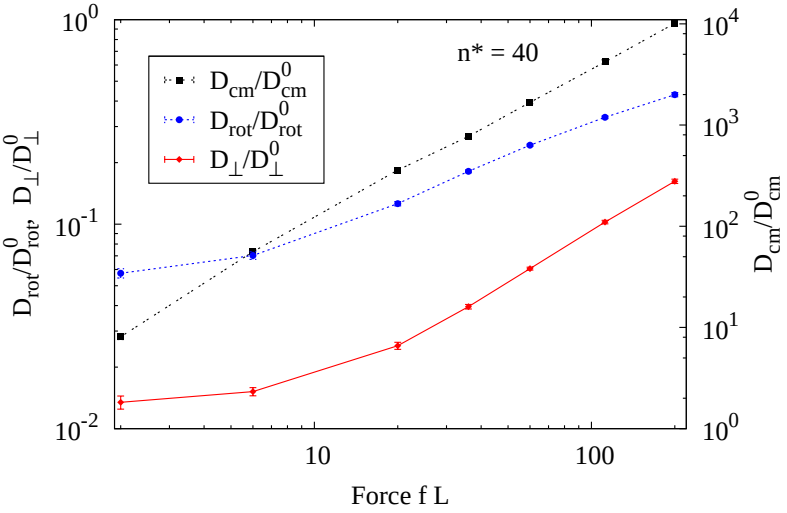

Figure 4.15: Diffusion coefficients for constant density $n^* = 40$ and varying longitudinal force. The center of mass diffusion is displayed at the right axis, the rotational motion and the perpendicular diffusion in the body frame at the left axis.

4.4.3 Correlation functions of fourth order: non-Gaussian parameter

The three microscopic stochastic processes that generate the diffusion of the rod in the body frame are Gaussian processes, cf. Eqs. (3.64) and (3.67). Nevertheless, already the freely diffusing rod shows non-Gaussian statistics for $t \lesssim \tau_{\mathrm{rot}}$ due to the transformation to the space-fixed inertia frame, as demonstrated in Fig. 3.3. At nonzero density, this is considerably more pronounced: Fig. 4.16 displays a strongly non-Gaussian time window $\tau_{\mathrm{conf}} \lesssim t \lesssim \tau_0$ even in the rotational dynamics, an observable that is strictly Gaussian when the diffusion is unconfined. This time window corresponds to the plateau regime in the mean-square displacement, thus the obvious conclusion is that the suppression of rotational motion inside the tube accounts for the non-Gaussian statistics. The center of mass non-Gaussian parameter shows a prolonged plateau decaying only at $t \gtrsim \tau_{\mathrm{rot}}$, in accordance with the effective Perrin theory. The plateau value is $\left(D_a/\bar{D}\right)^2/2$, converging to 1/2 for large densities. Towards the microscopic regime, the center of mass non-Gaussian parameter leaves the plateau of the effective theory when $t \lesssim \tau_{\mathrm{conf}}$, to approach for smaller times

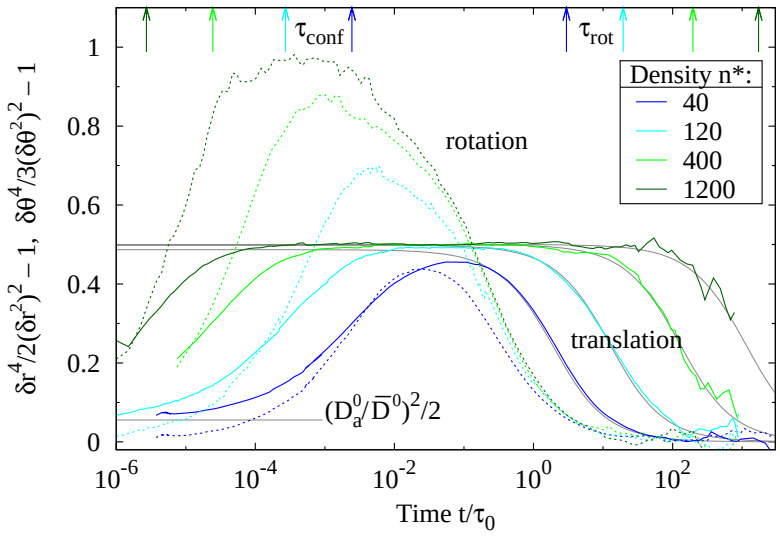

Figure 4.16: Non-Gaussian parameter for the center of mass motion (continuous lines) and the rotational diffusion (dashed lines). The effective Perrin theory for the center of mass according to Eq. (3.37) is displayed by gray lines.

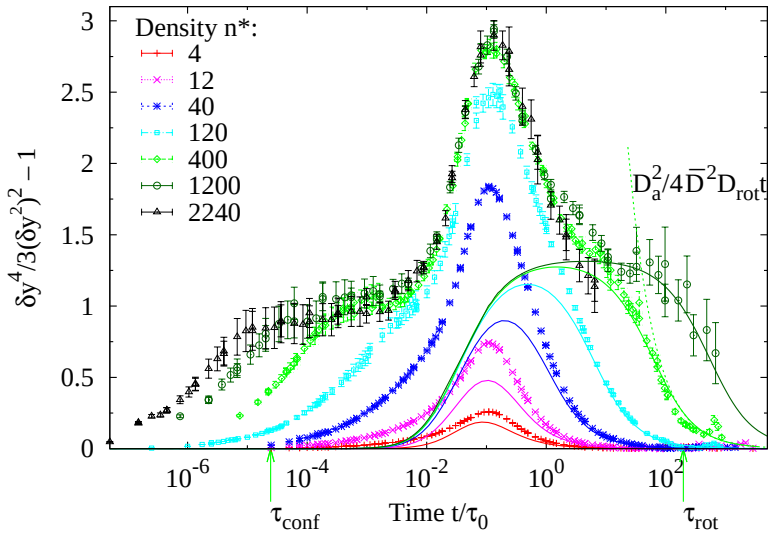

Figure 4.17: Non-Gaussian parameter for the motion perpendicular to a fixed initial orientation. Symbols are simulation results, color-coded lines the corresponding functions from the effective Perrin theory. The timescale that corresponds to the onset of the plateau and that of the terminal decay are indicated at the bottom for the example of $n^* = 400$.

the microscopic plateau $\left(D_a^0/\bar{D}^0\right)^2/2$ that is also visible in Fig. 3.3.

In the space-fixed frame, the non-Gaussian parameter of the transverse motion is remarkable, see Fig. 4.17. Here, the effective Perrin theory only holds when $t \gg \tau_0$, especially at large densities. The theory predicts a peak broadening towards a plateau around $t \approx \tau_0$; in contrast, in the simulation data a different plateau emerges in the confined regime, $\tau_{\text{conf}} < t \ll \tau_0$. Furthermore, a sharp peak develops, located at $t \approx 0.1\tau_0$ independent of n^*. The height of this peak seems to converge to the value 3 at very large densities. Asymptotically, the non-Gaussian parameter decays to zero proportional to t^{-1} for $t \gtrsim \tau_{\text{rot}}$, as expected for a stochastic process with cumulants linear in time.

4.5 Self-intermediate scattering function

Based on the simulation results for the intermediate scattering function, we test the range of validity of the effective Perrin theory in Fig. 4.18. The quality of our data, approaching a signal-to-noise ratio of 10^{-4} in the scattering function, allows for a clear distinction of features on a large range of

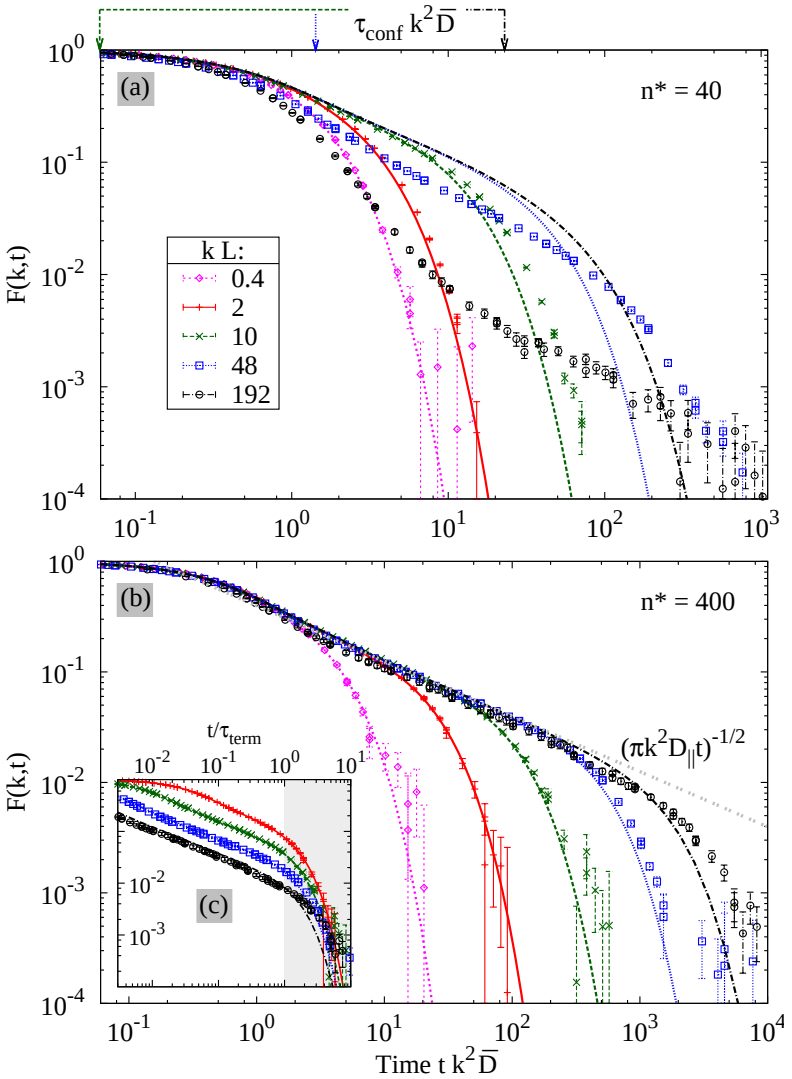

Figure 4.18: Time and wavenumber dependence of the intermediate scattering function for densities (a) $n^* = 40$, and (b), (c) $n^* = 400$. Symbols represent simulation results, lines the effective Perrin theory, Eq. (3.51), and time is in units of $k^2\bar{D}$. By rescaling time with τ_{term}, inset (c) visualizes the terminal relaxation.

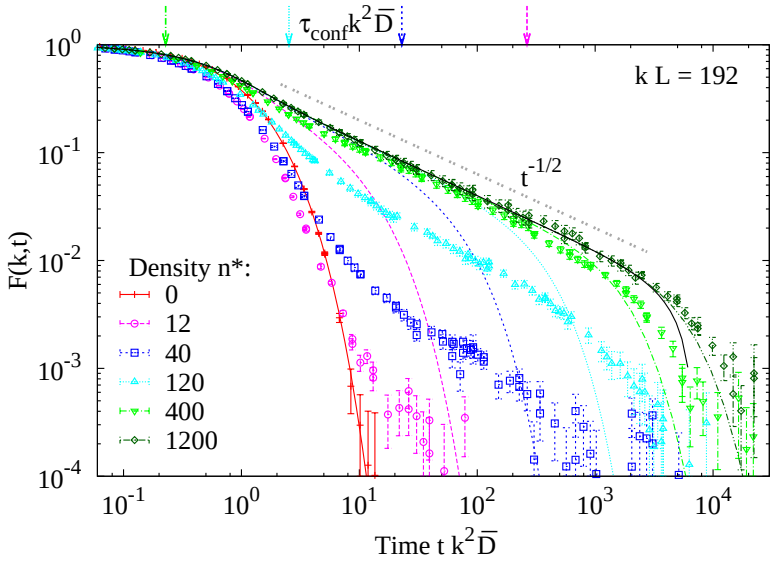

Figure 4.19: Intermediate scattering function for fixed wavenumber and varying density. Increasing confinement is manifested in the simulations (symbols) by the development of a power law decay. Lines show the effective Perrin theory; the first order perturbative solution, Eq. (4.15), is indicated by the thick black line for $n^* = 1200$.

time and length scales.[2] The agreement of theory and data becomes increasingly accurate as the wave number decreases [panels (a) and (b)]. Second, deviations are shifted to larger wavenumbers for higher densities. We conclude that there is a density-dependent length scale determining the validity of our coarse-grained approach. From all simulated densities, we have identified this length scale as the typical distance between obstacles, $\xi := n^{-1/2}$; for the shown densities, $n^* = 40$ and $n^* = 400$, the corresponding wavenumbers $2\pi/\xi$ are $40L^{-1}$ and $126L^{-1}$, respectively. The relevance of ξ is corroborated further in Figs. 4.20 and 4.21. From the first set of plots we deduce that the measured intermediate scattering function, displayed as a function of time, is in fact accurately described by the effective theory when $k\xi/2\pi \lesssim 1$. Above this threshold, a distinct microscopic regime separates out at short times, resulting from the free Brownian motion inside the tube. At larger times, the confinement by the surrounding obstacles becomes effective, and the exponential decay of the free microscopic motion crosses over to the transitional power law $t^{-1/2}$. When the scattering function is displayed as a function of the wavenumber, the quantitative and qualitative change as compared to the Perrin theory is directly visible, once a length scale of the order of $2\pi L/\xi$ is approached. Fig. 4.21 exemplifies this for a medium and a large density—as long as $k \ll 2\pi/\xi$, the effective approach is appropriate, especially for high densities.

The slowing down of the dynamics with increasing confinement is displayed in Fig. 4.19. For high wavenumbers $k \sim 2\pi/d$ the intermediate scattering function probes the formation of the tube at time scales τ_{conf}, see Figs. 4.18a and 4.19. Once the tube confinement becomes effective, an intermediate algebraic decay emerges, $F(\boldsymbol{k}, t) \sim 1/kt^{1/2}$, which we attribute to the sliding motion inside the tube. This power law is cut off by an exponential relaxation at τ_{term} as derived in Eq. (3.52), see Fig. 4.18c.

[2] To achieve sufficient statistics, we collected at least 350 trajectories for each density. For the largest densities, the simulation of a single trajectory took about 13 days of CPU time on an AMD Opteron® 2.6 GHz core.

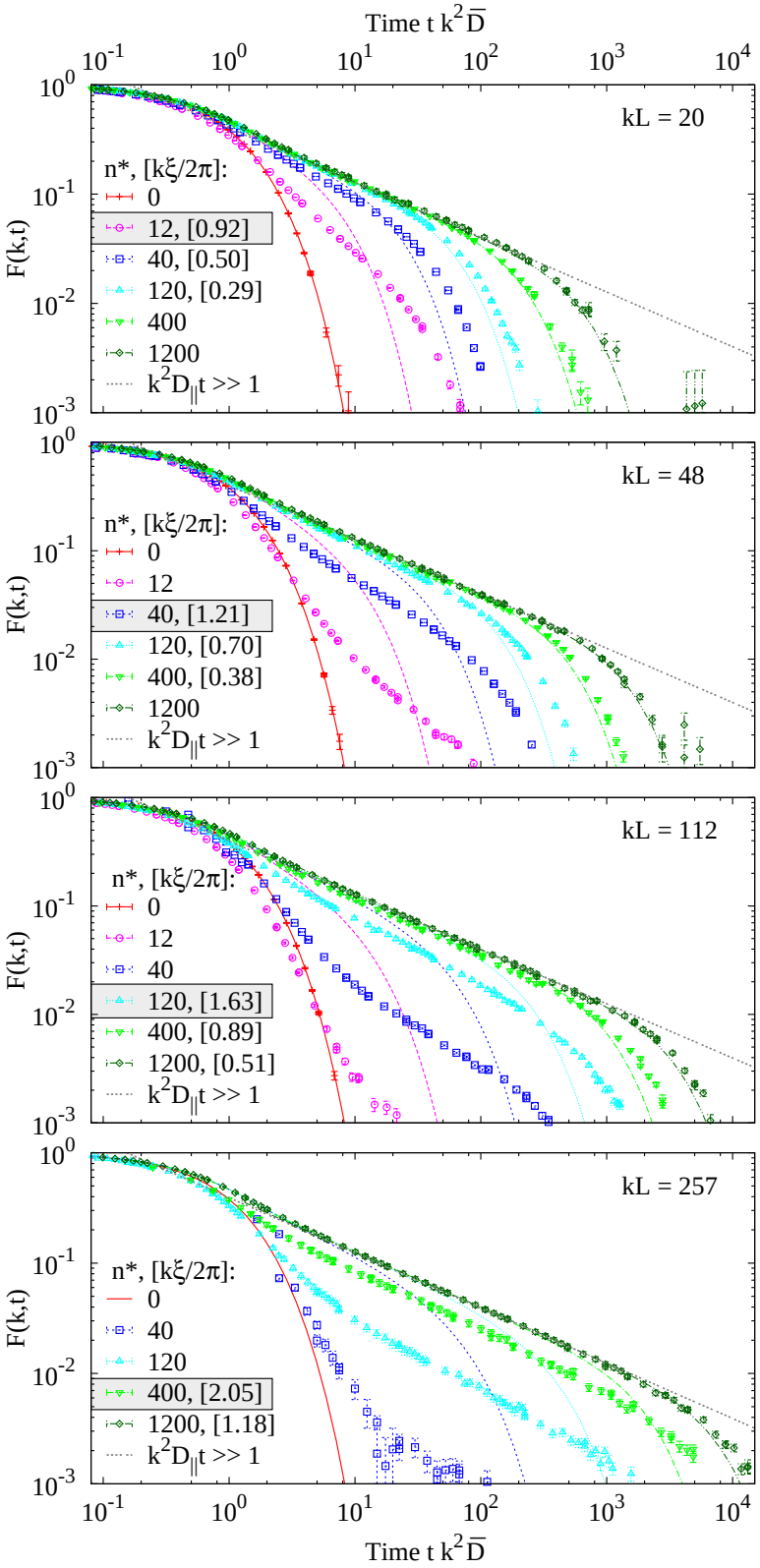

Figure 4.20: Intermediate scattering function measured with four different wave vectors k (increasing from top panel to bottom panel), each for various densities n^*. Symbols are simulation results, color-coded lines the corresponding curves from the effective Perrin theory. For each of the four panels, the data for the density highlighted by a box in the corresponding key is just *not* grasped correctly anymore by the effective theory, since $k\xi/2\pi$ is slightly too large. For reference, the free motion, $n^* = 0$, is also shown for each k. The gray lines show the power law according to the asymptotic expansion in Eq. (4.9). Note that each time axis is rescaled with the corresponding $k^2\bar{D}$.

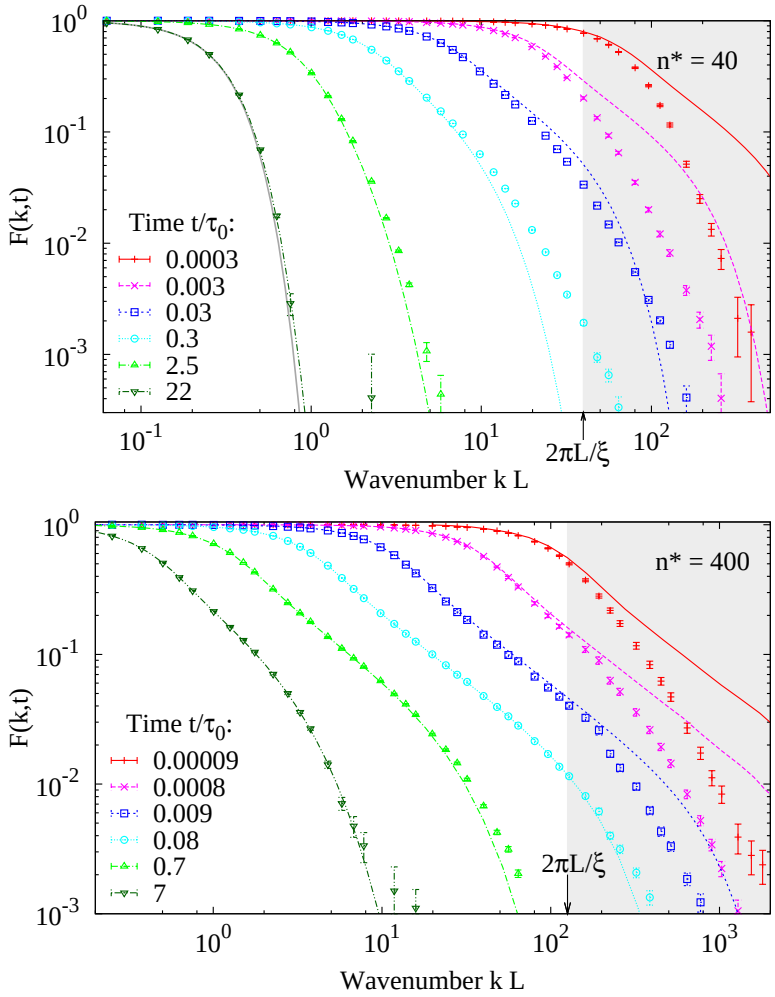

Figure 4.21: Intermediate scattering function as a function of the wavenumber k, for two densities, top and bottom, and several fixed times each. Pronounced differences between the simulations (symbols) and the Smoluchowski-Perrin theory (lines) are visible for $k \gtrsim 2\pi/\xi$, i.e., in the shaded regimes. In case of the medium density, $n^* = 40$, the scattering function for large times is still dominated by a single Gaussian, given by the prefactor of Eq. (3.48), $\exp\big(-k^2\bar{D}t\big)$; for comparison, this function is displayed as a gray line for $t/\tau_0 = 22$.

4.5.1 Origin of the power law

The power law is hidden in Eq. (3.51) in the sum of many exponentials for $q \gg 1$. For strongly suppressed perpendicular and rotational motion, Eq. (3.40) is approximated by the ordinary differential equation $\partial_t G_{\boldsymbol{k}} = -k^2 D_\parallel \cos^2(\vartheta)\, G_{\boldsymbol{k}}$, which yields

$$F(\boldsymbol{k},t) = \mathrm{e}^{-k^2 D_\parallel t/2} I_0\big(k^2 D_\parallel t/2\big) \simeq \big(\pi k^2 D_\parallel t\big)^{-1/2}. \tag{4.9}$$

The second relation results from an expansion of the modified Bessel function of the first kind $I_0(z)$ for large argument; it quantitatively reproduces the scattering function in the power law regime, shown in Figs. 4.18b and 4.20.

Eq. (4.9) can be improved systematically by a perturbation expansion in terms of D_{rot}. The zeroth order solution for the characteristic function,

$$G^{(0)}_{\boldsymbol{k}}(\vartheta,t|\vartheta_0) = \mathrm{e}^{-k^2(\bar{D}+D_a\cos 2\vartheta)t} G_{\boldsymbol{k}}(\vartheta,0|\vartheta_0), \tag{4.10}$$

with the initial condition $G_{\boldsymbol{k}}(\vartheta,0|\vartheta_0)=\delta(\vartheta,\vartheta_0)$ yields the scattering function

$$\begin{aligned} F_{\mu\nu}(\boldsymbol{k},t) &= \frac{1}{2\pi}\int_0^{2\pi}\mathrm{d}\vartheta_0\int_0^{2\pi}\mathrm{d}\vartheta\,\mathrm{e}^{-\mathrm{i}\mu\vartheta}\mathrm{e}^{\mathrm{i}\nu\vartheta_0}G_{\boldsymbol{k}}(\vartheta,t|\vartheta_0) \\ &= (-1)^n\mathrm{e}^{-k^2\bar{D}t}I_n\left(k^2D_at\right)+\mathcal{O}(D_{\mathrm{rot}}), \qquad 2n:=\mu-\nu. \end{aligned} \tag{4.11}$$

$I_n(z)$ is the modified Bessel function of the first kind, with the integral representation $\int_0^{2\pi}\cos(n\vartheta)\,\mathrm{e}^{-z\cos\vartheta}\mathrm{d}\vartheta/2\pi=(-1)^nI_n(z)$. The result only depends on the difference of the helicities, which must be an even number for symmetry reasons, as shown in Eq. (3.7). An asymptotic expansion of the Bessel function in Eq. (4.11) and $D_\perp=0$ then reproduces the power law already anticipated in Eq. (4.9). The first order equation for the characteristic function,

$$\partial_t G^{(1)}_{\boldsymbol{k}}=\partial^2_\vartheta G^{(0)}_{\boldsymbol{k}}-k^2\left(\bar{D}+D_a\cos2\vartheta\right)G^{(1)}_{\boldsymbol{k}}, \tag{4.12}$$

is solved by

$$G_{\boldsymbol{k}}(\vartheta,t|\vartheta_0)=\mathrm{e}^{-k^2\left(\bar{D}+D_a\cos2\vartheta\right)t}\left[1+4D_{\mathrm{rot}}D_ak^2t^2\left(\frac{1}{2}\cos2\vartheta+\frac{1}{3}D_ak^2t\sin^2 2\vartheta\right)\right]G_{\boldsymbol{k}}(\vartheta,0|\vartheta_0)+\mathcal{O}\left(D^2_{\mathrm{rot}}\right), \tag{4.13}$$

corresponding to the scattering function

$$\begin{aligned} F_{\mu\nu}(\boldsymbol{k},t)=(-1)^n\mathrm{e}^{-k^2\bar{D}t}\Big\{&I_n\left(k^2D_at\right)\left(1-\frac{8}{3}n^2D_{\mathrm{rot}}t\right) \\ &-\frac{1}{3}D_{\mathrm{rot}}D_ak^2t^2\left[I_{n-1}\left(k^2D_at\right)+I_{n+1}\left(k^2D_at\right)\right]\Big\}+\mathcal{O}\left(D^2_{\mathrm{rot}}\right). \end{aligned} \tag{4.14}$$

This expression now contains three successive Bessel functions. The helicities again reduce to $2n:=\mu-\nu$; in first order perturbation theory, the diagonal elements of the scattering function are thus independent of the orientational dynamics,

$$F_{\mu=\nu}(\boldsymbol{k},t)=F(\boldsymbol{k},t)=\mathrm{e}^{-k^2\bar{D}t}\left\{I_0\left(k^2D_at\right)-\frac{2}{3}D_{\mathrm{rot}}D_ak^2t^2I_1\left(k^2D_at\right)\right\}+\mathcal{O}\left(D^2_{\mathrm{rot}}\right). \tag{4.15}$$

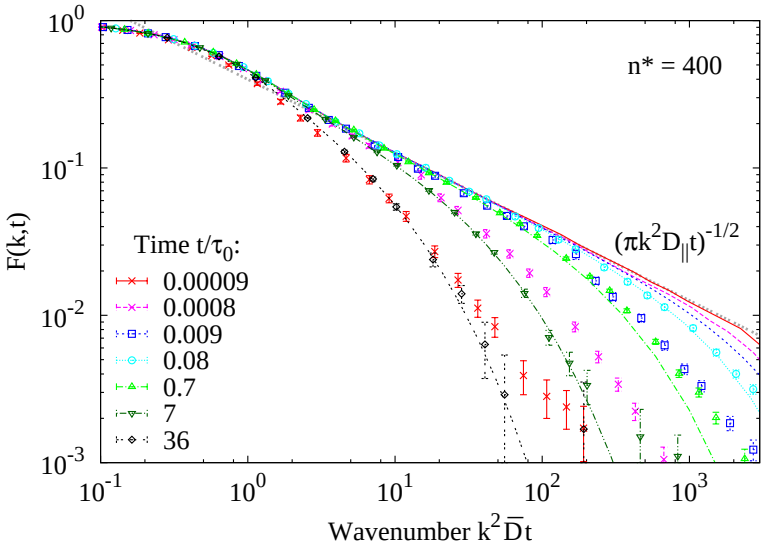

Figure 4.22: Intermediate scattering function as a function of the wavenumber k, at $n^*=400$. Here the horizontal axis is rescaled such that the initial exponential decay coincides, in difference to the presentation in the bottom panel of Fig. 4.21. The power law $(\pi k^2 D_\parallel t)^{-1/2}$ is shown by the broken gray line. For this data, $\tau_{\mathrm{conf}}/\tau_0\simeq 2.5\cdot10^{-5}$.

This function is shown Fig. 4.19. Apart from the short time exponential and the power law itself, it also captures the terminal relaxation at large times. The corresponding timescale has been derived from an asymptotic expansion of the eigenvalues in Eq. (3.52); it is also visible when expanding the Bessel functions in Eq. (4.14) for $k^2 D_a t \gg 1$, which yields the algebraic expression

$$F_{\mu\nu}(\boldsymbol{k},t) = (-1)^n \frac{\mathrm{e}^{-k^2 D_\perp t}}{\sqrt{2\pi k^2 D_a t}} \left\{ 1 - \frac{D_{\mathrm{rot}} t}{3} \left[8n^2 + 2k^2 D_a t \right] \right\} + \mathcal{O}\left(1/k^2 D_a t, D_{\mathrm{rot}}\right). \tag{4.16}$$

For $n = 0$, the second term in curly brackets dominates the first one when $\tau_{\mathrm{term}}^{-2} t^2 \gg 1$, with $\tau_{\mathrm{term}}^{-1} \approx k\sqrt{2 D_a D_{\mathrm{rot}}}$. Fig. 4.22 displays the wave number dependence of the scattering function, rescaled such that data coincide at the power law. Once again the transient nature of the algebraic decay is visible; it is not observed both at very short times, $t \lesssim \tau_{\mathrm{conf}}$, as well as very long times, $t \gg \tau_0$.

4.5.2 Angle-resolved scattering

In the intermediate scattering functions displayed so far all information about the orientation has been integrated out; the helicities, i.e., the conjugated variables of the angle, have been chosen to zero. Fig. 4.23 displays the scattering function with three helicities $\nu \neq 0$, for a highly entangled system. When the sliding motion inside the tube is resolved, i.e., for $kL \gg 1$ and $t \lesssim \tau_0$, the rod does not rotate and the curves for different ν coincide. For larger times, the curves for different ν drift apart; specifically, the smaller kL, the more the curves fan out, due to the more and more pronounced rotational motion. In any case, the Perrin theory accurately matches the data, since $k \ll 2\pi/\xi \simeq 126/L$ at the shown density. The macroscopic approximation is only adequate at $kL \ll 1$, otherwise it only reproduces the initial decay.

4.5.3 Scattering from the whole rod

The interpretation of the intermediate scattering function becomes more subtle when the whole rod is labeled. At a medium density, see Fig. 4.24, the picture is qualitatively similar to the center of mass scattering displayed in Fig. 4.18a: The simple exponential for small wavevectors crosses over at large spatial resolution to three separate regimes. First, the short time exponential resolving the

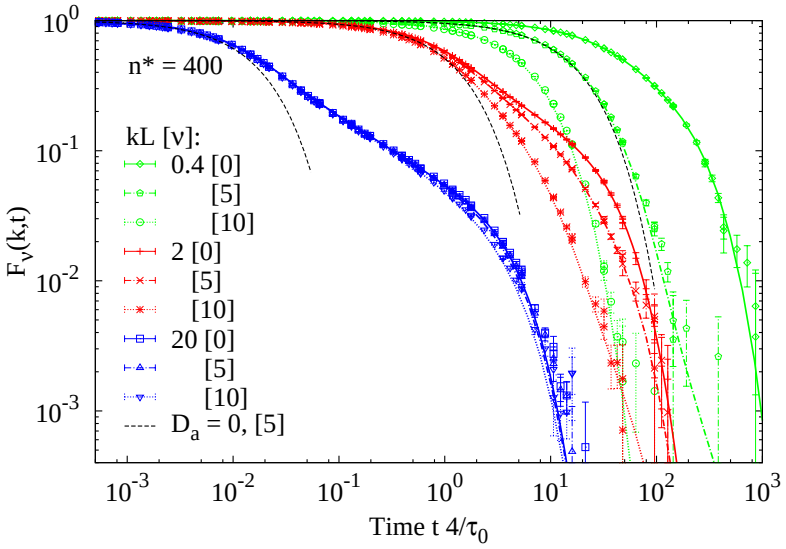

Figure 4.23: $F_\nu(k,t)$ for three wavenumbers k and helicities ν, with $n^* = 400$. The macroscopic approximation, Eq. (3.74), is shown by black lines for $\nu = 5$.

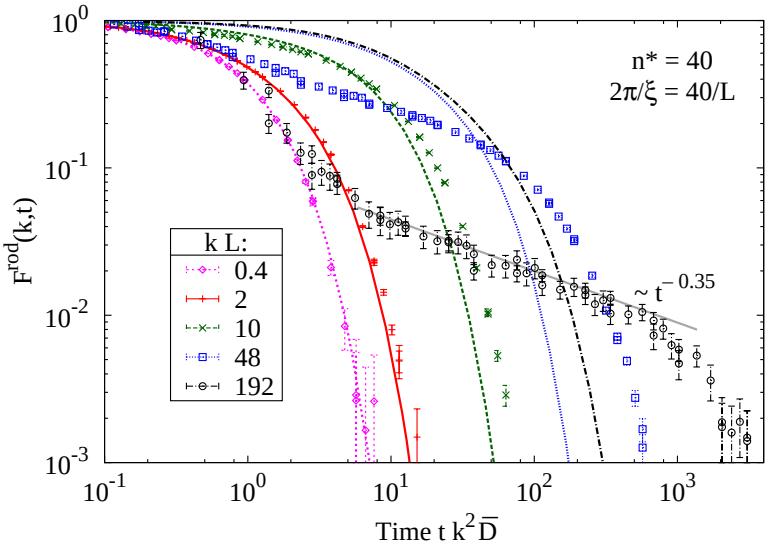

Figure 4.24: Time dependence of the scattering response from the whole rod, for a medium density, $n^* = 40$. Data points show simulation results, color-coded lines the corresponding Perrin theory. The magenta curve for $kL = 0.4$ coincides with the exponential $\mathrm{e}^{-k^2\bar{D}t}$.

microscopic free diffusion, second, the intermediate power law caused by the constrained sliding motion, and finally the terminal decay. The exponent of the power law however is different from the asymptotic approximation derived in Sec. 4.5.1.

The situation changes at larger densities, exemplified in Fig. 4.25. Although the familiar power law emerges with rising k until $kL \approx 2$, it then disappears again for still larger wavenumbers. This is in strong contrast to the center of mass scattering as shown in Fig. 4.18, where the power law monotonously enlarges with k until the microscopic motion becomes visible. The disappearing power law is connected to the observation that the timescale of the initial decay does not shrink with k^{-2} anymore, but appears to be independent of k.

The essential features of this intermediate scale-free regime, transient both in the wavenumber and in the time, can be reproduced for strongly confined systems at the level of the perturbation approach for vanishing rotational diffusion. To this end, we rewrite the scattering function for the rod by taking advantage of the statistic formulation of the characteristic function, given in Eq. (3.9), $G_{\boldsymbol{k}}(\vartheta, t|\vartheta_0) = 2\pi \left\langle \mathrm{e}^{-\mathrm{i}\boldsymbol{k}\cdot\boldsymbol{r}(t)} \delta\big(\vartheta, \theta(t)\big) \delta\big(\vartheta_0, \theta(0)\big) \right\rangle$. By means of two integrals over the angles we find a relation to the scattering function Eq. (3.55),

$$F^{\mathrm{rod}}(\boldsymbol{k}, t) = \frac{1}{2\pi \mathcal{N}(kL/2) L^2} \int_{-L/2}^{L/2} \mathrm{d}s \int_{-L/2}^{L/2} \mathrm{d}s' \int_0^{2\pi} \mathrm{d}\vartheta \int_0^{2\pi} \mathrm{d}\vartheta_0 \, \mathrm{e}^{-\mathrm{i}\boldsymbol{k}\cdot\boldsymbol{u}(t)s} \mathrm{e}^{\mathrm{i}\boldsymbol{k}\cdot\boldsymbol{u}(0)s'} G_{\boldsymbol{k}}(\vartheta, t|\vartheta_0).$$

The integrals over the contour parameters are easily evaluated, for simplicity again in a coordinate frame with $\boldsymbol{k} = k\boldsymbol{e}_x$. This yields

$$F^{\mathrm{rod}}(\boldsymbol{k}, t) = \frac{1}{2\pi \mathcal{N}(kL/2)} \int_0^{2\pi} \mathrm{d}\vartheta \int_0^{2\pi} \mathrm{d}\vartheta_0 \, \mathrm{sinc}\left(\frac{kL}{2}\cos\vartheta\right) \mathrm{sinc}\left(\frac{kL}{2}\cos\vartheta_0\right) G_{\boldsymbol{k}}(\vartheta, t|\vartheta_0). \tag{4.17}$$

The characteristic function can now be inserted, e.g., as obtained in Eqs. (4.10) and (4.13); then, the δ-function in the initial condition reduces the evaluation of Eq. (4.17) to a single integral. With the help of the zeroth order approximation, Eq. (4.10), we can extract the power law by exploiting the fact that the major contribution to the integral will be located around $\vartheta = \pi/2$. There the sinc-function is roughly approximated by 1, and one again ends up with the result from Eq. (4.11) with $\mu = \nu = 0$, only modified by the norm $\mathcal{N}(kL/2)$. Fig. 4.25 demonstrates that this matches the scattering function in the power law regime as obtained in the simulations. A numerical calculation

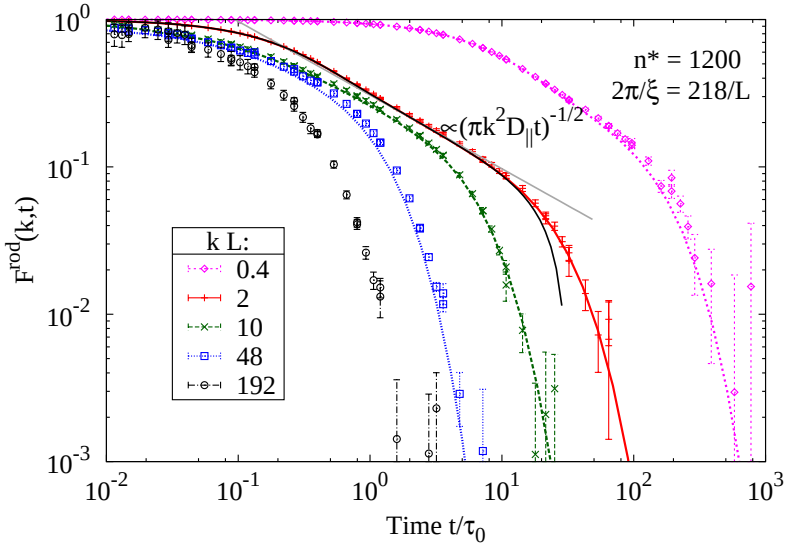

Figure 4.25: Scattering from the whole rod, for a large density, $n^* = 1200$. Data points show simulation results, color-coded lines the corresponding Perrin theory. For $kL = 2$, two results from perturbation theory are shown: the straight gray line indicates the asymptotic power law $1/\mathcal{N} k\sqrt{\pi D_\parallel t}$, i.e., the result from the center of mass scattering, Eq. (4.9), with the amplitude given by the norm $\mathcal{N} = \mathcal{N}(kL/2)$ of Eq. (3.57). The continuous black line represents the first order perturbation theory for the scattering from the whole rod, Eq. (4.17) with the characteristic function Eq. (4.13). Note that the horizontal axis is not rescaled with k^2, in contrast to the preceding Figs. 4.24 and 4.18. This presentation is chosen due to the different initial decay of the curves for $kL \geq 2$ in the present figure.

of the integral (4.17) with the first order characteristic function Eq. (4.13) improves this result in the convergence to the correct value at short times, and the termination of the power law at τ_{term}, see the black line in Fig. 4.25. The significance of the first order result is preserved also for larger wavenumbers, when the power law fades away and the terminal decay dominates.

To shed some more light on the alteration of the power law as compared to the center of mass results, Fig. 4.26 visualizes the scattering function for two fixed wavevectors, with each of the two plots covering two decades in the range of sample densities. At $kL = 2$, the intermediate power law $1/k\sqrt{t}$ arises as expected with increasing density, similar to Fig. 4.19 for the scattering from the center of mass. For this wavenumber, the effective description of the Perrin theory works excellently, since the probed length scale is beyond the typical mesh size for all displayed densities, i.e., $k \ll 2\pi/\xi$. With a wavenumber nearly two orders of magnitude larger, $kL = 112$, the behavior is qualitatively inverted. For medium densities, the transient power law is visible in the time window between microscopic dynamics and terminal relaxation—the exponent however gradually weakens with rising density. Instead of shifting towards the asymptotic power law, as observed in Fig. 4.19, the scattering function bends over to approach a time lapse that appears to be a stretched exponential. Here, Perrin theory becomes appropriate only at the largest displayed densities due to the large k.

From the preceding we infer that the difference in the fully-labeled scattering as compared to the center of mass results seems to propose a varying mechanism in the representation of the strongly confined, anisotropic motion. As expected, the way of labeling the rod is irrelevant at large length scales, $kL \ll 1$, since the observed motion will be increasingly similar, the more the spatial resolution is coarse grained. In contrast, the entangled dynamics in the mesoscopic regime

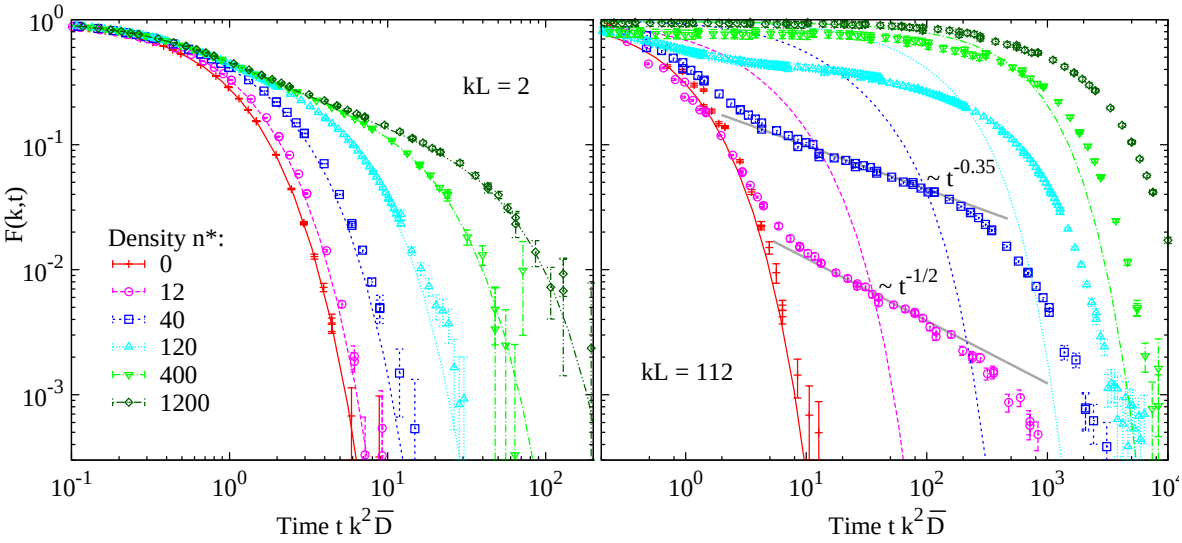

Figure 4.26: Scattering from the whole rod, for two fixed wavenumbers, left and right, each for various densities. *Left:* At $kL = 2$, the intermediate power law $\sim 1/k\sqrt{t}$ arises with increasing density. For visualization of the power law at the maximum density consult also Fig. 4.25. *Right:* When $kL = 112$, the power law weakens in the exponent with increasing density, while keeping approximately constant the affected time window.

yields different characteristics, when analyzed based on the motion of the whole rod. The detailed understanding of these features is still an open problem.

4.6 Conclusion

From our analysis we conclude that the motion of thin rods in semi-dilute suspensions exhibits a rich interplay of time and length scales, as exemplified in the mean-square displacements and intermediate scattering function. The hindered motion leads to a strong anisotropic dynamics manifested in a significant translation-rotation coupling which persists up to macroscopic length and time scales, L_{rot} and τ_{rot}. This dynamically induced coupling is an emergent phenomenon with long memory effects. The confinement in the tube gives rise to a well separated spectrum of length scales $d \ll \xi \ll L \ll L_{\mathrm{rot}}$. The tube becomes effective once the rod encounters new steric constraints—thus the interparticle distance ξ constitutes the lower length scale of a mesoscopic window, where an effective theory with renormalized parameters becomes valid; this regime extends up to L_{rot}. Note that such a window opens only in the strongly anisotropic regime and is absent for, e.g., ellipsoids with moderate aspect ratio. Since the orientation changes only gradually by tube renewals, it has to be included in the set of slow degrees of freedom in addition to the translation. The effective Perrin theory constitutes a Markov process in these variables, and the long memory observed in the intermediate scattering function is generated by integrating out the slowly varying orientation. This mesoscopic description is independent of the details of the tube generation; in particular, the obstacle may also fluctuate in time and space, or even disappear.

The Perrin approach fails to capture the fact that strongly confined needles have to diffuse along their axis a distance L to relax the tube constraint. However, since the rotational diffusion D_{rot} is much slower than $D_{\parallel}/L^2$, this appears to be negligible, at least on the scales investigated here.

It is straightforward to extend the concept of an effective Perrin theory to three-dimensional

suspensions of long, thin rods since the motion in the tube is essentially one-dimensional. The formal solution is then provided in terms of spheroidal wave functions [5, 119], which serves as a starting point to calculate the intermediate scattering function. In particular, the confined motion of rods is characterized again by a power law decay of the intermediate scattering function, which we predict to $F(\boldsymbol{k},t) \simeq \left(4k^2 D_{\parallel} t/\pi\right)^{-1/2}$. This algebraic decay constitutes a generic feature of the sliding motion and should be observable directly in scattering experiments.

Chapter 5

Dynamics of dilute semiflexible polymers in a flow field

In the course of evolution, nature found a both amazingly simple and robust way to sustain the mechanical stability of biological cells, while at the same time providing them with extraordinary dynamic capabilities, like growing, moving, and dividing. The basic structure elements making this possible are semiflexible polymers, in the cytoskeleton present in form of F-actin, intermediate filaments and microtubuli. Two characteristic properties distinguish them from most of the other natural and synthetic polymers: They possess a certain stiffness which energetically suppresses bending, and they are to a high degree inextensible, i.e., their backbone cannot be stretched or compressed. Moreover, electric charge and polarity effects as well as the ability to assemble and disassemble are essential for the dynamics of the whole cytoskeleton network.

In the last 15 years enormous progress has been made in experimental observation and theoretical description of these physical aspects. To give some examples, fluorescence video microscopy of labeled filaments has allowed for the detailed study of statistic properties of F-actin [91], DNA [107], and microtubules [120]. Quantities like the end-to-end distance [165] and force-extension relations [88] have been calculated and verified experimentally [20, 95], the latter being accessible by means of optical and magnetical tweezers. Furthermore, fluorescence correlation spectroscopy [103, 137, 166] and light scattering [89] have been used to obtain, e.g., the mean-square displacement and dynamic structure factor.

In this work we concentrate on the theoretical description of the dynamics of a single semiflexible polymer. This is the relevant model not only in the dilute limit, but also essential for the understanding of the medium and high frequency response of networks of semiflexible filaments [48]. Concerning the theory, the textbook models of Rouse and Zimm [31] have to be extended, since they apply to Gaussian chains only and thus fail to incorporate the effects of semiflexibility. A systematic analysis of the dynamics was limited in this field to the linear regime until recently, when the dynamic propagation and relaxation of tension could be elucidated [15, 61], and a comprehensive, unified theory worked out [62]. The numerical approach usually adopted for polymeric systems is to construct a polymer from a finite number of beads, each of which is connected with two neighbors by a stiff rod or spring [13]. Our goal is to set up a different method more suited to the subtleties of semiflexibility, such that the numerical description of these filaments becomes tractable when they are subjected to fluid flow. The purpose of this work is twofold: First, we want to establish a new method that covers the above-mentioned goals, and second, the results we present in applying this technique are directly relevant to experiments with polymers in a shear

flow.

Many authors have addressed systems with semiflexible polymers by means of different bead–rod/spring based techniques [38, 42, 58, 74, 114]. However, maintaining the mechanical constraint of a constant bond length becomes complicated with increasing resolution, since it couples the motion of all beads. The controversial question arises whether this requirement has to be implemented as a literally rigid constraint or by an infinitely stiff potential, since these two cases differ in their statistical mechanics [154]. One often chooses to address an infinitely stiff bead-spring chain by means of a rigidly constrained system, which is more feasible concerning computational time. Then, an additional pseudo-potential has to be applied to guarantee the correct equilibrium Boltzmann distribution [68, 121]. Moreover, timescales present major limitations when solving stiff systems numerically [40]. The characteristic relaxation time of a bending mode imposed on the filament is inversely proportional to the fourth power of the corresponding wavenumber. The largest wavenumber that can be resolved by discretized models is proportional to the number of beads. Hence the time step one has to choose is inversely proportional to the quartic number of monomers, for the shortest wavelength undulations to be sampled correctly. At the same time, the longest mode needs to have enough time to relax to equilibrium, and since these two times differ by the fourth power of the resolution of the spatial discretization, the necessary computational time can become prohibitively long.

As a consequence, the numerical approach has been limited, when semiflexible systems with constraints were to be investigated. Some dynamic properties could be grasped by a suitable combination of multiple short runs [40], but this is not possible when further external timescales enter, which do not match the intrinsic limitations. For instance, this is the case when the polymer is subject to a fluid flow. Corresponding simulations have been reported with a quite small resolution of nine beads [111]. On the other hand, experiments of this type have already been carried out for DNA [50, 122, 136, 138, 147], and simulations have been presented to examine their findings [76, 127, 135]. Indeed, the latter have always been done with models that allow for a finite or even infinite extensibility of the chains. This might be a suitable approach for coil–like DNA molecules, but it would miss important physics, if applied to stiffer filaments like F-actin or (pre–)stretched DNA [117].

Recently, a new idea has been presented [164] for an alternative approach that avoids these difficulties for two-dimensional systems. This concept starts from a continuous model for the semiflexible polymer and uses a suitable normal mode analysis. Some of these ideas have been utilized before to describe the deterministic [9], linear behavior of semiflexible filaments in a viscous solution [162]. However, the extension to the nonlinear case at finite temperature has proven to be subtle, and it is the goal of this work to consistently establish the approach and explore some of the possibilities it can offer.

5.1 A spectral method for single filaments

In our model, a semiflexible polymer is represented by a space curve $\boldsymbol{r}(s,t)$, parametrized by the arclength s (Fig. 5.1). The minimal model for the description of a semiflexible polymer in this representation is the wormlike chain [87, 131], valid when the detailed properties on the atomic and monomeric scale are not important anymore [31]. Then, the Hamiltonian for the elastic energy is given by the integral of the squared curvature $c(s,t)$, multiplied with the bending modulus κ,

$$\mathcal{H}_{\mathrm{el}} = \frac{\kappa}{2}\int_0^L \mathrm{d}s\, c^2. \tag{5.1}$$

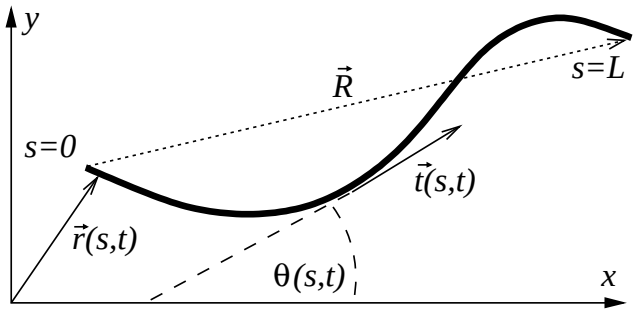

Figure 5.1: Sketch of a polymer of length L, represented by a continuous space curve $\boldsymbol{r}(s,t)$. An example is shown for the local unit tangent vector $\hat{t}(s,t)$, as well as the end-to-end distance vector $\boldsymbol{R}$.

The bending modulus can be expressed in terms of the persistence length ℓ_p, the characteristic length for the exponential decay of the tangent autocorrelation [92, §127]:

$$\kappa = k_B T \ell_p (\mathrm{dim} - 1)/2, \tag{5.2}$$

where "dim" denotes the dimension of the embedding space. For synthetic polymers, the persistence length is typically of the order of the polymer's diameter, $\ell_p \approx a$. The tangential correlations thus decay very fast, hence these polymers are called flexible. Semiflexible are polymers with $\ell_p \gg a$, which is the case for the biopolymers inside the cell. Depending on the ratio of contour length and persistence length we can distinguish different regimes: In case of DNA one usually deals with the flexible limit, $L \gg \ell_p$; in this work however we are exploring the stiff regime, where $\ell_p \geq L$. The latter matches in nature, e.g., to the properties of F-actin and microtubuli.

Due to low Reynolds numbers, the motion of μm-sized objects like biopolymers in solution is overdamped, i.e., friction exceeds inertia by several orders of magnitude [46]. As a consequence, inertia terms can safely be neglected, and the equations of motion are of first order in time. The stochastic dynamics of a polymer in a quiescent solvent can thus be described by the Langevin equation [31, 90]

$$\frac{\partial}{\partial t}\boldsymbol{r}(s,t) = \int_0^L \mathrm{d}s' \, \mathbf{H}[\Delta \boldsymbol{r}] \left\{ -\frac{\delta \mathscr{H}[\boldsymbol{r}(s'',t)]}{\delta \boldsymbol{r}(s',t)} + \boldsymbol{\xi}(s',t) \right\}. \tag{5.3}$$

Here $\mathbf{H}[\Delta \boldsymbol{r}]$ is the mobility tensor, with $\Delta \boldsymbol{r} \equiv \boldsymbol{r}(s,t) - \boldsymbol{r}(s',t)$, and $\boldsymbol{\xi}$ the noise, which we assume to be Gaussian distributed with mean zero. The energetic part of the Hamiltonian $\mathscr{H}[\boldsymbol{r}]$ is given by $\mathscr{H}_{\mathrm{el}}$, and we will discuss necessary additions below.

Concerning hydrodynamics, we adopt the free draining approximation, i.e., neglect all nonlocal interactions. This approximation can be justified by evaluating the Fourier transformation of the Green's function of a hydrodynamic force field (Oseen tensor), which gives only a very weak, i.e. logarithmic, mode dependence of the mobility [47]. The underlying physical rationale is the mostly straight conformation of a stiff filament. For the same reason, excluded volume effects can safely be neglected. We implement the local friction of the polymer by using the anisotropic mobility of a stiff rod, which differs by a factor of two for the motion parallel and perpendicular to its tangent vector $\hat{t} = \partial_s \boldsymbol{r}$. Hence $\mathbf{H}[\Delta \boldsymbol{r}] \to \mathscr{P}(r(s,t))\delta(s-s')$, with the local mobility [8, 31]

$$\mathscr{P} = \mu_\perp \hat{n} \otimes \hat{n} + \mu_\parallel \, \hat{t} \otimes \hat{t}. \tag{5.4}$$

Here, $\hat{n}$ denotes the unit normal vector. The tangent and normal vector are related by the Frenet-Serret-equations, which in two dimensions read $\partial_s \hat{t} = c\hat{n}$, $\partial_s \hat{n} = -c\hat{t}$. The friction coefficients (per length) are obtained from the solvent viscosity η and polymer diameter a by $\mu_\perp = \frac{1}{2}\mu_\parallel = \ln(L/a)/2\pi\eta$.

Due to the presumed Gaussian nature of the noise we only need to specify the second moment of $\boldsymbol{\xi}$. By relating Eq. (5.3) to the appropriate Smoluchowski equation [49] and requiring a Boltzmann distribution in equilibrium we obtain

$$\left\langle \boldsymbol{\xi}(s,t) \otimes \boldsymbol{\xi}(s',t') \right\rangle = 2k_B T \mathscr{P}^{-1} \delta(s-s')\delta(t-t'). \tag{5.5}$$

Based on physical considerations given in appendix C.1 we will interpret the noise according to Ito [153]. In fact, some of the algebra necessary in the following relies on this interpretation.

A further important ingredient to the wormlike chain model is the inextensibility of the filament: We assume the local length to be constant by imposing the constraint $\partial_s \boldsymbol{r}^2 \equiv \hat{t}^2 = 1$. To satisfy it, we introduce a Lagrange multiplier function $\Lambda(s,t)$ such that the full Hamiltonian reads [54]

$$\mathscr{H} = \mathscr{H}_{\mathrm{el}} - \frac{1}{2}\int_0^L \mathrm{d}s\, \Lambda(s,t)[\partial_s \boldsymbol{r}(s,t)]^2. \tag{5.6}$$

Although the constraint is identically satisfied in the arclength parametrization, we do need a Lagrange multiplier function here to make the variation of the coordinates in Eq. (5.3) independent of each other [1]. In the following, we will be able to solve the equations of motion perturbatively for the Lagrange multiplier $\Lambda(s,t)$, hence the validity of the inextensibility constraint is guaranteed locally for all times. Physically, $\Lambda(s,t)$ corresponds to the tension acting against forces that would elongate or compress the filament's backbone.

In evaluating the functional derivative of Eq. (5.6) we obtain from Eq. (5.3) the nonlinear equation of motion

$$\dot{\boldsymbol{r}} - \boldsymbol{\Gamma}\cdot\boldsymbol{r} = \mathscr{P}\left\{-\kappa \boldsymbol{r}'''' - (\Lambda \boldsymbol{r}')' + \boldsymbol{\xi}\right\}. \tag{5.7}$$

On the left hand side we have subtracted the incompressible, homogeneous [2] flow $\boldsymbol{u} = \boldsymbol{\Gamma}\cdot\boldsymbol{r}$ to account for the influence of an externally driven flow field. In Eq. (5.7) and the following, a prime indicates a derivative with respect to the arclength.

When constrained systems similar to Eq. (5.7) are approximated by discrete bead–rod models, one has to introduce a pseudo-potential (also called metric force) for the system to evolve into the correct equilibrium state [42, 68, 111]. In contrast, we use a spectral approach, in which the arclength dependence is continuous (before explicitly evaluated on a computer, of course), but we truncate the expansion in terms of a finite number of wavelengths. Evaluating the metric determinant by means of the recursion relation proposed in Ref. 41 leads to contributions proportional to powers of the spatial resolution. Thus in case of a continuous representation, we do not need to bother corrections of this kind.

To grasp the essential physics we will from now on consider the two-dimensional motion of a filament in a three-dimensional embedding fluid. This is actually a standard situation for experiments [107, 147], since the interesting dynamics is often restricted to two dimensions, while still allowing for a three-dimensional transfer of momentum to the environment. Note that this is distinct from systems where the hydrodynamics is confined to two dimensions. Thus in the following, the analysis will be presented for dim = 2, cf. Eq. (5.2). The tangent and normal vectors then are given by (Fig. 5.1) $\hat{t} = (\cos\theta, \sin\theta)$, and $\hat{n} = (-\sin\theta, \cos\theta)$. To transform the equation of motion to variables which are scalar, we differentiate Eq. (5.7) with respect to the arclength and project

[1] For the thermodynamics, a Smoluchowski equation chosen appropriately leads to a constraint fulfilled exactly [31]. This has to be contrasted with the thermodynamic approach of Lagrange transformations, which only enforce mean values.

[2] A homogeneous flow can be parametrized linearly in Cartesian coordinates.

the result onto the normal and tangent vector, respectively. Using the Frenet-Serret-Equations, we arrive at

$$\dot{\theta} = \hat{n}\cdot\mathbf{\Gamma}\cdot\hat{t} + \mu_\perp\left\{-\kappa\left[c''' - (d+1)\left(c^3\right)'\right] - (d+1)\Lambda' c - \Lambda c' + \left[\hat{n}\partial_s + (d-1)c\hat{t}\right]\cdot\boldsymbol{\xi}\right\}, \tag{5.8a}$$

$$0 = \hat{t}\cdot\mathbf{\Gamma}\cdot\hat{t} + \mu_\perp\left\{-\kappa\left[c^4 - 3d(cc')' - cc''\right] + c^2\Lambda - d\Lambda'' + \left[d\,\hat{t}\partial_s + (d-1)c\hat{n}\right]\cdot\boldsymbol{\xi}\right\}. \tag{5.8b}$$

These equations describe the motion of a semiflexible filament in its center of mass inertia frame, since the information on the absolute coordinate gets lost in evaluating the additional derivative of Eq. (5.7). The constant d gives the ratio of parallel and perpendicular friction, $\mu_\perp = \mu_\parallel/d$. Slender-body hydrodynamics is described by the anisotropic case ($d = 2$), physically corresponding to the difference in drag between normal and tangential motion of a slender body in Stokes flow. The simpler isotropic equations are obtained with $d = 1$.

5.1.1 Normal mode analysis

The leading contribution governing the elastic dynamics of Eq. (5.8a) is the second term on the right hand side, $-\kappa\partial_s^3 c(s,t) = -\kappa\partial_s^4\theta(s,t)$. For a suitable normal mode decomposition of the equations (5.8a) and (4.5) we thus may use the eigenfunctions of the biharmonic operator ∂_s^4. Here, we consider free boundary conditions $\boldsymbol{r}''(0) = \boldsymbol{r}''(L) = 0$, $\boldsymbol{r}'''(0) = \boldsymbol{r}'''(L) = 0$ [93, 163], corresponding to the situation of a filament fluctuating freely in flow. In angular coordinates this translate into

$$\theta'(0) = \theta'(L) = 0, \text{ and } \theta''(0) = \theta''(L) = 0. \tag{5.9}$$

Furthermore, the tension has to vanish at the boundaries, $\Lambda(0) = \Lambda(L) = 0$.

The biharmonic operator is not Hermitian with respect to a single set of eigenfunctions obeying (5.9); however, it is Hermitian with respect to a *bi*orthogonal set of functions, where the first set $w^\alpha(s)$ obeys the boundary conditions of Eqs. (5.9), and the second set $w_\alpha(s)$ satisfies

$$w_\alpha(0) = w_\alpha(L) = 0, \text{ and } w_\alpha'''(0) = w_\alpha'''(L) = 0. \tag{5.10}$$

These functions are solutions of the eigenvalue problems $\partial_s^4 w^\alpha = k_\alpha^4/L^4\, w^\alpha$, $\partial_s^4 w_\alpha = k_\alpha^4/L^4\, w_\alpha$, respectively, with identical eigenvalues k_α^4, to be found from the solvability condition $\cos k_\alpha \cosh k_\alpha = 1$. The general solutions $w^\alpha(s)$, $w_\alpha(s)$ are linear combinations of trigonometric and hyperbolic functions [93], and a polynomial of third order for the zeroth eigenvalue $k_0 = 0$. They are explicitly given in Appendix C.2. Some nice experimental snapshots of the mode dynamics of F-actin can be found in Ref. 159.

The completeness of these two sets of eigenfunctions has not been shown yet. Neither a variational approach [25] nor a comparison with a complete basis [18] seem to work in our case. However, we do not regard this as a major issue, since the failure is only due to our specific nonstandard set of boundary conditions—for other boundary conditions completeness can be shown [25]. Furthermore, in order to implement the spectral approach, we will have to truncate all mode expansions, anyway.

We make use of the two sets of eigenfunctions to obtain normal mode expansions of the angle and tension (latin indices always start from 1, greek ones from 0):

$$\theta(s,t) = \theta_0(t) + \epsilon\sum_{j=1}^{\infty}\theta_j(t)\,w^j(s), \tag{5.11}$$

$$\Lambda(s,t) = \sum_{\nu=0}^{\infty}\Lambda^\nu(t)\,w_\nu(s). \tag{5.12}$$

In the first line we have separately written the zeroth mode $\theta_0(t)$, since it is independent of the arclength; it describes the motion of a stiff rod. The higher modes include undulations with successively smaller wavelength. The perturbation parameter ϵ will be defined by equipartition, as illustrated below. Equivalently, the zeroth tension mode $\Lambda^0(t)$ gives the tension distribution in a straight rod. By using the spectral expansion of the tension in the second line we assigned two additional boundary conditions to the tension [rightmost part of Eq. (5.10)]. We do not expect this vanishing cubic contribution to be a noticeable restriction to the tension at the edges. However, there is no simple physical interpretation to it.

As a first application of the mode expansions we insert Eq. (5.11) into the wormlike chain Hamiltonian (5.1), which in two dimensions can be written as

$$\mathscr{H}_{\mathrm{el}} = \frac{\kappa}{2}\int_0^L \mathrm{d}s\,(\partial_s\theta)^2.$$

By means of the equipartition theorem and Eq. (5.2) we get an expression for the mean size of the mode amplitudes (cf. Appendix C.2), dependent only on the relative persistence length:

$$\epsilon\sqrt{\left\langle\theta_j^2\right\rangle} = \sqrt{2\frac{L}{\ell_p}\frac{1}{k_j}}. \tag{5.13}$$

This suggests to define a flexibility parameter $\epsilon = \sqrt{L/\ell_p}$, which is small for stiff filaments. In the following section we will use ϵ to set up a perturbation expansion for the equations of motion. By definition Eq. (5.11), all angular modes θ_β are of order 1 with respect to this expansion.

5.1.2 Perturbation expansion

The temperature T enters the equation of motion in two ways: First, in the amplitude of the noise, Eq. (5.5), and second, in the expression for the bending stiffness, Eq. (5.2). A perturbation theory with respect to a single independent parameter ϵ will thus in general lead to different results, depending on the choice of the dependent parameter, κ or T. However, a difference only appears in the expressions of cubic order in ϵ. Since we aim to a solution in second order, this is of no concern for us. For concreteness, we choose the example of a constant curvature. Then, ϵ enters the equations only via the temperature in the noise correlator. We make all variables dimensionless by $t\kappa\mu_\perp/L^4 \to t$, $\boldsymbol{\xi}L^3/\epsilon\kappa \to \boldsymbol{\xi}$, $\Lambda L^2/\kappa \to \Lambda$, $\mathscr{P}^{-1}\mu_\perp \to \mathscr{P}^{-1}$, and $\dot\gamma L^4/\kappa\mu_\perp \to \dot\gamma$, insert the expansions (5.11), (5.12) into the equations of motion and project them on mode w_β. The projection, if not evaluated, is abbreviated by

$$[\ldots]_\beta := \int_0^L \mathrm{d}s\, w_\beta \ldots.$$

We furthermore introduce for the flow dependent terms

$$\dot\gamma g_\beta^\parallel := [\hat t\cdot\boldsymbol{\Gamma}\cdot\hat t]_\beta/L, \qquad \dot\gamma g_\beta^\perp := [\hat n\cdot\boldsymbol{\Gamma}\cdot\hat t]_\beta/L,$$

where $\dot\gamma$ is the strength of the flow in units of inverse seconds. g_β are dimensionless, θ-dependent functions that have to be expanded to the appropriate order. In these terms we obtain the following equations of motion:

$$\epsilon\,\partial_t\theta_j = -\epsilon k_j^4\theta_j - \epsilon\sum_{\nu=0,i=1}\Lambda^\nu\theta_i\Xi^i_{j\nu} + \epsilon\eta_j^\perp + \dot\gamma g_j^\perp + \mathscr{O}\left(\epsilon^3\right), \tag{5.14a}$$

$$\partial_t\theta_0 = -\epsilon\sum_{\nu=0,i=1}\Lambda^\nu\theta_i\Xi^i_{0\nu} + \epsilon\eta_0^\perp + \dot\gamma g_0^\perp + \mathscr{O}\left(\epsilon^3\right), \tag{5.14b}$$

$$0 = d\tilde k_\beta^2\Lambda^\beta + \epsilon\eta_\beta^\parallel + \dot\gamma g_\beta^\parallel + \mathscr{O}\left(\epsilon^2\right). \tag{5.14c}$$

Here, a threefold overlap integral of eigenfunctions is abbreviated by

$$\Xi^{\alpha}_{\beta\nu} = \frac{1}{2}\left[(d+1)\int_0^1 \mathrm{d}s\, w^{\alpha}\left(\tilde{k}^2_{\nu} w^{\nu} w_{\beta} - \tilde{k}^2_{\beta} w^{\beta} w_{\nu}\right) + (d-1)k^2_{\alpha}\int_0^1 \mathrm{d}s\, w_{\alpha} w_{\beta} w_{\nu}\right], \tag{5.15}$$

and the projected noise is expressed as

$$\begin{aligned} \eta^{\perp}_{\beta} &= \left[\left(\hat{n}\partial_s + (d-1)(\partial_s\theta)\,\hat{t}\right)\cdot\boldsymbol{\xi}\right]_{\beta}, \\ \eta^{\parallel}_{\beta} &= \left[\left(d\,\hat{t}\partial_s + (d-1)(\partial_s\theta)\,\hat{n}\right)\cdot\boldsymbol{\xi}\right]_{\beta}. \end{aligned} \tag{5.16}$$

Note its dependence on ϵ, via θ and via the unit vectors $\hat{t}$, $\hat{n}$. Furthermore we would like to mention that $g^{\perp}_j$ has no contribution to zeroth order in ϵ, thus all terms of Eq. (5.14a) are at least linear in ϵ. A linear stability analysis of the bending modes described by Eq. (5.14a) is obtained by expanding $g^{\perp}_j$ [164]. Finally, the dimensionless noise has the second moment

$$\left\langle \boldsymbol{\xi}(s,t)\otimes\boldsymbol{\xi}(s',t')\right\rangle = 2\mathscr{P}^{-1}\delta(s-s')\delta(t-t').$$

Since the tension contribution to Eqs. (5.14a) and (3.73) is always of first order in ϵ, it is sufficient to expand it to one order less than the angular equations. For this reason Eq. (5.14c) is an algebraic equation. To obtain the given expression we have furthermore taken advantage of the eigenfunction's property $w''_{\alpha} = -\tilde{k}^2_{\alpha} w^{\alpha}$ (see Appendix C.2). The tension modes Λ^{β} can thus be inserted directly into the angular equations. [3]

Concerning the noise, one obvious method to simplify Eqs. (5.16) would be to evaluate the projection integrals and find an expression for the correlation of the integrated noise. However, there are some complications in our case. It turns out that the correlation of the integrated noise is neither diagonal with respect to the mode projection (subscript β) nor with respect to the direction of the vector projection (superscripts $\perp$, $\parallel$). Furthermore, the order of the nondiagonal corrections is such that they have to be accounted for in an expansion up to order ϵ^2. Thus a computational solution would have to include a numerical diagonalization of the conformation dependent noise in each step. To avoid this we diagonalize the inverse mobility matrix $\mathscr{P}^{-1}$ analytically and calculate the arclength integrals in each time step by numerical means. As a drawback this includes the necessity of a fast random number generator, but still the implementation seems to us to be easier and faster.

The eigensystem of $\mathscr{P}^{-1} = \hat{n}\otimes\hat{n} + \hat{t}\otimes\hat{t}/d$ can immediately be read off, and the corresponding transformation matrix $\mathbf{S}$ is used to rotate the noise locally, $\tilde{\boldsymbol{\xi}} := \mathbf{S}\cdot\boldsymbol{\xi}$. For the calculation of the second moment of the rotated noise we necessarily need it to be of Ito type, since the matrix $\mathbf{S}$ is nonanticipating only in this case. We obtain

$$\left\langle \tilde{\boldsymbol{\xi}}(t,s)\otimes\tilde{\boldsymbol{\xi}}(t,s)\right\rangle = 4\mathscr{P}^{-1}_{D}\delta(t-t')\delta(s-s'), \tag{5.17}$$

where the diagonalized mobility matrix

$$\mathscr{P}^{-1}_{D} = \mathbf{S}\cdot\mathscr{P}^{-1}\cdot\mathbf{S} = \begin{pmatrix} 1 & 0 \\ 0 & 1/d \end{pmatrix}.$$

[3] Using Eq. (5.14c) for the case of a vanishing background flow, one can calculate the correlation of the tension:

$$\left\langle \Lambda(s,t)\Lambda(s',t')\right\rangle = \frac{(k_B T)^3 \ell_p^2 \mu_{\perp}}{2dL^7}\delta(t-t')\sum_{\alpha=0}\frac{w_{\alpha}(s)w_{\alpha}(s')}{\tilde{k}^2_{\alpha}}.$$

This might give a hint for estimating a reasonable size of the spring constant of bead-spring systems, when calculating their Brownian dynamics.

The new stochastic variable $\tilde{\boldsymbol{\xi}}$ simplifies the stochastic integrals (5.16) of the equations of motion:

$$\eta_\beta^\perp = \int_0^1 \mathrm{d}s \left(d\, w_\beta (\partial_s \theta) \tilde{\xi}_2 - w'_\beta \tilde{\xi}_1 \right), \tag{5.18}$$

$$\eta_\beta^\parallel = -d \int_0^1 \mathrm{d}s\, w'_\beta \tilde{\xi}_2 + \mathcal{O}(\epsilon). \tag{5.19}$$

Using this in Eqs. (5.14) allows us to conveniently solve the coupled stochastic differential equations by numerical integration [84]. The final equations *without flow* are a coupled set of *linear* equations (although of quadratic order in ϵ) with multiplicative noise. Nevertheless, they cannot be solved analytically, due to the complicated structure of the coefficients.

5.2 Results from Brownian dynamics simulations

5.2.1 Verification without flow field

We have computed equilibrium averages of the squared mode amplitudes to compare them with the equipartition result, Eq. (5.13). This is to check the validity of the approximations we made in the previous section and of the numerical solution technique. For the first eleven modes shown in Fig. 5.2, the agreement is excellent in case of $\ell_p/L \geq 9$, i.e. $\epsilon \leq 1/3$. Slight deviations due to the limited validity of the ϵ-expansion become visible at $\epsilon = 1/3$; in case of $\epsilon = 1$, results differ by about 14%. To analyze these errors in more detail, we have plotted the relative differences of analytical and numerical values for the mean square mode amplitudes versus ϵ^{-1} in Fig. 5.3. These relative errors decrease like ϵ^2, as shown by the gray bar. This is consistent with our second order perturbation expansion, since the first terms we neglected are of third order, thus their contribution to the relative error is proportional to ϵ^2.

In addition to that, Fig. 5.3 shows the relative errors of the mean end-to-end distance R of the polymer. The corresponding exact result is $\langle R^2 \rangle = L^2 f_D(L/\ell_p)$, with $f_D(x) = 2(e^{-x} - 1 + x)/x^2$ [87, 131]. The deviations again decrease as expected proportional to ϵ^2.

To validate dynamic properties, we compare the scaling behavior of fluctuations of the mean-square end-to-end distance $\Delta_R(t) = \left\langle [R(t) - R(0)]^2 \right\rangle$ with the analytically known and experimen-

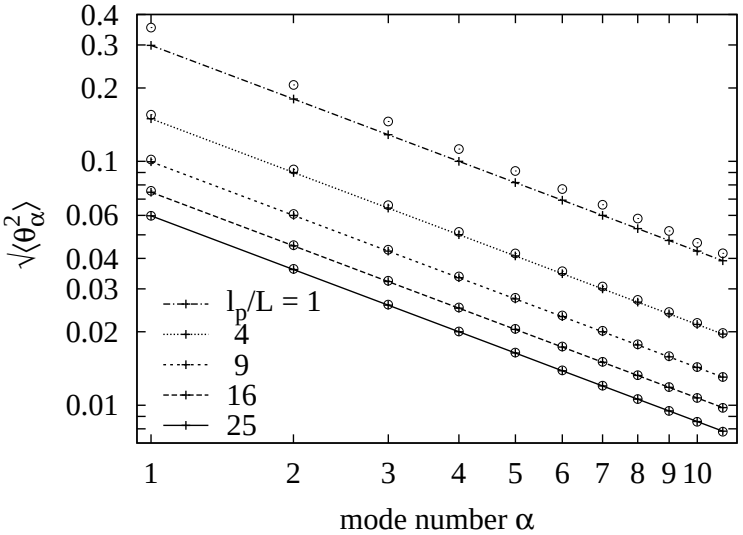

Figure 5.2: Mean squared amplitudes of normal modes for different persistence length. Open circles are numerical results, "+" interconnected by lines are given by Eq. (5.13). Significant deviations between both are visible only for $\epsilon = \sqrt{L/\ell_p} = 1$. They are of order ϵ^3, terms neglected in the perturbative solution Eq. (5.14a) (cf. also Fig. 5.3).

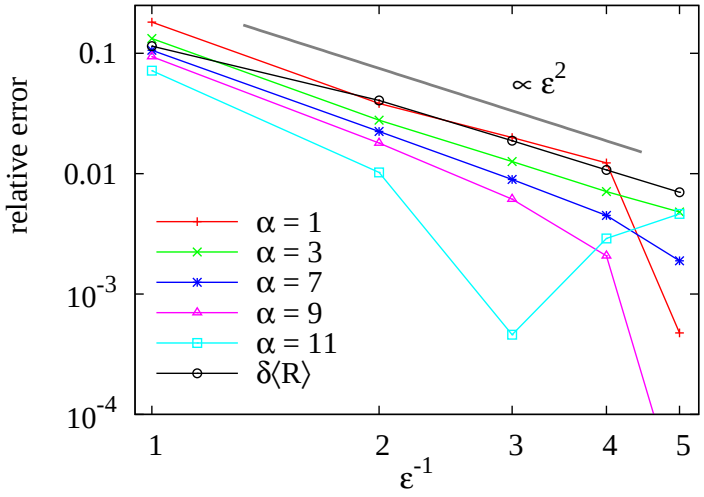

Figure 5.3: Relative errors of some mean-square mode amplitudes $\epsilon\sqrt{\langle\theta_\alpha^2\rangle}$ (colored) and mean end-to-end distance (black circles) versus inverse expansion parameter ϵ. Lines are shown to guide the eye. As expected from the order of the expansion of the equations of motion, the relative error vanishes proportional to ϵ^{-2}, thus the absolute error is $\propto \epsilon^{-3}$.

tally verified [57, 95] behavior: For short times, $\Delta_R(t)$ grows subdiffusively like $t^{3/4}$, for long times it approaches the equilibrium value of $\Delta_R(t\to\infty) = 2(L/\ell_p)^2/45$. Our numerical results in Fig. 5.4 reproduce this pattern in excellent quality; effects of the perturbation expansion can only be seen in slight deviations from the expected plateau value at long times. Comparing Fig. 5.4 to corresponding experimental results (Fig. 3 of Ref. [95]) even shows a similar downturn for times $t/\tau_1 < 10^{-3}$. In case of Ref. 95 this is due to insufficient statistics at small times because of a limited observation period. In our case, the finite number of modes accounted for causes a slight suppression of fluctuations at these short times. [4]

To summarize this part, we find that our method reproduces all tested equilibrium and dynamic observables very well within the accuracy expected from the perturbation expansion. In principle, one could think of even enhancing the accuracy of the equations. However, in spite of the simplicity of the equipartition expression, such a correction by means of an additional drift term is quite involved. This is caused by the strongly coupled nature of the equations, coming from the Lagrangian constraint and the noise projection. We dismissed such additions for this work, since the deviations are of minor importance for the applications we have in mind.

In the following section we will turn to an example of a nonequilibrium system that can nicely be worked out by means of the technique presented above. We always present results for filaments with persistence length $\ell_p/L \geq 4$, thus the systems show the correct equilibrium behavior, as demonstrated by now.

5.2.2 Motion in shear flow

A shear flow is a laminar flow with a velocity field as depicted in Fig. 5.5. In terms of the velocity gradient matrix $\boldsymbol{\Gamma}$ this reads $\boldsymbol{\Gamma} = \dot\gamma\left(\begin{smallmatrix}0&1\\0&0\end{smallmatrix}\right)$, with respect to the coordinate axes of Fig. 5.1.

To gain some understanding of the basics we briefly discuss the case of a stiff rod exposed to shear. By re-implementing dimensionalized quantities in Eq. (5.14b) and afterwards taking the limit $\epsilon \to 0$ we obtain the equation of motion (cf. Ref. 127)

$$\partial_t\theta_0(t) = -\dot\gamma\sin^2\theta_0(t) + \sqrt{D}\eta(t). \tag{5.20}$$

[4] For very short times, local fluctuations parallel to the tangent show a $t^{7/8}$ behavior [40, 94]. However, this is a property of terms of the order ϵ^3 and higher in the equations of motion, and hence cannot be seen from our calculations.

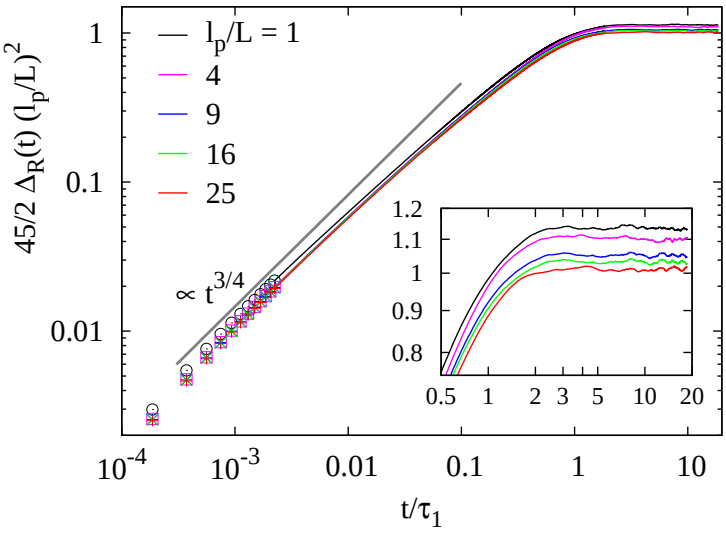

Figure 5.4: Time dependence of the mean-square displacement $\Delta_R(t)$ of the end-to-end distance. The calculations are done in 12-dimensional mode space. Symbols are replaced by lines were they would become very dense. The rescaled data for different persistence length collapses onto one master curve, which behaves $\propto t^{3/4}$ for short times. τ_1 is the relaxation time of the longest mode, $\tau_1 = k_1^{-4}$, in our units (cf. Eq. (3.58), and Ref. 95). The *inset* shows a magnification of the long-time behavior. The stiffer the filament, the closer the numerical results are to the correct equilibrium value 1.

Here, the noise is δ-correlated in time, and the diffusion constant $D = 2\mu_r k_B T/L$, with the rotational mobility of a rod $\mu_r = \mu_\perp 12/L^2$ [31]. In the deterministic case, i.e. $\eta \equiv 0$, Eq. (5.20) can be solved easily and results in a single rotation of the rod, which reaches the stall line at $\theta = 0$ for long times like t^{-1}. In terms of stability analysis the deterministic dynamics corresponds to a flow on a circle with a half stable fixed point at $\theta = 0$. When noise is present, η is the control parameter of a saddle node bifurcation at $\eta = 0$ [142]. The effect of this is that the stochastic forces drive the rod across the stall line after some time, such that a new rotational cycle begins. Driven by the shear and the noise, the rod will now rotate again and again, such that one can e.g. measure the rotational times to characterize the stochastic process.

For finite ϵ, we have the additional influence of the bending modes. Apart from shear-induced bending this can also change the behavior close to the stagnation line, since filaments with curved conformations might wiggle easier across this threshold.

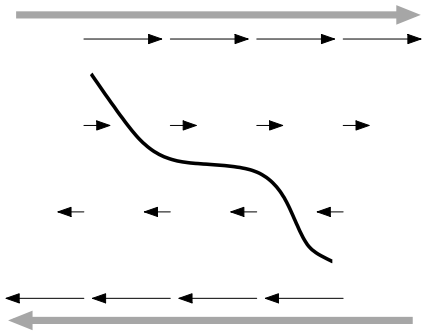

Figure 5.5: Sketch of a semiflexible filament in shear flow. The two gray arrows indicate walls moving with constant speed, black arrows the velocity of the fluid. At the fluid–wall interface, the fluid is transported with the velocity of the wall, due to no-slip boundary conditions.

In Fig. 5.6 we show a sample trajectory of a filament with relative stiffness $\ell_p/L = 6.5$. Here the rotations appear as a flip of the angular mode θ_0 from $-\pi/2$ to $+\pi/2$. These flips are usually accompanied by a peak in the first mode θ_1, indicating a sudden bending event triggered by the rotation. Furthermore, the end-to-end distance often shows a short dip corresponding to this intermediate bending.

Extensive experimental [50, 136, 138, 147], numerical [76, 111, 127, 135], and some theoretical work [22, 127] has been presented to characterize the motion of DNA in shear flow. However, the relative persistence length ϵ^{-2} of DNA is typically about two to three orders of magnitude smaller than that of F-actin, as already denoted in the beginning of Sec. 5.1. Consequently, the physics of these two kinds of semiflexible polymers will be quite different. When rotating in shear, for example, DNA more or less crawls along itself [136], whereas F-actin shows a clear stretch-out in our computations even at intermediate conformations, i.e., when the end-to-end distance is oriented perpendicular to the flow direction. Due to the different physics, the numerical methods used for DNA in the references above are not applicable in case of stiffer filaments like F-actin. In contrast to those techniques, our method always guarantees the local inextensibility of the filament.

A useful observable to get insight into the periodic and stochastic behavior is the power spectral density (PSD) $P(f)$, the Fourier transformation of the autocorrelation function of an observable x:

$$P(f) := \mathcal{FT}\{\langle x(t)x(0)\rangle\}.$$

In Fig. 5.7 we show the PSD of the end-to-end distance R of a filament with persistence length $\ell_p/L = 6.5$, both with shear and without. The strength of the flow is $\dot\gamma = 1.03/\mathrm{s}$ or $\mathrm{Wi} = 0.55$, where $\mathrm{Wi} = \dot\gamma\tau_c$ is the dimensionless Weissenberg number, the product of flow rate and characteristic relaxation time τ_c of the system. For τ_c one may choose the mean exponential decay rate of the autocorrelation function of the end-to-end distance. In terms of the dimensionless formulation chosen in Sec. 5.1.2, the bending stiffness κ is constant, and only temperature varies when changing the stiffness parameter ϵ. Thus in this formulation the relaxation rate is identical for all ℓ_p. Our data result in a mean of $\tau_c = 0.53 \pm 0.02\,\mathrm{s}$, so flow rates $\dot\gamma$ have to be multiplied by this factor to obtain them in Wi-units.

Without shear, the PSD shows a characteristic Lorentz-like behavior, where the only timescale in the system separates the long time plateau from the short time decay. In case of the end-to-end distance R, the short time regime obeys the power law $P(f) \propto f^{-7/4}$ [51, 115], which immediately follows from the mean square displacement $\propto t^{3/4}$. With shear, there is first of all a pronounced

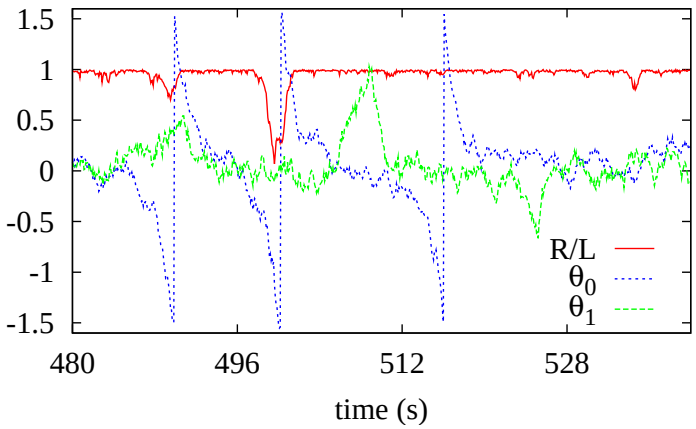

Figure 5.6: Sample trajectories of the end-to-end distance R and the first two angular modes, for a flow of strength $\dot\gamma = 1.03/\mathrm{s}$

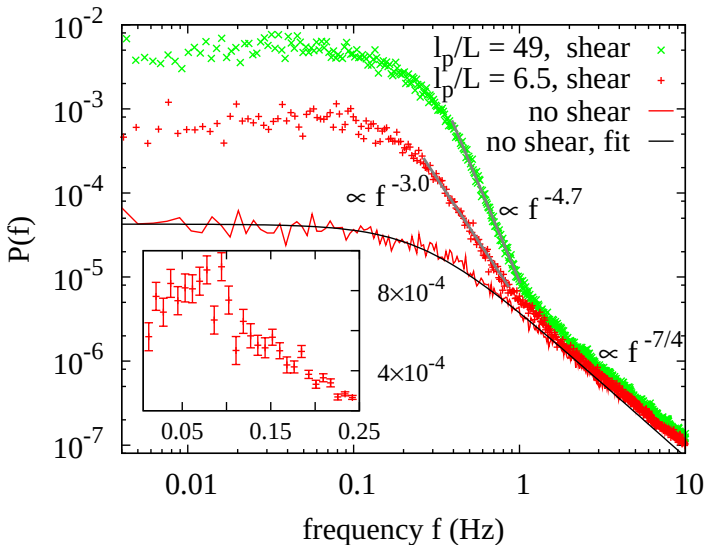

Figure 5.7: Power spectral densities $P(f)$ of the end-to-end distance without flow, and with a shear of strength $\dot{\gamma} = 1.03$ (Wi = 0.55). Green '×': $\ell_p/L = 49$, red '+': $\ell_p/L = 6.5$. The smooth black curve is a fit of the result in quiescent solvent with the appropriate Lorentzian [51, 115], used for the plot of the relative PSD in Fig. 5.9. With shear, a bump between 0.05 and 0.09 Hz shows the characteristic time of rotation of the filament. A different scaling regime appears for frequencies smaller than 1 Hz, with an exponent depending on properties of the filament. PSD-data for $\ell_p/L = 49$ have been multiplied by a factor 60 for the purpose of an easier visualization. Calculated with 10 ($\ell_p/L = 6.5$) and 8 ($\ell_p/L = 49$) modes resolution. *Inset*: Nonlogarithmic version of the region around the bump for $\ell_p/L = 6.5$, with estimated error bars. The number of data points has been reduced by averaging.

increase in correlations at small frequencies, indicating stronger long-time correlations due to periodic tumbling events. A shallow bump appears in the region between 0.05 and 0.09 Hz, indicating a typical frequency of rotation for the given flow strength. This bump is visible more clearly in Fig. 5.9, where we show the ratio of the PSDs with and without flow.

Coming back to Fig. 5.7, we identify an additional timescale in the decay for frequencies below 1 Hz, separating the high frequency power law $f^{-7/4}$ from a regime with an exponent with a larger absolute value. This intermediate sharp decay arises due to a subtle interplay between thermal fluctuations and frictional driving of the shear flow [76, 135]. However, the power law of this decay is not generic—it depends on ℓ_p in a nontrivial manner. The detailed study of this phenomenon is deferred to a later work.

In the experiments with DNA cited above, the end-to-end distance itself could not be measured due to the limited optical resolution; instead, the molecular extension was recorded, as measured by the mean projected extension in flow direction. However, it is reported that this observable does not show a typical frequency for a deterministic cycle associated with the tumbling motion in flow, in contrast to our results for the end-to-end distance of F-actin. We conjecture that this relatively weak effect might also be connected to the inextensibility of the filament.

Fig. 5.8 shows PSDs of the first two modes for the angle and tension. In the absence of flow, the stiff filament mode θ_0 is to first order given by the rotational diffusion of a stiff rod. This leads to a f^{-2} decay in the PSD with nonperiodic boundary conditions (not shown), which still gives the high frequency regime of the results in shear. The bumps of the PSDs of R and θ_0 are located at about the same frequency—in this regard it is interesting to note that the end-to-end distance is *independent* of θ_0.

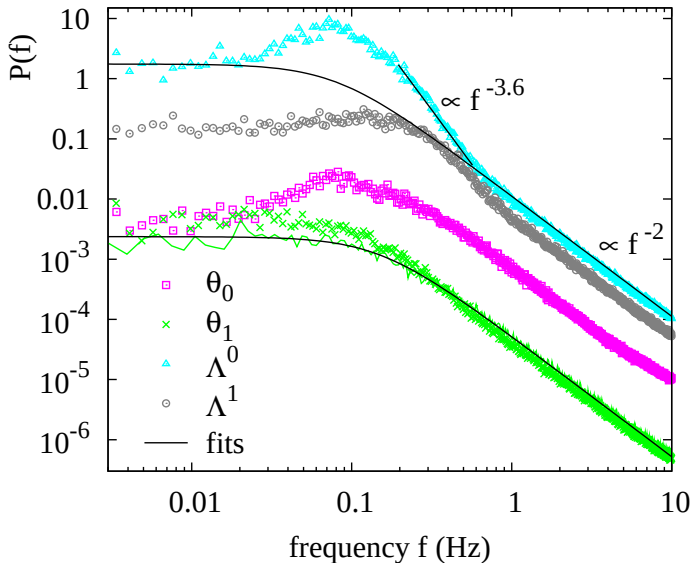

Figure 5.8: Power spectral density of tension modes Λ^0, Λ^1, and angular modes θ_0, θ_1. Symbols give results with a shear flow of strength $\dot{\gamma} = 1.03/s$ (Wi = 0.55). The light line (green online) shows the behavior of θ_1 without flow, smooth black curves are fitted Lorentzians, as explained in the text. A peak in θ_0 and Λ^0 around 0.5 Hz is a sign of the tumbling time of the filament. Concerning θ_1, shear still increases correlations at low frequencies.

In a quiescent solvent, Eqs. (5.14) give Ornstein-Uhlenbeck behavior for the higher angular modes θ_i, with small deviations due to the coupling of the equations and the multiplicative noise. In Fig. 5.8 we only show the first mode θ_1, where the case without flow has been fitted to a Lorentzian, whose coefficients differ from the Ornstein-Uhlenbeck process by at most some percent. The differences between observables recorded with and without flow are better visible in Fig. 5.9, where we identify an increase below 0.3 Hz and a slight decrease for higher frequencies. The increase of the plateau for θ_1 is a characteristic of filaments with a relative persistence length of the order one: Stiffer filaments do not buckle at all during a rotation, and floppier ones show a different behavior for strong flows (crawling near the stall line), or thermally fluctuate so heavily that a buckling due to shear cannot be identified. The next mode θ_2 still shows a similar behavior, but in an already much weaker manner.

The tension modes finally only show noise fluctuations around zero when no flow is present (not shown), which is obvious from Eq. (5.14c). In shear flow the power spectrum changes towards a behavior as characteristic to Lorentzian curves for low and high frequencies. This is caused by the fact that there is a strong linear coupling between each tension mode Λ^β and its corresponding angular mode θ_β, visible by expanding the flow dependent part of Eq. (5.14c). The intermediate frequency region of the PSDs of the tension modes clearly shows signs of driving by shear: A bump, indicating a typical correlation time, followed by a sharp decay. These properties are even more pronounced in the tension modes, when comparing to the angular mode with the same index, respectively. In case of Λ^0 we identify a strong peak at the very same position of maximum height already mentioned for the PSDs of θ_0 and R, and a sharper power law decay $f^{-3.6}$ towards higher frequencies. We conclude from this that the periodicity of the tumbling events can be found directly in the autocorrelation of the tension modes. This is very reasonable, since it follows that a rotation in shear triggers specific frictional forces acting on the backbone of the polymer, which have to be withstand by the constraining forces. In Fig. 5.9 we show the PSD of Λ^0 relative to a Lorentzian fitted to the generic short- and long-time behavior to demonstrate the flow specific peak.

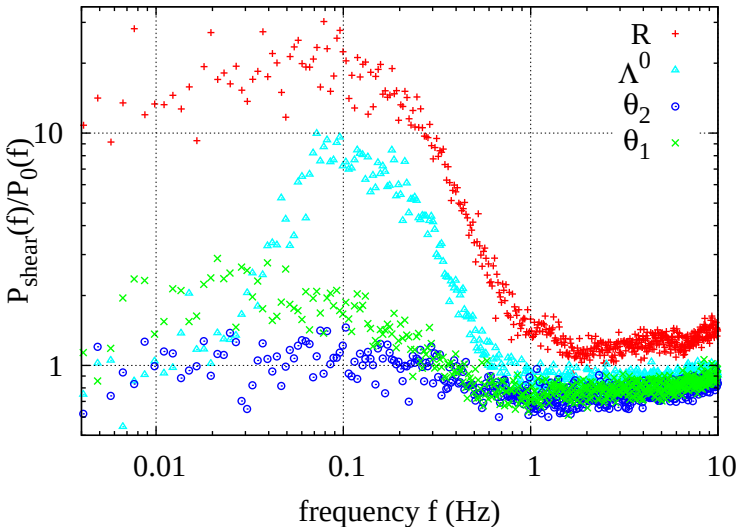

Figure 5.9: Ratio of power spectral density $P(f)$ with shear flow to that without flow, for the data of Figs. 5.7 and 5.8. Correlations of R are increased by a factor of more than 10 at frequencies of 0.3 Hz and below, with a peak between 0.05 and 0.09 Hz. Similarly, correlations of the first angular mode θ_1 are pronounced by a factor of 2 below 0.1 Hz, and slightly decreased around 1 Hz. This is a signature of the semiflexible nature of the polymers under investigation, since it refers to the buckling events occurring periodically during their rotation in shear. Concerning the second angular mode θ_2 (not shown in Fig. 5.8), there is still a change from decreased to increased correlations visible when going from $f = 1$ Hz to 0.1 Hz and below. The tension mode Λ^0 shows a strong tenfold peak at 0.1 Hz when compared to a Lorentzian which has been fitted to the generic short- and long-time behavior.

5.2.3 Statistics of tumbling in shear

A further point of interest is the mean time it takes the polymer to rotate. Experiments with DNA report a power law increase of the tumbling frequency with shear strength proportional to $\mathrm{Wi}^{0.67}$, confirmed by appropriate simulations and scaling analysis [136]. Furthermore, analytic results for Brownian rods in strong shear consistently give $\mathrm{Wi}^{2/3}$ [127].

Fig. 5.10 shows our results for the mean rotating frequency of filaments with various persistence lengths. We defined a flip to be a *single* half turn of an angle π. As a check of consistency, the frequency of rotation of a filament corresponding to Figs. 5.7 and 5.8 is 0.066 ± 0.002 Hz, which lies very well within the observed peak width of these figures.

The maximum flow strength for which we can obtain results numerically is limited by the ϵ-expansion we have exploited in Sec. 5.1.2. Since this expansion requires a small curvature, it breaks down when a powerful flow strongly bends the filament. For comparison we also plotted numerical results for a rotating stiff rod, which obeys the expected $\dot{\gamma}^{2/3}$ power law. The exponent shows a slight crossover behavior in the semiflexible regime, in deviation from both the stiff and the flexible limit: As an example, the rotational frequency of a filament with persistence length $\ell_p/L = 6.5$ scales like $\dot{\gamma}^{0.72\pm0.01}$. The data of Fig. 5.10 furthermore demonstrate that the exponent becomes closer to 2/3 the stiffer the filament, as expected from the stiff rod limit. Note that this relatively weak crossover effect does not vanish $\propto \epsilon^3$, and thus seems not to be caused by deviations due to the perturbation expansion.

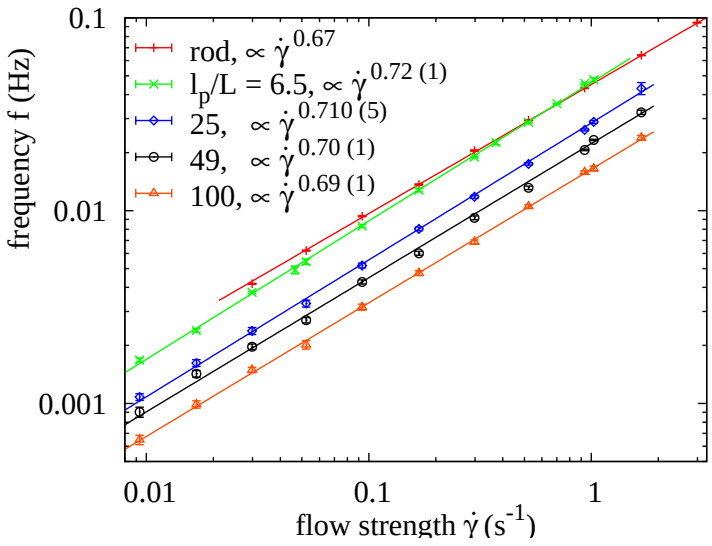

Figure 5.10: Tumbling frequency of semiflexible polymers with different persistence length versus strength of shear flow. The change of the power law form $\dot\gamma^{0.72}$ at $\ell_p/L = 6.5$ towards $\dot\gamma^{2/3}$ for a stiff rod indicates a crossover behavior between rods and flexible polymers. The amplitude shift appears due to the parametrization we have chosen (cf. Sec. 5.1.2) and has not been removed for reasons of readability.

5.3 Effective bundle dynamics

The spectral analysis of the wormlike chain Hamiltonian not only allows for the efficient simulation of single filament dynamics, but also makes possible the description of *bundles* of wormlike chains, by means of an effective mode-dependent bending stiffness. Heussinger et al. [67] have shown that the three contributions of the wormlike bundle Hamiltonian, i.e., the stretching energy and the shear energy, in addition to the bending term Eq. (5.1), can be condensed into a simple expression for a renormalized bending stiffness in Fourier space,[5]

$$\kappa_n(N,\lambda) = N\kappa\left[1+\left(\frac{1}{N-1}+(k_n\lambda)^2\right)^{-1}\right]. \tag{5.21}$$

Apart from the bundle size N there is only a single new parameter λ, which is a length scale comprising all microscopic properties of the bundle, e.g., the shear stiffness, the cross-link spacing, the stretching stiffness, and the interfilament distance. Three different elastic regimes have been identified and explained by this effective bundle theory: First, in the *decoupled regime* with $k^{-1} \ll \lambda$, the bending stiffness is constant, $\kappa_n = N\kappa$, since all filaments can move laterally independent. Second, at larger wavelength $\lambda\sqrt{N} \gg k^{-1} \gg \lambda$, an intermediate *shear-dominated* regime follows, in which the full mode dependence of Eq. (5.21) has to be accounted for, such that modes with smaller wavelength become floppier. Lastly, for even larger wavelength, the bending becomes *fully coupled*, and the bundle elasticity is equivalent to that of a homogeneous beam with $\kappa_n \sim N^2$. These three regimes are visualized in Fig. 5.11 by a plot of $\kappa_n(N,\lambda)$ as a function of the cutoff length λ; the intermediate regime is the most interesting one, since here N and λ can be chosen such that the effective stiffness varies considerably for different wave numbers k_n.

The implications of this effective theory for the equilibrium statistical mechanics of semiflexible bundles are large, altering fundamentally, e.g., the scaling properties of the force extension relation and the shear modulus, as well as the elasticity of networks [67]. Complementary, the spectral method presented in the preceding sections constitutes a framework to analyze the dynamics of such semiflexible bundles. The only change that is necessary for computer simulations of effective

[5] Eq. (5.21) is identical to Eq. (6) of Ref. 67, with $\hat\kappa_f = 1/12$ from continuum elasticity.

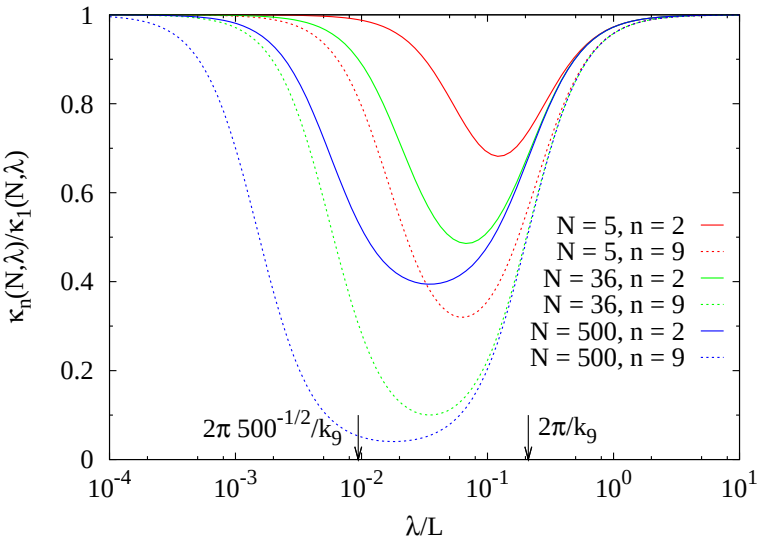

Figure 5.11: Mode dependent stiffness $\kappa_n(N,\lambda)$ of a semiflexible bundle, for three values of the bundled size N, and two mode numbers n each. Each curve is normalized with respect to the corresponding one for $n = 1$. Arrows at the bottom axis indicate the regime boundaries for the example of $n = 9$ and bundle size $N = 500$.

bundle dynamics instead of single semiflexible polymers is the inclusion of the mode dependent stiffness, Eq. (5.21). We use the notation $\kappa_n(N,\lambda) =: N\kappa\tilde{\kappa}_n(N,\lambda)$; then, in place of Eq. (5.13), we redefine the perturbation parameter $\epsilon^2 := L/\ell_p N\tilde{\kappa}_1$. The units given in Sec. 5.1.2 are changed accordingly, such that the unit of time is rewritten as $t\,N\kappa\tilde{\kappa}_1\mu_\perp/L^4 \to t$, the noise $\boldsymbol{\xi}L^3/\epsilon N\kappa\tilde{\kappa}_1 \to \boldsymbol{\xi}$, the tension $\Lambda L^2/N\kappa\tilde{\kappa}_1 \to \Lambda$, and the strength of the flow $\dot{\gamma}L^4/N\kappa\tilde{\kappa}_1\mu_\perp \to \dot{\gamma}$. In Eq. (5.14a), the prefactor of the term for the bending stiffness changes,

$$\partial_t\theta_j = -\frac{\tilde{\kappa}_j}{\tilde{\kappa}_1}k_j^4\theta_j - \sum_{\substack{\nu=0\\ i=1}}\Lambda^\nu\theta_i\Xi^i_{j\nu} + \eta_j^\perp + \frac{\dot{\gamma}}{\epsilon}g_j^\perp + \mathcal{O}\left(\epsilon^3\right); \tag{5.22}$$

Eqs. (5.14c) and (5.14b) are unchanged. In these terms, the equations of motion describe the mode dynamics of a semiflexible bundle relative to the stiffness of the first mode, and different bundle sizes N enter via the ratio $\tilde{\kappa}_j/\tilde{\kappa}_1$, and via ϵ.

As a proof of principle, we explore one sample system covering some of the emergent phenomena of bundle dynamics. In an elongational flow field, the initial orientation of the filament is chosen to the compressional direction of the flow. Within a deterministic propagation in time, the rod buckles under the compressional force, and then rotates by $\pi/2$ to finally line up along the elongational direction. This well-defined cycle is evaluated for bundles with fixed size N, but varying cutoff length λ. By integrating the squared mode amplitudes in time over such a cycle, one obtains a measure for the bending energy that is transferred from the flow to the bundle and vice versa. A set of curves obtained this way is displayed in Fig. 5.12, for an initial configuration with only the first mode set to a small nonzero value. The normalization with respect to the behavior of a single filament reveals a large variation of the stored bending energy with respect to λ within the shear-dominated regime. In this parameter window the higher modes become increasingly softer, based on the effective stiffness, Eq. (5.21). The detailed quantitative behavior, however, is not generic, but depends strongly on the choice of the initial conditions. Thus though the softness of the modes with small wavelength is a qualitatively persistent future, the peak structure in the shear-dominated regime is not.

Several interesting future projects derive from the framework of effective bundle dynamics. An analysis of the stochastic motion should also directly show the implications of the effective stiff-

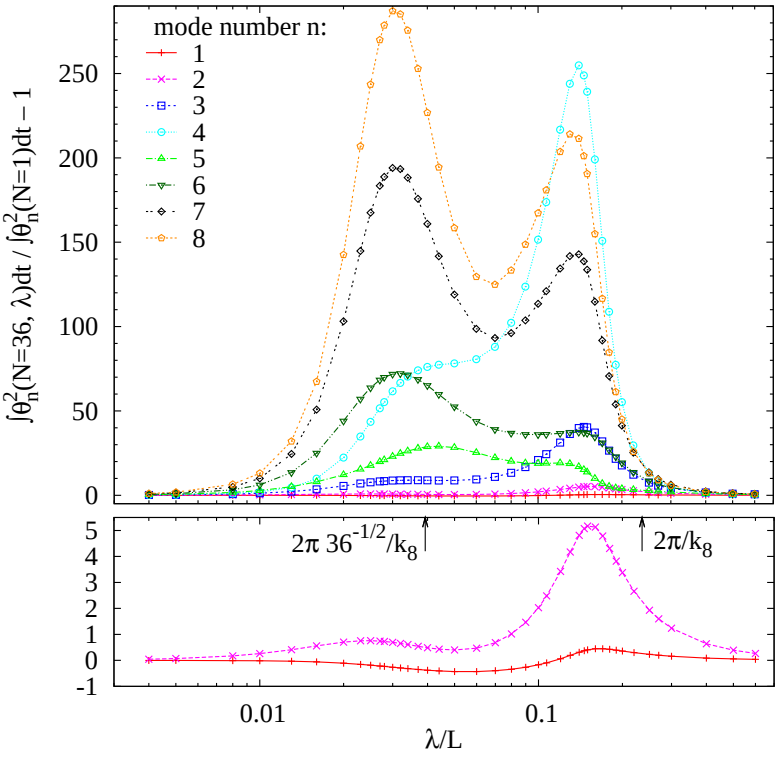

Figure 5.12: Squared mode amplitudes of a bundle with $N = 36$, integrated in time over a rotation cycle in elongational flow, and normalized with respect to the same evolution of a single filament. The plot displays the variation of this observable with respect to the cutoff length of the bundle, λ. To guide the eye, lines interconnect the data points of the results of the deterministic simulations. The initial conditions are set to $\theta_1(0) = 0.01$, $\theta_{i\geq 2}(0) = 0$, and $\theta_0(0)$ is set such that the filament is oriented along the compressive direction of the flow.

ness, e.g., for a system in shear flow, as worked out in Sec. 5.2.2. Moreover, the spectral dynamics equations analyzed so far are limited to linear order in the angular modes. Various important nonlinear effects are thus not grasped, e.g., the Euler buckling instability, and tension propagation. They should be accounted for in the mode dynamics by considering the higher order contributions in Eqs. (5.8).

5.4 Conclusion

We have presented a newly developed method for describing the dynamics of single semiflexible filaments in a viscous solution, subject to external flow fields. Due to the mainly elongated conformations, hydrodynamic backflow effects are marginal and thus the dynamics can be formulated in the free draining approximation. In contrast to previous approaches based on bead-rod/spring models in real space we have adopted a spectral method of the equations of motion. A further simplification can be achieved upon using an angular representation of the polymer conformations. This has the advantage that there is no approximation in the bending energy. All of the above allows us to give an efficient computational approach for calculating Brownian trajectories for the polymers, and to include nonlinear effects of the environment without inherent limitations.

The computational time necessary for these numerical solutions is proportional to the fourth power of the mode number, and linear in the spatial resolution of the noise along the space curve. The main advantages regarding numerics are, compared to bead–rod models, first, mode dynamics offers a natural approach to the long-time dynamics, since the high wavenumber fluctuations are increasingly irrelevant (cf. Fig. 5.2). Second, the additional time necessary to satisfy the local constraint of constant length is very small. One reason for this is that no pseudo–potentials have to be calculated. Finally, one could even enhance the speed by adapting time and spatial resolution

appropriately to each individual mode, a technique we did not apply, yet. In summary, we are able to monitor conformational properties very precisely, while taking account to all modes that give essential contributions to the dynamics of stiff semiflexible filaments.

Conceptually, our approach should be understood as being complementary to bead-rod and bead-spring models. In some cases the latter are advantageous, e.g. when dealing with dense solutions of flexible polymers, such that excluded volume effects are important.

Quantitative tests of the numerical solution show that the method correctly describes the fluctuations of semiflexible filaments in a quiescent solvent. We have demonstrated that our technique is capable of describing the long time dynamics in a sheared environment within reasonable computational time. For the first time we have calculated power spectral densities and mean rotational frequencies of F-actin in shear, taking into account exactly the local inextensibility constraint. The results have enabled us to point on two crossover phenomena still to be described in more detail. For the future, extensions of the method should be possible to include e.g. charge effects or different boundary conditions. A more challenging task is to extend the analysis to three dimensions.

An experimental test of the behavior of Actin filaments in shear or elongational flow has not been reported, to our knowledge. However, the setup used for sheared DNA [136, 138] might also work for F-actin, and elongational flows are constructed easily by means of microfluidic techniques [86]. Thus experiments could in principle be possible without too much technical effort.

Chapter 6

Summary and outlook

Diffusive transport processes on the nanometer scale play an essential role for understanding colloidal systems of any kind—in applications of biological origin they are of vital importance. In this dissertation I have examined the diffusive motion of macromolecules in different environments, based on three typical model scenarios.

The central part of this work investigates the dynamics of thin rods in suspensions. Here, the shape of a rod constitutes an idealization of elongated anisotropic particles on the microscale. A simplified model is presented, reducing the problem to the motion of a single rod in a two-dimensional course of point-like obstacles. I explore this model in two ways: First, I have developed molecular dynamics simulations that calculate the Brownian motion of the rod, covering up to nine decades in time. Experimentally relevant observables are measured in statistically excellent quality, e.g., the intermediate scattering function with a noise level of 10^{-4}. Second, I formulate an analytical description of this dynamics on a mesoscopic scale, based on the Smoluchowski-Perrin equation for free diffusion. To this end, I present for the first time the full solution of this equation in two dimensions, and demonstrate that the measurement of two diffusion coefficients is sufficient to obtain a quantitative mesoscopic theory for systems with obstacles.

A comparison of the simulations with the theory allows for a thorough quantitative understanding of the dynamics in suspensions of thin rods, characterized by various time and length scales. I substantiate the validity of the effective theory down to length scales of the order of the mean distance between the particles, and corroborate the so far unproven predictions of the scaling theory of Doi and Edwards. A discussion of several observables calculated from the time dependent spatial displacement reveals the strongly anisotropic motion of the constrained rod, with longitudinal and transverse diffusion coefficients differing by up to five orders of magnitude. Markedly non-Gaussian dynamics is observed for the constrained diffusion inside the tube, and also in the dynamic transitions towards a stepwise relaxation of this constraint. Furthermore, I identify and explain an intermediate power law in the scattering functions. This is interpreted as a generic characteristic of the anisotropic dynamics of rods in disordered suspensions with strong mutual steric constraints. It is visible in all calculated intermediate scattering functions, independent of which part of the rod responds to the scattering, e.g., only the center of mass, its ends, or the whole rod.

In addition to this topic, the first part of this work addresses the subject of diffusive transport in heterogeneous environments of fractal geometry. This is relevant for the dynamics in, e.g., porous media and biological cells, the latter characterized by a very crowded and heterogeneous interior.

This chapter is an extended translation of the “Zusammenfassung” in german on page v.

In the context of the Lorentz model I represent this dynamics by the diffusion of a single isotropic particle in the void space between randomly distributed hard spheres. Large scale computer simulations are presented, in connection with a detailed scaling analysis of the critical dynamics close to the percolation transition. In the vicinity of the critical point I observe anomalous diffusion in a time interval covering four orders of magnitude. This outstanding precision enables us to extract the universal dynamic scaling function from the transition to the asymptotic behavior; since the convergence to the anomalous regime is very slow, the inclusion of an universal correction to the power law is necessary. Simulation results calculated with two different microscopic laws of motion yield identical behavior at criticality, corroborating the notion of universality.

The last part of this thesis is devoted to the dynamics of a single semiflexible filament, which constitute, e.g., an essential ingredient of the cytoskeleton of the cell. The equation of motion of such a polymer in a flowing solvent is expressed in terms of the two-dimensional dynamics of the eigenmodes of the polymer, taking into account the constraint of longitudinal inextensibility. Based on this formulation, I analyze the rotation of a semiflexible polymer in shear flow, and elaborate corresponding properties of the mode spectra and the end-to-end distance. A first examination of bundle dynamics by means of an effective mode-dependent stiffness opens up an additional perspective for applications of this theory.

In summary, my results deepen fundamentally the knowledge of dynamic processes of diffusing macromolecules, and give predictions for experimentally relevant observables. Specifically, the intermediate power law found in the intermediate scattering functions of a suspension of thin rods is considered as a general property of the reptation motion of rods.

Combinations of the model systems subject of this work promise a rich class of highly interesting models at the interfaces between statistical physics, biological physics and the physics of colloidal systems. As an outlook, I would like to mention three possible examples that go further steps towards understanding the complex dynamics of suspensions of rods:

- In the Lorentz model, the tracer particle can be substituted by a rod. This combines the steric hindrance effects of a heterogeneous environment with the reptation motion of a rod—both contributions should be visible in the dynamics, in terms of effects described in Chapters 2 and 4 of this thesis.

- The simulations of the thin rod can be extended to three dimensions. For this, the two-dimensional array of pointlike obstacles has to be substituted by a three-dimensional network of rods of finite or infinite length. The results will probably not be substantially different from those presented here, as already stated in Sec. 4.6; however, this is the basic building block of future investigations of more realistic systems.

- A finite bending flexibility can be introduced into the dynamics of the rod in the obstacle course. This is either possible in real space, in terms of a finite number of connected elements that possess a certain degree of flexibility with respect to each other. Alternatively, one may utilize the mode dynamics elaborated in Chapter 5. We expect different kinds of creeping motion to emerge, since a semiflexible rod will explore trajectories in dense collections of obstacles that a stiff rod cannot pass. The dynamics predicted by the tube concept might change depending on the degree of flexibility.

Acknowledgment

Many people contributed to the progress of this work, both regarding scientific and nonscientific issues; only the sum of all this help made possible the emergence of the dissertation you have in your hands. I try to acknowledge this here, although incompletely.

The continuous support of my supervisors has been indispensable to me. First of all, I am indebted to Thomas Franosch. The main part of this thesis, i.e., the entangled needle, the Perrin theory, and the Lorentz model evolved from his ideas and suggestions. I enjoyed the enlightening discussions with him, since he had much patience with my numerous basic questions, and a very supportive confidence in my progress. Essential help has furthermore been provided by Felix Höfling, as well concerning physical as technical problems. My Brownian dynamics simulations of the Lorentz model and the entangled needle are built on his elaborate program code for ballistic dynamics—I could not have obtained so convincing numerical results without the sophisticated algorithms of his as a starting point. In addition, I got interesting suggestions for the dynamics of a needle from Matthias Fuchs, whom I had the pleasure to visit in Konstanz.

The semiflexible polymer dynamics has been worked out together with Chris Wiggins and Oskar Hallatschek, supervised by Erwin Frey. Claus Heußinger has proposed to me the simulations of bundle dynamics; I am sad that time constraints prevented me from more work in this area. The large scale computer simulations that represent a significant part of all projects presented here have been made possible by the IT infrastructure set up by Frederik Wagner, who unprecedentedly boosted our group in computational power.

Apart from Erwin Frey's important help in all polymer related problems, I appreciate very much his permanent and reliable support as the chairholder of the group. He spends an admirable effort in our assistance and promotion, and gave me the possibility to attend to several interesting schools and conferences.

In the course of my PhD work in his group, I came to take something for granted that definitely not is: I have always enjoyed very much the working atmosphere with my colleagues and friends. Discussions are very open, as are the office doors, and several very nice group events have further encouraged us. I find it an extraordinary privilege to get acquainted to so many kind, different and interesting people, and hope I could give something back. Outside university, I benefited even more: Among the many things I have learned are swing dancing, skiing, playing skat, white-water rafting, and photographing—not to mention the countless hiking tours in the Alps. Specifically, I would like to thank those who have shared a long time with me: Marta Balbás Gambra, Frederik Wagner, Wolfram Möbius, and Karen Alim; just as well, I have enjoyed very much the time with Valentina Áquila, Sebastian Fischer, Andrea Thoma, Matthäus Bartsch and Marisa Pamplona.

Finally, many thanks to my parents Angela & Heinrich and my brothers Raphael & Felix for the confidence that the things I am doing in my life make sense—something I am not always convinced of.

Appendix A

Short-time velocity correlations

In Secs. 2.3.2 and 4.2, we have pointed to the effect of non-vanishing velocity correlations for $t > \tau_B$ in the Brownian dynamics simulations. Here we explain this behavior quantitatively within a toy model.

The essential components for the derivation are, first, a random walk which is continuous in space but evaluated on a fixed time grid, and second, a hard wall restricting the available volume through ballistic reflections. The most simple configuration is given by a point-like particle performing a two-dimensional random walk between two parallel walls with a fixed absolute value v of the velocity.

The calculation of the velocity-autocorrelation function $\psi(t)$ is elementary for the first two time steps τ_B. Choosing a coordinate system with the walls parallel to the y-axis, we parametrize the velocity during time step n by an angle φ_n to the x-axis, $\boldsymbol{v}_n(t) = \boldsymbol{v}_n(n\tau_B < t < (n+1)\tau_B) = v(\cos\varphi_n, \sin\varphi_n)$. There are four cases to be distinguished, depending on whether the particle collides with the wall or not during the first and the second time step, respectively. Symmetry reduces this to two cases, differentiated by the propagation within the first time interval; the geometry is sketched in Fig. A.1.

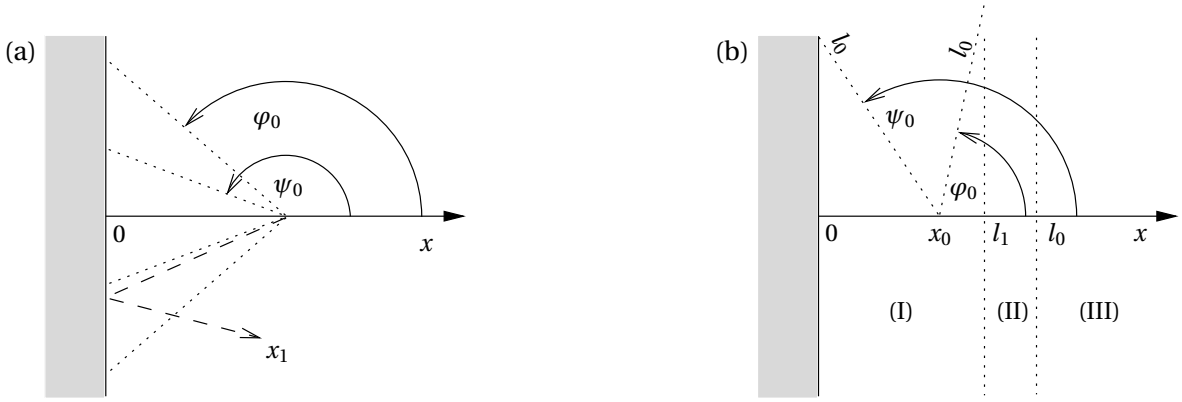

Figure A.1: Geometry of the trajectory within the first time step,. (a): *with* a collision; (b): *without* a collision, and the particle starting in region (I).

Collision within the first time interval

We calculate the correlation between the initial velocity $\boldsymbol{v}_0(0)$ and the velocity one time step later, $\boldsymbol{v}_1(t > \tau_\mathrm{B})$, when a collision happens both in the first and in the second time interval τ_B:

$$\begin{aligned}\langle \boldsymbol{v}_0(0)\cdot\boldsymbol{v}_1(\tau_\mathrm{B}+\Delta t)\rangle &= v^2\overline{(\sin\varphi_0\sin\varphi_1-\cos\varphi_0\cos\varphi_1)}.\\ &= \frac{2}{L}v^2\int_0^{l_0}\mathrm{d}x_0\,2\int_{\varphi_0}^{\psi_0}\frac{\mathrm{d}\varphi_0'}{2\pi}\int_{\varphi_1}^{2\pi-\varphi_1}\frac{\mathrm{d}\varphi_1'}{2\pi}\left(\sin\varphi_0'\sin\varphi_1'-\cos\varphi_0'\cos\varphi_1'\right).\end{aligned} \tag{A.1}$$

$l_i(t) = v\Delta t$ is the distance traveled in one direction during the time interval i. The lower bounds φ_0 and φ_1 are the minimum angles which lead to a collision with the wall within the corresponding time interval. There is no contribution from the y-component of the velocity to the innermost integral of Eq. (A.1), so

$$\langle \boldsymbol{v}_0(0)\cdot\boldsymbol{v}_1(\tau_\mathrm{B}+\Delta t)\rangle = \frac{2v^2}{L\pi^2}\int_0^{l_0}\mathrm{d}x_0\int_{\varphi_0}^{\psi_0}\mathrm{d}\varphi_0'\cos\varphi_0'\sin\varphi_1. \tag{A.2}$$

Since $\cos(\pi-\varphi_1) = x_1/l_1(\Delta t) = (-v_{0x}\tau_\mathrm{B}-x_0)/v\Delta t$, we find as condition for φ_1:

$$\cos\varphi_1 = \frac{\tau_\mathrm{B}}{\Delta t}\left(\cos\varphi_0+\frac{x_0}{v\tau_\mathrm{B}}\right) \tag{A.3}$$

If the first collision happens too early, a second is not possible in the interval $\tau_\mathrm{B} < \tau_\mathrm{B}+\Delta t \le 2\tau_\mathrm{B}$, since $x_1(x_0,\varphi_0) \le l_1(t)$. From $x_1 = l_1(\Delta t)$ we obtain the upper bound ψ_0 for φ_0',

$$\cos\psi_0 = -\frac{\Delta t}{\tau_\mathrm{B}}-\frac{x_0}{v\tau_\mathrm{B}} \tag{A.4}$$

If the absolute value of the right-hand side of Eq. (A.4) is bigger than 1, ψ_0 is fixed to π. The sin in Eq. (A.2) can now be expressed as a function of $\cos\varphi_0'$, yielding

$$\langle \boldsymbol{v}_0(0)\cdot\boldsymbol{v}_1(\tau_\mathrm{B}+\Delta t)\rangle = \frac{2v^3\tau_\mathrm{B}}{L\pi^2}\int_0^1 dy\int_{\varphi_0}^{\psi_0}d\varphi_0'\cos\varphi_0'\sqrt{1-\left(\frac{\tau_\mathrm{B}}{\Delta t}\right)^2\left(\cos\varphi_0'+y\right)^2}, \tag{A.5}$$

where L is the distance between the walls, and the boundaries of the inner integral are defined by

$$\cos\varphi_0 = -y; \qquad \cos\psi_0 = \begin{cases}-\left(y+\frac{\Delta t}{\tau_\mathrm{B}}\right), & y+\frac{\Delta t}{\tau_\mathrm{B}} < 1,\\ \cos\pi, & y+\frac{\Delta t}{\tau_\mathrm{B}} \ge 1.\end{cases}$$

No collision within the first time interval

The integrands are the same as above, only the upper bound of the outer integral changes to l_0+l_1. Concerning the bounds of the integral over φ_0', the lower bound for φ_0' is for all three regions of x_0

$$\cos[\varphi_0(x_0)] = \frac{l_1-x_0}{l_0} = \frac{\Delta t}{\tau_\mathrm{B}}-\frac{x_0}{v\tau_\mathrm{B}}.$$

For the upper bound we get

$$\cos[\psi_0(x_0)] = \begin{cases} -x_0/l_0, & x_0/l_0 < 1 \quad \text{(I, II)}, \\ \cos\pi, & x_0/l_0 \geq 1 \quad \text{(III)}. \end{cases}$$

The result thus reads

$$\langle \boldsymbol{v}_0(0) \cdot \boldsymbol{v}_1(\tau_\mathrm{B} + \Delta t) \rangle = \frac{2v^3\tau_\mathrm{B}}{L\pi^2} \int_0^{1+\Delta t/\tau_\mathrm{B}} \mathrm{d}y \int_{\varphi_0(y)}^{\psi_0(y)} \mathrm{d}\varphi_0' \cos\varphi_0' \sqrt{1 - \left(\frac{\tau_\mathrm{B}}{\Delta t}\right)^2 \left(\cos\varphi_0' + y\right)^2}, \tag{A.6}$$

with the boundaries

$$\cos[\varphi_0(y)] = -y + \frac{\Delta t}{\tau_\mathrm{B}}, \qquad \cos[\psi_0(y)] = \begin{cases} -y, & y < 1, \\ \cos\pi, & y \geq 1. \end{cases}$$

Eqs. (A.5) and (A.6) can be evaluated numerically; they coincide for symmetry reasons. The results obtained from this calculations are in excellent agreement with simulations of the toy model, see Fig. A.2. In principle, $\psi(t)$ can be obtained for longer times $t > 2\tau_\mathrm{B}$ too, but the calculations are quite involved.

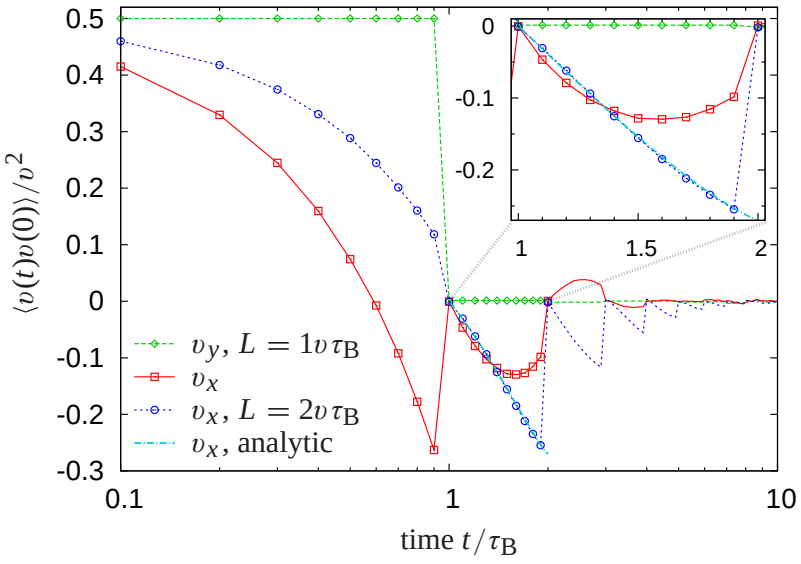

Figure A.2: Velocity-autocorrelation function for the two-dimensional motion of a point-like particle moving between two walls oriented parallel to the y-axis. The walls are separated by a distance L in x-direction. The particle is reflected ballistically at the walls, and the direction of the velocity is changed randomly in intervals τ_B. The inset displays a magnification of the regime $\tau_\mathrm{B} < t < 2\tau_\mathrm{B}$ on the linear scale. The analytic curve responding to Eq. (A.5) is shown for $L = 2v\tau_\mathrm{B}$; it matches perfectly the simulation results.

Appendix B

Supplementary material for the dynamics of a rod

B.1 Perturbation theory for the characteristic function: longitudinal force

For a nonzero force, the results for the characteristic function and the scattering function given in Sec. 3.2 have to be supplemented by additional terms. The full expression for the matrix elements of the characteristic functions, cf. Eq. (3.25), reads:

$$
\begin{aligned}
\langle \nu|\hat{G}_{\boldsymbol{k}}(t)|n\rangle = \langle \nu|\hat{G}_{\boldsymbol{k}}(t)|n\rangle|_{f=0} + \mathrm{e}^{-\nu^2 D_{\mathrm{rot}} t}\Bigg\{ & -f^2\frac{D_\parallel^2 k^2}{4D_{\mathrm{rot}}^2}\left(T^{1+2\nu}_{n^2-(\nu+1)^2}(t)+T^{1-2\nu}_{n^2-(\nu-1)^2}(t)\right)\delta_{\nu,n} \\
+\mathrm{i}f\frac{D_\parallel}{2}\left[-\tau_{1+2\nu}(t)+\frac{k^2}{D_{\mathrm{rot}}^2}\left(\bar{D}\left(T^0_{n^2-\nu^2}(t)+T^{1+2\nu}_0(t)\right)+\frac{D_a}{2}\left(T^{4(1+\nu)}_{n^2-(\nu+2)^2}(t)+T^{1-2\nu}_{n^2-(\nu-1)^2}(t)\right)\right)\right]k_-\delta_{\nu+1,n} \\
+\mathrm{i}f\frac{D_\parallel}{2}\left[-\tau_{1-2\nu}(t)+\frac{k^2}{D_{\mathrm{rot}}^2}\left(\bar{D}\left(T^0_{n^2-\nu^2}(t)+T^{1-2\nu}_0(t)\right)+\frac{D_a}{2}\left(T^{4(1-\nu)}_{n^2-(\nu-2)^2}(t)+T^{1+2\nu}_{n^2-(\nu+1)^2}(t)\right)\right)\right]k_+\delta_{\nu-1,n} \\
-\frac{f^2D_\parallel^2}{4D_{\mathrm{rot}}^2}\left[T^{1+2\nu}_{n^2-(\nu+1)^2}(t)k_-^2\delta_{\nu+2,n}+T^{1-2\nu}_{n^2-(\nu-1)^2}(t)k_+^2\delta_{\nu-2,n}\right] \\
+\mathrm{i}f\frac{D_\parallel D_a}{4D_{\mathrm{rot}}^2}\left[\left(T^{4(1+\nu)}_{n^2-(\nu+2)^2}(t)+T^{1+2\nu}_{n^2-(\nu+1)^2}(t)\right)k_-^3\delta_{\nu+3,n}+\left(T^{4(1-\nu)}_{n^2-(\nu-2)^2}(t)+T^{1-2\nu}_{n^2-(\nu-1)^2}(t)\right)k_+^3\delta_{\nu-3,n}\right]\Bigg\} \\
+\mathcal{O}\left(fk^5,f^2k^4,f^3k^3\right). \qquad \text{(B.1)}
\end{aligned}
$$

The scattering function, Eq. (3.26), then adds up to

$$\begin{aligned}
F_\nu(\boldsymbol{k},t|\vartheta_0) = F_\nu(\boldsymbol{k},t|\vartheta_0)|_{f=0} + \mathrm{e}^{-\nu^2 D_{\mathrm{rot}} t}\Bigg\{ & -f^2\frac{D_\parallel^2 k^2}{4D_{\mathrm{rot}}^2}\left(T^{1+2\nu}_{-2\nu-1}(t)+T^{1-2\nu}_{2\nu-1}(t)\right) \\
& + \mathrm{i}f\frac{D_\parallel}{2}\left[-\tau_{1+2\nu}(t)+\frac{k^2}{D_{\mathrm{rot}}^2}\left(\bar{D}\left(T^0_{1+2\nu}(t)+T^{1+2\nu}_0(t)\right)+\frac{D_a}{2}\left(T^{4(1+\nu)}_{-2\nu-3}(t)+T^{1-2\nu}_{4\nu}(t)\right)\right)\right]k_-\mathrm{e}^{\mathrm{i}\vartheta_0} \\
& + \mathrm{i}f\frac{D_\parallel}{2}\left[-\tau_{1-2\nu}(t)+\frac{k^2}{D_{\mathrm{rot}}^2}\left(\bar{D}\left(T^0_{1-2\nu}(t)+T^{1-2\nu}_0(t)\right)+\frac{D_a}{2}\left(T^{4(1-\nu)}_{2\nu-3}(t)+T^{1+2\nu}_{-4\nu}(t)\right)\right)\right]k_+\mathrm{e}^{-\mathrm{i}\vartheta_0} \\
& - \frac{f^2D_\parallel^2}{4D_{\mathrm{rot}}^2}\left[T^{1+2\nu}_{3+2\nu}(t)k_-^2\mathrm{e}^{\mathrm{i}2\vartheta_0}+T^{1-2\nu}_{3-2\nu}(t)k_+^2\mathrm{e}^{-\mathrm{i}2\vartheta_0}\right] \\
& + \mathrm{i}f\frac{D_\parallel D_a}{4D_{\mathrm{rot}}^2}\left[\left(T^{4(1+\nu)}_{5+2\nu}(t)+T^{1+2\nu}_{4(2+\nu)}(t)\right)k_-^3\mathrm{e}^{\mathrm{i}3\vartheta_0}+\left(T^{4(1-\nu)}_{5-2\nu}(t)+T^{1-2\nu}_{4(2-\nu)}(t)\right)k_+^3\mathrm{e}^{-\mathrm{i}3\vartheta_0}\right]\Bigg\} \\
& + \mathcal{O}\left(fk^5,f^2k^4,f^3k^3\right). \qquad \text{(B.2)}
\end{aligned}$$

For a specific value of ν, the preceding formula is simplified by inserting the explicit expression for the integrals $T^j_l(t)$ as given in Eq. (3.22). In case of $\nu=0$, the results is

$$\begin{aligned}
F(\boldsymbol{k},t|\vartheta_0) = 1 & - \bar{D}k^2t+\frac{\bar{D}^2}{2}t^2k^4+\frac{D_a}{2}\tau_4(t)\left(-1+\bar{D}tk^2\right)\left(k_-^2\mathrm{e}^{\mathrm{i}2\vartheta_0}+k_+^2\mathrm{e}^{-\mathrm{i}2\vartheta_0}\right) \\
& + \frac{D_a^2}{8D_{\mathrm{rot}}}\left[\left(t-\tau_4(t)\right)k^4+\frac{\tau_4(t)-\tau_{16}(t)}{6}\left(k_-^4\mathrm{e}^{\mathrm{i}4\vartheta_0}+k_+^4\mathrm{e}^{-\mathrm{i}4\vartheta_0}\right)\right] \\
& - \mathrm{i}f\frac{D_\parallel}{2}\tau_1(t)\left(k_-\mathrm{e}^{\mathrm{i}\vartheta_0}+k_+\mathrm{e}^{-\mathrm{i}\vartheta_0}\right)-\frac{f^2D_\parallel^2}{2D_{\mathrm{rot}}}\left(t-\tau_1(t)\right)k^2 \\
& + \mathrm{i}f\frac{D_\parallel}{2}k^2\left[\bar{D}t\tau_1(t)+\frac{D_a}{6D_{\mathrm{rot}}}\left(4\tau_1(t)-\tau_4(t)-3t\mathrm{e}^{-D_{\mathrm{rot}}t}\right)\right]\left(k_-\mathrm{e}^{\mathrm{i}\vartheta_0}+k_+\mathrm{e}^{-\mathrm{i}\vartheta_0}\right) \\
& - \frac{f^2D_\parallel^2}{12D_{\mathrm{rot}}}\left(\tau_1(t)-\tau_4(t)\right)\left(k_-^2\mathrm{e}^{\mathrm{i}2\vartheta_0}+k_+^2\mathrm{e}^{-\mathrm{i}2\vartheta_0}\right) \\
& + \mathrm{i}\frac{fD_\parallel D_a}{160D_{\mathrm{rot}}}\left(8\tau_4(t)-13\tau_9(t)+5\tau_1(t)\right)\left(k_-^3\mathrm{e}^{\mathrm{i}3\vartheta_0}+k_+^3\mathrm{e}^{-\mathrm{i}3\vartheta_0}\right) \\
& + \mathcal{O}\left(k^6,fk^5,f^2k^4,f^3k^3\right). \qquad \text{(B.3)}
\end{aligned}$$

B.2 Equivalence of Smoluchowski and Langevin formulation

The Smoluchowski-Perrin equation (3.2) can be rewritten in a standard formulation in two dimensions,

$$\partial_t\Psi = D_{\mathrm{rot}}\partial_\vartheta^2\Psi+\frac{1}{2}\sum_{i,j=1}^{2}\partial_i\partial_j\boldsymbol{B}_{ij}\Psi, \qquad \text{(B.4)}$$

with the matrix of the second jump moments

$$\boldsymbol{B} = 2\bar{D}\,\mathbb{1}+2D_a\begin{pmatrix}\cos 2\vartheta & \sin 2\vartheta\\ \sin 2\vartheta & -\cos 2\vartheta\end{pmatrix}. \qquad \text{(B.5)}$$

The indices i, j in Eq. (B.4) indicate the Cartesian components x, y. From this formulation one can read of the corresponding Langevin equation for the center of mass in textbooks [49, 153],

$$\partial_t \boldsymbol{r}(t) = \boldsymbol{\xi}(t), \tag{B.6a}$$

$$\left\langle \boldsymbol{\xi}(t)\boldsymbol{\xi}^{\mathsf{T}}(t') \right\rangle = \boldsymbol{B}\,\delta(t-t'). \tag{B.6b}$$

The matrix $\boldsymbol{B}$ can be diagonalized by the rotation matrix $\boldsymbol{S}$ given in Eq. (3.70). Then, a multiplication of Eq. (B.6a) with $\boldsymbol{S}^{-1}$ from the lefthand side results in the body frame equations (3.64).

To obtain the correct Smoluchowski-Perrin equation including a force that acts longitudinal to the orientation of the rod we rewrite the Langevin equations in the space-fixed frame by multiplying Eqs. (3.71) and (3.64b) with $\boldsymbol{S}$ from the lefthand side,

$$\boldsymbol{S}\cdot\partial_t \begin{pmatrix} r_\parallel(t) \\ r_\perp(t) \end{pmatrix} = \partial_t \boldsymbol{r}(t) = f D_\parallel^0 \boldsymbol{u}(t) + \boldsymbol{\xi}(t), \tag{B.7}$$

with the same noise correlation as already given in Eq. (B.6b). Thus the diffusion term in the corresponding Smoluchowski-Perrin equation equals that of Eq. (B.4), and we have one additional drift term:

$$\partial_t \Psi = -f D_\parallel^0 \boldsymbol{u}\cdot\partial_{\boldsymbol{R}}\Psi + \frac{1}{2}\sum_{i,j=1}^{2} \partial_i \partial_j \boldsymbol{B}_{ij}\Psi. \tag{B.8}$$

B.3 Varying the microscopic ratio of the diffusion coefficients

In Sec. 4.3, Fig. 4.8, we have shown data for the density dependence of diffusion coefficients. Cobb and Butler [23] have proposed that the power law approached for $n^* \gg 1$ depends on the ratio of the microscopic diffusion constants, $L^2 D_{\mathrm{rot}}^0 / D_{\mathrm{cm}}^0$. We have tested the validity of this conjecture, since it is in severe contradiction to the predictions of the tube theory of Doi and Edwards [31]. Our data strongly disagrees with the proposal of Cobb and Butler, as seen in Fig. B.1. Instead, the power law of the tube theory is preserved, and the conjecture of Cobb and Butler can be attributed to an insufficient range of simulated densities.

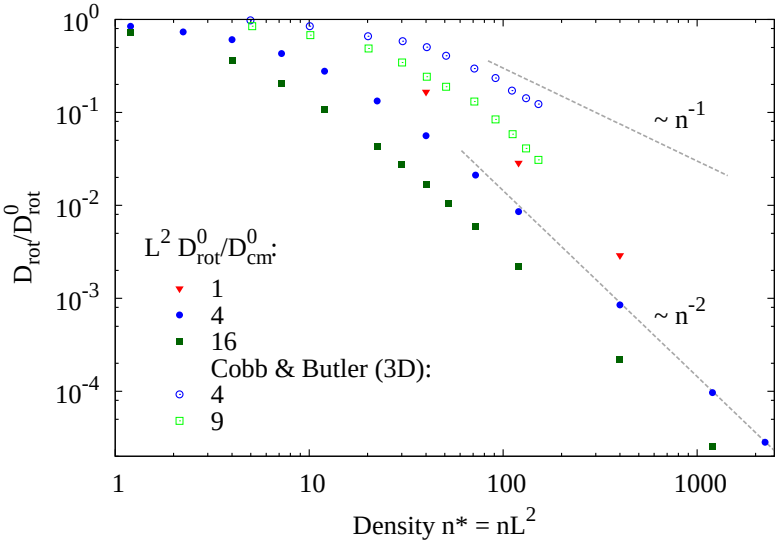

Figure B.1: Density dependence of the rotational diffusion coefficient, for different ratios $L^2 D_{\mathrm{rot}}^0 / D_{\mathrm{cm}}^0$, with $D_{\mathrm{cm}}^0 = D_\parallel + D_\perp^0$. Our data prove that the asymptotic power law $D_{\mathrm{rot}} \sim n^{-2}$ is independent of the ratio $L^2 D_{\mathrm{rot}}^0 / D_{\mathrm{cm}}^0$ within the simulated parameter range. The conjecture of Cobb and Butler [23] that the exponent approaches 1 for small ratios cannot be supported.

Appendix C

Supplementary material for the dynamics of a semiflexible polymer

C.1 The Stochastic integration

Stochastic equations are of Stratonovich type when the white noise they imply constitutes an approximation to a noise with finite correlation time. This seems to apply to us, since physically realistic random forces are never completely uncorrelated. However, this is not the only criterion for the decision, we also have to grasp correctly the physical relationship between the stochastic variable $\boldsymbol{r}$ and the noise $\boldsymbol{\xi}$ present in our specific system [153]. The term we have to decide about is the mobility $\mathscr{P}$, since it multiplies the noise in Eq. (5.7). Its physical meaning is to separate locally the velocity of the filament into a component parallel to its local tangent and another perpendicular to it. This separation will always refer to the current conformation and velocity of the space curve *at that very moment of time*; it will be unaffected by any stochastic forces in the future. This amounts to the definition of a nonanticipating function [49], and is equivalent to the demand to interpret the noise according to Ito.

C.2 Eigenfunctions

The normalized biharmonic eigenfunctions obeying the boundary conditions of Eqs. (5.9) and (5.10) are

$$w^0 = 1\,, \tag{C.1}$$

$$w^i = \frac{\cos k_i - \cosh k_i}{\sin k_i - \sinh k_i}\left(\cos\frac{k_i}{L}s + \cosh\frac{k_i}{L}s\right) + \sin\frac{k_i}{L}s - \sinh\frac{k_i}{L}s\,, \tag{C.2}$$

$$w_0 = 6\frac{s}{L}\left(1-\frac{s}{L}\right), \tag{C.3}$$

$$w_i = \frac{\cos k_i - \cosh k_i}{\sin k_i - \sinh k_i}\left(\cos\frac{k_i}{L}s - \cosh\frac{k_i}{L}s\right) + \sin\frac{k_i}{L}s + \sinh\frac{k_i}{L}s\,. \tag{C.4}$$

They are biorthonormal,

$$\int_0^L \mathrm{d}s\, w^\alpha w_\beta = L\delta^\alpha_\beta. \tag{C.5}$$

A useful property of these eigenfunctions is

$$w^{\alpha\prime\prime} = -k_\alpha^2/L^2\, w_\alpha, \qquad w''_\alpha = -\tilde{k}_\alpha^2/L^2\, w^\alpha.$$

Here, $\tilde{k}_0^2 \equiv 12$, and $\tilde{k}_i \equiv k_i$.

Appendix D

List of publications

Parts of the material of this thesis have been published or prepared for publishing in the following journals:

[D.1] T. Munk, O. Hallatschek, C. H. Wiggins, and E. Frey. Dynamics of semiflexible polymers in a flow field. *Phys. Rev. E*, 74(4):041911, 2006. URL http://link.aps.org/abstract/PRE/v74/e041911.

Contains most parts of Chapter 5.

[D.2] F. Höfling, T. Munk, E. Frey, and T. Franosch. Critical dynamics of ballistic and Brownian particles in a heterogeneous environment. *J. Chem. Phys.*, 128(16):164517, 2008. URL http://link.aip.org/link/?JCP/128/164517/1.

Chapter 3 constitutes the main part of this publication.

[D.3] F. Höfling, T. Munk, E. Frey, and T. Franosch. Entangled dynamics of a stiff polymer. *Phys. Rev. E*, 77(6):060904(R), 2008. URL http://link.aps.org/abstract/PRE/v77/e060904.

Contains Secs. 4.1 and 4.3. The supplementary material available online furthermore offers a movie that visualizes on three different length and time scales the constrained motion of a rod in a semi-dilute environment of point obstacles.

[D.4] T. Munk, F. Höfling, E. Frey, and T. Franosch. Effective Perrin theory for the anisotropic diffusion of a strongly hindered rod. arXiv:0808.0450 [cond-mat.soft], 2008. URL http://arxiv.org/abs/0808.0450. Submitted to Europhys. Lett.

Contains parts of Chapter 3 and of Secs. 4.4–4.6.

Bibliography

[1] T. Abete, A. de Candia, E. D. Gado, A. Fierro, and A. Coniglio. Static and dynamic heterogeneities in a model for irreversible gelation. *Phys. Rev. Lett.*, 98(8):088301, 2007. URL http://link.aps.org/abstract/PRL/v98/e088301. Page(s) 7

[2] M. Abramowitz and I. A. Stegun. *Pocketbook of Mathematical Functions*. Harri Deutsch, Frankfurt/Main, 1984. Page(s) 28, 29

[3] M. P. Allen. Diffusion coefficient increases with density in hard ellipsoid liquid crystals. *Phys. Rev. Lett.*, 65(23):2881–2884, 1990. URL http://link.aps.org/abstract/PRL/v65/p2881. Page(s) 21

[4] W. E. Alley. *Studies in molecular dynamics of the friction coefficient and the Lorentz gas*. PhD thesis, California Univ., Davis, 1979. Page(s) 12

[5] S. R. Aragón and R. Pecora. General theory of dynamic light scattering from cylindrically symmetric particles with translational-rotational coupling. *J. Chem. Phys.*, 82(12):5346–5353, 1985. URL http://link.aip.org/link/?JCP/82/5346/1. Page(s) 22, 65

[6] M. Arrio-Dupont, G. Foucault, M. Vacher, P. F. Devaux, and S. Cribier. Translational diffusion of globular proteins in the cytoplasm of cultured muscle cells. *Biophys. J.*, 78(2):901–907, 2000. URL http://www.biophysj.org/cgi/content/abstract/78/2/901. Page(s) 7

[7] F. M. Arscott. *Periodic Differential Equations*. Pergamon Press, 1964. Page(s) 28

[8] G. K. Batchelor. Slender-body theory for particles of arbitrary cross-section in stokes flow. *J. Fluid Mech.*, 44(3):419–440, 1970. URL http://journals.cambridge.org/action/displayAbstract?aid=383506. Page(s) 69

[9] L. E. Becker and M. J. Shelley. Instability of elastic filaments in shear flow yields first-normal-stress differences. *Phys. Rev. Lett.*, 87(19):198301, 2001. URL http://link.aps.org/abstract/PRL/v87/e198301. Page(s) 68

[10] D. ben Avraham and S. Havlin. *Diffusion and Reactions in Fractals and Disordered Systems*. Cambridge University Press, Cambridge, 2000. Page(s) 10, 16

[11] B. J. Berne and R. Pecora. *Dynamic Light Scattering*. John Wiley and Sons, New York, 1976. Page(s) 22, 23

[12] B. Bhaduri, A. Neild, and T. W. Ng. Directional brownian diffusion dynamics with variable magnitudes. *Appl. Phys. Lett.*, 92(8):084105, 2008. URL http://link.aip.org/link/?APL/92/084105/1. Page(s) 21

[13] B. Bird, C. Curtiss, R. Armstrong, and O. Hassager. *Dynamics of Polymeric Liquids*, volume 2. John Wiley & Sons, New York, 1987. Page(s) 67

[14] I. Bitsanis, H. T. Davis, and M. Tirrell. Brownian dynamics of nondilute solutions of rodlike polymers. 2. High concentrations. *Macromol.*, 23(4):1157–1165, 1990. URL http://pubs3.acs.org/acs/journals/doilookup?in_doi=10.1021/ma00206a039. Page(s) 21, 41

[15] Y. Bohbot-Raviv, W. Z. Zhao, M. Feingold, C. H. Wiggins, and R. Granek. Relaxation dynamics of semiflexible polymers. *Phys. Rev. Lett.*, 92(9):098101, 2004. URL http://link.aps.org/abstract/PRL/v92/e098101. Page(s) 67

[16] J. P. Boon and S. Yip. *Molecular Hydrodynamics*. Dover Publications, Inc., New York, 1991. Reprint, Page(s) 17

[17] J. Bouchaud and A. Georges. Anomalous diffusion in disordered media: Statistical mechanisms, models and physical applications. *Phys. Rep.*, 195(4-5):127–293, 1990. URL http://dx.doi.org/10.1016/0370-1573(90)90099-N. Page(s) 8, 9

[18] F. Brauer. Correction to "On the completeness of biorthogonal systems". *Michigan Math. J.*, 12(1):127–128, 1965. URL http://projecteuclid.org/euclid.mmj/1028999253. Page(s) 71

[19] C. Bruin. Logarithmic terms in the diffusion coefficient for the Lorentz gas. *Phys. Rev. Lett.*, 29(25):1670–1674, 1972. URL http://link.aps.org/abstract/PRL/v29/p1670. Page(s) 11

[20] C. Bustamante, Z. Bryant, and S. Smith. Ten years of tension: single-molecule DNA mechanics. *Nature*, 421:423–427, 2003. URL http://www.nature.com/nature/journal/v421/n6921/full/nature01405.html. Page(s) 67

[21] A. Caspi, R. Granek, and M. Elbaum. Diffusion and directed motion in cellular transport. *Phys. Rev. E*, 66(1):011916, 2002. URL http://link.aps.org/abstract/PRE/v66/e011916. Page(s) 7

[22] M. Chertkov, I. Kolokolov, V. Lebedev, and K. Turitsyn. Polymeric statistics in a random flow with mean shear. *J. Fluid Mech.*, 531:251–260, 2005. URL http://journals.cambridge.org/action/displayAbstract?aid=304358. Page(s) 77

[23] P. D. Cobb and J. E. Butler. Simulations of concentrated suspensions of rigid fibers: Relationship between short-time diffusivities and the long-time rotational diffusion. *J. Chem. Phys.*, 123(5):054908, 2005. URL http://link.aip.org/link/?JCP/123/054908/1. Page(s) 21, 41, 95

[24] A. Cortis and B. Berkowitz. Anomalous transport in "classical" soil and sand columns. *Soil Sci. Soc. Am. J.*, 68(5):1539–1548, 2004. URL http://soil.scijournals.org/cgi/content/abstract/soilsci;68/5/1539. Page(s) 7

[25] R. Courant and D. Hilbert. *Methoden der Mathematischen Physik I.* Springer, Berlin, 3rd edition, 1967. Page(s) 71

[26] R. Cush, D. Dorman, and P. S. Russo. Rotational and translational diffusion of tobacco mosaic virus in extended and globular polymer solutions. *Macromol.*, 37(25):9577–9584, 2004. URL http://pubs3.acs.org/acs/journals/doilookup?in_doi=10.1021/ma0490294. Page(s) 21

[27] P. G. de Gennes. Reptation of a polymer chain in the presence of fixed obstacles. *J. Chem. Phys.*, 55(2):572–579, 1971. URL http://link.aip.org/link/?JCP/55/572/1. Page(s) 40

[28] E. Del Gado, L. de Arcangelis, and A. Coniglio. Viscosity critical behaviour at the gel point in a 3d lattice model. *Eur. Phys. J. E*, 2(4):359–365, 2000. URL http://dx.doi.org/10.1007/s101890050018. Page(s) 7

[29] P. Dhar, T. Fischer, Y. Wang, T. Mallouk, W. Paxton, and A. Sen. Autonomously moving nanorods at a viscous interface. *Nano Letters*, 6(1):66–72, 2006. URL http://pubs3.acs.org/acs/journals/doilookup?in_doi=10.1021/nl052027s. Page(s) 25, 54

[30] M. Doi and S. F. Edwards. Dynamics of rod-like macromolecules in concentrated solution. Part 1. *J. Chem. Soc., Faraday Trans. 2*, 74:560–570, 1978. URL http://www.rsc.org/Publishing/Journals/F2/article.asp?doi=F29787400560. Page(s) 39, 45

[31] M. Doi and S. F. Edwards. *The Theory of Polymer Dynamics*. Oxford University Press, Oxford, 1986. Page(s) 22, 30, 33, 39, 43, 67, 68, 69, 70, 76, 95

[32] M. Doi, I. Yamamoto, and F. Kano. Monte carlo simulation of the dynamics of thin rodlike polymers in concentrated solution. *J. Phys. Soc. Jpn.*, 53(9):3000–3003, 1984. URL http://jpsj.ipap.jp/link?JPSJ/53/3000/. Page(s) 45

[33] S. F. Edwards. The statistical mechanics of polymerized material. *Proc. Phys. Soc.*, 92(1):9–16, 1967. URL http://stacks.iop.org/0370-1328/92/9. Page(s) 40

[34] A. Einstein. Über die von der molekularinetischen Theorie der Wärme geforderte Bewegung von in ruhenden Flüssigkeiten suspendierten Teilchen. *Ann. Phys. (Leipzig)*, 17:549–560, 1905. Page(s) 22

[35] W. T. Elam, A. R. Kerstein, and J. J. Rehr. Critical properties of the void percolation problem for spheres. *Phys. Rev. Lett.*, 52:1516, 1984. URL http://link.aps.org/abstract/PRL/v52/p1516. Page(s) 10, 15, 16

[36] R. J. Ellis. Macromolecular crowding: obvious but underappreciated. *Trends Biochem. Sci.*, 26(10):597–604, 2001. URL http://www.sciencedirect.com/science/article/B6TCV-443JM41-H/2/d5fab5a5de408097f610e9f0a6e32156. Page(s) 7

[37] R. J. Ellis. Macromolecular crowding: an important but neglected aspect of the intracellular environment. *Curr. Opin. Struct. Biol.*, 11(1):114–119, 2001. URL http://www.sciencedirect.com/science/article/B6VS6-42BSR81-M/2/3fe3b90f897d5c5598856064169a6511. Page(s) 7

[38] D. Ermak and J. McCammon. Brownian dynamics with hydrodynamic interactions. *J. Chem. Phys.*, 69(4):1352–1360, 1978. URL http://link.aip.org/link/?JCPSA6/69/1352/1. Page(s) 68

[39] M. H. Ernst and A. Weijland. Long time behaviour of the velocity auto-correlation function in a Lorentz gas. *Phys. Lett. A*, 34:39, 1971. URL http://dx.doi.org/10.1016/0375-9601(71)90987-X. Page(s) 9

[40] R. Everaers, F. Jülicher, A. Ajdari, and A. C. Maggs. Dynamic fluctuations of semiflexible filaments. *Phys. Rev. Lett.*, 82(18):3717–3720, 1999. URL http://link.aps.org/abstract/PRL/v82/p3717. Page(s) 68, 75

[41] M. Fixman. Classical statistical mechanics of constraints: A theorem and application to polymers. *Proc. Natl. Acad. Sci.*, 71(8):3050–3053, 1974. URL http://www.pubmedcentral.nih.gov/articlerender.fcgi?artid=388618. Page(s) 70

[42] M. Fixman. Simulation of polymer dynamics. I. General theory. *J. Chem. Phys.*, 69(4):1527–1537, 1978. URL http://link.aip.org/link/?JCP/69/1527/1. Page(s) 68, 70

[43] D. Frenkel and J. F. Maguire. Molecular Dynamics study of infinitely thin hard rods: Scaling behavior of transport properties. *Phys. Rev. Lett.*, 47(15):1025–1028, 1981. URL http://link.aps.org/abstract/PRL/v47/p1025. Page(s) 45

[44] D. Frenkel and J. F. Maguire. Molecular Dynamics study of the dynamical properties of an assembly of infinitely thin hard rods. *Mol. Phys.*, 49(3):503–541, 1983. URL http://www.informaworld.com/10.1080/00268978300101331. Page(s) 45

[45] D. Frenkel and B. J. Smit. *Understanding Molecular Simulation*. Academic Press, London, 2 edition, 2001. Page(s) 11

[46] E. Frey and K. Kroy. Brownian motion: a paradigm of soft matter and biological physics. *Ann. Phys. (Leipzig)*, 14(1-3):20–50, 2005. URL http://dx.doi.org/10.1002/andp.200410132. Page(s) 8, 69

[47] E. Frey and D. R. Nelson. Dynamics of flat membranes and flickering in red blood cells. *Journal de Physik I (France)*, 1(12):1715–1757, 1991. URL http://dx.doi.org/10.1051/jp1:1991238. Page(s) 69

[48] M. L. Gardel, J. H. Shin, F. C. MacKintosh, L. Mahadevan, P. A. Matsudaira, and D. A. Weitz. Scaling of F-actin network rheology to probe single filament elasticity and dynamics. *Phys. Rev. Lett.*, 93(18):188102, 2004. URL http://link.aps.org/abstract/PRL/v93/e188102. Page(s) 67

[49] C. W. Gardiner. *Handbook of Stochastic Methods*. Springer, Berlin, 2004. Page(s) 70, 95, 97

[50] S. Gerashchenko and V. Steinberg. Statistics of tumbling of a single polymer molecule in shear flow. *Phys. Rev. Lett.*, 96:038304, 2006. URL http://link.aps.org/abstract/PRL/v96/e038304. Page(s) 68, 77

[51] F. Gittes and F. C. MacKintosh. Dynamic shear modulus of a semiflexible polymer network. *Phys. Rev. E*, 58(2):R1241–R1244, 1998. URL http://link.aps.org/abstract/PRE/v58/pR1241. Page(s) 77, 78

[52] T. Gleim, W. Kob, and K. Binder. How does the relaxation of a supercooled liquid depend on its microscopic dynamics? *Phys. Rev. Lett.*, 81(20):4404–4407, 1998. URL http://link.aps.org/abstract/PRL/v81/p4404. Page(s) 8

[53] I. Golding and E. C. Cox. Physical nature of bacterial cytoplasm. *Phys. Rev. Lett.*, 96(9):098102, 2006. URL http://link.aps.org/abstract/PRL/v96/e098102. Page(s) 7

[54] R. E. Goldstein and S. A. Langer. Nonlinerar dynamics of stiff polymers. *Phys. Rev. Lett.*, 75 (5):1094, 1995. URL http://link.aps.org/abstract/PRL/v75/p1094. Page(s) 70

[55] W. Götze, E. Leutheusser, and S. Yip. Dynamical theory of diffusion and localization in a random, static field. *Phys. Rev. A*, 23:2634, 1981. URL http://link.aps.org/abstract/PRA/v23/p2634. Page(s) 9, 10

[56] W. Götze, E. Leutheusser, and S. Yip. Correlation functions of the hard-sphere Lorentz model. *Phys. Rev. A*, 24:1008, 1981. URL http://link.aps.org/abstract/PRA/v24/p1008. Page(s) 9, 10

[57] R. Granek. From semi-flexible polymers to membranes: Anomalous diffusion and reptation. *J. Phys. II France*, 7:1761–1788, 1997. URL http://dx.doi.org/10.1051/jp2:1997214. Page(s) 75

[58] P. Grassia and E. J. Hinch. Computer simulations of polymer chain relaxation via brownian motion. *J. Fluid Mech.*, 308:255–288, 1996. URL http://dx.doi.org/10.1017/S0022112096001474. Page(s) 68

[59] G. Guigas, C. Kalla, and M. Weiss. Probing the nanoscale viscoelasticity of intracellular fluids in living cells. *Biophys. J.*, 93(1):316–323, 2007. URL http://www.biophysj.org/cgi/content/abstract/93/1/316. Page(s) 7

[60] D. Hall and A. P. Minton. Macromolecular crowding: qualitative and semiquantitative successes, quantitative challenges. *BBA-Proteins Proteom*, 1649(2):127–139, 2003. URL http://www.sciencedirect.com/science/article/B73DJ-48KVYVM-1/2/554623fd1e0adbdc1e757bc6200e44d7. Page(s) 7

[61] O. Hallatschek, E. Frey, and K. Kroy. Overdamped stress relaxation in buckled rods. *Phys. Rev. E*, 70:031802, 2004. URL http://link.aps.org/abstract/PRE/v70/e031802. Page(s) 67

[62] O. Hallatschek, E. Frey, and K. Kroy. Propagation and relaxation of tension in stiff polymers. *Phys. Rev. Lett.*, 94:077804, 2005. URL http://link.aps.org/abstract/PRL/v94/e077804. Page(s) 67

[63] B. I. Halperin, S. Feng, and P. N. Sen. Differences between lattice and continuum percolation transport exponents. *Phys. Rev. Lett.*, 54:2391–2394, 1985. URL http://link.aps.org/abstract/PRL/v54/p2391. Page(s) 16

[64] Y. Han, A. M. Alsayed, M. Nobili, J. Zhang, T. C. Lubensky, and A. G. Yodh. Brownian motion of an ellipsoid. *Science*, 314(5799):626–630, 2006. URL http://www.sciencemag.org/cgi/content/abstract/314/5799/626. Page(s) 21, 27, 33

[65] P. Hänggi and F. Marchesoni. Introduction: 100 years of Brownian motion. *Chaos*, 15:026101, 2005. URL http://link.aip.org/link/?CHAOEH/15/026101/1. Page(s) 8

[66] E. R. Hansen. *Global optimization using interval analysis*. Dekker, New York, 1992. Page(s) 41

[67] C. Heussinger, M. Bathe, and E. Frey. Statistical mechanics of semiflexible bundles of wormlike polymer chains. *Phys. Rev. Lett.*, 99(4):048101, 2007. URL http://link.aps.org/abstract/PRL/v99/e048101. Page(s) 81

[68] E. J. Hinch. Brownian motion with stiff bonds and rigid constraints. *J. Fluid Mech.*, 271: 219–234, 1994. URL http://journals.cambridge.org/action/displayAbstract?aid=352738. Page(s) 68, 70

[69] F. Höfling. *Dynamics of Rod-Like Macromolecules in Heterogeneous Materials*. PhD thesis, Ludwig-Maximilians-Universität München, München, 2006. ISBN 978-3-86582-426-4, Page(s) 10, 19, 41, 45, 46

[70] F. Höfling and T. Franosch. Crossover in the slow decay of dynamic correlations in the Lorentz model. *Phys. Rev. Lett.*, 98(14):140601, 2007. URL http://link.aps.org/abstract/PRL/v98/e140601. Page(s) 9

[71] F. Höfling, E. Frey, and T. Franosch. Dynamics of an entangled needle with constraint release. in preparation, Page(s) 49

[72] F. Höfling, T. Franosch, and E. Frey. Localization transition of the three-dimensional Lorentz model and continuum percolation. *Phys. Rev. Lett.*, 96:165901, 2006. URL http://link.aps.org/abstract/PRL/v96/e165901. Page(s) 7, 10, 16, 17, 18, 19, 20

[73] F. Höfling, E. Frey, and T. Franosch. Enhanced diffusion of a needle in a planar array of point obstacles. *Phys. Rev. Lett.*, 101(12):120605, 2008. URL http://link.aps.org/abstract/PRL/v101/e120605. Page(s) 21

[74] T. Hofmann, R. G. Winkler, and P. Reineker. Dynamics of a polymer chain in an elongational flow. *Phys. Rev. E*, 61(3):2840, 2000. URL http://link.aps.org/abstract/PRE/v61/p2840. Page(s) 68

[75] J. L. Höög, C. Schwartz, A. T. Noon, E. T. O'Toole, D. N. Mastronarde, J. R. McIntosh, and C. Antony. Organization of interphase microtubules in fission yeast analyzed by electron tomography. *Developmental Cell*, 12(3):349–361, 2007. URL http://www.sciencedirect.com/science/article/B6WW3-4N688G9-8/2/62a94ec2272978ae588a914e35126ad9. Page(s) 4

[76] J. Hur and E. S. Shaqfeh. Brownian dynamics simulations of single DNA molecules in shear flow. *J. Rheol.*, 44(4):713, 2000. URL http://dx.doi.org/10.1122/1.551115. Page(s) 68, 77, 78

[77] M. E. Kainourgiakis, E. S. Kikkinides, A. K. Stubos, and N. K. Kanellopoulos. Simulation of self-diffusion of point-like and finite-size tracers in stochastically reconstructed vycor porous glasses. *J. Chem. Phys.*, 111(6):2735–2743, 1999. URL http://link.aip.org/link/?JCP/111/2735/1. Page(s) 7

[78] M. E. Kainourgiakis, E. S. Kikkinides, A. Galani, G. C. Charalambopoulou, and A. K. Stubos. Digitally reconstructed porous media: Transport and sorption properties. *Transp. in Porous Med.*, 58(1):43–62, 2005. URL http://dx.doi.org/10.1007/s11242-004-5469-1. Page(s) 7

[79] J. Käs, H. Strey, and E. Sackmann. Direct imaging of reptation for semiflexible actin filaments. *Nature*, 368(6468):226–229, 1994. URL http://dx.doi.org/10.1038/368226a0. Page(s) 40, 49

[80] J. Kertész. Percolation of holes between overlapping spheres: Monte carlo calculation of the critical volume fraction. *J. Phys. (Paris)*, 42:L 393, 1981. Page(s) 15

[81] J. Kertész and J. Metzger. Properties of the density relaxation function in classical diffusion models with percolation transition. *J. Phys. A*, 16:L735–L739, 1983. Page(s) 10

[82] I. C. Kim and S. Torquato. Diffusion of finite-sized Brownian particles in porous media. *J. Chem. Phys.*, 96(2):1498–1503, 1992. URL http://link.aip.org/link/?JCP/96/1498/1. Page(s) 7

[83] T. Kirchhoff, H. Löwen, and R. Klein. Dynamical correlations in suspensions of charged rodlike macromolecules. *Phys. Rev. E*, 53(5):5011–5022, 1996. URL http://link.aps.org/abstract/PRE/v53/p5011. Page(s) 21

[84] P. Kloeden and E. Platen. *Numerical Solution of Stochastic Differential Equations*. Springer, Berlin, 1995. Page(s) 33, 74

[85] W. Kob, C. Donati, S. J. Plimpton, P. H. Poole, and S. C. Glotzer. Dynamical heterogeneities in a supercooled lennard-jones liquid. *Phys. Rev. Lett.*, 79(15):2827–2830, 1997. URL http://link.aps.org/abstract/PRL/v79/p2827. Page(s) 17

[86] S. Köster, D. Steinhauser, and T. Pfohl. Brownian motion of actin filaments in confining microchannels. *J. Phys. Cond. Mat.*, 17:S4091–S4104, 2005. Page(s) 84

[87] O. Kratky and G. Porod. Röntgenuntersuchung gelöster Fadenmoleküle. *Rec. Trav. Chim.*, 68:1106–1122, 1949. Page(s) 68, 74

[88] K. Kroy and E. Frey. Force-extension relation and plateau modulus for wormlike chains. *Phys. Rev. Lett.*, 77(2):306–309, 1995. URL http://link.aps.org/abstract/PRL/v77/p306. Page(s) 67

[89] K. Kroy and E. Frey. Dynamic scattering from solutions of semiflexible polymers. *Phys. Rev. E*, 55(3):3092, 1997. URL http://link.aps.org/abstract/PRE/v55/p3092. Page(s) 67

[90] K. Kroy and E. Frey. *Scattering in Polymeric and Colloidal Systems*, chapter 5: Dynamic Scattering from Semiflexible Polymers. Edited by Wyn Brown and Kell Mortensen. Gordon and Breach, 2000 69

[91] J. Käs, H. Strey, J. Tang, D. Finger, R. Ezzell, E. Sackmann, and P. Janmey. F-actin, a model polymer for semiflexible chains in dilute, semidilute, and liquid crystalline solutions. *Biophys. J.*, 70:609–625, 1996. Page(s) 67

[92] L. D. Landau and E. M. Lifschitz. *Lehrbuch der theoretischen Physik, Band V, Statistische Physik (Teil I)*. Akademie Verlag, Berlin, 1987. Page(s) 69

[93] L. D. Landau and E. M. Lifschitz. *Lehrbuch der theoretischen Physik, Band VII, Elastizitätstheorie*. Akademie Verlag, Berlin, 1991. Page(s) 71

[94] L. Le Goff, F. Amblard, and E. M. Furst. Motor-driven dynamics in actin-myosin networks. *Phys. Rev. Lett.*, 88(1):018101, 2002. URL http://link.aps.org/abstract/PRL/v88/e018101. Page(s) 75

[95] L. Le Goff, O. Hallatschek, E. Frey, and F. Amblard. Tracer studies on F-actin fluctuations. *Phys. Rev. Lett.*, 89(25):258101, 2002. URL http://link.aps.org/abstract/PRL/v89/e258101. Page(s) 67, 75, 76

[96] M. P. Lettinga and E. Grelet. Self-diffusion of rodlike viruses through smectic layers. *Phys. Rev. Lett.*, 99(19):197802, 2007. URL http://link.aps.org/abstract/PRL/v99/e197802. Page(s) 21

[97] M. P. Lettinga, E. Barry, and Z. Dogic. Self-diffusion of rod-like viruses in the nematic phase. *Europhys. Lett.*, 71(4):692–698, 2005. URL http://stacks.iop.org/0295-5075/71/692. Page(s) 21

[98] H. A. Lorentz. Le mouvement des electrons dans les metaux. *Arch. Néerl. Sci. Exact Natur.*, 10:336–370, 1905. Page(s) 9

[99] C. D. Lorenz and R. M. Ziff. Precise determination of the bond percolation thresholds and finite-size scaling corrections for the sc, fcc, and bcc lattices. *Phys. Rev. E*, 57:230–236, 1998. Page(s) 19

[100] C. P. Lowe and A. J. Masters. The long-time behaviour of the velocity autocorrelation function in a Lorentz gas. *Physica A*, 195(1-2):149–162, 1993. URL http://www.sciencedirect.com/science/article/B6TVG-46X9KCC-55/2/5aa7b0dcc901d714e7f3d8add885272f. Page(s) 9

[101] H. Löwen. Anisotropic self-diffusion in colloidal nematic phases. *Phys. Rev. E*, 59(2):1989–1995, 1999. Page(s) 21

[102] K. Luby-Phelps, P. E. Castle, D. L. Taylor, and F. Lanni. Hindered diffusion of inert tracer particles in the cytoplasm of mouse 3T3 cells. *Proc. Natl. Acad. Sci. USA*, 84(14):4910–4913, 1987. URL http://www.pnas.org/cgi/content/abstract/84/14/4910. Page(s) 7

[103] D. Lumma, S. Keller, T. Vilgis, and J. O. Rädler. Dynamics of large semiflexible chains probed by fluorescence correlation spectroscopy. *Phys. Rev. Lett.*, 90(21):218301, 2003. URL http://link.aps.org/abstract/PRL/v90/e218301. Page(s) 67

[104] J. Machta and S. M. Moore. Diffusion and long-time tails in the overlapping Lorentz gas. *Phys. Rev. A*, 32:3164, 1985. Page(s) 10, 15, 16

[105] H. Maeda and Y. Maeda. Direct observation of brownian dynamics of hard colloidal nanorods. *Nano Letters*, 7(11):3329–3335, 2007. URL http://pubs3.acs.org/acs/journals/doilookup?in_doi=10.1021/nl071577i. Page(s) 2

[106] J. J. Magda, H. T. Davis, and M. Tirrell. The transport properties of rod-like particles via molecular dynamics. I. Bulk fluid. *J. Chem. Phys.*, 85(11):6674–6685, 1986. URL http://link.aip.org/link/?JCP/85/6674/1. Page(s) 45

[107] B. Maier and J. O. Rädler. Conformation and self-diffusion of single DNA molecules confined to two dimensions. *Phys. Rev. Lett.*, 82:1911–1914, 1999. URL http://link.aps.org/abstract/PRL/v82/p1911. Page(s) 67, 70

[108] A. Masters and T. Keyes. Diffusion, percolation, and trapping in the Lorentz gas via variational kinetic theory. *Phys. Rev. A*, 26:2129, 1982. Page(s) 10

[109] A. Meyer, J. Horbach, W. Kob, F. Kargl, and H. Schober. Channel formation and intermediate range order in sodium silicate melts and glasses. *Phys. Rev. Lett.*, 93(2):027801, 2004. URL http://link.aps.org/abstract/PRL/v93/e027801. Page(s) 7

[110] R. Miller, A. Presley, and M. Francis. Self-assembling light-harvesting systems from synthetically modified tobacco mosaic virus coat proteins. *J. Am. Chem. Soc.*, 129(11):3104–3109, 2007. URL http://pubs3.acs.org/acs/journals/doilookup?in_doi=10.1021/ja063887t. Page(s) 2

[111] A. Montesi, D. C. Morse, and M. Pasquali. Brownian dynamics algorithm for bead-rod semiflexible chain with anisotropic friction. *J. Chem. Phys.*, 122:084903, 2005. Page(s) 68, 70, 77

[112] A. Moreno. Simulations of a 2D Lorentz gas of soft disks. priv. comm., 2004, Page(s) 20

[113] A. J. Moreno and W. Kob. Dynamics of a rigid rod in a glassy medium. *Europhys. Lett.*, 67(5):820–826, 2004. URL http://stacks.iop.org/0295-5075/67/820. Page(s) 45

[114] D. C. Morse. Theory of constrained brownian motion. *Adv. Chem. Phys.*, 128:65–189, 2004. Page(s) 68

[115] D. C. Morse. Viscoelasticity of tightly entangled solutions of semiflexible polymers. *Phys. Rev. E*, 58(2):R1237, 1998. Page(s) 77, 78

[116] D. Mukhija and M. J. Solomon. Translational and rotational dynamics of colloidal rods by direct visualization with confocal microscopy. *J. Coll. Interf. Science*, 314(1):98–106, 2007. Page(s) 21

[117] B. Obermayer, O. Hallatschek, E. Frey, and K. Kroy. Stretching dynamics of semiflexible polymers. *Europ. Phys. J. E*, 23(4):375–388, 2007. URL http://dx.doi.org/10.1140/epje/i2006-10221-y. Page(s) 68

[118] L. Onsager. The effects of shape on the interaction of colloidal particles. *Ann. N. Y Acad. Sci.*, 51:627–659, 1949. URL http://dx.doi.org/10.1111/j.1749-6632.1949.tb27296.x. Page(s) 21

[119] M. Otto, T. Aspelmeier, and A. Zippelius. Microscopic dynamics of thin hard rods. *J. Chem. Phys.*, 124(15):154907, 2006. URL http://link.aip.org/link/?JCP/124/154907/1. Page(s) 21, 45, 51, 65

[120] F. Pampaloni, G. Lattanzi, A. Jonáš, T. Surrey, E. Frey, and E.-L. Florin. Thermal fluctuations of grafted microtubules provide evidence of a length-dependent persistence length. *Proc. Natl. Acad. Sci.*, 103(27):10248–10253, 2006. URL http://www.pnas.org/content/103/27/10248.abstract. Page(s) 67

[121] M. Pasquali and D. C. Morse. An efficient algorithm for metric correction forces in simulations of linear polymers with constrained bond length. *J. Chem. Phys.*, 116(5):1834–1838, 2002. Page(s) 68

[122] T. Perkins, D. Smith, and S. Chu. Single polymer dynamics in an elongational flow. *Science*, 276:2016, 1997. URL http://www.sciencemag.org/cgi/content/abstract/276/5321/2016. Page(s) 68

[123] F. Perrin. Mouvement brownien d'un ellipsoide (I). Dispersion diélectrique pour des molécules ellipsoidales. *J. Phys. Radium*, 5(10):33, 1934. Page(s) 22

[124] F. Perrin. Mouvement brownien d'un ellipsoide (II). Rotation libre et dépolarisation des fluorescences. Translation et dffusion de molecules ellipsoidales. *J. Phys. Radium*, 7(1):1, 1936. Page(s) 22

[125] K. N. Pham, A. M. Puertas, J. Bergenholtz, S. U. Egelhaaf, A. Moussaid, P. N. Pusey, A. B. Schofield, M. E. Cates, M. Fuchs, and W. C. K. Poon. Multiple Glassy States in a Simple Model System. *Science*, 296(5565):104–106, 2002. URL http://www.sciencemag.org/cgi/content/abstract/296/5565/104. Page(s) 7

[126] V. Pryamitsyn and V. Ganesan. Screening of hydrodynamic interactions in brownian rod suspensions. *J. Chem. Phys.*, 128(13):134901, 2008. URL http://link.aip.org/link/?JCP/128/134901/1. Page(s) 4, 41

[127] A. Puliafito and K. Turitsyn. Numerical study of polymer tumbling in linear shear flows. *Physica D*, 211:9–22, 2005. Page(s) 68, 75, 77, 80

[128] S. Ramanathan and D. C. Morse. Simulations of dynamics and viscoelasticity in highly entangled solutions of semiflexible rods. *Phys. Rev. E*, 76(1):010501, 2007. URL http://link.aps.org/abstract/PRE/v76/e010501. Page(s) 40, 41

[129] M. D. Rintoul. Precise determination of the void percolation threshold for two distributions of overlapping spheres. *Phys. Rev. E*, 62:68–72, 2000. Page(s) 15

[130] S. Romer, F. Scheffold, and P. Schurtenberger. Sol-gel transition of concentrated colloidal suspensions. *Phys. Rev. Lett.*, 85(23):4980–4983, 2000. Page(s) 7

[131] N. Saitô, K. Takahashi, and Y. Yunoki. The statistical mechanical theory of stiff chains. *J. Phys. Soc. Jpn.*, 22:219–226, 1967. Page(s) 68, 74

[132] M. J. Saxton. Anomalous diffusion due to obstacles: a Monte Carlo study. *Biophys. J.*, 66: 394–401, 1994. URL http://www.biophysj.org/cgi/content/abstract/66/2_Pt_1/394. Page(s) 7

[133] A. Scala, T. Voigtmann, and C. De Michele. Event-driven brownian dynamics for hard spheres. *J. Chem. Phys.*, 126(13):134109, 2007. URL http://link.aip.org/link/?JCP/126/134109/1. Page(s) 11, 12

[134] K. M. Schmoller, O. Lieleg, and A. R. Bausch. Cross-linking molecules modify composite actin networks independently. *Phys. Rev. Lett.*, 101(11):118102, 2008. URL http://link.aps.org/abstract/PRL/v101/e118102. Page(s) 3

[135] C. Schroeder, R. Teixeira, E. Shaqfeh, and S. Chu. Dynamics of DNA in the flow-gradient plane of steady shear flow: Observations and simulations. *Macromol.*, 38:1967–1978, 2005. Page(s) 68, 77, 78

[136] C. M. Schroeder, R. E. Teixeira, E. S. G. Shaqfeh, and S. Chu. Characteristic periodic motion of polymers in shear flow. *Phys. Rev. Lett.*, 95:018301, 2005. URL http://link.aps.org/abstract/PRL/v95/e018301. Page(s) 68, 77, 80, 84

[137] R. Shusterman, S. Alon, T. Gavrinyov, and O. Krichevsky. Monomer dynamics in double- and single-stranded DNA polymers. *Phys. Rev. Lett.*, 92(4):048303, 2004. Page(s) 67

[138] D. Smith, H. Babcock, and S. Chu. Single-polymer dynamics in steady shear flow. *Science*, 283:1724, 1999. URL http://www.sciencemag.org/cgi/content/abstract/283/5408/1724. Page(s) 68, 77, 84

[139] M. Smoluchowski. Zur kinetischen Theorie der Brownschen Molekularbewegung und der Suspensionen. *Ann. Phys. (Leipzig)*, 21:756, 1906. Page(s) 22

[140] D. Stauffer and A. Aharony. *Introduction to Percolation Theory*. Taylor & Francis, London, 2 edition, 1994. Page(s) 10, 16

[141] O. Stenull and H. Janssen. Conductivity of continuum percolating systems. *Phys. Rev. E*, 64 (5):56105, 2001. Page(s) 15

[142] S. H. Strogatz. *Nonlinear Dynamics and Chaos*. Westview Press, Cambridge, MA, 2000. Page(s) 76

[143] B. J. Sung and A. Yethiraj. The effect of matrix structure on the diffusion of fluids in porous media. *J. Chem. Phys.*, 128(5):054702, 2008. URL http://link.aip.org/link/?JCP/128/054702/1. Page(s) 7

[144] G. Szamel. Reptation as a dynamic mean-field theory: Study of a simple model of rodlike polymers. *Phys. Rev. Lett.*, 70(24):3744–3747, 1993. URL http://link.aps.org/abstract/PRL/v70/p3744. Page(s) 21, 48

[145] Y.-G. Tao, W. K. den Otter, J. T. Padding, J. K. G. Dhont, and W. J. Briels. Brownian dynamics simulations of the self- and collective rotational diffusion coefficients of rigid long thin rods. *J. Chem. Phys.*, 122(24):244903, 2005. URL http://link.aip.org/link/?JCP/122/244903/1. Page(s) 33, 41

[146] Y.-G. Tao, W. K. den Otter, J. K. G. Dhont, and W. J. Briels. Isotropic-nematic spinodals of rigid long thin rodlike colloids by event-driven brownian dynamics simulations. *J. Chem. Phys.*, 124(13):134906, 2006. URL http://link.aip.org/link/?JCP/124/134906/1. Page(s) 33, 41

[147] R. Teixeira, H. Babcock, E. Shaqfeh, and S. Chu. Shear thinning and tumbling dynamics of single polymers in the flow-gradient plane. *Macromol.*, 38:581–592, 2005. Page(s) 68, 70, 77

[148] I. M. Tolić-Nørrelykke, E.-L. Munteanu, G. Thon, L. Oddershede, and K. Berg-Sørensen. Anomalous diffusion in living yeast cells. *Phys. Rev. Lett.*, 93(7):078102, 2004. URL http://link.aps.org/abstract/PRL/v93/e078102. Page(s) 7

[149] S. Torquato and I. C. Kim. Efficient simulation technique to compute effective properties of heterogeneous media. *Appl. Phys. Lett.*, 55(18):1847–1849, 1989. URL http://link.aip.org/link/?APL/55/1847/1. Page(s) 7

[150] H. van Beijeren. Transport properties of stochastic Lorentz models. *Rev. Mod. Phys.*, 54(1): 195–234, 1982. Page(s) 9

[151] M. P. B. van Bruggen, H. N. W. Lekkerkerker, G. Maret, and J. K. G. Dhont. Long-time translational self-diffusion in isotropic and nematic dispersions of colloidal rods. *Phys. Rev. E*, 58 (6):7668–7677, 1998. URL http://link.aps.org/abstract/PRE/v58/p7668. Page(s) 21

[152] S. C. van der Marck. Network approach to void percolation in a pack of unequal spheres. *Phys. Rev. Lett.*, 77(9):1785–1788, 1996. Page(s) 15

[153] N. G. van Kampen. *Stochastic Processes in Physics and Chemistry*. Elsevier Science, Amsterdam, 2001. Page(s) 32, 70, 95, 97

[154] N. G. van Kampen and J. J. Lodder. Constraints. *Am. J. of Phys.*, 52(5):419–424, 1984. URL http://dx.doi.org/10.1119/1.13647. Page(s) 68

[155] J. M. J. van Leeuwen and A. Weijland. Non-analytic density behaviour of the diffusion coefficient of a Lorentzgas I. *Physica (Amsterdam)*, 36:457–490, 1967. Page(s) 9

[156] J. S. van Zon and P. R. ten Wolde. Green's-function reaction dynamics: A particle-based approach for simulating biochemical networks in time and space. *J. Chem. Phys.*, 123(23): 234910, 2005. URL http://link.aip.org/link/?JCP/123/234910/1. Page(s) 39

[157] G. Viramontes-Gamboa, M. Medina-Noyola, and J. L. Arauz-Lara. Brownian motion of colloidal particles in a model porous medium. *Phys. Rev. E*, 52(4):4035–4044, 1995. Page(s) 7

[158] T. Voigtmann and J. Horbach. Slow dynamics in ion-conducting sodium silicate melts: Simulation and mode-coupling theory. *Europhys. Lett.*, 74(3):459–465, 2006. Page(s) 7

[159] L. Vonna, L. Limozin, A. Roth, and E. Sackmann. Single-filament dynamics and long-range ordering of semiflexible biopolymers under flow and confinement. *Langmuir*, 21:9635–9643, 2005. Page(s) 71

[160] A. Weijland and J. M. J. van Leeuwen. Non-analytic density behaviour of the diffusion coefficient of a Lorentz gas II. *Physica (Amsterdam)*, 38:35, 1968. Page(s) 9

[161] M. Weiss, M. Elsner, F. Kartberg, and T. Nilsson. Anomalous subdiffusion is a measure for cytoplasmic crowding in living cells. *Biophys. J.*, 87(5):3518–3524, 2004. URL http://www.biophysj.org/cgi/content/abstract/87/5/3518. Page(s) 7

[162] C. H. Wiggins. *Elastohydrodynamics in the Biological Context*. PhD thesis, Princeton University, New Jersey, 1998. Page(s) 68

[163] C. H. Wiggins, D. Riveline, A. Ott, and R. E. Goldstein. Trapping and wiggling: Elastohydrodynamics of driven microfilaments. *Biophys. J.*, 74:1043–1060, 1998. Page(s) 71

[164] C. H. Wiggins, A. Montesi, and M. Pasquali. The stochastic spectral dynamics of bending and tumbling. arXiv:cond-mat/0307551, 2003. URL http://arxiv.org/abs/cond-mat/0307551. Page(s) 68, 73

[165] J. Wilhelm and E. Frey. Radial distribution function of semiflexible polymers. *Phys. Rev. Lett.*, 77:2581–2584, 1996. URL http://link.aps.org/abstract/PRL/v77/p2581. Page(s) 67

[166] R. G. Winkler, S. Keller, and J. O. Rädler. Intramolecular dynamics of linear macromolecules by fluorescence correlation spectroscopy. *Phys. Rev. E*, 73:041919, 2006. Page(s) 67

[167] E. Zaccarelli, S. V. Buldyrev, E. L. Nave, A. J. Moreno, I. Saika-Voivod, F. Sciortino, and P. Tartaglia. Model for reversible colloidal gelation. *Phys. Rev. Lett.*, 94:218301, 2005. URL http://link.aps.org/abstract/PRL/v94/e218301. Page(s) 7